MITIGATING COLD FLOW PROBLEMS OF BIODIESEL: STRATEGIES WITH ADDITIVES

A Thesis Submitted to the Committee on Graduate Studies

in Partial Fulfillment of the Requirements for the Doctor of Philosophy in the

Faculty of Arts and Science

TRENT UNIVERSITY

Peterborough, Ontario, Canada

© Copyright by Athira Mohanan 2015

Materials Science PhD. Graduate Program

January 2016

Abstract

Mitigating Cold Flow Problems of Biodiesel: Strategies with Additives

Athira Mohanan

The present thesis explores the cold flow properties of biodiesel and the effect of vegetable oil derived compounds on the crystallization path as well as the mechanisms at play at different stages and length scales. Model systems including triacylglycerol (TAG) oils and their derivatives, and a polymer were tested with biodiesel. The goal was to acquire the fundamental knowledge that would help design cold flow improver (CFI) additives that would address effectively and simultaneously the flow problems of biodiesel, particularly the cloud point (CP) and pour point (PP). The compounds were revealed to be fundamentally vegetable oil crystallization modifiers (VOCM) and the polymer was confirmed to be a pour point depressant (PPD).

The results obtained with the VOCMs indicate that two *cis*-unsaturated moieties combined with a *trans*-/saturated fatty acid is a critical structural architecture for depressing the crystallization onset by a mechanism wherein while the straight chain promotes a first packing with the linear saturated FAMEs, the kinked moieties prevent further crystallization. The study of model binary systems made of a VOCM and a saturated FAME with DSC, XRD and PLM provided a complete phase diagram including the thermal transformation lines, crystal structure and microstructure that impact the phase composition along the different crystallization stages, and elicited the competing effects of molecular

mass, chain length mismatch and isomerism. The liquid-solid boundary is discussed in light of a simple thermodynamic model based on the Hildebrand equation and pair interactions.

In order to test for synergies, the PP and CP of a biodiesel (Soy1500) supplemented with several VOCM and PLMA binary cocktails were measured using a specially designed method inspired by ASTM standards. The results were impressive, the combination of additives depressed CP and PP better than any single additive. The PLM and DSC results suggest that the cocktail additives are most effective when the right molecular structure and optimal concentration are provided. The cocktail mixture achieves then tiny crystals that are prevented from aggregating for an extended temperature range. The results of the study can be directly used for the design of functional and economical CFI from vegetable oils and their derivatives.

Keywords

Acknowledgements

As an international student in Canada, it was not easy for me to adapt here and pursue my PhD. I would never be able to finish this PhD without extensive help from many beautiful hearts in several ways. I am taking this pleasant opportunity to thank all of them.

First and foremost I thank my supervisor, Prof. Suresh S Narine for accepting me in his group. Without his incredible help and support it was unable for me to finish my PhD. I thank him for all the priceless learning I have achieved from his group and all the opportunities he has provided. I also thank all my supervisory committee members Dr. Anatoli Chkrebtii, Dr. Matthew Thompson, Dr. Bill Atkinson for all their valuable suggestions and support.

I would like to thank Dr. Laziz Bouzidi for mentoring me throughout my research time. His doors were always open for me to discuss my work, get right directions and suggestions. I thank him from for all his care, assistance, and the knowledge he has shared with me. I also thank Dr. Shaojun Li, for his help in the chemistry side of my project.

I must thank particularly Mr. Prasanth Kumar S. who has been incredibly supportive in my academic and personal life. Without his unconditional backing and valuable companionship I would not be able to finish my PhD.

I should thank all my colleagues, especially Ms. Latchmi Regunanan, Ms. Shegufa Merchant, Mr. Michael Floros, Mr. Michael Tessier, and Mr. Avinaash Persaud for their extensive help. I have learned the value of professionalism, mutual support and team work from them. I admit valuable help and support from Mr. Arun Gopinath L. who was my

Table of Contents

List of Figures

List of Schemes

List of Tables

List of Abbreviations

A	Area
ASTM	American Society for Testing and Materials
CFI	Cold Flow Improver
CFPP	Cold Filter Plugging Point
CLM	Chain Length Mismatch
CP	Cloud Point
CPD	Cloud Point Depressant
D	Dimer
DCL	Double Chain Length
DSC	Differential Scanning Calorimetry
EEE	Trielaidin
EOE	1,3-dielaidioyl -2-oleoyl-sn- glycerol
EEO	1,2-dielaidioyl -3-oleoyl-sn- glycerol
ESI-MS	Electrospray Ionization Mass Spectrometry
F	Fraction
FAME	Fatty Acid Methyl Ester
GC	Gas Chromatography
GPC	Gel Permeation Chromatography
H	Enthalpy
HPLC	High Performance Liquid Chromatography
LF	Liquid Fraction
LLP	1,2-dilinoleyol-3-palmitoyl-sn- glycerol
LLS	1,2-dilinoleyol-3-stearoyl-sn- glycerol
LPL	1,3-dilinoleyol-2-palmitoyl-sn- glycerol
LSL	1,3-dilinoleyol-2-stearoyl-sn- glycerol
LnPLn	1,3-dilinoleinoyl-2-palmitoyl-sn-glycerol
LnLnP	1,2-dilinoleinoyl-3-palmitoyl-sn-glycerol
LnLnS	1,2-dilinoleinoyl-3-staroyl-sn-glycerol
LnSLn	1,3-dilinoleinoyl-2-staroyl-sn-glycerol
MeLn	Methyl Linoleate
MeO	Methyl Oleate
MeS	Methyl Stearate
Mw	Molecular weight
MSBO	Self-Metathesized Soybean Oil
MTO	Self-Metathesized Triolein
NMR	Nuclear Magnetic Resonance
OOO	Triolein
OOE	1,2-dioleoyl-3-elaidioyl-sn- glycerol
OPO	1,3-dioleoyl-2-palmitoyl-sn- glycerol
OOP	1,2-dioleoyl-3-palmitoyl-sn- glycerol
OSO	1,3-dioleoyl-2-stearoyl-sn- glycerol
PP	Pour Point

PMTAG	Metathesized Palm Oil
PPD	Pour Point Depressant
PLM	Polarized Light Microscopy
PLMA	Poly Lauryl Methacrylate
Q	Quatrimers
SAXD	Small Angle X-Ray Diffraction
SSS	Tristerin
SSO	1,2-distearoyl-3-oleoyl-sn-glycerol
SOS	1,3-distearoyl-2-oleoyl-sn-glycerol
SF	Solid fraction
T	Temperature
T	Time
TAG	Triacylglycerol
TCL	Triple Chain Length
VOCM	Vegetable Oil Derived Crystallization Modifiers
WAXD	Wide Angle X-Ray Diffraction
XRD	X-ray Diffraction

Subscripts

C	Crystallization
F	Fractionation
M	Melting
P	Peak
R	Retention
On	Onset
Off	Offset
W	Weight
i/ind	Induction time
X	Molar Fraction

To My Parents

1.   Introduction

1.1   Motivation

Biodiesel is currently the subject of considerable research and development efforts due to the increase in demand for environmentally responsible alternatives to conventional fossil fuel [1, 2]. However, its use in countries which have prolonged cold winters such as Canada, the US and some parts of Europe is currently limited due to inherent cold flow issues. These problems are commonly mitigated with the use of cold flow improver (CFI) additives. However, current additives are generally not cost effective [3, 4] and cannot simultaneously address the most common operability parameters of biodiesel such as the cloud point (CP), the pour point (PP), and the cold filter plugging point (CFPP). It has become clear that the development of cost effective CFI additives specific to biodiesel is tributary of a more fundamental understanding of the role of the additive's structural elements in the overall crystallization and aggregation process of biodiesel mixtures. The disruptive effect that leads to the improvement of the cold flow characteristics of biodiesel is the result of specific interactions that the additive develops with the components of biodiesel at particular length scales along the phase transformation path from the liquid state until it cannot pour. Specific structural architectures are required for an additive to encourage the disruptive effects that can manifest in measurable depressions in the CP and PP, for example.

Vegetable oils appear to be the ideal feedstock from which effective CFI structures can be sourced not only because they are environment friendly renewable alternatives to petroleum but also because they are the best prospect source for compatible and biodiesel

specific chemical architectures. The present work was framed starting with the examination of the positive effect on the onset of crystallization of methyl soyate, a biodiesel made from soy bean oil, of a metathesized triacylglycerol (TAG) oil, namely the product of the self-metathesis of soybean oil stripped of its olefins (referred to simply as MSBO). MSBO was shown to depress the crystallization point of the biodiesel by ~ 2.5 °C at loadings as low as 1% w/w. [5]. The challenge was to determine the compounds in MSBO responsible for this behaviour and the requirements for such structures to disrupt the typical crystallization of the biodiesel, and uncover the specific mechanisms of their action. The goal was to acquire the fundamental knowledge specific to the phase behavior of biodiesel and additives systems, and establish the structure-function relationships relevant to the low temperature flow behavior of biodiesel so to enable the rational design of effective lipid-based CFI additives.

1.2   Biodiesel

At present, about 80% of the energy consumed globally is met using fossil fuels [6]. The related environmental problems and looming climate change crisis are driving strong research efforts to find environmentally responsible alternative fuel sources [7, 8]. Biodiesel, bioethanol, and biomethanol are some of the alternative bio-based energy resources that are nowadays common in the fuel market and fast growing.

Biodiesel is a particularly attractive fuel because it possesses many of the characteristics of conventional diesel and can be used neat or as blends with petroleum diesel in unmodified existing diesel engines [9]. It is made from triacylglycerols (TAG) oils and fats using a chemical reaction called transesterification [10]. During transesterification, the TAGs react with an alcohol in the presence of a catalyst to produce

monoalkyl esters and glycerol via the exchange of alkoxy moieties between the alcohol and the TAGs (Scheme 1.1). Although a variety of alcohols such ethanol and butanol can be used for the production of biodiesel, methanol is the most commonly used alcohol industrially because it is cheap and highly reactive [11, 12].
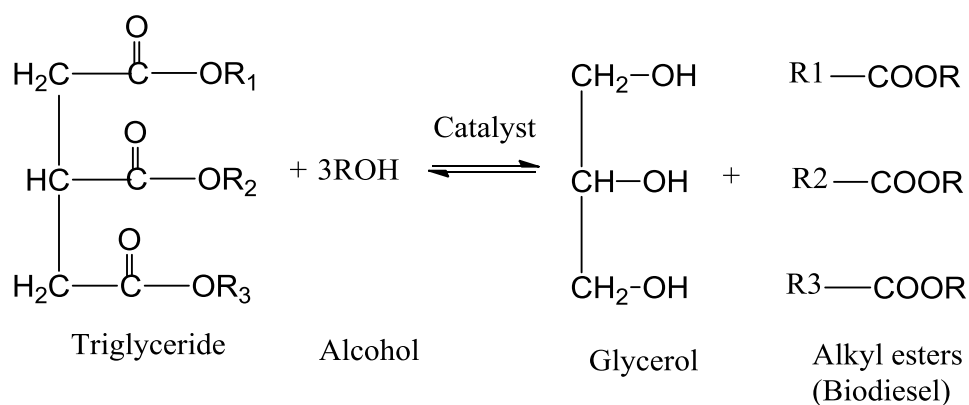
Scheme 1.1. Transesterification of a triacylglycerol molecule with an alcohol. R, R1, R2 and R3 represent alkyl groups.

The properties of biodiesel are determined by its composition inherited from the fatty acid profile of the source oil as well as the alcohol used for the transesterification [13]. As a result, biodiesel offers several important advantages such as a high cetane number (CN), inherent lubricity (even in blends of 1–2%), low toxicity, superior flash point, high biodegradability, and negligible sulfur content. Furthermore, its use results in significant reduction of exhaust emissions. It also presents certain disadvantages over conventional diesel fuel, such higher feedstock cost, inferior storage and oxidative stability, lower volumetric energy content, inferior low temperature operability, and in some cases, higher NOx exhaust emissions [14].

The quality of biodiesel accepted for commercial application is regulated by national or regional standards such ASTM D6751 in the United States and EN 14214 in the European Union. The quality of biodiesel is determined by certain fuel properties which are specified in the standards. The most relevant properties of a biodiesel specified in the standards are kinematic viscosity, oxidative stability, cetane number, acid value, flash point, specific gravity and flow properties [15]. The temperature operability parameters of biodiesel such as the CP, PP and CFPP are also determined by methods specified by these standards. The most common test methods for the CP, PP and CFPP are ASTM D2500, ASTM D97 or D5949 and ASTM D6371, respectively.

1.3   Cold Flow Problems of Biodiesel

The low temperature flow problems of biodiesel are a major issue that prevents its wider use in cold climates. Common biodiesels present cloud points and pour points that are much higher than petro-diesel. For example, soybean oil and palm oil biodiesel present CP values of ~0 °C and 15 °C, respectively, whereas, No. 1 diesel has a CP of about -40 °C. Furthermore, biodiesels tend to have a narrow range of temperatures between their CP and PP, adding to their cold weather operability problems.

Most of the cold flow problems of common biodiesel are associated with the relatively high crystallization temperature (25 °C to 35 °C) of its saturated fatty acid methyl ester (FAME) components, such as methyl stearate (MeS) and methyl palmitate (MeP) prevalent in the north American biodiesel, and subsequent rapid transformation into a gelling network [13, 16]. The low temperature performance of biodiesel is therefore fundamentally a lipid crystallization and aggregation issue.

1.4 Crystallization of Biodiesel

Considerable efforts have been devoted to the study of lipid systems and understanding of the interactions implicated in the crystallization process. The resulting abundant literature has been extensively reviewed, see for example [17-22]. The knowledge so gathered as well as the variety of experimental and theoretical tools available for the study of fat crystallization can be directly used to help investigate biodiesel systems.

Like any other lipid system, biodiesel crystallization also involves three main stages: nucleation, crystal growth, and agglomeration. These stages are reflected in the formation of defined structural hierarchies of a complex fat network. A schematic representation of the crystallization steps of biodiesel is shown in Figure 1.1 Nucleation is the primary stage of crystallization. It is a two-step process; first, amorphous ensembles of molecules form in the undercooled liquid and then transform into ordered small entities; the nuclei [23]. The stable nuclei grow into crystal domains of specific crystalline form. The nanoscale nature and bimolecular lamellar structure of these domains have been recently visualized by transmission electron microscopy [24]. These primary domains cluster to form larger entities held together by weak attractive dispersion forces like the London-van der Waals interactions and short range binding forces [25]. These clusters may be seen with the naked eye when they reach micrometer dimensions. At this stage of biodiesel crystallization, the microstructures can be detected by the cloud point test. The microstructures eventually aggregate and create a three dimensional network which traps the remaining liquid. This is the stage of biodiesel crystallization where it stops pouring. This point is detected by the pour point test.
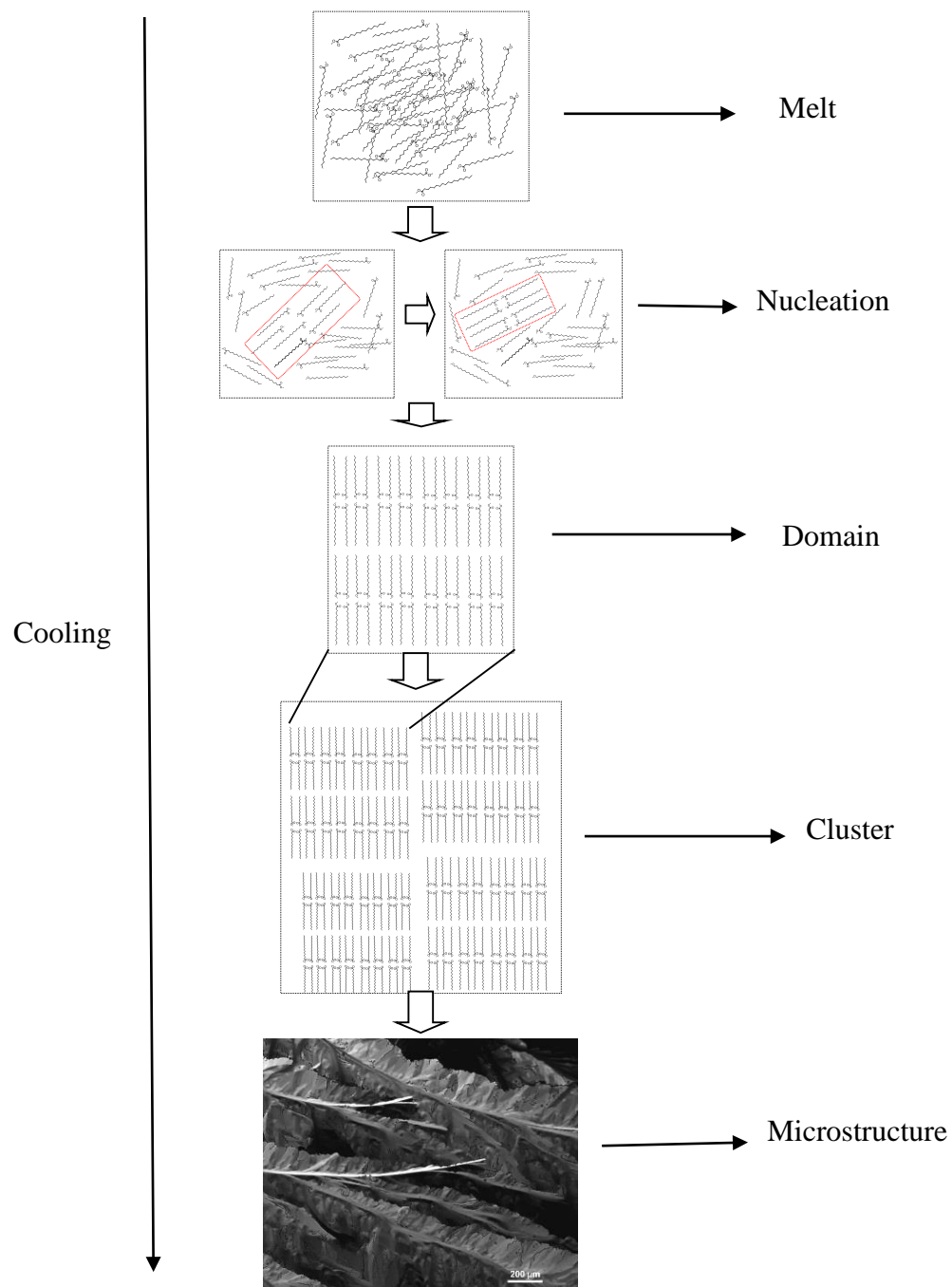
Figure 1.1. Structural hierarchy of a fatty acid methyl ester crystal network.

The thermal transition behavior of lipid systems is normally investigated with differential scanning calorimetry (DSC) [26]. The DSC technique is particularly suitable for studying the liquid-solid phase transformation behaviour of biodiesel. It was shown, for example, that characteristics such as the onset temperature of crystallization and the first peak of crystallization are closely associated with the CP and the PP of biodiesel, and can also be reliably used to assess its cold flow properties [27, 28]. In fact, DSC is being increasingly used to investigate the flow properties of biodiesel in lieu of and in correlation with the CP, PP and CFPP [29, 30]. The DSC technique even offers additional benefits by providing important information on the phase composition and trajectories involved in the thermal transformation of the biodiesel.

Lipid systems do not always crystallize into their thermodynamically most stable phases. Due to the high flexibility of their long chain hydrocarbons, lipid molecules can arrange into different crystalline forms depending on the nature of the molecules and the processing conditions. These crystal phases, known as polymorphs, can be formed directly from the melt upon cooling or via crystallization mediated by melting [31]. The crystal structures of lipid systems are normally described by the layering type of their hydrocarbon chains and the type of the subcell structure within the layers. The main subcell hydrocarbon-chain packing modes are commonly denoted as the α, β' and β polymorphs [32].

The phase transition behavior of biodiesel and its mixtures can be studied *in situ* effectively with time- and temperature-resolved (t/TR) techniques. Such techniques are commonly used for the description of the phase structures and phase trajectories of lipid materials [33]. More crucially, lipids crystallize along paths that often involve metastable

intermediates [34] that can only be fully elucidated with t/TR techniques such as temperature controlled x-ray diffraction (XRD) coupled with DSC.

The microstructure is an important aspect directly related to the function of lipids that is commonly studied with polarized light microscopy (PLM). The microstructure development of the material can be investigated with t/TR- PLM. The temperature at which the first white spot appears in the PLM is considered as the induction temperature of crystallization and can be related to the DSC onset temperature of crystallization. PLM also allows access to the nucleation parameters when the rate of nucleation is low, i.e., practically, when individual crystals can be individually counted and considered as nuclei [35].

1.5   Phase behavior and Phase Diagrams of Biodiesel Systems

Phase diagrams are increasingly used in biodiesel studies, particularly at the liquid-solid transition as it is relevant to the behaviour of the individual components of biodiesel mixtures below the cloud point and therefore to its low temperature performance. DSC data, and especially the heating thermograms of multi-component mixtures are usually used for the construction of equilibrium and pseudo-equilibrium phase diagrams [36-38]. The variety of special thermal transitions that occur in lipid mixtures, such as eutectic [17, 39], monotectic [40], peritectic and metatectic behavior [38], and the formation of solid solutions [41] or molecular compounds [42] are represented in a phase diagram with special transformation points and lines.

A growing body of work including the phase diagrams of mixtures relevant to biodiesel such as the binary and ternary mixtures of saturated fatty esters [43, 44], mixed

saturated and unsaturated fatty esters [45], as well as biodiesel components with additives [46] have been probing the details of biodiesel crystallization. The determination and characterization of the transformation points in biodiesel systems can be utilized to promote desired transformations such as those motivated by eutectic relationships, which may be particularly important for biodiesel low temperature performance, since these provides the lowest crystallization points of mixtures [38] and avoided unwanted transformations such as encountered, for example, with metatectic relationships which leads to the formation of a significant amount of solids below the CP which may result in high PP [38].

The thermodynamic simulation of phase diagrams of model systems help elucidate the role of individual or group components in the transitions of interest and therefore provide important indications on how to improve the low temperature performance of biodiesel from a molecular perspective. The thermodynamic modeling of the phase boundaries in the phase diagrams of lipids is typically approached similarly to other equilibria and pseudo-equilibria systems [47-49]. Excess Gibbs free energy models are becoming a common tool for the description of the solid–liquid equilibria (SLE) of these mixtures, including systems presenting polymorphic transition and solid solutions [50, 51] and the formation of molecular compounds, including peritectic compounds [49, 52]. The most common thermodynamic models used for the calculation of the phase diagrams of lipids include activity based models such as Margules 2 [49] and Margules 3 [53] and UNIQAC (short for UNIversal QUAsiChemical) [36]. The thermodynamic model based on the Hildebrand equation [54] coupled with the Bragg-William approximation for non-ideality of mixing [55] is also popular and is a commonly used model to calculate the liquid-solid boundaries in the phase diagram of lipid mixtures. This model enables a simple

quantification of the molecular pair interactions involved during the liquid-solid transformations as well as of the miscibility behavior of the compounds of the system [47, 48, 56, 57].

1.6   Mitigating the Cold Flow Problems of Biodiesel: Strategies with Additives

Several approaches to mitigate the poor low-temperature performance of biodiesel have been tried over the past decade including the diversification of the fuel composition through genetic, chemical or/and physical modification of the feedstock, and treatment with cold flow improvers (CFI) additives [58]. Treatment with CFI additives is the most common approach. The strategies with additives are designed to decrease the operability temperatures of biodiesel such as the CP the PP and the CFPP. Many examples and reviews of such additives and their function are reported in the scientific and patent literature (see for example [59-63] and the works cited therein).

The existing CFI additives can be classified into two large categories. The first category comprises so-called wax crystalline modifiers (WCM) or simply crystallization modifiers, intended to delay the crystallization and promote the formation of small crystals. These additives participate and affect one or more stage of the crystallization process, i.e., nucleation, growth, or agglomeration. The WCMs mainly improve the CP and beneficially affect the CFPP [64]. Most of the additives which depress the CP work by disturbing the crystallization process at small length scales, principally at the nucleation and early stages of growth [65]. The growth and aggregation stages can however, follow quite rapidly, drastically limiting their effect on the PP.

The second category includes primarily pour point depressants (PPDs) designed to aid pumpability. They are typically composed of low molecular-weight copolymers and are similar in structure and melting point to *n*-alkane paraffins [10]. Some of the most efficient PPDs include olefin-ester copolymers [66], ethylene vinyl acetate [66], poly methyl acrylate [66] and poly lauryl methacrylate (PLMA) [67]. These additives function as crystal growth limiters, inhibiting crystalline growth without affecting nucleation. The PPDs affect CP and filterability of biodiesel marginally [68, 69].

The most depression in PP reported so far for a PPD is 30 °C, achieved by PLMA on canola biodiesel at 1.0%wt loading [70]. Interestingly, polymer additives do not work in high concentration. For example, the addition of 0.04% polymethyl acrylate into waste cooking oil biodiesel reduced its PP by 8 °C and CP by 1 °C but when the loading was doubled to 0.08%, it reduced PP by only 2 °C and CP by 1 °C [69]. The peculiar action of these polymer additives was explained by a mechanism in which the polymer is adsorbed to the growing surface, preventing the active growth faces from participating in further growth [71-73].

1.7   Gaps of Knowledge

Most commercial CFI additives were originally designed with a high degree of structural selectivity to treat petroleum derivatives, and generally fail to reduce the CP in neat and blended biodiesel in a significant way [74, 75]. Overall, the failure of the existing additives was due to their inability to properly affect the crystallization of the FAME beyond one level of structure. The design of additives that would have the structural architecture capable of adequately disturbing the crystallization path of biodiesel requires

a more comprehensive understanding of the phase behavior of the FAMEs of biodiesel in neat mixtures and in the presence of additives.

The literature show overwhelming evidence that despite the variety of additives, the mechanisms at the heart of the suppression of CP and PP of biodiesel is controlled by similar dominating structural drivers. The effectiveness of an additive can be traced back to the presence (or not) of structural elements that provide the necessary local interactions that in first favor the early attractions with the saturated molecules of biodiesel and then provide repulsions that are sufficient to prevent their packing. However, before the present work and to the best of our knowledge, neither the structures nor the mechanism were described in any detail.

A single additive that can simultaneously depress both the CP and the PP remains elusive. This is quite understandable because such a compound is required to have a chemical structural architecture that is versatile enough to develop specific interactions capable of altering the crystallization process at each of its very length different scales or stages. Although such additives maybe possible and maybe discovered serendipitously, the actual fundamental knowledge of the mechanism(s) of action at such wide length scales is not sufficient to design a universal single additive which would congruently contain both the structural features of a CPD and a PPD.

In order to design efficient CFI additives of biodiesel, it is imperative to develop compounds with increased selectivity towards biodiesel. Such compounds may well be derived from vegetable TAG oil and their derivatives, the closest homologues to biodiesel. The actual repository of studies of CFIs derived from vegetable oils is very limited.

The metathesis of vegetable oils provides new promising lipid based CFI architectures that is just beginning to be explored. The investigation of the compounds and the structural details from these reactions are still underway. The challenge, like with metathesized soybean oil [5] or ozonized vegetable oil [76] is to find the compounds and the specific structural elements responsible for the disruption to biodiesel crystallization, if any, and the mechanism(s) of their action.

The elucidation of the mechanism of action of additives, and the establishment of structure-function relationships of the additive and its mixtures with biodiesel or its individual components are critical for the rational design of more effective additives. Phase behaviour studies are particularly important to understand the mechanism of action of additive molecules on the crystallization and flow of fatty esters. Unfortunately, only a few number of such studies are available in the literature. In particular, one can single out the binary phase behaviour of fatty acid methyl esters with alkenes investigated to understand the behaviour of biodiesel in diesel fuel blends [46]. There are no reports of phase behaviour studies of FAMEs with additive molecules. Thus, the understanding that would emerge from the study of such model systems is missing. Also missing is how additives inhibit FAME crystallization at the different stages and length scales involved.

1.8 Objectives

The present work aims at determining the structural architectures in a complex lipid mixture, namely the product of the self-metathesis of soy bean oil (MSBO), that has been shown to effectively depress the crystallization of biodiesel, reveal the mechanism of action of these structures, and establish the structure-function relationships driving the phase

behavior of biodiesel-additive mixtures. The following are the major objectives of the present thesis.

I. Uncover the compounds of MSBO responsible for the depression of the onset temperature of crystallization of biodiesel and identify the structural elements responsible for the disruption of crystallization.

    a) Fractionate MSBO into different "families of compounds" using column chromatography and crystallization fractionation

    b) Investigate the effect of the different fractions of MSBO on biodiesel crystallization and identify the most effective structures

    c) Use model systems such as metathesized triolein (MTO) and its fractions, pure TAGs and oligomers of TAGs all present in MSBO to identify the structural architectures that are at the origin of the disruption of biodiesel crystallization.

II. Investigate the mechanism of action of the most effective additives derived from MSBO and establish the structure-function relationships.

    a) Study model binary systems made of the most effective structured additives and the saturated FAMEs prevalent in biodiesel, such as MeS and MeP.

    b) Use the crystal structure, polymorphism, thermal transition and microstructure data to construct the phase diagrams of these FAME-Additive systems.

    c) Use a thermodynamic model that takes into account pair interactions to calculate the liquidus line in the phase diagrams (solid-liquid equilibria) in order to evaluate the intermolecular interactions and the miscibility in the biodiesel-additive mixtures.

III. Investigate possible synergies between selected crystallization modifiers derived from vegetable oils (VOCMs) and pour point depressants (PPDs) and whether they would affect both CP and PP simultaneously and significantly.

   a) Design an apparatus based on ASTM standards to measure the CP and PP accurately so one can compare the results with the data reported by industry R&D and other biodiesel stakeholders.

   b) Test the most effective VOCMs in combination with a PPD that has a demonstrated effect on PP and optimize the concentration of the VOCM and PPD in the cocktail additive mixtures for the CP and PP.

   c) Establish a fundamental understanding of the synergies at work through the thermal transition behaviour and microstructure development of biodiesel in the presence of the cocktail additives

1.9 Hypotheses

In order to attain the goals of the study, the following hypotheses were formulated and tested.

I. MSBO comprise compounds which have the structural elements that disrupt the crystallization of biodiesel

   a) If not all the molecules of MSBO are functional, then only particular components or families of compounds of MSBO are effective and result in the depression of the onset temperature of crystallization of biodiesel

   b) The effective molecules of MSBO possess specific structural elements that help the interaction with biodiesel molecules in such a way to prevent the packing of biodiesel molecules, particularly its saturated FAMEs.

c) If the effectiveness of the additives depends on a particular structural architecture, then model systems such as MTO and its compounds, structured TAGs and TAG oligomers, because of their controlled specified structures, such as size, number of *cis/trans* unsaturated fatty acids and saturated fatty acids, and their positional configuration will have marked different effects on biodiesel crystallization.

II. The most effective components of MSBO disrupt the crystallization biodiesel starting at the nucleation stages through a mechanism that is determined by the uniqueness of their structure.

a) The effect of the additives at the nucleation and growth stages will be reflected measurably in the crystal structure and the microstructure of the biodiesel, particularly evidently on its saturated FAMEs.

b) The interaction between the additives and the FAMEs determines the solubility behavior in the liquid and solid states, and changes in solubility due to the structural features such as chain length, chain length mismatch, symmetry and molar mass or oligomerization level of the additives will result in changes in the polymorphism, phase trajectory, phase composition and microstructure development of the additive biodiesel mixtures, particularly evidently its saturated FAMEs.

III. The combination of a vegetable oil derived crystallization modifier (VOCM) and a pour point depressant (PPD) can provide significantly higher depressions in both the CP and the PP of biodiesel compared to the individual contributions through synergistic effects.

a) A VOCM combined with a PPD will affect the nucleation of the saturated FAMEs of biodiesel and provide a growing crystal surface that is most favorable for the polymer additive to adsorb and provide the barrier for further growth and further aggregation.

b) The optimization of the concentration of the VOCM and PPD in the cocktail mixtures will result in the optimum synergetic effects which will lead to important depressions in both CP and PP.

1.10 Thesis Outline

By addressing each of the objectives listed in Section 1.8, this work is expected to provide the fundamental understanding necessary for the design of economical and effective lipid-based additives which can be used to solve the cold flow problems of biodiesel. These are described in this thesis as follows:

Chapter 2 presents the results of the study conducted in order to reveal the compounds in MSBO responsible for the crystallization disruption of biodiesel, the structural elements behind their action and the configuration of the additives that are most effective (Objective 1). Chapter 3-6 present four studies of model binary systems made of a select vegetable oil derived crystallization modifier (VOCM) and a saturated FAME (MeS or MeP). The studies investigate the mechanisms of action of the effective VOCM additives at the different length scales of biodiesel crystallization and establishes the structure-function relationships (Objective 2). The phase behavior and the complete phase diagram of the 1, 3 dioleoyl 2-palmitoyl-sn-glycerol/methyl palmitate (OPO/MeP), 1, 3 dioleoyl 2-palmitoyl-sn-glycerol/methyl stearate (OPO/MeS), 1,2 dioleoyl 3-stearoyl -sn-glycerol/methyl stearate (SOO/MeS) and dimer of OPO/MeP binary systems are presented

in Chapter 3-6, respectively. The effect of chain length and similarity in structural aspects (Chapter 3), chain length mismatch (Chapter 4), and positional isomerism or symmetry (Chapter 5) are highlighted. The effect of oligomerization on the crystallization of saturated FAMEs is explored in chapter 6. Chapter 7 reports on the studies conducted to probe the synergistic action of VOCMs and PPDs on the crystallization and low temperature flow properties of biodiesel and the mechanisms of their action (Objective 3). A final conclusion and the implications of this study are provided in Chapter 8.

1.11 References

[1] Droege P. Renewable Energy and the City: Urban Life in an Age of Fossil Fuel Depletion and Climate Change. B Sci Technol Soc. 2002;22(2):87-99.

[2] Shafiee S, Topal E. When will fossil fuel reserves be diminished? Energy Policy. 2009;37(1):181-9.

[3] Dunn R, Shockley M, Bagby M. Improving the low-temperature properties of alternative diesel fuels: Vegetable oil-derived methyl esters. J Am Oil Chem Soc. 1996;73(12):1719-28.

[4] Smith PC, Ngothai Y, Dzuy Nguyen Q, O'Neill BK. Improving the low-temperature properties of biodiesel: Methods and consequences. Renew Energ. 2010;35(6):1145-51.

[5] Christensen SA, DiBiase SA, Rizvi SQA. Cold flow additives. In: EPO, editor. C10L 1/19 (2006.01); C10L 1/224 (2006.01) ed2012.

[6] Suganthi L, Samuel AA. Energy models for demand forecasting—A review. Renew Sust Energy Rev. 2012;16(2):1223-40.

[7] McGlade C, Ekins P. The geographical distribution of fossil fuels unused when limiting global warming to 2 [deg]C. Nature. 2015;517(7533):187-90.

[8] Nejat P, Jomehzadeh F, Taheri MM, Gohari M, Abd. Majid MZ. A global review of energy consumption, CO_2 emissions and policy in the residential sector (with an overview of the top ten CO_2 emitting countries). Renew Sust Energy Rev. 2015;43:843-62.

[9] Graboski MS, McCormick RL. Combustion of fat and vegetable oil derived fuels in diesel engines. Prog Energ Combust. 1998;24(2):125-64.

[10] Knothe G, Van Gerpen J, Krahl J. The Biodiesel Handbook. Champaign, IL: AOCS Press; 2005. p. 286.

[11] Fukuda H, Kondo A, Noda H. Biodiesel fuel production by transesterification of oils. J biosci bioeng. 2001;92(5):405-16.

[12] Knothe G. "Designer" Biodiesel: Optimizing Fatty Ester Composition to Improve Fuel Properties. Energy Fuels. 2008;22(2):1358-64.

[13] Knothe G. Dependence of biodiesel fuel properties on the structure of fatty acid alkyl esters. Fuel Process Technol. 2005;86(10):1059-70.

[14] Fazal MA, Haseeb ASMA, Masjuki HH. Biodiesel feasibility study: An evaluation of material compatibility; performance; emission and engine durability. Renew Sust Energ Rev. 2011;15(2):1314-24.

[15] Bajpai D, Tyagi VK. Biodiesel: Source, production, composition, properties and its benefits. J Oleo Sci. 2006;55(10):487-502.

[16] Dunn RO. Crystallization behavior of fatty acid methyl esters. J Am Oil Chem Soc. 2008;85(10):961-72.

[17] Timms R. Phase behaviour of fats and their mixtures. Prog Lipid Res. 1984;23(1):1-38.

[18] Sato K. Solidification and phase transformation behaviour of food fats - a review. Fett-Lipid. 1999;101(12):467-74.

[19] Sato K. Crystallization behaviour of fats and lipids - a review. Chem Eng Sci. 2001;56(7):2255-65.

[20] Sato K, Ueno S, Yano J. Molecular interactions and kinetic properties of fats. Progr Lipid Res. 1999;38(1):91-116.

[21] Himawan C, Starov VM, Stapley AGF. Thermodynamic and kinetic aspects of fat crystallization. Adv Colloid Interfac. 2006;122(1-3):3-33.

[22] Ghotra BS, Dyal SD, Narine SS. Lipid shortenings: a review. Food Res Int. 2002;35(10):1015-48.

[23] Erdemir D, Lee AY, Myerson AS. Nucleation of Crystals from Solution: Classical and Two-Step Models. Acc Chem Res. 2009;42(5):621-9.

[24] Acevedo NC, Marangoni AG. Nanostructured Fat Crystal Systems. Annu Rev Food Sci Technol. 2015;6:71-96.

[25] Marangoni AG, Acevedo N, Maleky F, Co E, Peyronel F, Mazzanti G, et al. Structure and functionality of edible fats. Soft Matter. 2012;8(5):1275-300.

[26] Chow CK. Fatty acids in foods and their health implications: CRC Press, 2007.

[27] Lee I, Johnson L, Hammond E. Use of branched-chain esters to reduce the crystallization temperature of biodiesel. J Am Oil Chem Soc. 1995;72(10):1155-60.

[28] Dunn R. Thermal analysis of alternative diesel fuels from vegetable oils. J Am Oil Chem Soc. 1999;76(1):109-15.

[29] Garcia-Perez M, Adams TT, Goodrum JW, Das K, Geller DP. DSC studies to evaluate the impact of bio-oil on cold flow properties and oxidation stability of bio-diesel. Bioresour Technol. 2010;101(15):6219-24.

[30] Claudy P, Létoffé J-M, Neff B, Damin B. Diesel fuels: determination of onset crystallization temperature, pour point and filter plugging point by differential scanning calorimetry. Correlation with standard test methods. Fuel. 1986;65(6):861-4.

[31] Sato K, Ueno S. Polymorphism in fats and oils. Bailey's industrial oil and fat products. 2005.

[32] Larsson K. Physical Properties - Structural and Physical Characteristics. In: Gunstone FD, Harwood JL, Padley FB, editors. The Lipid handbook. London: Chapman and Hall; 1986. p. 335-77.

[33] Sato K, Ueno S. Physical properties of fats in food. In: Rajah KK, editor. Fats in Food Technology. 2nd ed. Chicester, UK: John Wiley & Sons, Ltd; 2014. p. 1-38.

[34] Sato K. Molecular aspects in fat polymorphism. In: Widlak N, Hartel R, Narine S, editors. Crystallization and Solidification Properties of Lipids. Champaign, USA: Am Oil Chem Soc.; 2001. p. 1-16.

[35] Marangoni AG. The nature of fractality in fat crystal networks. Trends Food Sci Technol. 2002;13(2):37-47.

[36] Boros L, Batista MLS, Vaz RV, Figueiredo BR, Fernandes VFS, Costa MC, et al. Crystallization Behavior of Mixtures of Fatty Acid Ethyl Esters with Ethyl Stearate. Energy Fuels. 2009;23:4625-9.

[37] Costa MC, Boros LAD, Batista MLS, Coutinho JAP, Krahenbuhl MA, Meirelles AJA. Phase diagrams of mixtures of ethyl palmitate with fatty acid ethyl esters. Fuel. 2012;91(1):177-81.

[38] Costa MC, Boros LAD, Coutinho JAP, Krahenbuhl MA, Meirelles AJA. Low-Temperature Behavior of Biodiesel: Solid-Liquid Phase Diagrams of Binary Mixtures Composed of Fatty Acid Methyl Esters. Energy Fuels. 2011;25(7):3244-50.

[39] Ikeda E, Ueno S, Miyamoto R, Sato K. Phase Behavior of a Binary Mixture of 1,3-Dipalmitoyl-2-oleoyl-sn-glycerol and 1,3-Dioleoyl-2-palmitoyl-sn-glycerol in n-Dodecane Solution. J Phys Chem B. 2010;114(34):10961-9.

[40] Hastie J, Kihlborg L, Metselaar R, Thackeray132 M. Definitions of terms relating to phase transitions of the solid state. 1994.

[41] Minato A, Ueno S, Smith K, Amemiya Y, Sato K. Thermodynamic and kinetic study on phase behavior of binary mixtures of POP and PPO forming molecular compound systems. J Phys Chem B. 1997;101(18):3498-505.

[42] Takeuchi M, Ueno S, Sato K. Crystallization kinetics of polymorphic forms of a molecular compound constructed by SOS (1,3-distearoyl-2-oleoyl-sn-glycerol) and SSO (1,2-distearoyl-3-oleoyl-rac-glycerol). Food Res Int. 2002;35(10):919-26.

[43] Costa MC, Boros LAD, Souza JA, Rolemberg MP, Krahenbuhl MA, Meirelles AJA. Solid-Liquid Equilibrium of Binary Mixtures Containing Fatty Acids and Triacylglycerols. J Chem Eng Data. 2011;56(8):3277-84.

[44] Robustillo MD, Barbosa DF, de Almeida Meirelles AJ, de Alcântara Pessôa Filho P. Solid–liquid equilibrium in ternary mixtures of ethyl laurate, ethyl palmitate and ethyl myristate. Fluid Phase Equilib. 2014;361:188-99.

[45] Robustillo MD, Barbosa DF, Meirelles AJdA. Solid-liquid equilibrium in ternary mixtures of ethyl oleate, ethyl laurate and ethyl palmitate. Fluid Phase Equilib. 2012.

[46] Benziane M, Khimeche K, Dahmani A, Nezar S, Trache D. Experimental determination and prediction of (solid+ liquid) phase equilibria for binary mixtures of heavy alkanes and fatty acids methyl esters. J Therm Anal Calorim. 2013;112(1):229-35.

[47] Lee AG. Lipid Phase-Transitions and Phase-Diagrams .1. Lipid Phase-Transitions. Biochim Biophys Acta. 1977a;472(2):237-81.

[48] Lee AG. Lipid Phase-Transitions and Phase-Diagrams .2. Mixtures Involving Lipids. Biochim Biophys Acta. 1977b;472(3-4):285-344.

[49] Slaughter DW, Doherty MF. Calculation of solid-liquid equilibrium and crystallization paths for melt crystallization processes. Chem Eng Sci. 1995;50(11):1679-94.

[50] Maximo GJ, Costa MC, Meirelles AJA. The Crystal-T algorithm: a new approach to calculate the SLE of lipidic mixtures presenting solid solutions. PCCP. 2014;16(31):16740-54.

[51] Santos MTd, Roux GACL, Joulia X, Gerbaud V. Solid-Liquid Equilibrium Modelling and Stability Tests for Triacylglycerols Mixtures. In: Rita Maria de Brito Alves CAOdN, Evaristo Chalbaud B, editors. Computer Aided Chemical Engineering: Elsevier; 2009. p. 885-90.

[52] Costa MC, Rolemberg MP, Boros LAD, Krahenbuhl MA, de Oliveira MG, Meirelles AJA. Solid-liquid equilibrium of binary fatty acid mixtures. J Chem Eng Data. 2007;52(1):30-6.

[53] Maximo GJ, Carareto NDD, Costa MC, dos Santos AO, Cardoso LP, Krähenbühl MA, et al. On the solid–liquid equilibrium of binary mixtures of fatty alcohols and fatty acids. Fluid Phase Equilib. 2014;366(0):88-98.

[54] Hildebrand JH. Solubility XII. Regular solutions. J Am Chem Soc. 1929;51:66-80.

[55] Bragg WL, Williams EJ. The effect of thermal agitation on atomic arrangement in alloys. Proc R Soc. 1934;145(855):699-730.

[56] Abes M, Bouzidi L, Narine SS. Crystallization and phase behavior of 1,3-propanediol esters II. 1,3-Propanediol distearate/1,3-propanediol dipalmitate (SS/PP) and 1,3-propanediol distearate/1,3-propanediol dimyristate (SS/MM) binary systems. Chem Phys Lipids. 2007;150(1):89-108.

[57] Boodhoo MV, Bouzidi L, Narine SS. The binary phase behavior of 1, 3-dicaproyl-2-stearoyl- sn-glycerol and 1, 2-dicaproyl-3-stearoyl- sn-glycerol. Chem Phys Lipids. 2009;157(1):21-39.

[58] Knothe G. Biodiesel: Current Trends and Properties. Top Catal. 2010;53(11):714-20.

[59] Sorate KA, Bhale PV. Biodiesel properties and automotive system compatibility issues. Renew Sust Energy Rev. 2015;41(0):777-98.

[60] Zhang X, Rong J, Chen H, He C, Wang Q. Current Status and Outlook in the Application of Microalgae in Biodiesel Production and Environmental Protection. Front. Energy Res. 2014;2:32.

[61] Srivastava SP, Hancsók J. Fuel Additives. Fuels and Fuel-Additives: John Wiley & Sons, Inc; 2014. p. 177-269.

[62] Liu G. Development of low-temperature properties on biodiesel fuel: a review. International Journal of Energy Research. 2015;DOI: 10.1002/er.3334(Published Online March 2015).

[63] Makarevičienė V, Kazancev K, Kazanceva I. Possibilities for improving the cold flow properties of biodiesel fuel by blending with butanol. Renew Energ. 2015;75(0):805-7.

[64] Erhan SZ, Dunn RO, Knothe G, Moser BR. Fuel Properties and Performance of Biodiesel. In: Hou CT, Shaw J-F, editors. Biocatalysis and Bioenergy. Hoboken, NJ: John Wiley & Sons, Inc; 2008. p. 3-58.

[65] Ribeiro NM, Pinto AC, Quintella CM, da Rocha GO, Teixeira LS, Guarieiro LL, et al. The role of additives for diesel and diesel blended (ethanol or biodiesel) fuels: a review. Energy Fuels. 2007;21(4):2433-45.

[66] Boshui C, Yuqiu S, Jianhua F, Jiu W, Jiang W. Effect of cold flow improvers on flow properties of soybean biodiesel. Biomass Bioenergy. 2010;34(9):1309-13.

[67] Chastek TQ. Improving cold flow properties of canola-based biodiesel. Biomass Bioenergy. 2011;35(1):600-7.

[68] Sern CH, May CY, Zakaria Z, Daik R, Foon CS. The effect of polymers and surfactants on the pour point of palm oil methyl esters. Eur J Lipid Sci Technol. 2007;109(4):440-4.

[69] Wang J, Cao L, Han S. Effect of polymeric cold flow improvers on flow properties of biodiesel from waste cooking oil. Fuel. 2014;117, Part A(0):876-81.

[70] Chastek TQ. Improving cold flow properties of canola-based biodiesel. biomass and bioenergy. 2011;35(1):600-7.

[71] Zhang J, Wu C, Li W, Wang Y, Cao H. DFT and MM calculation: the performance mechanism of pour point depressants study. Fuel. 2004;83(3):315-26.

[72] Zhang J, Wu C, Li W, Wang Y, Han Z. Study on performance mechanism of pour point depressants with differential scanning calorimeter and X-ray diffraction methods. Fuel. 2003;82(11):1419-26.

[73] Zhang H, Liu H, Wang S. A new alternating copolymerized derivative as a cold flow improver for diesel fuel. Petroleum Science. 2009;6(1):82-5.

[74] Dunn R, Shockley M, Bagby M. Improving the low-temperature properties of alternative diesel fuels: vegetable oil-derived methyl esters. Journal of the American Oil Chemists' Society. 1996;73(12):1719-28.

[75] Edith O, Janius RB, Yunus R. Factors affecting the cold flow behaviour of biodiesel and methods for improvement—a review. Pertanika J Sci Technol. 2012;20:1-14.

[76] Soriano NU, Migo VP, Matsumura M. Ozonized vegetable oil as pour point depressant for neat biodiesel. Fuel. 2006;85(1):25-31.

2. Mitigating Crystallization of Saturated FAMES in Biodiesel: 1. Lowering Crystallization Temperatures via Addition of Metathesized Soybean Oil[1]

2.1 Introduction

Biodiesel is the subject of considerable research and development efforts due to environmental concerns, the decline of known petroleum reserves and price increase of fossil energy [1, 2]. Biodiesel is defined as the mono-alkyl esters of vegetable oils or animal fats and is produced using a variety of technological methods [3, 4]. The quality of biodiesel is regulated by standards, the two most utilized being ASTM D6751 in the United States and EN 14214 in the European Union.

Biodiesel is a renewable feedstock compatible with existing fuel distribution infrastructure that have less of an environmental impact compared to petroleum based diesel (petrodiesel). It is miscible with petrodiesel in any proportion and offers facile use in current diesel engines [5]. Biodiesel offers several important advantages over conventional diesel fuel. It has a high cetane number (CN), inherent lubricity (even in blends of 1–2%), low toxicity, superior flash point, high biodegradability, and negligible sulfur content. Furthermore, its use results in significant reduction of most regulated

---

exhaust emissions. Disadvantages of biodiesel include high feedstock cost, inferior storage and oxidative stability, lower volumetric energy content, inferior low temperature operability compared to petrodiesel, and in some cases, higher NOx exhaust emissions [6, 7]. Many of these deficiencies can be mitigated through blending with petrodiesel [8] and/or reducing storage time [9]. However, blending with petrodiesel is only effective at relatively low biodiesel proportions (up to 30 vol.%) [10, 11]. Standards have been introduced for inclusion of up to 20 vol. % biodiesel in petrodiesel (ASTM D975, ASTM-D7467 and EN 590).

One of the major limitations to wide-spread utilization of current biodiesel is its poor low-temperature performance [7]. Low-temperature operability of biodiesel is normally determined by three common parameters: cloud point (CP; ASTM D2500 or D5773), pour point (PP; ASTM D97 or D5949), and cold filter plugging point (CFPP; ASTM D6371). The thermal characteristics determined with DSC can be reliably used to assess the cold flow properties of biodiesel that are ordinarily obtainable by standard tests [12]. DSC provides some advantages over standard methods. Evaluating CP from DSC curves, for example, greatly minimizes experimental error associated with ASTM method D2500 visual detection. This technique offers additional benefits by providing important information on the transformation mechanisms involved in the crystallization process of the materials. In fact the DSC is being used increasingly to investigate the flow properties of biodiesel due to additives or other means of modification in lieu of and in correlation with the CP, PP and CFPP [13-18]. It was shown for example that the onset temperature of crystallization as well as the first crystallization peak characteristics are closely associated with CP and PP of biodiesel [14]. The temperature at which the first crystals

are observed is very closely related to the onset temperature of crystallization and is therefore a direct indication of CP [19]. A depression in PP due to additives, although less obvious as it relates to a later stage of crystallization, can be clearly indicated by the change in heat flow of the crystallization/melting peak because of its direct relationships to the amount of the solid phase [20]. For example, PP and CP, and CFPP have been obtained in a single DSC slow cooling experiment (0.5 °C/min) with better reproducibility than standard ASTM tests [18].

Several approaches to mitigate the poor low-temperature performance of biodiesel have been reported in the literature over the past decade [21], including the diversification of the fuel composition through genetic, chemical or/and physical modification of the feedstock [22, 23]. The common and most popular approach used to improve the cold flow properties of biodiesel is, however, treatment of the fuel with cold flow improver (CFI) additives. Many examples and reviews of such additives and their function are reported in the scientific and patent literature (see for example works cited in [24-28]).

Unfortunately, no one approach has yet been able to simultaneously address both PP and CP effectively. Most commercial CFI additives are designed with a high degree of structural selectivity to treat petroleum derivatives, and generally fail to effectively reduce CP in neat and blended biodiesel. In order to develop more efficient CFI additives specific to biodiesel, research efforts are currently directed to designing compounds with increased selectivity specific to biodiesel. The goal is to modify nucleation and disrupt crystalline growth of the high-melting-point alkyl ester compounds of biodiesel. Several approaches have been tried in this regard, including crystallization modifiers additives based on vegetable oils [29, 30], synthesis of fatty compounds similar in structure to saturated esters

and containing bulky moieties [31], branching of the unsaturated FAMEs [32-35], addition of branched diesters [36] and glycerol derivatives [37, 38]. Several small chain compounds have been tried also as diluents in biodiesel [39-41].

The present study arose from the observation that self-metathesized soybean oil (MSBO) stripped of olefins depresses the onset of crystallization of methyl soyate (biodiesel) at loadings as low as 1% [42]. The compounds in MSBO responsible for this behaviour were unclear, as was the mechanism.

Olefin metathesis is an important organic synthesis technique that is increasingly used in oleochemistry to produce fine chemicals [43-46]. It is a powerful tool that can increase the molecular diversify and reactivity of natural oils and fats dramatically. It produces novel compounds which can serve as petrochemical replacements. Olefin metathesis (Scheme 2.1) is a reversible reaction involving the exchange of alkylidene groups between the reactant alkene moieties in the presence of catalysts, typically transition metal complexes [46].

$$2\,R\text{-}CH=CH\text{-}R' \rightleftharpoons R\text{-}CH=CH\text{-}R + R'\text{-}CH=CH\text{-}R'$$
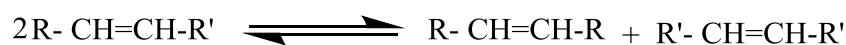
Scheme 2.1. Representation of olefin metathesis reaction.

Olefin metathesis is categorized as self-metathesis and cross metathesis [44, 46]. Self-metathesis (forward reaction in Scheme 2.1) is the process in which the same olefin molecules react to produce two different olefin products; whereas, cross metathesis (backward reaction in Scheme 2.1) is the process in which two different olefins are involved to produce a new olefin product. The self-metathesis of TAGs result in a complex mixture comprising linear oligomers (from dimer to pentamer), macrocyclic structures,

cross-linked polymers, as well as *trans-/cis* isomers [47]. Cross-metathesis of a vegetable oil with olefins results in a metathesized TAG (MTAG) mixture including modified TAG structures, such as terminal double bonds, not present in the natural oil. The actual composition of a metathesis product is highly dependent on the reaction conditions, such as such as starting materials, temperature, type of catalyst, etc., providing the possibility of controlling the product composition [48-51].

A number of approaches were therefore utilized to determine the compounds in MSBO responsible for this behaviour and to provide an understanding of the underlying mechanism. GPC, HPLC and MS methods were developed for analysing MSBO compositions. Due to the complexity of MSBO, only "families" of compounds can be separated on an HPLC or GPC. "Families" of compounds were separated from MSBO using column chromatography, and solvent-mediated crystallization, and then mixed at low weight percentages with biodiesel to evaluate their impact on crystallization. In order to contrast with a model unsaturated vegetable oil, metathesized triolein (MTO) and its component families obtained by column chromatography were also tested. Based on the findings that structured TAGs and oligomers of TAGs seemed to be particularly implicated in the modification of low temperature crystallization of biodiesel, a series of stereospecifically pure TAGs and oligomers of TAGs (dimers and quatrimers) were synthesized and mixed at low weight percentages with biodiesel and evaluated for their impact on crystallization. The DSC was used to investigate the low temperature behavior of these unconventional, lipid-based, compounds. The general structure of TAG monomers and TAG-oligomers present in metathesized soybean oil (MSBO) and metathesized triolein (MTO) is shown in Scheme 2.2. The nomenclature and IUPAC

names, structures and abbreviations of the TAGs and oligomers of TAGs used in this work are provided in the Appendix (listed in Tables A3 and A4).

Metathesized vegetable oils such as MSBO and MTO and their families are novel chemicals never used before as cold flow improvers (CFIs) of biodiesel. DSC measurements have facilitated the efficient screening of these families of compounds present in MSBO and MTO and generally in olefin metathesized vegetable oils and quantified their effectiveness as CFIs for the first time. The structures that are most effective in substantially lowering the crystallization point and consequently the flow properties of biodiesel were identified, as was the mechanism of their function. This general mechanism can now be used to generate superior designs of unconventional CFIs of biodiesel.
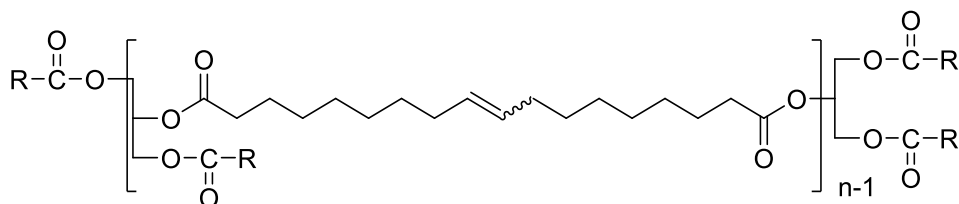
Scheme 2.2. General structure of triacylglycerols (TAGs) monomers and TAG-oligomers[a,b] of metathesized soybean oil (MSBO) and metathesized triolein (MTO).

[a] n represents oligomer level (n=1 represents TAG monomer, n= 2, dimer, n= 3, trimer, n= 4, quatrimer.)

[b] RCOOH= stearic acid (S), palmitic acid (P), linolenic acid (L), oleic acid (O), linoleic acid (Ln). Double bonds in R include *cis-* and *trans-* configurations such as in elaidic acid (E). R in MTO is from oleic acid, and R in MSBO is mainly from oleic acid, linoleic acid, linolenic acid, stearic acid or palmitic acid

2.2   Experimental

2.2.1   High Performance Liquid Chromatography

High performance liquid chromatography (HPLC) was carried out on a Waters Alliance e2695 HPLC instrument fitted with a Waters ELSD 2424 evaporative light scattering detector (Waters Corporation, Milford, MA). The HPLC system includes an inline degasser, a pump, and an auto-sampler. The temperature of the column (C18, 150 mm × 4.6 mm, 5.0 µm, XBridge column, Waters Corporation, Milford, MA) was maintained at 35 ºC. The ELSD nitrogen flow was set at 25 psi with nebulization and drifting tubes maintained at 12 ºC and 55 ºC, respectively. Gain was set at 500. The mobile phase was chloroform: acetonitrile (50:50) v run for 30 min at a flow rate of 0.2 ml/min. 1 mg/ ml (w/v) solution of crude sample in chloroform was filtered through a single step filter vial (Thomson Instrument Company, Oceanside, CA) and 0.5-2 µL of sample was passed through the C18 column by reversed-phase in isocratic mode. All solvents were HPLC grade and obtained from VWR International, Mississauga, ON. Waters Empower Version 2 software was used for data collection and data analysis. Purity of eluted samples was determined using the relative peak area. The reported purity is the average value obtained from at least three separate runs.

2.2.2   Gas Chromatography

Gas chromatography (GC) was carried out on a HP 5890 Hewlett Packard (Avondale, PA) equipped with a FID detector, using a ZB-5HT INFERNO fused silica capillary column (30 m×0.25 mm×0.10 um, Zebron-Phenomenex, Torrance, CA). The carrier gas was helium with a flow rate of 2.3 mL/min. The following column temperature conditions were employed. Soy 1500: 2 min initial hold at 150 ˚C then rising to 220 °C at a rate of

0.5 °C/min. MSBO and its fractions: 2 min initial hold at 50 °C, then rising to 350 °C at a rate of 10 °C/min, followed by a final hold at 350 °C for 10 min. The injector temperature was 380 °C. The samples were prepared as 5 mg/mL hexanes solution, and the injected volume was 1 μL.

2.2.3 Gel Permeation Chromatography

Molecular weight and distribution were determined by gel permeation chromatography (GPC). The measurements were carried out on a e2695 GPC instrument equipped with a Waters e2695 pump, Waters 2414 refractive index detector and a 5-μm Styragel HR5E column (Waters Alliance, Milford, MA)). Chloroform was used as eluent with a flow rate of 0.5 mL/min. The concentration of sample was 1 mg/mL and the injection volume was 10 μL. Polystyrene (PS) standards and pure TAG-oligomers (synthesized previously [52]) were used for calibration. Waters Empower Version 2 software was used for data collection and data analysis.

2.2.4 Nuclear Magnetic Resonance Spectroscopy (^{1}H-NMR and ^{13}C-NMR)

One-dimension ^{1}H-NMR and ^{13}C-NMR spectra were recorded at 25 °C on a Bruker Advance III 400 spectrometer (Bruker BioSpin MRI GmbH, Karlsruhe, Germany; $\nu(^1H)$= 400.22 MHz and $\nu(^{13}C)$= 100.65 MHz) equipped with a 5-mm Broadband Observe (BBO) probe. The ^{1}H-NMR spectra were acquired over a 16-ppm spectral window with a 1-s recycle delay, and 32 transients, and the ^{13}C-NMR spectra were acquired over a 240-ppm spectral window with a 0.2-s recycle delay, and 2048 transients. The spectra were Fourier transformed, phase corrected, and baseline corrected. Window functions were not applied prior to Fourier transformation. Chemical shifts were referenced to residual solvent peaks (CHCl$_3$, $\delta(^1H)$ = 7.24 ppm, $\delta(^{13}C)$ = 77.24 ppm).

2.2.5   Electrospray Ionization Mass Spectrometry

Electrospray ionization mass spectrometry (ESI-MS) analysis was performed using a QStar XL quadrupole time-of-flight mass spectrometer (AB Sciex, Concord, ON) equipped with an ion-spray source and a modified hot -source-induced desolvation (HSID) interface (Ionics, Bolton, ON, Canada). The ion source and interface conditions were adjusted as follow: ion-spray voltage (IS) = 4500 V, nebulizing gas (GS1) = 45, curtain gas (GS2) = 45, declustering potential (DP) = 60 V, and HSID temperature = 200 °C. Samples (~1-2 mg) were dissolved first in 200 μL CH_2Cl_2 and subsequently diluted ~1-5 μL in 200 μL CH_3OH. Approximately 2.5 μL aliquots of the sample solution were further diluted with CH_3OH to a final injection volume of 10 μL. Samples were analyzed via loop injection at a flow rate of 100 μL/min. The mobile phase was composed of 70% CH_3OH and 30% aqueous 10-mmol/L ammonium acetate to provide a cationizing agent. For the lower molecular weight oligomers up to ~1000 Da, strong ion signals were observed readily from both singly-protonated and singly-ammoniated TAGs. Higher molecular weight oligomers in the range ~1000 Da – 5000 Da were found to be decreasingly soluble in the methanol/aqueous ammonium acetate mobile phase, and poor ion signals only were observed from the sample injections in methanol (MeOH). The oligomers were subsequently 'eluted' from the sample loop by injection of 30:70 MeOH/CH_2Cl_2 (v/v) and/or CH_2Cl_2. The higher molecular weight TAG-oligomers were observed as singly- and multiply-ammoniated molecules over a wide m/z range, between m/z 1000 and m/z 4000. Multiply-charged ion signals were reconstructed using the BioTools 1.1.5 software package (AB Sciex, Concord, ON, Canada).

2.2.6   Differential Scanning Calorimetry

Differential scanning calorimetry (DSC) was carried out on a Q200 model DSC equipped with a RCS 90 refrigerated cooling system (TA Instruments, DE). Approximately 5.0 – 10.0 (±0.1) mg of fully melted and homogenously mixed sample was placed in an aluminum DSC pan which was then hermetically sealed. An empty aluminum pan was used as a reference and the measurements were performed under a nitrogen flow of 50 mL/min. The samples were subjected to the same thermal protocol to allow for comparison. The sample was equilibrated at 25 ºC for 5 min then cooled at 3 °C/min down to -50 °C to obtain the cooling profile. The sample was held at this temperature (-50 °C) for 5 min then subsequently reheated to 25 ºC at 3.0 ºC/min to obtain the melting profile. The "TA Universal Analysis" software was used to analyze the data and extract the main characteristics of the peaks. All measurement temperatures are reported to a certainty of better than ± 0.5 °C.

2.3   Materials

2.3.1   Biodiesel

The effect of the additives on the cold flow properties of biodiesel was evaluated on a commercial biodiesel (so-called Soy 1500). The composition of Soy 1500 as determined by GC is shown in Table 2.1.

Table 2.1. Composition of Soy 1500 as determined by GC. FAME: fatty acid methyl ester

FAME	%
Methyl Linoleate (MeLn)	53.8
Methyl Oleate (MeO)	29.9
Methyl Palmitate (MeP)	10.6
Methyl Stearate (MeS)	3.8
Unknown	1.9

2.3.2 Metathesized Soybean Oil (MSBO) and its Fractions

Metathesized Soybean Oil (MSBO) was provided by Elevance Renewable Sciences, Inc., Bolingbrook, IL. It was produced by neat self-metathesis of soybean oil, and then stripped of olefins. Its composition is very complex and includes monomers, oligomers and alkenes. It also contains *cis-*, *trans-* and *saturated* configurations [53, 54]. Because of this complexity, only families of MSBO components can be practically separated and tested to determine which compounds were responsible for the cold flow properties improvement observed in biodiesel. MSBO was separated into its main families of components by column chromatography, and also fractionated into a liquid and a solid portion by solvent aided crystallization.

2.3.3 Separation of MSBO by Column Chromatography

MSBO was fractionated into its main families of components by column chromatography with ethyl acetate and hexanes as eluting solvents. Five families of components, labeled MSBO-F1 to –F5, were collected and characterized. MSBO-F3 was separated into three sub-families (MSBO-F3a, MSBO-F3b and MSBO-F3c; yields: 4.8, 6.4, and 2.4%, respectively) and characterized with ^{1}H-NMR. The column

chromatography data including the eluting solvents and the yield for the fractions collected from MSBO by column chromatography are listed in Table 2.2.

Table 2.2. Fractions collected from MSBO column chromatography. Yield (%) is based on 25 g of sample. Hx:EA: hexanes : ethyl acetate

Families	Hx:EA	Yield (%)
MSBO-F1	1:0	5.6
MSBO-F2	20:1	7.9
MSBO-F3	20:1	30.0
MSBO-F4	15:1 to 10:1	49.8
MSBO-F5	0:1	2.5

Table 2.3. Molecular weight (Mw, g/mol) of TAG-oligomers. GPC calibration curves obtained with [a]TAG-oligomers standards, [b]Polystyrene standards

Compound	Mw (g/mol)		
	Calculated	GPC with TAG-oligomer standards [a]	GPC with polystyrene standards [b]
Triolein	885	891	1414
Dimer	1509	1524	2772
Trimer	2151	2124	4027
Quatrimer	2784	2638	5288
Pentamer	3416	3249	7797
Hexamer	3714	3405	7514

Note that the last family (MSBO-F5) was washed out from the column with ethyl acetate and contains all remaining polymeric materials. The average molecular weight (Mw) of the MSBO families was determined with GPC using calibration curves of TAG-

oligomer standards that were previously synthesized and fully characterized [52]. The molecular weight of the TAG-oligomer standards as determined by GPC are listed in Table 2.3.

2.3.4 Fractionation of MSBO by Crystallization in Solvent

10 mL of MSBO (9.2 g) was mixed with 40 mL of hexanes for 5 min using a vortex mixer. The solution was equilibrated at 25 °C for 5 min, cooled at 0.1 °C/min down to the fractionation temperature (T_F = -8, -20 or -25 °C) at which it was held for 1 h, and then the liquid fraction (MSBO-LF) was separated from the solid fraction (MSBO-SF). Both the solid and liquid fractions were dried on a rotary evaporator. The fractionation data are presented in Table 2.4.

Table 2.4. Solvent-crystallization fractionation data of MSBO. MSBO-LF: liquid fraction, MSBO-SF: solid fraction. Yield: yield of the liquid fraction

T_F (°C)	MSBO-LF (g)	MSBO-SF (g)	Yield (%)
-25	4.1	4.8	45
-20	5.0	3.9	54
-8	6.7	2.6	73

2.3.5 Metathesized Triolein (MTO) and its Fractions

Triolein, a model unsaturated vegetable oil, was metathesized and fractionated using column chromatography. The metathesized triolein (MTO) was prepared as reported in [53]. 5.6 g (99%) triolein was heated to 38 °C under N_2 protection. 144 mg Grubbs 2nd generation catalyst (Sigma Aldrich) was added. The reaction mixture was stirred at 38 ºC

for 6 h and then quenched by 20 ml ethyl vinyl ether. The reaction mixture was then concentrated on a rotary evaporator. The residue was re-dissolved into 200 ml hexanes. The solution was filtered through a celite layer (celite ® 545, from Sigma-Aldrich, ON, Canada) to give a clear yellow solution. The yellow solution was concentrated on a rotary evaporator and dried further under vacuum.

MTO was separated by column chromatography into its main families of components with ethyl acetate and hexanes as eluting solvents. Six families of components, labeled MTO-F1 to –F6, were collected and characterized. The column chromatography data are listed in Table 2.5. Olefins were separated from MTO by column chromatography using hexanes as eluting solvent. MTO-F2 was simply MTO stripped from its olefins and MTO-F1, the olefins. The detailed structures of MTO components (monomers (triolein), dimer, trimer and quatrimer) are provided in the Appendix in Table A2.

Table 2.5. Column chromatography data for MTO. Hx:EA = hexanes : ethyl acetate

Fraction	Hx:EA	Yield (%)
MTO-F1	1:0	21.4
MTO-F2	1:0 then 0:1	78.6
MTO-F3	30:1	21.1
MTO-F4	15:1	12.4
MTO-F5	15:1 to 10:1	16.3
MTO-F6	8:1	11.2

2.3.6   Structured TAGs and Oligomers of TAGs

Selected structured TAGs (seventeen) and oligomers of TAGs (three dimers: D1, D2 and D3, and four quatrimers: Q1, Q2, Q3 and Q4), some of the major components of MSBO, were synthesized in purities higher than 98% and evaluated as cold flow improver additives. Their general structures are shown in Scheme 2.1, and their IUPAC names, structures and abbreviations are provided in the Appendix listed in Table A3-A4.

2.4   Results and Discussion

2.4.1   Compositional Analysis of Column Chromatography Fractions of MSBO

^{1}H-NMR spectra of the MSBO column chromatography fractions are provided in the Appendix in Fig. A1a –A1f. The ^{1}H-NMR data revealed structures with moieties containing various carbon numbers, saturated fatty acids, and unsaturated double bonds, and include *cis-* and *trans-* configurations. In all the ^{1}H-NMR spectra, –**CH**=**CH**- was present at δ 5.40 - 5.30 ppm, -OC**H**$_2$CHC**H**$_2$O- at δ 4.4-4.0, –C(=O)C**H**$_2$CH$_2$- at δ 2.35 - 2.31 ppm, =CHC**H**$_2$- at δ 2.04-1-94 ppm, -C(=O)CH$_2$C**H**$_2$- at δ 1.65 ppm, -C**H**$_2$- at δ1.32-1.29 ppm, and -C**H**$_3$ at δ 0.88 ppm. The ratio of protons corresponding to -OC**H**$_2$CHC**H**$_2$O- and -C**H**$_3$, as well as the proton of O=CC**H**$_2$-, were used to identify the structures as reported previously [53]. The main alkenes present in MSBO are diene, triene and tetraene, with the average double bonds amounts matching. Their structures are provided in the Appendix in Table A1. Note that the olefins are 5.6% of the MSBO total material only. Compositional analysis data of the fractions as determined from ^{1}H-NMR are listed in Table 2.6. The amount of double bonds per TAG unit and the ratio of *trans*/*cis* configuration as estimated by ^{1}H-NMR for MSBO-F3a, MSBO-F3b and MSBO-F3c are

also listed in Table 2.6. Carbon numbers were not determined. HPLC data are listed in Table 2.7.

Table 2.6.   Fractions collected from MSBO column chromatography and their Compositional analysis. Component structures are those detected by ^{1}H-NMR. Molecular weight (Mw) was measured by GPC using calibration curves of pure TAG-oligomers standards. Amount (A%) is based on 25 g of sample.

Family	A(%)	Mw (g/mol)		Components	*trans/ cis ratio*	**Double bonds per TAG**
MSBO-F1	5.6	--		Alkene including diene, triene, tetriene	--	--
MSBO-F2	7.9	750-1062		Monomers		
MSBO-F3	30.0	1347-1648	F3a	Dimers	4.4	1.4
			F3b	Dimers	6.0	1.6
			F3c	Dimers	7.9	2.0
MSBO-F4	49.8	2060-2775		Trimer +quatrimer	--	--
MSBO-F5	2.0	--		Polymeric materials (pentamer and higher)	--	--

Table 2.7. HPLC peak retention times (t_R, min) and relative area of the associated peak (A%) measured for the fractions collected from MSBO column chromatography.

MSBO-F1		MSBO-F2		MSBO-F3a		MSBO-F3b		MSBO-F3c	
t_R	A%	t_R	A%	t_R	A%	t_R	A%	t_R	A%
8.35	66.3	8.88	6.6	8.90	16.3	12.39	37.6	15.50[a]	97.1
10.20	21.2	11.52	49.0	10.35	10.7	13.04	45.4	--	--
8.32	17.3	12.11	31.1	14.35	45.4	13.87	16.9	--	--
8.95	47.7	--	--	15.98	27.7	--	--	--	--
9.88	25.2	--	--	--	--	--	--	--	--
8.35	50.0	--	--	--	--	--	--	--	--
8.93	31.7	--	--	--	--	--	--	--	--
9.87	8.5	--	--	--	--	--	--	--	--
10.81	9.8	--	--	--	--	--	--	--	--

[a]very broad peak from 10.0 to 21.2, centered at 15.50 min

2.4.2 Compositional Analysis of Column Chromatography Fractions of MTO

The composition of the MTO fractions as detected by ^{1}H-NMR are provided in Table 2.8. All fractions are mixtures of *cis-* and *trans-* isomers and positional isomers at *sn-1* and *sn-2*. Retention time (t_R) and relative area (%) of the HPLC peak detected in each fraction are provided in Table 2.8. The molecular weight (*Mw*) of the MTO families as determined with electrospray ionization mass spectrometry (ESI-MS) is also provided in Table 2.8. The potential structures of the fractions are provided in the Appendix in Table A2.

Table 2.8. HPLC peak retention time t_R (min) detected in each fraction. Amount (A%) collected is based on 25 g of sample. Molecular weight (Mw, g/mol) was measured by electrospray ionization mass spectrometry (ESI-MS). Purity (%) as determined with the relative area (%) of the associated HPLC peak

Fraction	A (%)	Composition	t_R (min)	Purity (%)	Mw (g/mol)
MTO-F1	21.4	Olefin	--	100	--
MTO-F2	78.6	MTO without olefins	--	--	--
MTO-F3	21.1	Triolein	12.5	100	655
MTO-F4	12.4	Dimers	14.2	100	1535
MTO-F5	16.3	Trimers	15.9	95	2167
MTO-F6	11.2	Quatrimers	19.5	95	2801

2.4.3 Effect of MSBO and MSBO Components on Crystallization of Biodiesel (Soy 1500)

As reported before, MSBO stripped of olefins depresses the onset of crystallization of biodiesel [42]. The effect of the fractions of MSBO, added in 1, 2, 3 and 4 wt% loading, on the onset of crystallization of Soy 1500 is shown in Fig. 2.1a. As can be seen in Fig. 2.1a, the individual fractions were effective and depressed the onset of crystallization of the biodiesel by ~1 to 4 °C. The largest depression was obtained with 3% loading in all cases. The dimer fraction (MSBO-F3a) was the most effective, surpassing MSBO itself for the 1 to 3% loadings. The fraction comprising monomers (F2) was the least effective fraction. MSBO-F3a dimer fraction, which comprises the fewest double bonds per TAG and has the least *trans*-configuration content, depressed the onset of crystallization more than MSBO-F3b and MSBO-F3c, the two other dimer fractions.
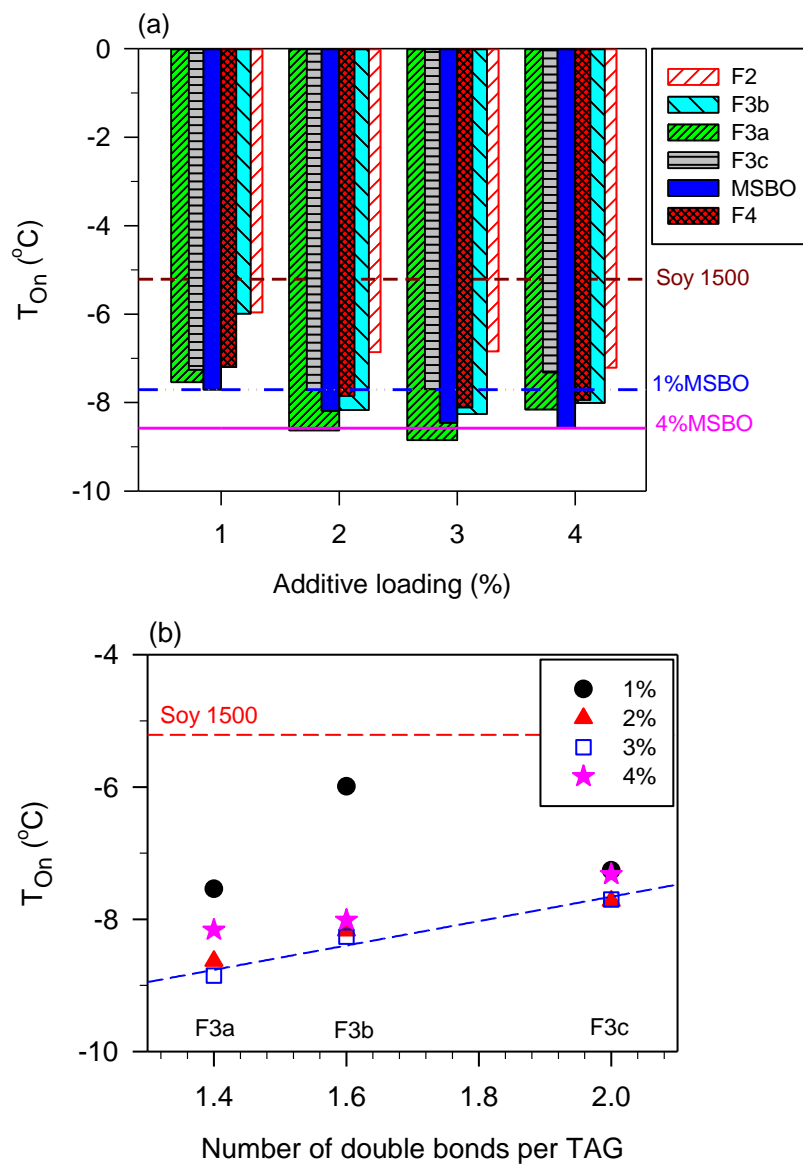
Figure 2.1. Onset temperature of crystallization (T_{On}) of biodiesel (Soy 1500) / MSBO

mixtures as a function of (a) additive loading, and (b) number of double bonds per TAG in

the case of the fractions (F3a-c) comprising dimers. F2, F3a-c and F4: MSBO-F2, MSBO-

F3a-c and MSBO-F4 fractions of MSBO obtained by column chromatography,

respectively

In fact, as shown in Fig. 2.1b representing the onset of crystallization of the dimer fractions as a function of the number of double bonds per TAG, T_{On} increased linearly with the increase of the number of double bonds per TAG at any given loading ($R^2 = 0.95847$; dashed line in Fig. 2.1b). Although not as effective as MSBO-F3a, the fraction comprising the trimers and quatrimers (MSBO-F4) was more effective than all the others, suggesting that even if chain length may play a role, structural elements such as the degree of saturation and *trans*-configuration content of the components can be overwhelming in the crystallization of the mixtures.

2.4.4 Effect of MTO and Its Fractions on Biodiesel Crystallization

The onset temperature of crystallization (T_{On}) of Soy1500 supplemented with the fractions obtained by column chromatography of MTO is shown in Fig. 2.2. The fractions comprising monomers (MTO-F3) and quatrimers (MTO-F6) outperformed the MTO stripped from its olefins (MTO-F2). The difference among the oligomers suggests that molecular size was one of the key parameters involved in depressing the onset temperature of crystallization of Soy 1500. As can be seen in Fig. 2.2, the MTO fractions were less effective than MSBO at 4% loading.

Even at the lowest loading of 1% used here, MSBO did as well as MTO-F6 and better than all the other fractions of MTO. Obviously, MSBO and its families contained more of the most effective structures than MTO and its families. Although the chemical structures present in MSBO and MTO fractions belong to the same categories (for example, both MTO-F4 and MSBO-F3 comprise dimers only), they present significant differences in terms of the diversity and type of TAG that constitute each category. The most important

difference between two families of the same category is the nature of the monomer composing the oligomers and the saturation structure. Also, both have *trans-* and *cis-* configurations but with a significantly different *trans/cis* ratio.
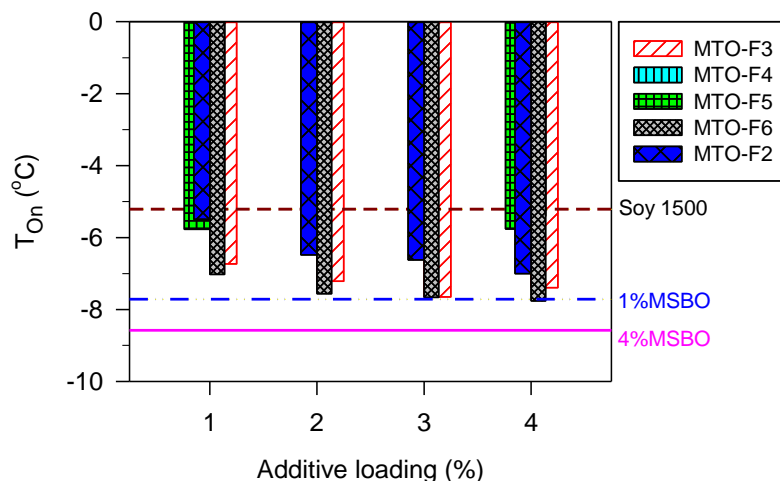
Figure 2.2. Onset temperature of crystallization (T_{On}) of Soy1500 supplemented with column chromatography fractions of MTO.

The MTO compounds are composed of triolein-like monomers (each MTO fraction was in fact a pure triolein oligomer) and do not have saturated fatty acids in any of the moieties. MTO *trans/cis* ratio varies from 4.8:1 to 3.6:1, depending on the oligomer; the *trans-* configuration being present in the bridges of the oligomers as well as in the fatty acids of the TAGs (see our published work [53]). On the other hand, MSBO oligomers are composed of modified soybean oil TAG structures, and have saturated fatty acids (~14% in total) as well as unsaturated fatty acids (for the TAG structure of the soybean oil see for example, Ref [55]). The *trans/cis* ratio in MSBO as determined in the present study by ^{1}H-NMR was 4.4 to 8 (See Table 2.6). In fact, MTO fractions contain oligomers with structural

elements such as all *cis*- or all *trans*-configurations that are not as functional as MSBO most functional components.

2.4.5   Effect of Structured Dimers and Quatrimers on Biodiesel Crystallization

In order to understand the effect saturation and *trans-/cis-* configuration, structured oligomers with controlled *cis/sat* ratio were synthesized and tested to verify the effect of the different permutations that are allowable. Onset temperature of crystallization (T_{On}) of Soy1500 supplemented with the synthesized dimers and quatrimers is presented in Fig. 2.3.

Clearly, as seen in Fig. 2.3, the efficacy of the dimers and quatrimers depends on the presence of *trans-/sat* and the position of saturated fatty acid chain to function, as well as molecular size. Firstly, note that D1 and D3 were more effective than D2. The presence of only one straight chain in TAG-oligomers, was more favorable to disturbing the crystallization of biodiesel. The minimal impact on lowering the crystallization onset of biodiesel by dimer D2, with two straight fatty acid chains, indicates that the presence of more than one straight chain in the structures is rather detrimental to the improvement of the low temperature characteristics of biodiesel. Also, the quatrimers Q3 and Q2 were more effective than Q4 at lowering onset temperatures. The low effectiveness of Q4 is attributable to the lack of a straight chain fatty moiety in this molecule, although this does demonstrate that the presence of a straight-chain bridge between TAGs in a TAG-oligomer contributes to a point in the disruption effect.
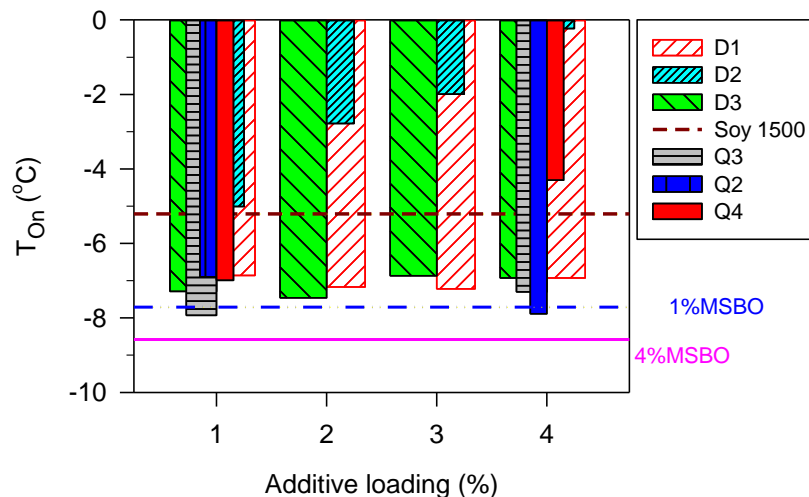
Figure 2.3. Onset temperature of crystallization (T_{On}) of Soy1500 supplemented with structured dimers and quatrimers. The nomenclature is provided in the Appendix in Table A4.

2.4.6 Effect of Pure Triacylglycerols on Biodiesel Crystallization

In order to understand the effect of TAG structure on the cold flow properties of biodiesel, the synthesized TAGs have been grouped in three types, depending on the position of the fatty acid moieties on the glycerol backbone. **Type I** TAGs are asymmetrical bi-fatty acids where the *sn-1* and *sn-2* position are occupied by one kind of fatty acid and the *sn-3* position by the other (Scheme 2.1). **Type II** TAGs are symmetrical bi-fatty acids or where the *sn*-1 and *sn*-3 position are occupied by one kind of fatty acid and the *sn*-2 position by the other (Scheme 2.1). **Type III** TAGs are mono fatty acid TAGs in which all the *sn*- position are occupied by the same type of fatty acid (Scheme 2.1).
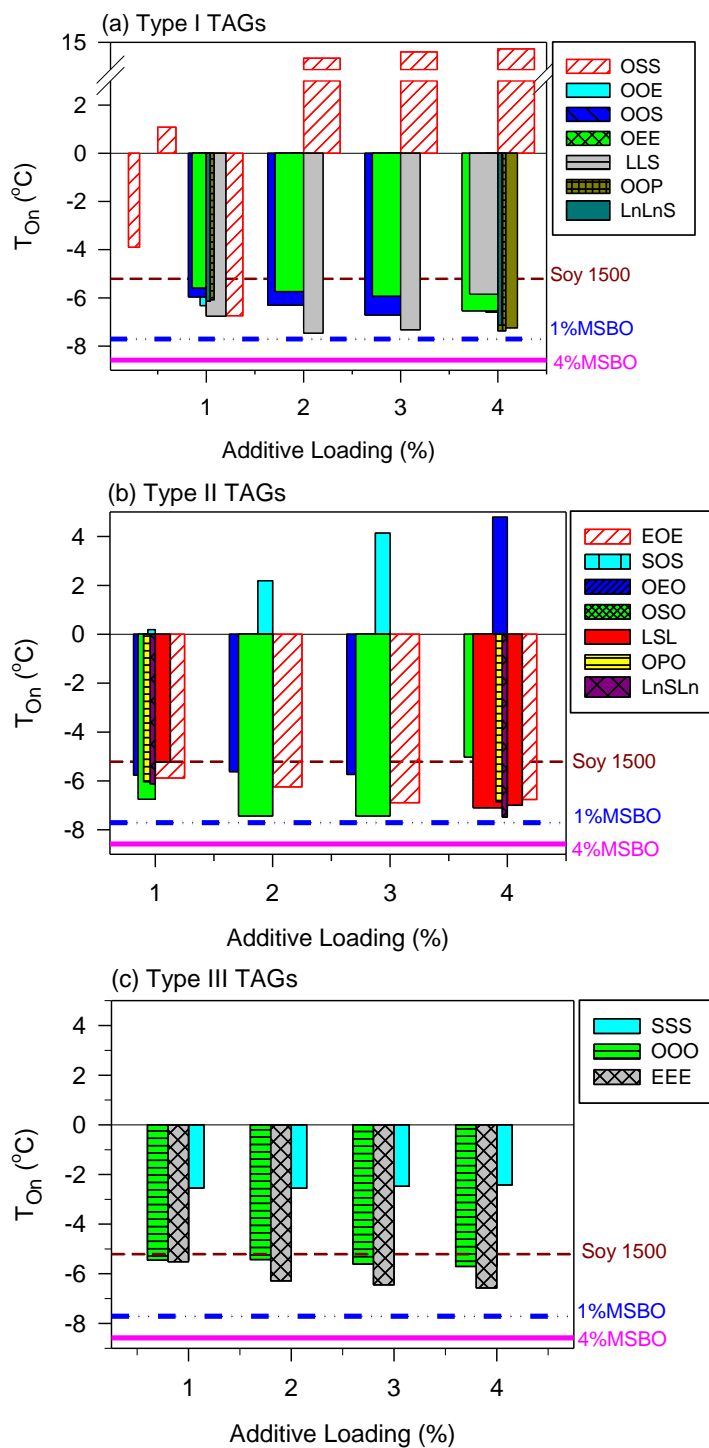
Figure 2.4. Effect of structured TAGs on crystallization onset of soy 1500. (a) Type I TAGs, (b) Type II TAGs, and (c) Type III TAGs. The IUPAC names of the TAG and nomenclature are provided in the Appendix in Table A3

T_{On} of Soy1500 supplemented with type I, type II and type III TAGs is represented in Figs. 2.4a –c. As can be seen in Figs. 2.4a-c, overall, type II TAGs were the most effective and type III the least effective. There was no depression with tri-saturated fatty acids. There was a reduced effect with tri-*cis* fatty acids and with tri-*trans* fatty acids, with the tri-*trans* case being more effective than the tri-*cis* case. Furthermore, the effect is greatly diminished so as to be ineffective when two *trans*-/saturated fatty acids and only one *cis*- fatty acid is present. For example, OSO and SOO are highly functional, but SSO and SOS are not.

TAGs with two fatty acids in the *cis*- configuration and a saturated fatty acid or a fatty acid in the *trans*- configuration were highly functional in depressing the onset of crystallization of biodiesel. The most effective stereospecificity is when the saturated fatty acid (or *trans*- configuration) is at the *sn*-2 position (Fig. 2.4c). The TAGs with the presence of multiple double bonds in the *cis*- configuration (Ln = linolenic acid, L = Linoleic acid) were even more effective at the cold flow modification with a certain loading, as shown for LLS, LnLnS, LSL (Fig. 2.4a) and LnSLn (Fig. 2.4b).

This means that other materials can mimic the cold-flow effect of MSBO, without having to use metathesis. The data suggests a mechanism where the saturated methyl esters in biodiesel form lamellae as precursors to a stable crystal – the *trans*-/saturate*d* fatty acid on the di-unsaturated TAG (SOO or OSO for example) can participate in this lamellar stack, but the presence of the remaining *cis*- fatty acids on the glycerol backbone sufficiently interrupts the packing so as to prevent crystallization. This mechanism suggests that OPO and OOP would be more effective at the cold flow modification of methyl palmitate and SOO and OSO more effective at the modification of methyl stearate.

Presence of Ln and L seem to enhance performance because of the presence of multiple double bonds in the *cis-* configuration which present increased difficulties for packing due to the proposed mechanism. This proposed mechanism also suggests that SLL, LSL, PLL, LPL, LnPLn, PLnLn, LnSLn, and SLnLn (Ln= linolenic acid, L= Linoleic acid) could be even more effective at the cold flow modification. These TAGs can be introduced by using high linoleic materials or flax in a directed interesterification process. Functional materials may be differentiated by using palmitic-rich or stearic-rich feedstock for palm-derived and soy and canola derived biodiesel. Due to the cost, this option may be the best solution for a business to deliver cold-flow modification for the biodiesel market.

Oligomers with similar *cis-* and *trans-* fatty acid configuration as in the TAG examples are also functional in depressing T_{on} of biodiesel. Indeed, the quatrimers and dimers, having a mixture of *cis-* and *trans-* configurations also show equivalent and even enhanced depression of crystallization. This is a startling result, given that oligomers from dimer to octamer when all the non-bridging fatty acids are in the *cis-* conformation are not functional materials for decreasing onset of crystallization of biodiesel.

This evidence supports the proposed mechanism – the entity disrupting packing is required to have a structural feature (*trans- or saturated fatty acid*) which participates in the lamellar organization of the saturated methyl esters of the biodiesel, and an irregular component which disrupts or interrupts the packing sequence.

2.4.7 Effect of Solid and Liquid Fractions of MSBO

The solvent fractionation of MSBO yielded solid fraction (SF-MSBO) that was rich in components that crystallize at higher temperatures. The components of SF-MSBO

include the molecules having mostly saturated and *trans*-fatty acids. As a result, the liquid fraction of MSBO (LF-MSBO) was enriched with molecules having *cis*-unsaturated fatty acids. The onset temperature of crystallization (T_{On}) of Soy1500 supplemented with solid and liquid fractions of MSBO (MSBO-SF and MSBO-LF, respectively) is listed in Table 2.9. As evident from Table 2.9, the temperature at which MSBO was fractionated did not significantly affect the effectiveness of both solid and liquid fractions in depressing the onset of crystallization of biodiesel. Overall, as illustrated in Fig. 2.5 showing T_{On} of mixtures of Soy 1500 with MSBO-LF and MSBO-SF obtained at T_F = -20 °C, the liquid fractions outperformed the solid fractions of MSBO as well as the original MSBO. Note that MSBO-SF was practically as effective as MSBO. Loading above 2% of MSBO fractions did not depress the onset of crystallization further significantly.
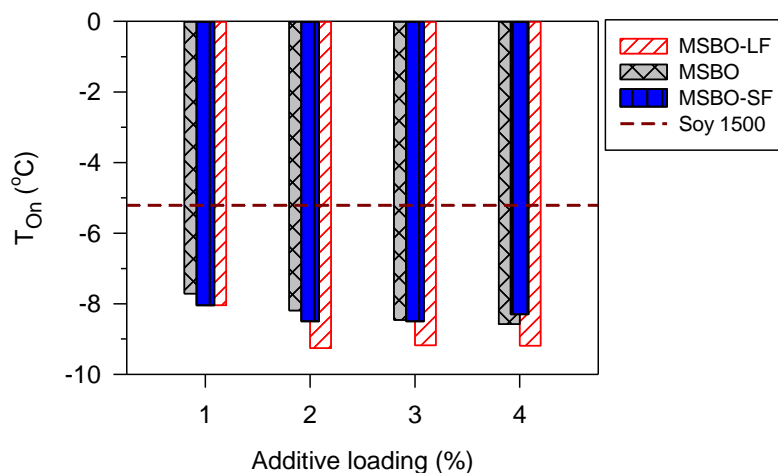
Figure 2.5. Onset temperature of crystallization (T_{On}) of mixtures of Soy 1500 supplemented with the liquid and solid fractions obtained by solvent aided crystallization. Fractionation temperature T_F = -20 °C. MSBO-LF: liquid fraction and MSBO-SF: solid fraction

Table 2.9. Crystallization onset (T_{On}) of Soy1500 supplemented with solid and liquid fractions obtained by solvent crystallization (MSBO-SF and MSBO-LF, respectively). T_F (°C): fractionation temperature, ΔT (°C): depression in onset of crystallization relative to Soy 1500. Onset temperature of crystallization of Soy1500= -5.2 °C. Temperatures are given in °C

Loading	1%		2%		3%		4%	
	T_{On}	ΔT	T_{On}	ΔT	T_{On}	ΔT	T_{On}	ΔT
MSBO	-7.7	-2.5	-8.2	-3.0	-8.5	-3.3	-8.6	-3.4
T_F (°C)	**Liquid Fraction of MSBO (MSBO-LF)**							
-25	-7.4	-2.2	-9.3	-4.1	--	--	--	--
-20	-8.0	-2.8	-9.3	-4.0	-9.2	-4.0	-9.2	-4.0
-8	-7.8	-2.6	-8.3	-3.1	-8.5	-3.3	-8.6	-3.4
T_F (°C)	**Solid Fraction of MSBO (MSBO-SF)**							
-25	-7.9	-2.7	-8.3	-3.0	--	--	--	--
-20	-8.04	-2.8	-8.5	-3.3	-8.5	-3.3	-8.3	-3.1
-8	-7.7	-2.4	-7.7	-2.5	-7.2	-2.0	-8.3	-3.1

2.4.8   Comparison with other CFI additives

MSBO, MTO and their molecular families are essentially crystallization modifiers of biodiesel. The most effective structures improved the onset of crystallization of biodiesel by as much as 5 °C with a loading as low as 2% wt. As discussed above in the Introduction Section, although the onset temperature of crystallization or the peak temperature provided by the DSC do not exactly match CP, PP or CFPP of the ASTM methods, they are strongly and directly correlated and the depression recorded in DSC temperatures perfectly match those of their related ASTM methods. One can therefore

safely compare the additives whether measured by DSC or ASTM methods. The best performing compounds studied here are generally comparable or even better than several other bio-based additives that have been reported in the literature. The results are in the range of those obtained with commercial additives which are often complex compositions carefully formulated to achieve a reduction of CP or PP for a specific biodiesel [56]. Vegetable oil derived additives such as palm oil polyol and dihydroxy fatty acid (1:1) % by wt. reduced CP of palm oil biodiesel by 10.5 °C and PP by 8 °C [57]. Ozonized vegetable oils are reported to more effectively depress PP than CP [58]. They were found to be most effective when both the ozonized material and the biodiesel were derived from the same vegetable oil, and mainly ineffective in biodiesels with significantly high saturated FAME such as palm oil biodiesel [58, 59]. For example, 1.5 % ozonized sunflower oil reduced PP and CP of sunflower oil biodiesel by 20 °C and 1 °C, respectively, those of soybean oil biodiesel by 8 °C and 2 °C, respectively, and those of palm oil by 1 °C and 5 °C, respectively.

Fatty acid, branched ester and glycerol derivatives were reported to depress both CP and PP. Geraldo et al. [60] observed that short chain glycerol acetals are generally more effective than the long chain derivatives. Silva et al. [38] reported that glycerol butanal acetal at 5% loading depressed PP of animal fat biodiesel by 5 °C; whereas, glycerol decanal acetal gave no depression at all. Glycerol ketals were less effective than glycerol acetals. Other complex lipid based structures such as branched diesters that have been tried in soybean biodiesel and yellow grease biodiesel by Moser et al. [36] reduced CP and PP by 0.7 to 5.3 °C, at loadings between 1% and 10% by vol. Some compounds were effective only at such high loadings that they can no longer be considered as additives. Addition of

20% of the most effective glycerol ketal, provided 3 °C depression only in cold filter plugging point [37]. Glycerol ketals are therefore suggested as components for diesel fuel [61]. Methyl oleate and isopropyl oleate achieved a 5 ℃ depression in CP and PP of sesame oil derived biodiesels at 30%, a high enough loading of unsaturated fatty esters to jeopardize the stability of biodiesel [62]. Esters of branched alcohols tried in soybean derived biodiesel [63] achieved depression in PP of less than ~6 ℃ at the significantly high concentration of 0.08mol/100 g of biodiesel. Other bio-based additives such as ethyl levenuate [39] and ethyl acetoacetate [40] depressed cotton seed oil and waste cooking oil biodiesels by a maximum of 3-4 °C at 20% by vol.

One can gather from the above studies overwhelming evidence that the action of the additives is driven by similar dominating mechanisms despite the variety and complexity of their chemical structures. High selectivity as well as effectiveness can be traced to the presence (or not) of structural elements that provide special features that allow the disruption of the crystallization process at given stages and given length scales. The overriding trend that emerges from the studies corroborates our finding that in order to be effective, the additive must have a structural element that initiates association with the FAMEs of the biodiesel and at least another structural element that prevents further growth or organization of the initial crystals and delays their aggregation.

2.5   Conclusions

The addition of MSBO stripped of olefins to methyl soyate (biodiesel) was confirmed to result in the depression of the onset temperature of crystallization. TAGs and oligomers of TAGs were found to be particularly implicated in the modification of low temperature crystallization of biodiesel. The results from MTO fractions indicate that *cis*-unsaturation

was a critical structural parameter for disrupting biodiesel crystallization, and that the stereospecific position of the fatty acids was an essential determinant of the degree of the effectiveness of the compounds to depress the onset of crystallization.

The presence of one straight chain only in the additive was most favorable to disturbing the crystallization of the biodiesel. The analysis of the data obtained with the structured dimers and quatrimers indicated that the presence of more than one straight chain in the structures, such as in the dimer D2, is rather detrimental to the improvement of the low temperature characteristics of biodiesel. The lack of a straight fatty moiety in a molecule results in a low effectiveness as seen in the behavior of the quatrimer Q4, but the straight bridge can contribute in a limited to the effect.

The analysis of the data obtained with structured TAGs evidenced that two fatty acids in the *cis-* configuration and a fatty acid in the *trans-* configuration or a *saturated* fatty acid were highly functional in depressing the onset of crystallization of biodiesel. The most effective stereospecificity is when the *trans-/saturated* fatty acid is at the *sn-*2 position, explaining the functionality of a metathesis product (MSBO) which converts *cis-*double bonds to *trans-* double bonds. There was a reduced effect with tri-*cis* fatty acids and with tri-*trans* fatty acids, with the tri-*trans* case being more effective than the tri-*cis* case. Furthermore, the effect is greatly diminished so as to be ineffective when two *trans-/saturated* fatty acids and only one *cis-* fatty acid is present. Generally, the best performing molecular structures are those which contained a moiety with a high degree of structural similarity with the high melting point alkyl esters.

The solvent fractionation of MSBO yielded a solid fraction (SF-MSBO) enriched in molecules containing mostly saturated and *trans*-fatty acids and a liquid fraction (LF-MSBO) enriched with molecules containing mostly *cis*-unsaturated fatty acids. As a result, LF-MSBO outperformed both MSBO and SF-MSBO in lowering the crystallization temperature of biodiesel. The knowledge gained on the mechanism of crystallization disruption and the structural architecture required to maximize this disruption suggests designs for more functional materials using practical methods of fractionation of MSBO and other metathesized vegetable oils.

2.6   References

[1] Droege P. Renewable Energy and the City: Urban Life in an Age of Fossil Fuel Depletion and Climate Change. B Sci Technol Soc. 2002;22(2):87-99.

[2] Shafiee S, Topal E. When will fossil fuel reserves be diminished? Energy Policy. 2009;37(1):181-9.

[3] Marchetti JM, Miguel VU, Errazu AF. Possible methods for biodiesel production. Renew Sustain Energy Rev. 2007;11(6):1300-11.

[4] Yusuf NNAN, Kamarudin SK, Yaakub Z. Overview on the current trends in biodiesel production. Energy Convers Manage. 2011;52(7):2741-51.

[5] Graboski MS, McCormick RL. Combustion of fat and vegetable oil derived fuels in diesel engines. Prog Energ Combust. 1998;24(2):125-64.

[6] Fazal MA, Haseeb ASMA, Masjuki HH. Biodiesel feasibility study: An evaluation of material compatibility; performance; emission and engine durability. Renew Sustain Energy Rev. 2011;15(2):1314-24.

[7] Misra RD, Murthy MS. Blending of additives with biodiesels to improve the cold flow properties, combustion and emission performance in a compression ignition engine—A review. Renew Sustain Energy Rev. 2011;15(5):2413-22.

[8] Benjumea P, Agudelo J, Agudelo A. Basic properties of palm oil biodiesel–diesel blends. Fuel. 2008;87(10-11):2069-75.

[9] Bondioli P, Gasparoli A, Della Bella L, Tagliabue S, Toso G. Biodiesel stability under commercial storage conditions over one year. Eur J Lipid Sci Technol. 2003;105(12):735-41.

[10] Dunn R, Shockley M, Bagby M. Improving the low-temperature properties of alternative diesel fuels: Vegetable oil-derived methyl esters. J Am Oil Chem Soc. 1996;73(12):1719-28.

[11] Moser BR. Impact of fatty ester composition on low temperature properties of biodiesel–petroleum diesel blends. Fuel. 2014;115(0):500-6.

[12] Dunn R. Thermal analysis of alternative diesel fuels from vegetable oils. J Am Oil Chem Soc. 1999;76(1):109-15.

[13] Garcia-Perez M, Adams TT, Goodrum JW, Das KC, Geller DP. DSC studies to evaluate the impact of bio-oil on cold flow properties and oxidation stability of bio-diesel. Bioresour. Technol. 2010;101(15):6219-24.

[14] Lee I, Johnson L, Hammond E. Use of branched-chain esters to reduce the crystallization temperature of biodiesel. J Am Oil Chem Soc. 1995;72(10):1155-60.

[15] Ramalho E, Carvalho Filho J, Albuquerque A, de Oliveira S, Cavalcanti E, Stragevitch L, et al. Low temperature behavior of poultry fat biodiesel: diesel blends. Fuel. 2012;93:601-5.

[16] Lai YB, Chen X, Yuan YN. Improving the Cold Flow Properties of Biodiesel Derived from Palm. Adv. Mat. Res. 2011;236:164-8.

[17] Yu L, Lee I, Hammond EG, Johnson LA, Van Gerpen JH. The influence of trace components on the melting point of methyl soyate. J Am Oil Chem Soc. 1998;75(12):1821-4.

[18] Claudy P, Létoffé J-M, Neff B, Damin B. Diesel fuels: determination of onset crystallization temperature, pour point and filter plugging point by differential scanning calorimetry. Correlation with standard test methods. Fuel. 1986;65(6):861-4.

[19] Hamada H, Kato H, Ito N, Takase Y, Nanbu H, Mishima S, et al. Effects of polyglycerol esters of fatty acids and ethylene-vinyl acetate co-polymer on crystallization behavior of biodiesel. Eur J Lipid Sci Technol. 2010;112(12):1323-30.

[20] Garcia-Perez M, Adams TT, Goodrum JW, Das K, Geller DP. DSC studies to evaluate the impact of bio-oil on cold flow properties and oxidation stability of bio-diesel. Bioresour. Technol.. 2010;101(15):6219-24.

[21] Knothe G. Biodiesel: Current Trends and Properties. Top Catal. 2010;53(11):714-20.

[22] Knothe G. "Designer" Biodiesel: Optimizing Fatty Ester Composition to Improve Fuel Properties. Energy Fuels. 2008;22(2):1358-64.

[23] Knothe G. Improving biodiesel fuel properties by modifying fatty ester composition. Energy Environ Sci. 2009;2(7):759-66.

[24] Sorate KA, Bhale PV. Biodiesel properties and automotive system compatibility issues. Renew Sustain Energy Rev. 2015;41(0):777-98.

[25] Zhang X, Rong J, Chen H, He C, Wang Q. Current Status and Outlook in the Application of Microalgae in Biodiesel Production and Environmental Protection. Front. Energy Res. 2014;2:32.

[26] Srivastava SP, Hancsók J. Fuel Additives. Fuels and Fuel-Additives: John Wiley & Sons, Inc; 2014. p. 177-269.

[27] Liu G. Development of low-temperature properties on biodiesel fuel: a review. International Journal of Energy Research. 2015;DOI: 10.1002/er.3334(Published Online March 2015).

[28] Makarevičienė V, Kazancev K, Kazanceva I. Possibilities for improving the cold flow properties of biodiesel fuel by blending with butanol. Renew Energ 2015;75(0):805-7.

[29] Hancsók J, Bubálik M, Beck Á, Baladincz J. Development of multifunctional additives based on vegetable oils for high quality diesel and biodiesel. Chem Eng Res Des. 2008;86(7):793-9.

[30] Moser BR, Cermak SC, Isbell TA. Evaluation of Castor and Lesquerella Oil Derivatives as Additives in Biodiesel and Ultralow Sulfur Diesel Fuels. Energy Fuels. 2008;22(2):1349-52.

[31] De Torres M, Jimenez-Oses G, Mayoral JA, Pires E. Fatty acid derivatives and their use as CFPP additives in biodiesel. Bioresour. Technol. 2011;102(3):2590-4.

[32] Moser BR, Erhan SZ. Branched chain derivatives of alkyl oleates: Tribological, rheological, oxidation, and low temperature properties. Fuel. 2008;87(10-11):2253-7.

[33] Smith PC, Ngothai Y, Dzuy Nguyen Q, O'Neill BK. Improving the low-temperature properties of biodiesel: Methods and consequences. Renew Energ. 2010;35(6):1145-51.

[34] Smith PC, Ngothai Y, Nguyen QD, O'Neill BK. Alkoxylation of biodiesel and its impact on low-temperature properties. Fuel. 2009;88(4):605-12.

[35] Smith PC, Ngothai Y, Nguyen QD, O'Neill BK. The addition of alkoxy side-chains to biodiesel and the impact on flow properties. Fuel. 2010;89(11):3517-22.

[36] Moser BR. Preparation and evaluation of multifunctional branched diesters as fuel property enhancers for biodiesel and petroleum diesel fuels. Energy Fuels. 2014;28(5):3262-70.

[37] De Torres M, Jimenez-Oses G, Mayoral JA, Pires E, de los Santos M. Glycerol ketals: Synthesis and profits in biodiesel blends. Fuel. 2012;94:614-6.

[38] Silva PH, Gonçalves VL, Mota CJ. Glycerol acetals as anti-freezing additives for biodiesel. Bioresour Technol. 2010;101(15):6225-9.

[39] Joshi H, Moser BR, Toler J, Smith WF, Walker T. Ethyl levulinate: A potential bio-based diluent for biodiesel which improves cold flow properties. Biomass and Bioenergy. 2011;35(7):3262-6.

[40] Cao L, Wang J, Liu K, Han S. Ethyl acetoacetate: A potential bio-based diluent for improving the cold flow properties of biodiesel from waste cooking oil. Applied Energy. 2014;114:18-21.

[41] Ali OM, Yusaf T, Mamat R, Abdullah NR, Abdullah AA. Influence of Chemical Blends on Palm Oil Methyl Esters' Cold Flow Properties and Fuel Characteristics. Energies. 2014;7(7):4364-80.

[42] Christensen SA, DiBiase SA, Rizvi SQA. Cold flow additives. In: EPO, editor. C10L 1/19 (2006.01); C10L 1/224 (2006.01) ed2012.

[43] Rybak A, Fokou PA, Meier MAR. Metathesis as a versatile tool in oleochemistry. Eur J Lipid Sci Technol. 2008;110(9):797-804.

[44] Mol JC, Buffon R. Metathesis in oleochemistry. J. Braz. Chem. Soc. 1998;9(1):1-11.

[45] Thomas RM, Keitz BK, Champagne TM, Grubbs RH. Highly selective ruthenium metathesis catalysts for ethenolysis. J Am Chem Soc. 2011;133(19):7490-6.

[46] Malacea R, Dixneuf PH. Alkene Metathesis and Renewable Materials: Selective Transformations of Plant Oils. Green Metathesis Chemistry: Springer; 2010. p. 185-206.

[47] Refvik M, Larock R. The chemistry of metathesized soybean oil. J Am Oil Chem Soc. 1999;76(1):99-102.

[48] Li SJ, Hojabri L, Narine SS. Controlling Product Composition of Metathesized Triolein by Reaction Concentrations. J Am Oil Chem Soc. 2012;89(11):2077-89.

[49] Pillai SK, Abidli A, Belkacemi K. Triacylglycerol self-metathesis over highly chemoselective methyltrioxorhenium supported on ZnCl2-promoted mesoporous alumina. Appl Catal A-Gen. 2014;479:121-33.

[50] Tian QP, Larock RC. Model studies and the ADMET polymerization of soybean oil. J Am Oil Chem Soc. 2002;79(5):479-88.

[51] Biermann U, Metzger JO, Meier MAR. Acyclic Triene Metathesis Oligo- and Polymerization of High Oleic Sun Flower Oil. Macromol Chem Phys. 2010;211(8):854-62.

[52] Li S, Bouzidi L, Narine SS. Synthesis and Physical Properties of Triacylglycerol Oligomers: Examining the Physical Functionality Potential of Self-Metathesized Highly Unsaturated Vegetable Oils. Ind Eng Chem Res. 2013;52(6):2209-19.

[53] Li S, Hojabri L, Narine S. Controlling Product Composition of Metathesized Triolein by Reaction Concentrations. J Am Oil Chem Soc. 2012;89(11):2077-89.

[54] Tian QP, Larock RC. Model studies and the ADMET polymerization of soybean oil. J Am Oil Chem Soc. 2002;79(5):479-88.

[55] Gunstone FD. Fatty Acid and Lipid Chemistry. New York, NY: Chapman and Hall, 1996.

[56] Erhan SZ, Dunn RO, Knothe G, Moser BR. Fuel Properties and Performance of Biodiesel. In: Hou CT, Shaw J-F, editors. Biocatalysis and Bioenergy. Hoboken, NJ: John Wiley & Sons, Inc; 2008. p. 3-58.

[57] Ming TC, Ramli N, Lye OT, Said M, Kasim Z. Strategies for decreasing the pour point and cloud point of palm oil products. Eur J Lipid Sci Technol. 2005;107(7-8):505-12.

[58] Soriano Jr NU, Migo VP, Matsumura M. Ozonized vegetable oil as pour point depressant for neat biodiesel. Fuel. 2006;85(1):25-31.

[59] Soriano NU, Migo VP, Sato K, Matsumura M. Crystallization behavior of neat biodiesel and biodiesel treated with ozonized vegetable oil. Eur J Lipid Sci Technol. 2005;107(9):689-96.

[60] Giraldo SY, Rios LA, Suárez N. Comparison of glycerol ketals, glycerol acetates and branched alcohol-derived fatty esters as cold-flow improvers for palm biodiesel. Fuel. 2013;108:709-14.

[61] Oprescu E-E, Stepan E, Dragomir RE, Radu A, Rosca P. Synthesis and testing of glycerol ketals as components for diesel fuel. Fuel Process Technol. 2013;110(0):214-7.

[62] Satapimonphan S, Pengprecha S. Improving cold flow property of biodiesel from white sesame seed oil. Conference Improving cold flow property of biodiesel from white sesame seed oil. p. 159-62.

[63] Soares VL, Nascimento RS, Albinante SR. Ester-additives as inhibitors of the gelification of soybean oil methyl esters in biodiesel. J. Therm. Anal. Calorim. 2009;97(2):621-6.

3. Mitigating Crystallization of Saturated FAMES in Biodiesel. 3. The Binary Phase Behavior of 1, 3-dioleoyl-2-palmitoyl glycerol – Methyl Palmitate - A Multi-Length Scale Structural Elucidation of Mechanism Responsible for Inhibiting FAME Crystallization[2]

3.1 Introduction

Various factors including fossil fuel depletion and environmental concerns have resulted in an increasing demand for renewable and environmentally responsible fuels. Biodiesel is sought as a viable alternative to petroleum based fuel as it is renewable and less harmful to the environment. The most common biodiesel is a fuel derived from the transesterification of vegetable oil/animal fat and is constituted of fatty acid methyl esters (FAMEs) of these lipids [1]. It is particularly attractive as it has many of the conventional diesel characteristics and can be used neat or in blends with petroleum diesel in unmodified existing diesel engines. Definition and detailed specifications of biodiesel are outlined in standards such as ASTM D 6751 in the United States and EN 14214 of the European Committee for Standardization, in Europe.

The poor low temperature performance of biodiesel, indicated by relatively high cloud points (CP, ASTM D2500) and pour points (PP, ASTM D97), is a serious limitation to its wider use, particularly in cold climates [2]. Several approaches to mitigate the low-temperature problems of biodiesel have been investigated over the past decade and are reported in the literature. They include blending with conventional diesel fuel, winterization, and use of synthetic additives [3-5]. The current most popular approach is the use of crystallization depressant additives which generally suppress the crystallization and retards the rate of nucleation and/or crystal growth [6]. The changes in the crystallization behavior of biodiesel due to the additives can be appreciated at different length scales through the modification introduced to the crystal structure, polymorphism, and microstructure.

The present work is part of a series of investigations triggered by promising cold flow results obtained with self-metathesized soybean oil (MSBO) additives to commercial biodiesel [7]. It has been found that particular components of MSBO such as TAGs and oligomers of TAGs with two fatty acids in the *cis-* configuration and a saturated fatty acid or a fatty acid in the *trans-* configuration are highly functional in depressing the onset of crystallization of biodiesel. The most effective stereospecificity is when the *trans/saturated* fatty acid is at the *sn-*2 position [8]. The paper reports on the phase behaviour of the model binary system made of methyl palmitate (MeP), a high melting point component of biodiesel, and 2-palmitoyl diolein (OPO). DSC thermograms were used to construct detailed kinetic phase diagrams, encompassing the liquidus line as well as the various transformations below the onset of crystallization. The liquidus line in the phase diagram obtained upon heating was modeled using the so-called Bragg-William

approximation, a thermodynamic model based on the Hildebrand equation and taking into account non-ideality of mixing. The work also investigates the polymorphism and microstructure of the OPO/MeP mixtures using XRD and polarized light microscopy (PLM).

XRD is a powerful tool for studying crystallization at the molecular and nanoscale levels. It allows access to the details of the lamellar packing as well as the subcell structure of the fat crystals and provides information on the intermolecular interactions at play during the development of the crystal phases [9]. XRD also provides valuable information on the crystal arrangement, homogeneity and order state at the crystallized domains which are usually at the nanoscale. The technique provides access to the electronic density map which in turn provides an indication of the localization of atoms/group of atoms. This in fact can be used to understand the molecular mechanisms involved in the crystallization of TAG/FAME systems and help unravel the role of TAGs in the dramatic reduction of crystallization temperature of FAMEs.

PLM is an efficient technique to study the microstructure of lipid systems. The development of fat crystals from the start of crystallization to the complete fat network can be exposed by time/temperature resolved PLM, or thermo-microscopy. The technique also allows access to nucleation parameters when the rate of nucleation is low or the rate of crystal formation (number of crystals per time) is low, i.e., when individual crystals can be individually counted and considered as nuclei [10].

3.2 Experimental Methods

3.2.1 Materials

1,3-dioleoyl-2-palmitoyl glycerol (OPO) was synthesized and purified in our laboratory according to known procedures [11, 12] and methyl palmitate (MeP) was purchased (Aldrich Chemical Co. Inc.). Their purities were greater than 99% as determined by high performance liquid chromatography (HPLC). OPO and MeP were mixed in 0.05 molar fraction increments. The melted sample was homogenized using a mechanical stirrer.

3.2.2 Differential Scanning Calorimetry (DSC)

DSC measurements were carried out on a Q200 model (TA Instruments, New Castle, DE) under a nitrogen flow of 50 mL/min. Approximately 4.0 to 5.0 ($\pm$0.1) mg of melted sample was placed in an aluminum DSC pan then hermetically sealed. An empty aluminum pan was used as a reference. The sample was fully melted and held for 5 min at 80 °C in order to erase crystal memory. It was then cooled at a rate of 5 K/min down to -90 °C, a temperature at which crystallization was deemed complete. The sample was equilibrated at this temperature for 5 min and subsequently reheated to 80 °C at a rate of 2 K/min to record the melting cycle.

The "TA Universal Analysis" software was used to analyze the data and extract the main characteristics of the peaks (peak (T_p), onset (T_{On}) and offset (T_{Off}) temperatures, and enthalpy (ΔH). Non-resolved peaks were located using first and second derivatives of the heat flow versus temperature curve.

3.2.3 Polarized Light Microscopy

A polarized light microscope (PLM, Leica DM2500P, Leica Microsystems, Wetzlar, Germany) fitted with a Leica (DFC420C) digital camera was used for image capture. A Linkam LS 350 temperature – controlled stage (Linkam Scientific Instruments, Tadworth, Surrey, UK) fitted to the PLM was used to process the samples. A small droplet of material was carefully pressed between a preheated glass microscope slide and cover-slip ensuring a uniform thin layer of sample. The sample was melted at 80 ºC for 5 min to delete all crystal memory then cooled at 1 K/min down to -50 °C. Images were recorded at 50X, 100X and 500X magnification.

The sample was measured as it was cooling using the automatic multi-time image capture available in the PLM. The start temperature of crystallization (T_S) was recorded at the appearance of the first "white spot" in the PLM. The development of the size and shape of the crystals were determined as a function of temperature. The final crystal network was particularly scrutinized.

3.2.4 X-Ray Diffraction

A Panalytical Empyrean X-ray diffractometer (PANalytical B.V., Lelyweg, The Netherlands) equipped with a filtered Cu- K_α radiation source (λ = 0.1542 nm) and a PIXcel^{3D} detector was used in line-scanning mode (255 lines over 3.347 degree wide detector) for XRD measurements. The XRD patterns were recorded between 1 and 60° (2θ) in 0.026∘ steps, at 45 kV and 40 mA. The procedure was automated and controlled by PANalytical's Data Collector (V 3.0c) software. The samples were processed in the XRD chamber, similarly to PLM as described in previous section, using a 700 Series Cryostream

Plus cooling system (Oxford Cryosystems, Oxford, UK) fitted to the diffractometer. The temperature was controlled to better than $\pm$ 0.5 °C. The data were processed and analyzed using the Panalytical'sX'PertHighScoreV3.0 software. We refer to the range $2\theta = [1 - 15]°$ and [15 - 60]° as the small- and wide-angle x-ray diffraction regions (SAXD and WAXD), respectively.

3.3   Results and Discussion

3.3.1   Crystallization Behaviour

The DSC cooling thermographs of the OPO/MeP mixtures are displayed in Fig. 3.1a & b) and the related crystallization characteristics (T_{on} and peak temperatures, T_p) are shown in Fig. 3.1c. The MeP thermogram presented a single exotherm (P1, T_{p1}~24.09 $\pm$ 0.49 °C, Fig. 3.1a). As the concentration of OPO was increased, and up to 0.45_{OPO}, a second exotherm (P2 in Fig. 3.1a), associated with an OPO- rich phase, appeared at the lower temperature side. Peak temperature of P1 shifted almost linearly and reached an apparent eutectic point at 0.45_{OPO} (Arrow E1 in Fig. 3.1c) with a eutectic temperature (T_{E1}) of 2.81 $\pm$ 0.03 °C.

On the OPO- rich side of the concentration range, the DSC cooling thermogram of pure OPO presented a two-step crystallization process with a small leading exotherm followed by a large peak (P1 at ~ -12 °C and P2 at~ -20 °C, Fig. 3.1b). Interestingly, the addition of up to 20 mol.% of MeP shifted the leading peak to higher temperature by 7 °C but did not affect the main peak indicating that MeP altered the overall transformation path, particularly at the early stages of crystallization, but did not affect the nature of the final crystal structure of OPO. As can be seen in Fig. 3.1b, the height of the leading peak

increased relatively substantially with increasing MeP, indicating that MeP involvement at the early stages of the crystallization process of OPO, i.e., nucleation, was important.
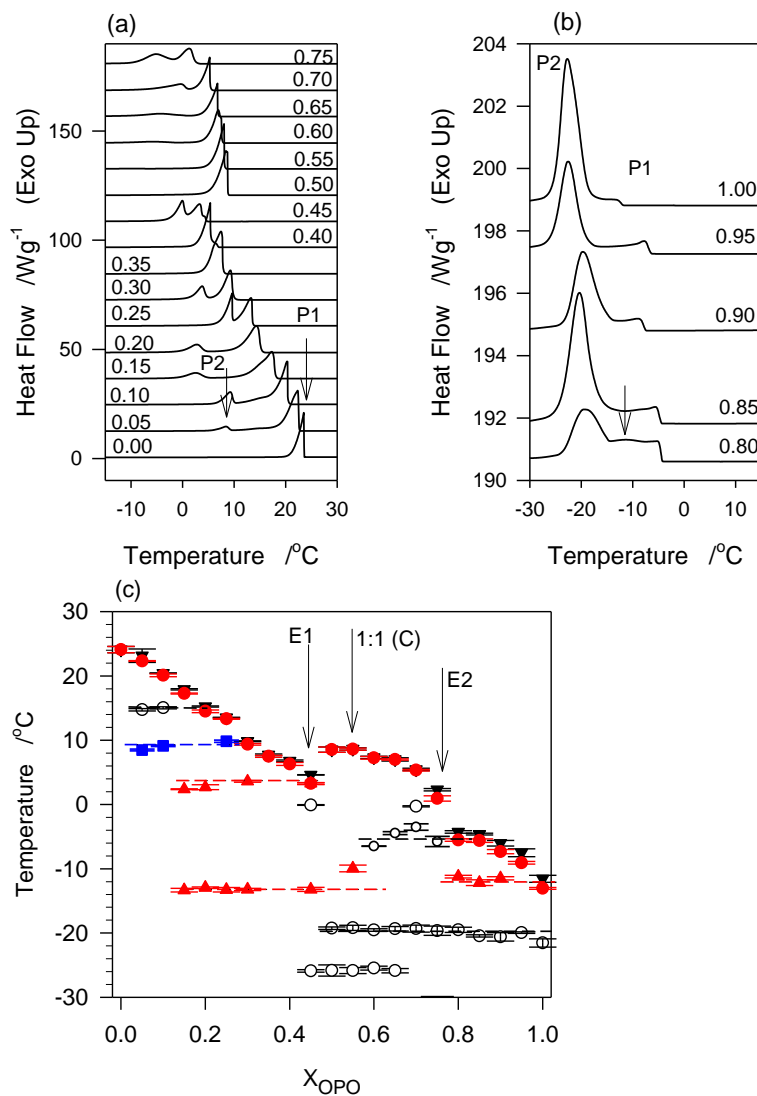
Figure 3.1: (a and b) DSC cooling (5 °C/min) thermograms of OPO/MeP mixtures. OPO molar fraction is indicated above each thermogram, and (c) characteristic temperatures of crystallization from Figs. 3.1a and b. Symbols: down triangles (▼): Onset temperature of crystallization (T_{On}), circles (○): Peak temperature (T_p), up triangles (▲): eutectic temperature, squares (■): metatectic temperature.

The intermediary peak appearing at ~ -12 °C (arrow in Fig. 3.1b) indicated that MeP is involved in the formation of the first lamellae, probably in a mixed phase with OPO. Furthermore, peak height of the main exotherm, P2, decreased and its FWHM increased steadily suggesting that at these concentration levels, MeP dramatically increases the OPO phase disorder and leads to the formation of more inhomogeneous networks. The 0.75_{OPO} mixture presented a sudden shift of its T_{On} to higher temperature and a dramatic increase in the intensity of its leading peak. This change in phase development is particularly reflected by a "jump" in the liquidus line of the cooling phase diagram of the OPO/MeP binary system (arrow E2 in Fig. 3.1c).

While the leading exotherm (P1) observed in the 0.75_{OPO} mixture remained relatively strong as MeP content was increased, the low temperature peak (P2) broadened and decreased dramatically, and disappeared for the 0.55_{OPO} and 0.50_{OPO} mixtures. These two last mixtures are also particular as they form a maximum in the liquidus line of the cooling phase diagram of the binary system (Arrow C, Fig. 3.1c); a clear indication of the formation of a 1:1 (mol:mol) compound [13]. The experimental phase diagram obtained on cooling displays in fact two eutectics (at $X_{E1} = 0.45_{OPO}$ and $X_{E2} = 0.80_{OPO}$) separated by the singularity (at $X_C = 0.55_{OPO}$, $T_C = 8.64 \pm 0.18$ °C). Note that as suggested by the DSC traces of the mixtures with X_{OPO} between 0.5 and 0.65, the phase of the 1:1 compound is probably dominant over a sizable concentration range.

The complexity of the transformations occurring in this binary systems is revealed by the several transformation lines shown in the phase diagram (dotted horizontal lines, Fig. 3.1c). Although most of them understandably involved little enthalpy of

transformation, eutectic lines (at ~3 ℃, spanning from 0.15_{OPO} to 0.45_{OPO} and at ~-5.5 ℃,

spanning from 0.60_{OPO} to 0.80_{OPO}) as well as possible metatectic lines (at ~9 ℃, spanning

from 0.05_{OPO} to 0.30_{OPO} and at ~15 °C, spanning from 0.05_{OPO} to 0.20_{OPO}) can be noticed.

3.3.2   Melting Behaviour and Phase Development

The DSC traces of the OPO/MeP mixtures obtained upon heating (Fig. 3.2a&b)

revealed the multiphase nature of the OPO/MeP system and the complexity the

transformation paths that are possible for the OPO/MeP mixtures. The complete kinetic

phase diagram of the OPO/MeP binary system constructed using the temperatures

characteristic of the heating cycles is displayed in Fig. 3.2c. The peak temperature (T_M)

of the last endotherm (solid circles in Fig. 3.2c), and T_{Off} (solid down triangles in Fig. 3.2c)

represent the liquidus line and T_M of the other peaks was used to represent the solid-solid

transition lines and the solidus line after correction for the transition widths of the pure

components.

The two pure constituents of the system displayed quite different melting behaviors

and had profound and distinct effects on each other. One can clearly notice that the melting

behavior of MeP is profoundly affected by the addition of OPO at very low concentration

and induced several thermal events in the mixtures. OPO is relatively resilient to the

influence of MeP and the phase development of the OPO-rich mixtures seems to be mainly

driven by recrystallizations from the melt as evidenced by the initial multiple exothermic

events observed in their DSC heating thermograms (arrows in Fig. 3.2c).
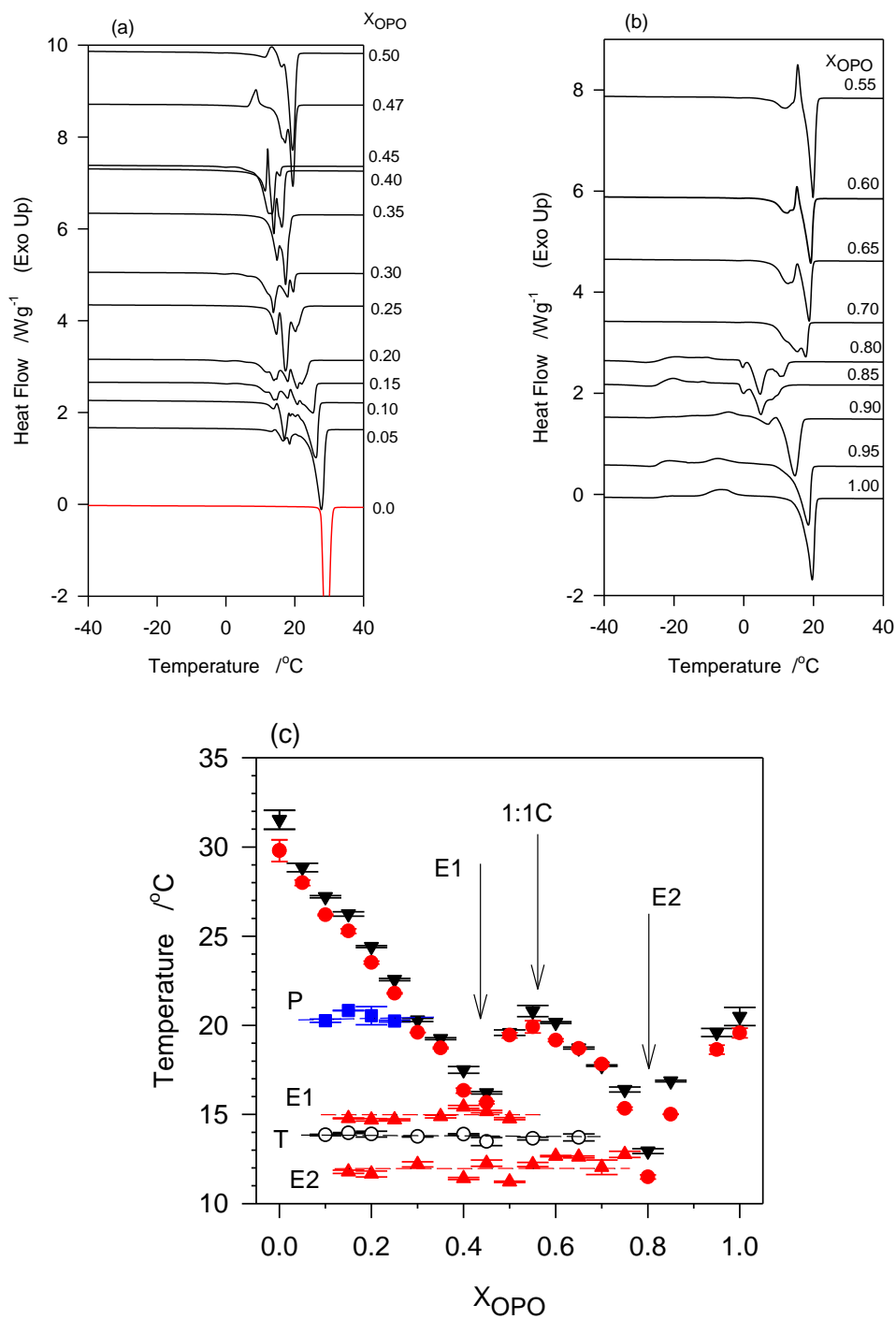
Figure 3.2. (a & b) DSC heating (2 °C/min) thermograms of MeP/OPO mixtures previously cooled at 5 °C/min, and (c) characteristic melting temperatures from Figs. 3.2a&b. Symbols: ▼: offset temperature (T_{Off}, circles (●): peak temperatures (T_P), up triangles (▲): eutectic temperatures, and squares (■): metatectic temperature

The multiple "recrystallizations" occurring in the OPO/MeP mixtures spun over a very large temperature range (~ 37.7 °C in the case of pure OPO). The transformation path of pure OPO and OPO-rich mixtures (up to 0.80_{OPO}) is a succession of at least two direct recrystallizations, from the pre-existing phase(s) which formed upon cooling into more stable phases followed by their subsequent melting as evidenced by the well-resolved endotherms. The high temperature endotherm ($T_P = 19.8$ °C) observed in the thermogram of OPO is probably the recording of the melting of the most stable phase of OPO that is reachable with the thermal protocol used, i.e., β_1. This endotherm remained strong and sharp (FWHM ~ 2.3 °C) even when 10% of MeP was added to OPO, indicating that the very well-organized OPO crystal phase is not significantly affected at these levels. The heat flow recorded for the exothermic transformations did not weaken significantly as MeP was added, suggesting that a pure OPO phase was still developing. However, shoulders appeared at the lower temperature side as soon as MeP was added, a sign that another phase, probably a MeP phase, has formed. As MeP content was increased, T_P of the last endotherm decreased steadily from a value of ~ 19.6 °C for pure OPO, to ~ 11.5 °C at the 0.80_{OPO} composition, indicative of an apparent eutectic (Arrow E1 in Fig. 3.2c).

The heating trace of pure MeP presented two overlapping peaks ($T_{P1} \sim 29$ °C and $T_{P2} \sim 30$ °C) attributable to the melting of two very close crystal phases. Such a thermogram has been previously reported and attributed without further evidence to a polymorphic transition followed by the complete melting of MeP [14]. However, it is more likely that this is the recording of the successive non-resolved melting of two coexisting crystal phases of MeP (both β') formed upon the non-isothermal cooling. The effect of OPO on the

transformation path of MeP is dramatic even at small concentrations as clearly illustrated by the variety of thermal events presented by the MeP-rich mixtures. The addition of even small amounts of OPO to MeP induced a dramatic broadening of the melting window in which a large number of transitions were available for the system. The 0.05_{OPO} to 0.25_{OPO} mixtures, for example, presented five additional well-resolved endotherms. Note also that no exotherm was recorded for the mixtures having less than 45% OPO. The addition of OPO to MeP caused a sharp drop in T_{Off} (and T_P of the last endotherm) of ~16 °C from the pure FAME to the 0.45_{OPO} mixture at which point a second eutectic is demonstrated by the binary system (Arrow E2 in Fig. 3.2c).

The mixtures between the two eutectic compositions presented relatively simpler heating traces with two prominent endotherms separated by a very sharp exotherm indicating the recrystallization from the melt of a homogeneous phase. Furthermore, T_{Off} of these mixtures (as well as T_P of their last endotherm) presented a marked maximum at 0.50_{OPO} (Arrow S in Fig. 3.2c). This type of singularity in the phase diagram is indicative of the formation of a 1:1 (mol:mol) molecular compound (MC) which forms a eutectic with each pure component [13]. Clearly, specific intermolecular interactions between OPO and MeP are at play and have a profound impact on the phase development and intersolubility of the OPO/MeP binary mixtures.

Two eutectic lines can be clearly distinguished (E1 at ~ 16°C and E2 at ~ 11.5°C, Fig. 3.2c). The first eutectic line (line E1, Fig. 3.2c) is related to the "MeP/MC" system and the second (line E2, Fig. 3.2c) to the "OPO/MC" system. A solid-solid transition is present between the two eutectic lines at ~ 14 °C (line T, Fig. 3.2b). The endothermic peak

associated with the 16 °C eutectic line was first observed at 0.20_{OPO}. As OPO concentration was increased, the height of this peak reached a maximum at 0.40_{OPO} at which point it decreased to disappear at 0.55_{OPO}. This is a Tamman plot -like behavior of the enthalpy supporting the existence of a eutectic transformation and delimiting its range.

There is no obvious peritectic point. The transformation line located at ~21 °C (■ in Fig. 3.2c) may be attributed to a metatectic reaction. The endothermic peak related to this transformation appeared first for 0.10_{OPO} as a small shoulder to the last endotherm then developed into a more resolved peak as OPO content is increased to 0.30_{OPO}.

The compound appears to be a key player in the crystallization behaviour of the OPO/MeP binary system. Obviously, OPO by forming a compound with MeP perturbs the crystallization in a very dramatic way. The formation of abrupt eutectics between the compound and the pure constituents reflects the complexity of the interactions involved and hence the solubility behavior and subsequent nucleation processes driving the phase development in this system.

3.3.3 Thermodynamic Analysis of the Liquidus Line

T_M of the last endotherm, or T_{Off} is suitable for studying equilibrium properties because it is determined by the most stable crystal. This point of the OPO/MeP binary system (down triangle in Fig. 3.3) was used to model the liquidus line in the kinetic phase diagram, as typically done in the study of binary lipid mixtures [14-17].

A thermodynamic model based on the Hildebrand equation [18] coupled with the Bragg-William approximation for non-ideality of mixing [19] was used to simulate the

liquidus line in the phase diagram. This model is commonly used to investigate the miscibility in studies of binary mixtures of lipids [17, 20, 21]. The mathematical approach is based on the Hildebrand equation which describes so-called regular solutions in which chemical effects are disregarded [18, 22]. In this model, only the enthalpy of the "solute" is taken into consideration as it is the crystallizing entity, and the solubility limit of the solute in the solvent is given by Eq. (3.1) [22]:

$$\ln x_s = \frac{-\Delta H_s}{R}\left(\frac{1}{T} - \frac{1}{T_s}\right) \tag{3.1}$$

Where R is the gas constant. x_s is the solubility limit (in mole fraction units) at temperature T, ΔH_S is the molar enthalpy of fusion of the solute, and T_S is the melting temperature of the pure solute. The phase line (liquidus line for instance) is therefore calculated simply with a knowledge of the melting point (T_S) and heat of fusion of the solute (ΔH_S). In a (A/B) binary mixture presenting a eutectic point, the solute may be A or B depending on whether the composition is smaller or larger than the eutectic composition (X_E). Both branches are described by Eq. (3.1) with s= A or B, for the concentration region where A or B is the solute, i.e., the left- or right- hand side branch of the eutectic [23, 24].

The non-ideality of mixing due to molecular interactions is introduced using the Bragg-Williams approximation framework [19]. This model attributes the origin of the non-ideality of mixing to the enthalpy term of the free energy of mixing and assumes the same entropy term as in the ideal mixing case [25]. In order to account for the free energy due to mixing the Bragg-Williams model introduces a non-ideality of mixing parameter (

ρ (J/mol); Eq. 3.2), which is the difference in interaction energy between pairs of unlike molecules and the interaction energy between pairs of like molecules.

$$\rho = z\left(u_{AB} - \frac{u_{AA} + u_{BB}}{2}\right) \qquad (3.2)$$

where z is the first coordination number, and u_{AA}, u_{AB} and u_{BB} are the interaction energies for AB, AA and BB pairs, respectively.

In this approximation, the liquidus line as described by the Hildebrand equation (Eq. 3.1) is simply adjusted by introducing the extra energy term. According to this approximation, the solubility limit of the "solute" in the "solvent" is given by:

$$\ln X_s + \frac{\rho(1 - X_s)^2}{RT} = -\frac{\Delta H_s}{R}\left(\frac{1}{T} - \frac{1}{T_s}\right) \qquad (3.3)$$

For ideal mixing, the intermolecular interaction of like-pairs is equal to that of mixed-pairs and consequently $\rho = 0$. Negative values of ρ reflect a tendency for pairing of unlike molecules (i.e. A-B), whereas, positive values of ρ indicate like pairing tendencies (i.e. A-A or B-B). The non-ideality of mixing parameter, ρ, can therefore be used as an indication of the intersolubility of two molecules; a negative value would indicate a tendency for order and a positive value would reflect a tendency of like molecules to cluster indicating immiscibility order [24].

The liquidus line of the OPO/MeP system present a eutectic formed by MeP and the molecular compound and another eutectic formed by the molecular compound and OPO. Applying Eq. (3.3) to the two pairs of branches requires T_S and ΔH_S parameters of MeP

for branch I and of the molecular compound for branch II for the first eutectic and T_s and

ΔH_S parameters of the compound for branch III and of OPO for branch IV of the second

eutectic. The parameters T_S and ΔH_S used to simulate the different branches of the

liquidus line were determined by DSC and are summarised in Table 3.1.

Table 3.1: Thermodynamic parameters used in the Bragg – William approximation (Eq. 3.3) for the different segments of the liquidus line, and values of the non-ideality of mixing parameter obtained. MC: 1:1 molecular compound. Enthalpy of melting, ΔH_S and melting temperature, T_S of the solute in each branch. The solute for Branch I: MeP, for Branch II: MC (the first eutectic), and the solute for Branch III: MC and for Branch IV: OPO (the second eutectic). The values of T_S and ΔH_S were determined by DSC

Segment	Region	T_S (K)	ΔH_S (kJ/mol)	ρ (kJ/mol)
I	$0.0 \leq X_A \leq 0.40$	302.93±0.63	27.6 ± 3.7	0.68
II	$0.40 \leq X_A \leq 0.55$	293.95±0.31	156.2 ± 5.3	-58.48
III	$0.55 \leq X_A \leq 0.80$	293.95±0.31	156.2 ± 5.3	-6.50
IV	$0.80 \leq X_A \leq 1.0$	293.65±0.51	123.5 ± 12.1	-62.54

The best fit liquidus line and subsequent value of ρ were calculated in two stages. T was calculated for each segment starting with an educated guess of the value of ρ and repeated using ρ increments of ± 1 kJ/mol. The standard method of least squares approach was used to obtain the best fit. In this method the sum of squared residuals, i.e., difference between the observed value (T_{exp}) and the calculated value (T_C), is minimized. The value

of ρ which yielded the smallest sum of squared residual was then used as the starting value to refine the fit. In the second stage, the ρ - value obtained in stage 1 was varied by smaller increments of ± 0.01 kJ/mol and calculations are repeated until the sum of the squared residuals is minimized again, yielding a value of ρ that was deemed the best fit parameter. Note that smaller steps than 0.01 kJ/mol yield improvements in the fit that are smaller than the uncertainty attached to the measured data.

As expected, the calculated liquidus line assuming an ideal mixture using Eq. (3.1) did not reproduce the experimental liquidus line and is not shown. The experimental liquidus line has been very satisfactorily reproduced by considering the two eutectics separated by the singularity at 0.55_{OPO} and using Eq. (3.3) for each eutectic and a non-ideality of mixing parameter ρ for each branch (Table 3.1). The calculated ρ-values are comparable to published values for binary lipid systems [16, 17, 26]

The simulated four segments of the liquidus line (labeled I to IV) are represented by solid lines in Fig. 3.3. The singularity has been confirmed at 0.55_{OPO}. The eutectic points obtained by the intersection of the two segments were confirmed at 0.40_{OPO} and 0.80_{OPO} and T_E of 16 °C and 11.5 °C, respectively.

The simulation yielded negative values of ρ for all segments (Table 3.1) except the MeP rich region (Region I in Fig. 3.3) where it is 0.68 kJ/mol. The Bragg-Williams approximation attributes the origin of the non-ideality of mixing to the enthalpy term of the free energy of mixing and assumes the same entropy term as in the ideal mixing case

[25]. The non-ideality of mixing parameter, ρ, is the energy difference between (A–B) pair and the average of (A–A) pair and (B–B) pair (Eq. 3.2).
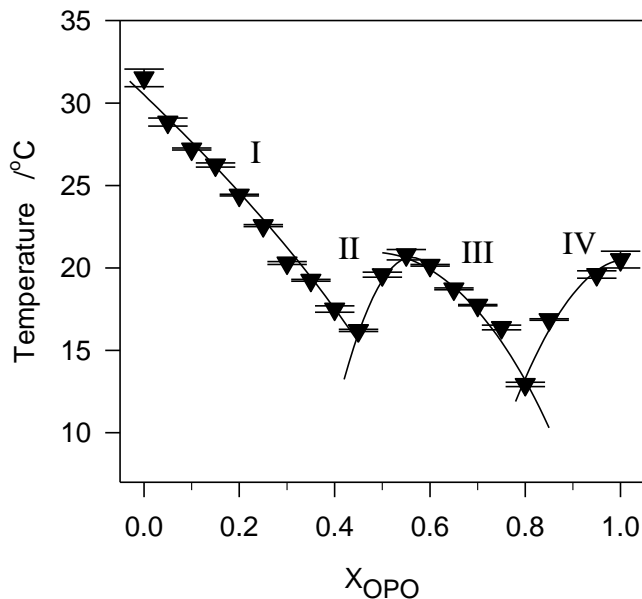
Figure 3.3. Experimental (▼) and calculated (solid line) liquidus line of the MeP/OPO binary system. Regions I – IV indicate the segments of Table 3.1

The value of ρ obtained for MeP- rich mixtures (region I in Fig. 3.3) is a rather small value close to zero which indicates an ideal mixing behaviour. On the OPO rich region (Region IV in Fig. 3.3) the fit yielded a ρ-value of -62.54 kJ/mol reflecting a strong tendency for order [24]. This is a clear indication of strong molecular interactions which tend to favour the formation of OPO-compound pairs in the liquid state rather than OPO-OPO or compound-compound pairs. The negative values for ρ in the compound region indicate that unlike pairing is energetically favoured between the OPO and the compound as well as between MeP and the compound (Table 3.1). Note, however, that the absolute value of ρ obtained for Region II is nine times greater than that for Region III, indicating that the tendency of unlike pairing with the compound is much more pronounced with MeP

than OPO. This result and the very large value obtained for ρ in the OPO- rich region is an indication that disturbance of the MeP/OPO's crystal packing is significant even at low concentration of OPO in the MeP, or of MeP in the OPO.

3.3.4 Microstructure of the Crystallized Mixtures

Figure 3.4 shows the microstructures of selected OPO/MeP mixtures taken at -50 °C with 100X magnification. Table 3.2 provides a brief description of their microstructure (crystal shape, average particle size and distribution, and density) and lists the start temperature of crystallization (T_S) recorded at the appearance of the first "white spot" (representing the first nucleus/crystal) in the PLM, and the corresponding onset temperature of crystallization (T_{On}) obtained by DSC using the same thermal protocol. Note that the smallest structures observable in a light microscope are of the order of 0.5 μm, due to the limitation induced by light diffraction. Therefore, structures detected by the light microscope are significantly larger than nuclei. However, as convincingly argued by Marangoni and co-workers, [10, 27] for well-behaved (i.e. slow crystallizing) systems, one may assume individual crystals detected at early stages of crystallization correspond to individual nuclei.

The OPO/MeP mixtures presented a variety of fat networks with distinctive crystal shapes and sizes, and a variety of spatial distributions of the solid phases. The fat networks with very large crystals were relatively not uniform compared to the networks containing smaller crystals.
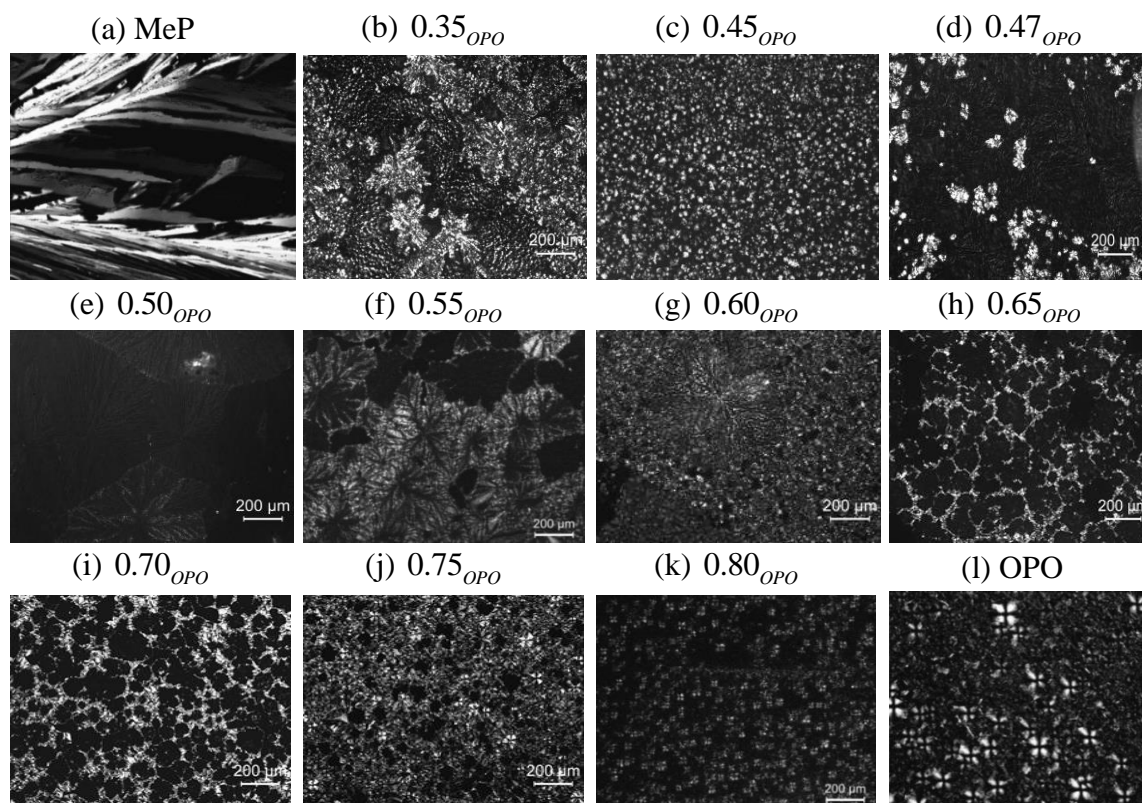
Figure 3.4. PLM (100X magnification) of selected OPO/MeP mixtures obtained at -50 ºC, (a) MeP, (b) 0.35_{OPO} (c) 0.45_{OPO}, (d) 0.47_{OPO}, (e) 0.50_{OPO}, (f) 0.55_{OPO}, (g) 0.60_{OPO}, (h) 0.65_{OPO}, (i) 0.70_{OPO}, (j) 0.75_{OPO} (k) 0.80_{OPO}, (l) OPO

As can be seen in Fig. 3.4, the fully crystallized pure materials (MeP and OPO) presented a microstructure startlingly different from all their mixtures. Overall, the shape of the crystals was altered and their average size considerably reduced as soon as OPO was added. The very large crystals of the solid network of pure MeP (Fig. 3.4a) contrast dramatically with the smaller crystals of all the MeP/OPO mixtures. The typical shape of MeP crystals was no longer observed upon addition of OPO. The 0.35_{OPO} mixture (Fig. 3.4b), for example, presented dispersed, medium sized highly branched dendrites of ~200 μm diameter, compared to the very long (>2500 μm) smooth leaflets of MeP. These results

indicate that OPO effectively suppressed the crystal growth of MeP. The detailed quantification of this suppression is presented in the following paragraphs.

The microstructures of the special mixtures, i.e., the eutectic compositions E1 (Fig. 3.4c, 0.45_{OPO}) and E2 (Fig. 3.4k, 0.80_{OPO}) and the compound (Fig. 3.4f) are particularly interesting. These mixtures delimit concentration regions of fundamentally different microstructures. The two eutectics displayed very dense crystal networks made of small spherulitic entities. Contrary to the microstructure of E1, whose crystal network presented a granular texture at the 100X magnification, the microstructure of E2 presented fully discernible spherulites, albeit with some crystal clustering. Although smaller, the crystals constituting the microstructure of E2 are reminiscent of the Maltese cross shaped crystals of OPO, suggesting that OPO was the entity initiating their crystal habit. This was also observed for all the OPO-rich mixtures. The compound mixture on the other hand formed a very peculiar network made of dendritic-like crystals, originating from the center and bifurcating radially (Fig. 3.4f-g), indicating the presence of low energy facets which evolve in a complex manner.

The special mixtures delimit concentration regions in the phase diagram where key elements of the final microstructure are shared. These concentration regions match perfectly the segments of the liquidus line in the phase diagram (Fig. 3.3). More interestingly, as can be seen in Fig. 3.5 showing the average size of the largest crystals versus OPO molar ratio, the change in crystal size observed for the OPO/MeP mixtures mirrored that of the liquidus line.
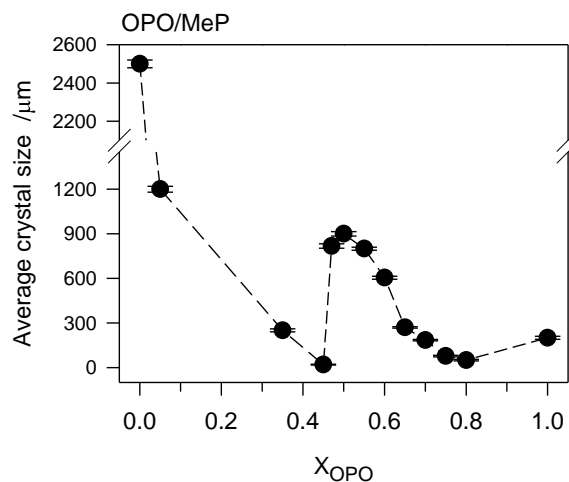
Figure 3.5. Average crystal size of the OPO/MeP mixtures obtained by PLM with 100X magnification

3.3.5 Development of the Crystal Networks

The similarities and differences are particularly manifest in the time-temperature (1 °C/min) resolved PLM. The evolution of the fat network from the appearance of the first crystallites to the fully developed solid development from the melt perfectly distinguishes the microstructures. The first crystals observed under the PLM have sizes in the 5-20 μm range and are probably not the primary crystals formed upon nucleation, but already grown crystals because nucleation is generally quickly followed by crystal growth.

As expected, T_S decreased significantly as OPO was added to MeP, in a similar fashion to the DSC onset temperature of crystallization, T_{On}. One can note however that T_S is slightly above the corresponding T_{On} for all samples (Table 3.2). This is understandable not only because of the way the latter is determined, but also because at the early stages of crystallization, the heat released from the formation of the first few nuclei may not be captured by DSC. More fundamentally, techniques of low sensitivity for solid

contents which measure crystal growth, such as DSC or pNMR, cannot evaluate accurately nucleation effects [28].

Table 3.2 Summary of the description of the microstructure (crystal shape, particle distribution, average crystal size, and network description) of the different OPO/MeP mixtures as observed by PLM after complete crystallization. The mixtures were cooled from the melt at a rate of 1 °C/min. T_S (°C) $\pm$ 0.5: induction temperature of crystallization as determined by PLM; T_{On} (°C) $\pm$ 0.3: onset temperature of crystallization as determined by DSC; E1 and E2: eutectics 1 and 2; 1:1 C: 1:1 molecular compound

	T_s (°C)	T_{On} (°C)	Crystal shape	Crystal size (µm)	Network description
MeP	26.0	24.1	Radial needle-like fibres originating from the nucleus with palm leaf-like forking.	Very large, > 2500	Uniform. only 1 crystal observed on a slide at the 50X magnification
0.05_{OPO}	24.7	23.2	leaf-like	1200	Heterogeneous with intricate distribution of the leaves
0.35_{OPO}	8.3	7.7	Dispersed, medium sized highly branched dendrites		Heterogeneous with intricate distribution of the branches.
E1: 0.45_{OPO}	6.5	4.6	Very grainy Small Maltese crosses	17 - 23	Uniform Very homogeneous. Very dense.
0.47_{OPO}	7.0		Primary nucleation of large spherulites followed by small bright secondary crystals	Large- 825 132	Very Uniform and homogeneous distribution of the large crystals. Secondary crystals formed on top of the primary crystals. Phases are clearly separated.
0.50_{OPO}	12.0	8.5	Large radially grown branched crystals	Large- 1100 208	Very Uniform and homogeneous distribution of the crystals. Very sharp lines of impingement.

1:1 C 0.55$_{OPO}$	10.0	8.6	Non-uniformly distributed, radially grown leaf-like dendrites – not connected dendrites	360-600	Relatively heterogeneous distribution of the crystals. Not uniform
0.60$_{OPO}$	7.0	7.3	Primary Non-uniformly distributed, radially grown leaf-like dendrites – not connected dendrites followed by secondary small crystals	Large-735 Small-610	Relatively Homogeneous and uniform underlying network of the large crystals. Very dense and heterogeneous upper layer of the small crystals Secondary crystals formed on top of the primary crystals. Phases are clearly separated
0.65$_{OPO}$	10.0	6.7	Relatively small bright Maltese crosses connected to form a two-phase microstructure	215	Heterogeneous with intricate large honeycomb (about 200 μm) distribution of one phase enclosing the other. Low density
0.70$_{OPO}$	9.0	5.4	Relatively small bright Maltese crosses connected to form a two-phase microstructure	184	Heterogeneous with intricate honeycomb (about 100 μm) distribution of one phase enclosing the other. Medium density
0.75$_{OPO}$	8.0	2.3	small bright Maltese crosses connected to form a two-phase microstructure	77	Heterogeneous with intricate small honeycomb (about 30 μm) distribution of one phase enclosing the other. High density
E2: 0.85$_{OPO}$	-3.0	-4.3	Very Small typical Maltese crosses	50 - 80	Very Uniform. Medium density
OPO	-9.5	-11.6	Small typical Maltese crosses	200	Very uniform, homogeneous and dense

Microstructure Development of MeP and OPO

MeP crystallized so very rapidly at ~26 ºC that only one single crystal was observed

in the entire PLM slide. This can be related to the very narrow exotherm displayed by the

cooling DSC thermogram of this FAME. OPO, on the other hand, crystallized much slowly, forming Maltese cross shaped crystals, typical of a spherulitic growth. As shown in Figs. 3.6a-d, representing selected PLMs taken as OPO was cooling, the apparent size of the crystals increased from an estimated diameter of 20-μm for the first "early crystal" imaged at -9.5 °C to plateau three (3) minutes later with an average size of 200 μm. The relatively slow growth observed by PLM is attributable for a large part to the effect of the peculiar geometry of the OPO molecule due to the *cis*-double bonds on crystal growth.

(a) -9.5 ° C   (b) -11.0 ° C   (c) -12.5 ° C   (d) -17.5 ° C
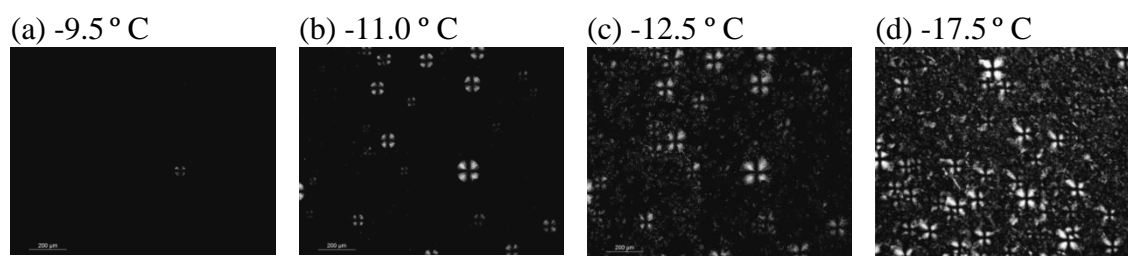
Figure 3.6. Selected PLM images (100X) taken during the development from the melt of OPO, (a) -9.5 ° C, (b) -11.0 ° C, (c) -12.5 ° C, (d) -17.5 ° C.

Microstructure Development of Eutectic E1

The first white small spot in the PLM of the eutectic composition E1 ($X_{OPO} = 0.45$) was observed at 6.5° C (Fig. 3.7a). This first crystallite, contrary to the case of OPO, was followed by a burst of small crystals filling the PLM slide within a very short interval of time (Fig. 3.7a-b). These crystals developed very rapidly into small spherulites of ~17 to 23 μm average sizes (Fig. 3.7c). The microstructure developed further into a dense and very homogeneous grainy network in which the crystals appeared to gradually lose their individuality due to clustering (Fig. 3.7d). There were no noticeable changes in the microstructure of E1 below 3 °C.

(a) 6.5 °C   (b) 6.0 °C   (c) 5.5 °C   (d) 4.5 °C
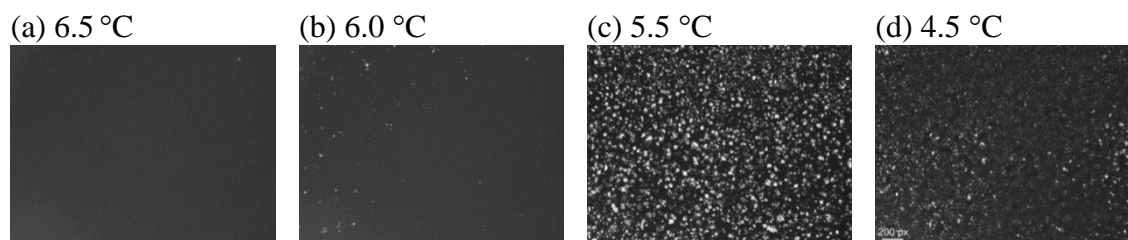
Figure 3.7. Selected PLM images (100X) taken during the development from the melt of the microstructure of the first eutectic composition, E1 ($X_{OPO} = 0.45$). Measurement temperatures are reported on top of the images

Microstructure Development of Eutectic E2

The first crystals (nucleation) of the second eutectic composition E2 ($X_{OPO} = 0.80$) were observed at -4 °C (Fig. 3.8a). Similarly to E1, the first white spot observed in the PLM was followed by the formation of very small spherulitic crystals which very rapidly filled the microscope slide (Fig. 3.8b). The crystals grew relatively slowly and reached sizes of 50 – 80 nm at ~-7.5 °C (Fig. 3.8c).

(a) -4.0 °C   (b) -5.5 °C   (c)-7.5 °C
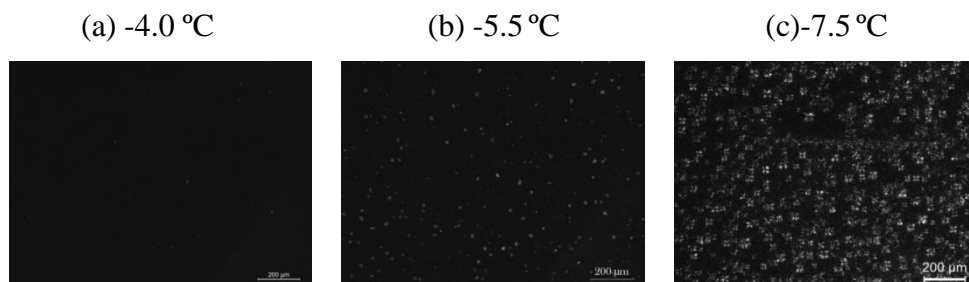
Figure 3.8. Selected PLM images (100X) taken during the development from the melt of the microstructure of the second eutectic composition, E2 ($X_{OPO} = 0.80$). Measurement temperatures are reported on top of the slides

Note that some of the crystals eventually clustered, but unlike for the microstructure observed at E1, the individuality of the crystallites seems to be preserved as suggested by the relatively well resolved impingement boundaries.

Microstructure Development of the Compound and Mixtures between the Eutectics

The compound is central to the understanding of the microstructure development in the OPO/MeP binary system. The crystallization of the compound composition (0.55_{OPO}) started at 9.5 ℃ and completed at 5 ℃ (Fig. 3.9a - c). The number of apparent crystals increased relatively rapidly as crystallization proceeded, but contrary to the microstructure development at E1 and E2, slowly enough to allow for an accurate counting of the crystals during 3 min. The crystals grew radially forming dendritic bifurcations. From a 50-µm diameter when they were first spotted, the size of the crystals increased to ~100 µm 30 s later to reach ~500-800 µm at the complete crystallization, indicating a relatively high growth rate. Note that no new crystal or further growth was observed below 7 °C. In fact, the microstructure of the mixture did not show any further change upon cooling down to -50 °C.

(a) 9.5 ° C   (b) 9 ° C   (c) 5.5 ° C   (d) -50 ° C
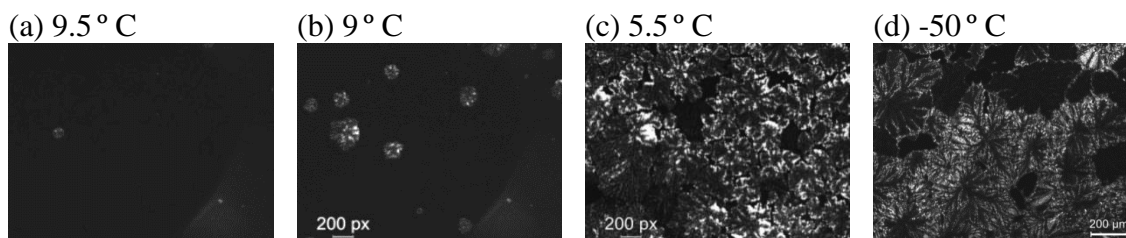
Figure 3.9. Selected PLM images (100X) taken during the development from the melt of the microstructure of the compound mixture (0.55_{OPO}). Measurement temperatures are reported on top of the images

The final microstructure was formed of a complex intertwined network of these relatively large dendritic spherulites (Fig. 3.9d). Note that the 0.50_{OPO} sample presented a similar crystal development with spherulitic crystals made of very complex leaflet-like branches with size comparable to those of the 0.55_{OPO}.

On the two sides of the 50% mixture, the microstructure of the 0.47_{OPO} and 0.60_{OPO} samples evolved similarly from the melt and formed similar networks. The crystallization in both mixtures started with very few small crystals (one or two) which grew rapidly into very large spherulites reminiscent of the crystals observed for the 0.50_{OPO} sample. As the sample was cooled further, small and bright crystals formed via secondary nucleation on top of the existing network in both cases. However, the secondary crystals of 0.47_{OPO} evolved into bifurcating flocks, whereas, those of 0.60_{OPO} were very small Maltese crosses. It is reasonable to assume that crystals (large spherulites) observed for the 0.50_{OPO} sample are those of a phase made of the 1:1 compound which coexisted with a MeP phase (small flocks) in the case of the 0.47_{OPO} sample and with an OPO phase (small Maltese crosses) in the case of 0.60_{OPO}. Obviously, the presence of the compound hindered the full development of both MeP and OPO into the respective networks that they would achieve alone.

Microstructure Development of the Microstructure of 0.65 OPO, 0.70 OPO and 0.75 OPO

The PLMs of the 0.65_{OPO}, 0.70_{OPO} and 0.75_{OPO} samples taken at selected temperatures during cooling (1 °C/min) are shown in Figs. 3.10 – 12, respectively. The crystal development (formation, growth, size and type of crystals) and final fat network of

these mixtures are similar to those of the second eutectic composition. The PLM of these mixtures started showing a very small number of crystals which increased rapidly. The crystals themselves grew slowly then impinged to form an intricate honeycomb-like microstructure. Beside the two different morphologies observed in the fully crystallized material (white honeycomb contour and fill) which are probably constituted of the two solid phases of the binary eutectic reaction, one can notice a coexisting third phase made of Maltese cross – like crystals (arrow in Fig. 3.10), reminiscent of an OPO-rich phase. As the concentration approaches the eutectic (PLMs from 0.65_{OPO} to 0.75_{OPO}), the number of starting crystals became higher and their size smaller. Also, the honeycombs making up the final microstructure became smaller, indicating that it is OPO related.

(a) 7.8 ℃   (b) 6.1 ℃   (c) 3.1 ℃   (d) -4.0 ℃
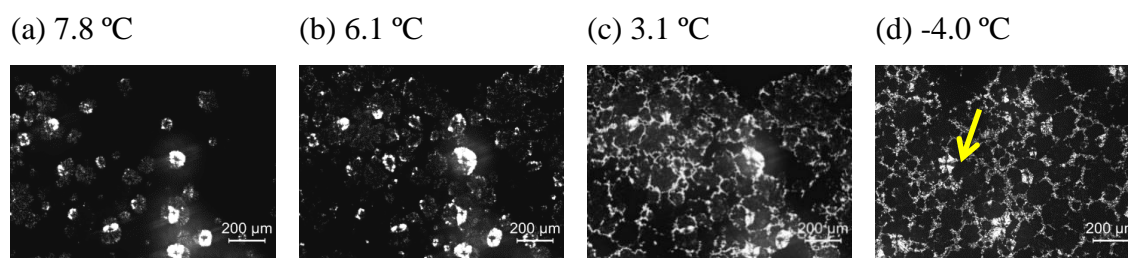
Figure 3.10. PLM of 0.65_{OPO} taken at selected temperatures (reported on top of the images). Images are taken at 100X magnification during the cooling process.

(a) 6.8 ℃   (b) 3.8 ℃   (c) 2.3 ℃   (d) 0.8 ℃
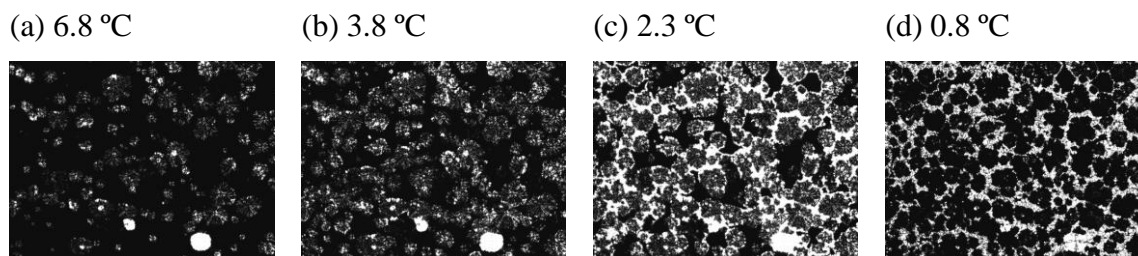
Figure 3.11. PLM of 0.70_{OPO} taken at selected temperatures (reported on top of the images). Images are taken at 100X magnification during the cooling process. Multi time images were taken in intervals of 5 s

(a) 7.5 ℃   (b) 5.5 ℃   (c) 3.0 ℃   (d) 2.0 ℃
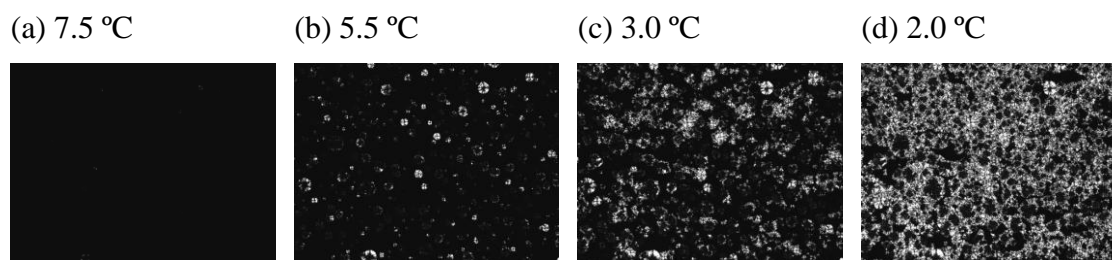
Figure 3.12. PLM of 0.75_{OPO} taken at selected temperatures (reported on top of the images). Images are taken at 100X magnification during the cooling process. Multi time images were taken in intervals of 5 s

3.3.6   Nucleation Progress Estimated by PLM

The nucleation progress can be estimated by following the evolution of the number of individual crystals showing in the PLM when such counting is possible. The variation of the number of crystals with temperature gives an idea of the rate of formation of the crystals. However, when individual crystals can be individually counted and the rate of nucleation is low, the rate of crystals formation (number of crystals per time) can be reasonably substituted for the rate of nucleation [10, 28]. Note that there is a limit to which the number of crystals can be accurately counted in a PLM slide.

(a) t= 0 min   (b) t= 5 min   (c) t= 7 min   (d) t= 11 min
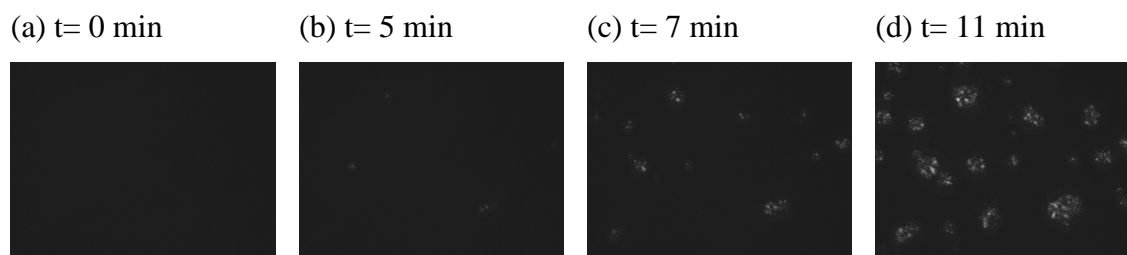
Figure 3.13. PLMs taken at selected times (500X magnification) during the isothermal crystallization (T= -4 °C) of the second eutectic composition E2 ($X_{OPO} = 0.80$)

The evolution of the microstructure of second eutectic composition E2 ($X_{OPO} = 0.80$) was followed isothermally at the temperature (-4 °C) at which the first "nucleus" was spotted. PLM taken at selected times are shown in Fig. 3.13a-d (500X magnification). As can be seen in the figures, the crystallization proceeded through sporadic nucleation and spherulitic growth. The estimated number of crystals versus time is shown in Fig. 3.14a. The data were successfully fitted with a typical sigmoidal function. Such a trend suggests that the transformation proceeded through a simple crystallization mechanism.

The number of such crystals at the two eutectics increased so rapidly during the non-isothermal crystallization that it was impossible to follow their progress. Obviously, nucleation rate was very high. The number of apparent crystals of OPO (Fig. 3.14b) and compound mixture (Fig. 3.14c) versus temperature curves presented typical sigmoidal shapes with plateaus at ~ 7.5 °C and -12.5 °C, respectively. Note that it was no longer possible to count individual crystals beyond these temperatures, due to clustering.

Although the plot of the number of crystals versus time gave the typical sigmoidal shaped curve; it is not a measure of the volume of the new phase to which the Avrami model is usually applied. It is rather a function of the spatial distribution of mass and only in part a function of the solid content which can be described by an Avrami-like model (Eq. 3.6).

$$\frac{y}{y_{\max}} = 1 - \exp\left(-k\left(t - t_0\right)^n\right) \tag{3.6}$$

y describes the number fraction of crystals as a function of time and y_{max} is its limiting value as time approaches infinity. k is an Avrami-like apparent rate constant and n an Avrami-like exponent. t is the time and t_0 is the induction time.
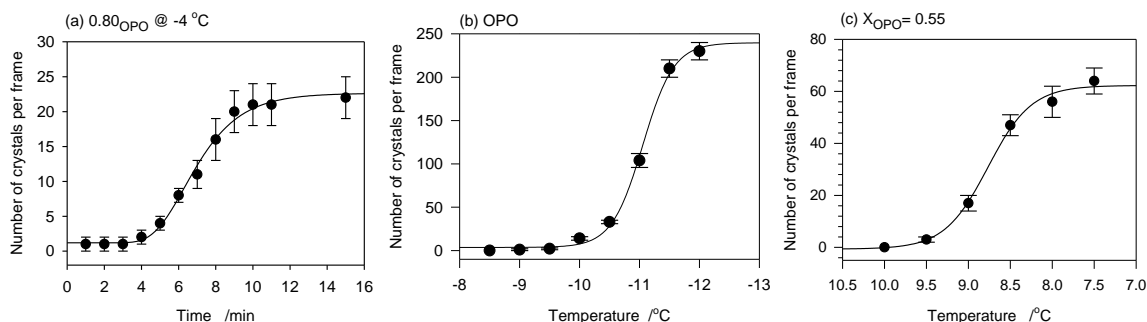
Figure 3.14. (a) Estimated number of crystals per frame as a function of time during the isothermal crystallization (-4 °C) of the second eutectic mixture, (b) and (c) as a function of temperature during the non-isothermal crystallization of OPO; and compound mixture, respectively. The solid line is a fit of experimental data to a sigmoidal function and a guide for the eye.

This is particularly relevant when clusters are present or when already grown crystals "absorb" emerging nuclei. However, PLM is a sensitive enough technique to study nucleation but needs special care for the analysis of its results and the number of single (discernible) entities can be used as a lower limit for the description of nucleation progress [28]. The results of the application of the model despite its obvious restriction would provide a means of comparison. As can be seen from Table 3.3, the Avrami-like parameters of OPO and the compound are very different indicating differences in both nucleation and spatial distribution of the crystals and can be related to differences in crystal growth.

Table 3.3. Results of the application of an Avrami-like model to number of crystal of OPO and the compound mixtures shown in Fig. 3.11a and 3.11b, respectively

	R^2	Std Err	k	n
OPO	0.9945	0.0339	0.008 ± 0.003	4.9 ± 0.4
Compound	0.9876	0.0511	0.086 ± 0.027	3.3 ± 0.4
OPO (T= -4 ºC)	0.9953	0.0289	0.001 ± 0.001	3.9 ± 0.2

3.3.7   Crystal Structure of OPO/MeP

The main subcell hydrocarbon-chain packing modes are commonly denoted as the α, β' and β polymorphs. The chain packing of the α - polymorph is hexagonal with non-specific chain-chain interactions. The common subcell packing of the β'-polymorph is orthorhombic, and the hydrocarbon chains of the β-polymorph are ordinarily packed parallel to each other in a triclinic (or monoclinic, if the angles α and γ are 90 °C) parallel subcell ($T_{//}$). The β-polymorph is the most stable crystal form, with the highest melting temperature, and the α-polymorph is the least stable crystal form, with the lowest melting temperature [29]. The hydrocarbon chain layering is responsible for the characteristic small-angle (long-spacing) reflections. The period of layers normally observed for TAG structures is usually proportional to the acyl chain lengths by a factor of two or three, suggesting a double-chain length (DCL) or a triple-chain length (TCL) packing [30, 31].
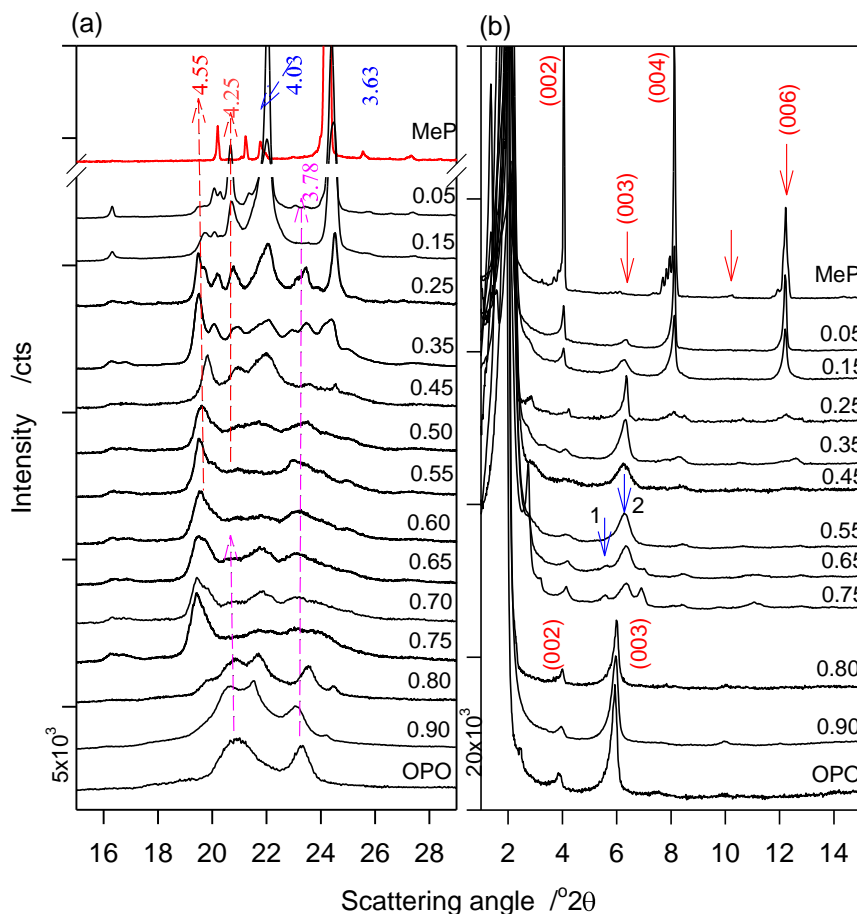
Figure 3.15. (a) WAXD spectra (15 - 30° scattering angle), and (b) SAXD spectra (1 - 15° scattering angle) of OPO/MeP mixtures measured at -40 °C after cooling from the melt at 1 °C/min. OPO molar ratio is reported on the right side above the patterns

Wide Angle X-Ray diffraction and Subcell Structure

The WAXD spectra (15 - 30° scattering angle) of selected compositions of OPO/MeP measured at -40 °C after cooling from the melt at a constant rate (1 °C/min) are shown in Fig. 3.15a. The d-spacing and corresponding Miller indices are listed in Table 3.4. As can be seen in the figure, the crystal lines of the OPO/MeP mixtures were superimposed onto a wide halo, particularly noticeable for mixtures with more than 25% molar OPO, indicating the presence of a liquid phase at the measurement temperature (-40 °C).

Table 3.4. WAXD data: d-spacing of resolved peaks and corresponding Miller indices. Samples were cooled from the melt at 1 °C/min. Patterns measured at -40 °C. Uncertainty= ± 0.05

	010_β		$110_{\beta'}$	$0\bar{1}0_\beta$		102_β or $020_{\beta'}$	$\bar{1}00_\beta$	$200_{\beta'}$		100_β
MeP	--	4.45	4.29	4.17	4.10	4.02	3.87			3.65
0.05_{OPO}	4.52	--	4.29		4.08	4.03	3.84	3.79		3.64
0.15_{OPO}	4.50	--	4.28	4.24	4.09	4.03	3.84	3.77		3.64
0.25_{OPO}	4.56	--	--	--	--	4.03	--	--	--	--
0.35_{OPO}	4.55	4.42	4.29	4.23	4.07	4.02	3.87	3.78		3.64
0.45_{OPO}	4.54	4.48	--	4.24	4.07	4.00	3.9	3.76		3.63
0.50_{OPO}	4.56	--	--	4.23	4.07	--	--	--	--	--
0.55_{OPO}	4.55	4.49	4.29	4.27	4.06	--	3.86	--	3.72	3.54
0.60_{OPO}	4.54	--	--	4.28	--	4.01	--	--	--	--
0.65_{OPO}	4.56	4.47	--	4.26	4.08	4.04	3.84	--	3.71	3.64
0.70_{OPO}	4.47	--	--	4.28	--	4.07	--	--	--	--
0.75_{OPO}	4.56	4.46	--	4.22	4.06	--	--	3.78	--	3.66
0.80_{OPO}	--	4.47	--	4.25	4.09	3.97	--	3.78	--	3.64
0.90_{OPO}	--	4.48	--	--	--	--	3.85	3.79	--	3.67
OPO	--	--	--	4.22	--	--	--	3.87	--	--

Three polymorphic forms were detected: the monoclinic structure of MeP (β_M), the orthorhombic form of OPO (β') and a triclinic structure (β) found in all mixtures with varying content. The reader is advised that careful attention should be taken in order to follow the variation of the relative polymorphic contents because some of the characteristic

lines are very close. The presence of the relatively large liquid phase introduces an extra uncertainty in the estimation of the relative content of the coexisting phases. The analysis of the WAXD crystal peaks were carried out after the contribution of the liquid phase was removed. Therefore, the trends obtained allowed an accurate description of the qualitative as well quantitative changes in the crystal phases as a function of concentration.

The variation of the intensity of the 3.65 Å line is shown in Fig. 3.16. The dramatic decrease observed from pure MeP to the eutectic composition E1 (0.45_{OPO}) indicates that it originated from the β_M - phase and can, therefore, be used to estimate the variation of the monoclinic phase in this region of concentration.
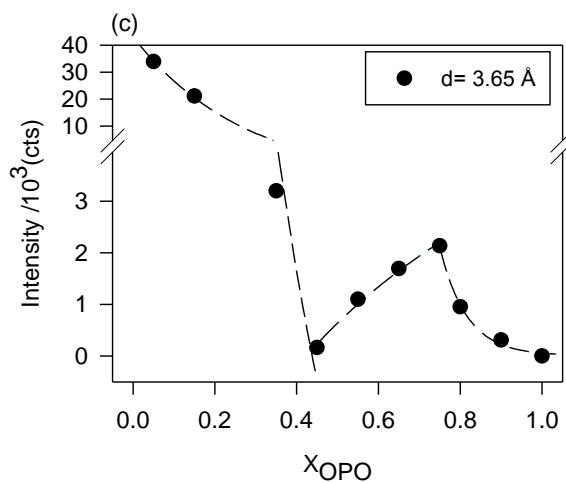
Figure 3.16. Intensity of the 3.65 Å peak versus OPO molar fraction

The XRD pattern of OPO displayed two main peaks characteristic of the β' - form at d-spacing of 4.23 ± 0.07 Å (110) and 3.86 ± 0.04 Å (200). The 4.55 Å and 3.63 Å lines, characteristic peaks of the β - form which were detected in the 0.90_{OPO} mixture, increased dramatically and reached a maximum intensity for the 0.75_{OPO} mixture. These two lines

also appeared for the MeP rich mixtures. As OPO was added to MeP their intensity increased steadily to reach a maximum before the eutectic composition. In this concentration region, the β-phase coexisted with but increased at the detriment of the monoclinic phase of MeP as OPO content was increased. Note that the monoclinic phase content decreased from 0 to 0.45_{OPO} where it disappeared. The mixtures between 0.45_{OPO} and 0.75_{OPO} presented only the characteristic lines of the triclinic symmetry. The WAXD pattern of the compound composition was unique although clearly one of a β-polymorph. It showed unique features such as the appearance of a line at ~ 4.0 Å which is distinct from the 4.03 Å line shown by the WAXD patterns of MeP rich mixtures, and the extinction of a few peaks between $2\theta= 19.6º$ and $23º$. Note that unlike the shoulder-line at 4.50 Å whose intensity varied with concentration, the intensity of the 4.55 Å line remained almost constant for the mixtures of this range of concentration. This indicates that even if the overall crystal structure remained the same, the details of the subcell organisation and electronic density distribution varied as a function of OPO content.

The WAXD data clearly indicates that two different b- phases are at play in the OPO/MeP binary system. The pure OPO at -40 ºC only showed the characteristic reflections from the orthorhombic crystal system. As soon as MeP molecules were included the ensemble of OPO molecules, a rearrangement of molecules occurred in order to accommodate the MeP with OPO. As the concentration of MeP was increased to 0.75_{OPO} (second eutectic) the intensity of the (4.55 Å) characteristic reflection of the β-form increased dramatically while its corresponding d-spacing decreased due to better molecular rearrangements and order along the 010 direction.

The microstructure observed for the MeP- rich mixture is associated with the monoclinic phase which was predominant in this range. The large decrease of the size of the crystals making up this phase indicates that the monoclinic symmetry is versatile enough to accommodate such a wide range of crystal sizes. The relatively large crystals observed for the compound and the mixtures which where exclusively triclinic, suggest that the β - form is limited in the range of microstructures that it can accommodate. It is obviously favouring inhomogeneous fat networks made of large crystals. The small size of the crystals of the OPO- rich mixtures indicates that the orthorhombic symmetry is more prone to constitute a more homogeneous microstructure with small crystals. This finding may help in the designing of specific protocols for biodiesel and biodiesel additives which would mitigate both the crystallization temperature and the crystal size related problems of biodiesel.

Small angle X-ray diffraction and Lamellar Packing

SAXD spectra (1 - 15° scattering angle) of selected compositions of OPO/MeP measured at -40 °C after cooling from the melt at a constant rate (1 °C/min) are shown in Fig. 3.15b. The d-spacing and corresponding Miller indices are listed in Table 3.5. The SAXD of the pure MeP displayed a number of sharp and strong peaks. The d-value of the first order (001) reflection represents the thickness of the molecular layers and higher order (00l)-reflections indicate regular, periodic structures and represent the periodical sequence of electronic density differences in multiple layers [32].

Table 3.5. SAXD data: d-spacing and corresponding Miller indices. Samples were cooled from the melt at a rate of 1 °C/min. Patterns measured at -40 °C. Uncertainty= $\pm$ 0.15

	(001)	(002)	(003)	(004)	(005)	(006)
MeP	43.87	21.74	14.42	10.87	8.61	7.23
0.05_{OPO}	43.01	21.77	14.07	10.86	--	--
0.15_{OPO}	41.74	21.75	14.04	10.87	--	--
0.25_{OPO}	41.86	--	13.89	--	--	--
0.35_{OPO}	41.80	21.07	13.95	10.63	--	--
0.45_{OPO}	41.80	21.51	14.09	10.49	--	--
0.50_{OPO}	42.41	--	13.97	--	--	--
0.55_{OPO}	42.26	21.33	13.96	10.25	--	--
0.80_{OPO}	44.15	22.06	14.69	--	--	--
0.90_{OPO}	45.20	22.07	14.76	--	--	--
OPO	44.24	22.34	14.58	--	--	--

	S1				I_2/I_1	S2		
	(001)	002	(003)	004		(001)	002	(004)
0.60_{OPO}	42.38	21.21	13.91	10.44	**0.1**	63.05	--	--
0.65_{OPO}	42.50	--	13.59	--	**0.2**	63.15	31.50	15.15
0.70_{OPO}	43.31	21.07	13.93	--	**0.5**	63.30	31.70	--
0.75_{OPO}	42.87	21.17	13.87	--	**1.5**	63.35	31.93	15.29

There are three distinct groups of patterns each sharing similar features indicative of similar lamellar arrangements. They are delimited by the eutectic compositions (0.45_{OPO}, 0.80_{OPO}) and the compound composition 0.55_{OPO}. The XRD patterns of the mixtures with

$X_{OPO} \leq 0.45$ displayed the same $00l$ reflections as MeP (uppermost pattern in Fig. 3.15b). In this group, the intensity of the 001 reflection remained almost constant whereas that of 002, 004 and 006 decreased dramatically and disappeared completely for the eutectic composition (see for example the variation of the intensity of the 006 reflection in Fig. 3.15b). The special case of the 003 reflection is discussed in the following paragraphs. This clearly indicates the dramatic disrupting effect of OPO on the periodical sequence of electronic density differences in the layering of MeP. Although the repeat unit d_{001} decreased from ~ 44 Å for pure MeP to 42 Å from 0.15_{OPO} to 0.45_{OPO}, the period of layers along the layer normal observed for these structures is proportional to the acyl chain lengths by a factor of two. This limited shortening of repeat unit length is probably due to adjustments of the MeP head groups to the glycerol backbone of OPO.

The SAXD patterns of the mixtures with $X_{OPO} > 0.75$ presented the same reflections as OPO, with a repeat layering unit of ~44.5 Å. This is very close to published values of the double chain length (DCL) stacking of the β'- form of OPO [33-36]. The 003 reflection which was very weak in MeP increased to reach a maximum for the 0.55_{OPO} mixture then decreased to disappear from the SAXD pattern of 0.80_{OPO}. Such a variation of this reflection with X_{OPO} is associated with the presence of the compound (in the β - form) alongside a MeP- rich phase and an OPO- rich phase on the left and right concentration sides.

The mixtures from 0.60_{OPO} to 0.75_{OPO} presented two types of stacking (Table 3.5). The first (S1 in Table 3.5) is similar to the patterns of the compound with a repeat layer

unit of 42.5 Å and hence associated with the layering of its β - phase. The second stacking (S2 in Table 3.5) presented a 001 line at ~63.5 Å accompanied with weak 002 and 004 reflections. Mixtures showing the two 001 reflections of 0.65_{OPO} and 0.75_{OPO} mixtures, the intensity of the 63.5 Å line increased dramatically relatively to the 42.5 Å line from ~0.01 to 1.5 as OPO ratio was increased (Table 3.5) clearly indicating an OPO-rich phase origin. Similarly to what was published for the triple chain structure of the OPO [13, 37], the 63.5 Å line is undoubtedly associated with the β - form of OPO, and specifically to its highest stability β_1 - form. The coexistence of these two crystal structures in these mixtures can be directly related to the two phases observed in their microstructure observed by PLM (see Section 3.1.). Schematic representations of the crystalline structures of the β' - and β_1 - phases of OPO, and the β - phase of the compound depicted on the basis of the lamellar distances obtained from X-ray diffraction are shown in Fig. 3.17.

The SAXD lines from the 0.60_{OPO} to 0.75_{OPO} compositions were less intense compared to those of MeP and OPO, indicating a less localized electronic density, probably due to relaxed packing of OPO and MeP in the unit. The larger width of all the (00l) reflections detected for these mixtures indicated also that chain arrangement in this new packing is looser and much more disordered that that of the pure constituents of the mixtures.
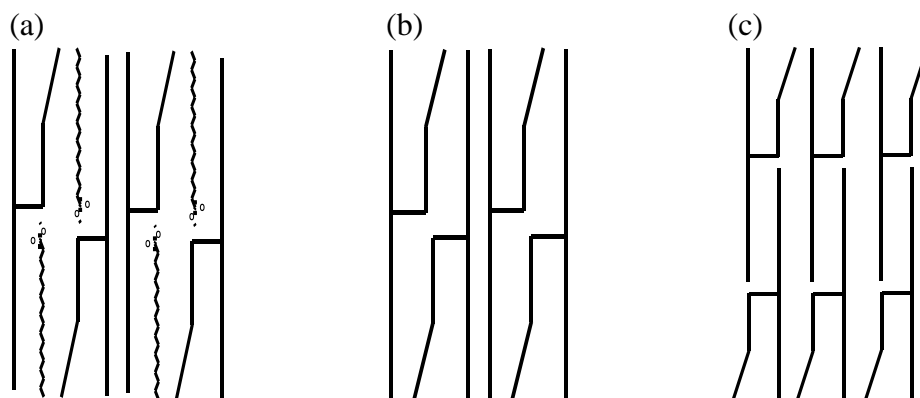
Figure 3.17. Schematic representations of the crystalline structures of OPO and OPO:MeP molecular compound on the basis of x-ray diffraction data. (a) β - form of the OPO:MeP (1:1) molecular compound in the double layer packing structure (d_{001} = 42.5 Å); (b) β'- of OPO in the double layer packing structure (d_{001} = 44.5 Å); (c) β_1- form of OPO in the triple layer packing structure (d_{001} = 63.5 Å).

3.3.8   Mechanism of Disruption of Biodiesel Crystallization by TAGs

The disturbance to crystallization is manifest at both the nanostructure and microstructure levels. At the nucleation level, the additive delayed the formation of critical nuclei from embryo clusters through molecular-level interactions between the crystallizing host molecules (MeP) and the interfering additive molecules (OPO). The crystal growth is retarded when the additive prevents the adsorption and incorporation of crystallizing host molecules at the growing crystal surfaces. The additive is very efficient as both length scales are impacted. We propose, therefore that in the case of the bi-*cis*-unsaturated TAG molecules (such OPO of the present study), that the mechanism for disruption of crystallization is dependent on the peculiar geometry of the TAG: the "straight" acid chain promote the interaction with the FAME (MeP) and participates easily in the lamellar

packing of the equally "straight" FAME, whilst its two kinked unsaturated oleic acid chains effectively halts additional saturated FAMEs from participating in the packing due to steric hindrances. The interaction of the relatively large glycerol group of the TAG with the FAME molecules could be repulsive, adding to the suppression of the crystallization effect. This is realistic since the crystallization behaviour of TAGs and FAMEs, and more generally of oils and fats, is directly related to structural details such as the length of the acyl chains, degree of unsaturation and conformation of the glycerol groups. The findings support that in order to suppress the crystallization, an additive must concurrently have a structural similarity with the crystallizing substances in order to favor the required interaction, and features that would suppress the formation of organized structures [38].

3.4   Conclusions

The heating and cooling DSC thermographs obtained for OPO/MeP mixtures demonstrated complex phase trajectories with several thermal transitions including recrystallization from the melt. The liquidus line in the phase diagram constructed from the heating data presented two eutectics compositions, at 0.45_{OPO} and 0.80_{OPO} with eutectic temperatures at 15 °C and 12 °C, respectively, separated by a singularity at 0.55_{OPO} indicative of the formation of a 1:1 compound. The application of the Bragg-William approximation to the experimental liquidus line indicated a relatively complex intersolubility of MeP and OPO in the liquid phase. The non-ideality of mixing parameter values indicated an ideal mixing behaviour for the mixtures in the $X_{OPO} = [0, 0.40]$ concentration range and a strong tendency for the formation of 'MeP-OPO' unlike pairs for all the other concentrations. The thermal data indicated that OPO disrupts the crystallization process at both the nucleation and growth stages and effectively delays the

crystallization of MeP. The findings of this study indicate that additive formulations containing OPO in low concentrations may be used to measurably improve the cold flow properties, such as PP and CP, of biodiesel by disturbing the easy packing of linear FAMEs and repressing the crystallization temperature.

The analysis by PLM and XRD of the 1,3-dioleoyl-2-palmitoyl glycerol (OPO) and methyl palmitate (MeP) mixtures provided detailed information of the microstructure and crystal structure of the binary system. OPO was found to profoundly impact the polymorphism as well as the microstructure development of MeP. The study of the binary system at the nano- and micro- length scales proved that the OPO impacted the phase behavior of MeP at both the nucleation and crystal growth processes levels. The mechanism proposed for the manner in which the TAG delays crystallization and reduces crystal size was supported by convincing evidence. The disturbance of crystallization manifested at both the nanostructure and microstructure levels. The changes induced by OPO in the crystallization of MeP were evidenced by specific changes to crystal structure and polymorphism, and microstructure, i.e., fat network and crystal shape and habit. OPO promoted the formation of a significant number of nuclei resulting in reduced crystal size of the FAME. The dramatic decrease in crystal size is closely associated to the variation in melting temperature as described by the onset temperature of crystallization determined by PLM and as shown by the liquidus line in the phase diagram constructed by DSC. Furthermore, the polymorphism of OPO/MeP correlated very well with the changes observed in microstructure. The MeP – rich mixtures crystallized presented a monotectic subcell alongside a growing MeP- triclinic subcell whereas the OPO – rich mixtures

crystallized in the orthorhombic alongside a growing OPO-rich triclinic subcell. The compound mixture presented only a triclinic phase.

3.5 References

[1] Hoekman SK, Broch A, Robbins C, Ceniceros E, Natarajan M. Review of biodiesel composition, properties, and specifications. Renew Sust Energ Rev. 2012;16(1):143-69.

[2] Dunn RO. Cold-Flow Properties of Soybean Oil Fatty Acid Monoalkyl Ester Admixtures†. Energy Fuel. 2009;23(8):4082-91.

[3] De Torres M, Jimenez-Oses G, Mayoral JA, Pires E. Fatty acid derivatives and their use as CFPP additives in biodiesel. Bioresour Technol. 2011;102(3):2590-4.

[4] Dunn RO. Effects of minor constituents on cold flow properties and performance of biodiesel. Progress Energ Combust. 2009;35(6):481-9.

[5] Misra RD, Murthy MS. Blending of additives with biodiesels to improve the cold flow properties, combustion and emission performance in a compression ignition engine—A review. Renew Sust Energ Rev. 2011;15(5):2413-22.

[6] Smith PC, Ngothai Y, Dzuy Nguyen Q, O'Neill BK. Improving the low-temperature properties of biodiesel: Methods and consequences. Renew Energy. 2010;35(6):1145-51.

[7] Christensen SA, DiBiase SA, Rizvi SQA. Cold flow additives. In: EPO, editor. C10L 1/19 (2006.01); C10L 1/224 (2006.01) ed2012.

[8] Mohanan A, Bouzidi L, Li S, Narine SS. Mitigating crystallization of saturated FAMES in biodiesel: 1. Lowering the crystallization temperature via addition of metathesized soybean oil. Unpublished- Submitted to Energy.

[9] Sato K, Ueno S, Yano J. Molecular interactions and kinetic properties of fats. Progr Lipid Res. 1999;38(1):91-116.

[10] Marangoni AG. The nature of fractality in fat crystal networks. Trends Food Sci Technol. 2002;13(2):37-47.

[11] Chandran DV, Bhatnagar RK. A method for synthesis of α-monoricinolein. J Am Oil Chem Soc. 1968;45(8):581-2.

[12] Bentley PH, McCrae W. Efficient synthesis of symmetrical 1,3-diglycerides. J Org Chem. 1970;35(6):2082-3.

[13] Minato A, Ueno S, Yano J, Smith K, Seto H, Amemiya Y, et al. Thermal and structural properties of sn-1,3-dipalmitoyl-2-oleoylglycerol and sn-1,3-dioleoyl-2-palmitoylglycerol

binary mixtures examined with synchrotron radiation X-ray diffraction. J Am Oil Chem Soc. 1997;74(10):1213-20.

[14] Costa MC, Boros LAD, Coutinho JAP, Krahenbuhl MA, Meirelles AJA. Low-Temperature Behavior of Biodiesel: Solid-Liquid Phase Diagrams of Binary Mixtures Composed of Fatty Acid Methyl Esters. Energy Fuel. 2011;25(7):3244-50.

[15] Inoue T, Hisatsugu Y, Ishikawa R, Suzuki M. Solid–liquid phase behavior of binary fatty acid mixtures: 2. Mixtures of oleic acid with lauric acid, myristic acid, and palmitic acid. Chem Phys Lipids. 2004;127(2):161-73.

[16] Boodhoo MV, Bouzidi L, Narine SS. The binary phase behavior of 1, 3-dipalmitoyl-2-stearoyl-sn-glycerol and 1, 2-dipalmitoyl-3-stearoyl-sn-glycerol. Chem Phys Lipids. 2009;160(1):11-32.

[17] Boodhoo MV, Bouzidi L, Narine SS. The binary phase behavior of 1,3-dicaproyl-2-stearoyl-sn-glycerol and 1,2-dicaproyl-3-stearoyl-sn-glycerol. Chem Phys Lipids. 2009;157(1):21-39.

[18] Hildebrand JH. Solubility XII. Regular solutions. J Am Chem Soc. 1929;51:66-80.

[19] Bragg WL, Williams EJ. The effect of thermal agitation on atomic arrangement in alloys. Proc R Soc. 1934;145(855):699-730.

[20] Abes M, Bouzidi L, Narine SS. Crystallization and phase behavior of 1,3-propanediol esters II. 1,3-Propanediol distearate/1,3-propanediol dipalmitate (SS/PP) and 1,3-propanediol distearate/1,3-propanediol dimyristate (SS/MM) binary systems. Chem. Phys. Lipids. 2007;150(1):89-108.

[21] Bouzidi L, Boodhoo MV, Kutek T, Filip V, Narine SS. The binary phase behavior of 1,3-dilauroyl-2-stearoyl-sn-glycerol and 1,2-dilauroyl-3-stearoyl-sn-glycerol. Chem Phys Lipids. 2010;163(6):607-29.

[22] Hildebrand JR, Prausnitz RL, Scott RL. Regular and Related Solutions: the Solubility of Gases, Liquids, and Solids. New York, NY: Van Nostrand Reinhold Co., 1970.

[23] Tenchov BG. Non-uniform lipid distribution in membranes. Prog Surf Sci. 1985;20(4):273-340.

[24] Lee AG. Lipid Phase-Transitions and Phase-Diagrams .2. Mixtures Involving Lipids. Biochim Biophys Acta. 1977b;472(3-4):285-344.

[25] Moore WJ. Physical Chemistry 4th ed. Englewood Cliffs, New Jersey: Prentice-Hall, 1972.

[26] Boodhoo MV, Kutek T, Filip V, Narine SS. The binary phase behavior of 1,3-dimyristoyl-2-stearoyl-sn-glycerol and 1,2-dimyristoyl-3-stearoyl-sn-glycerol. Chem Phys Lipids. 2008;154(1):7-18.

[27] Narine SS, Marangoni AG. Microscopic and rheological studies of fat crystal networks. J Cryst Growth. 1999;198–199(2):1315-9.

[28] Martini S, Herrera M. Practical considerations in nucleation studies: The polarized light microscopy technique. Journal of the American Oil Chemists' Society. 2002;79(4):411-2.

[29] Ghotra BS, Dyal SD, Narine SS. Lipid shortenings: a review. Food Research International. 2002;35(10):1015-48.

[30] Fahey DA, Small DM, Kodali DR, Atkinson D, Redgrave TG. Structure and polymorphism of 1,2-dioleoyl-3-acyl-*sn*-glycerols - 3-layered and 6-layered structures. Biochem. 1985;24(14):3757-64.

[31] Mykhaylyk OO, Smith KW, Martin CM, Ryan AJ. Structural models of metastable phases occurring during the crystallization process of saturated/unsaturated triacylglycerols. J Appl Crystallogr. 2007;40(s1):s297-s302.

[32] Dorset DL. From waxes to polymers - crystallography of polydisperse chain assemblies. Struct Chem. 2002;13(3):329-37.

[33] Ikeda E, Ueno S, Miyamoto R, Sato K. Phase Behavior of a Binary Mixture of 1,3-Dipalmitoyl-2-oleoyl-sn-glycerol and 1,3-Dioleoyl-2-palmitoyl-sn-glycerol in n-Dodecane Solution. J Phys Chem B. 2010;114(34):10961-9.

[34] Bayes-Garcia L, Calvet T, Cuevas-Diarte MA, Ueno S, Sato K. Heterogeneous microstructures of spherulites of lipid mixtures characterized with synchrotron radiation microbeam X-ray diffraction. Cryst Eng Comm. 2011;13(22):6694-705.

[35] Minato A, Ueno S, Smith K, Amemiya Y, Sato K. Thermodynamic and kinetic study on phase behavior of binary mixtures of POP and PPO forming molecular compound systems. J Phys Chem B. 1997;101(18):3498-505.

[36] Minato A, Yano J, Ueno S, Smith K, Sato K. FT-IR study on microscopic structures and conformations of POP-PPO and POP-OPO molecular compounds. Chem Phys Lipids. 1997;88(1):63-71.

[37] Bayes-Garcia L, Calvet T, Cuevas-Diarte MA, Ueno S, Sato K. In situ synchrotron radiation X-ray diffraction study of crystallization kinetics of polymorphs of 1,3-dioleoyl-2-palmitoyl glycerol (OPO). Cryst Eng Comm. 2011;13(10):3592-9.

[38] Sangwal K. Additives and Crystallization Processes: From Fundamentals to Applications Chichester, UK: John Wiley & Sons, 2007.

4. Mitigating Crystallization of Saturated FAMES in Biodiesel: 4. The Phase Behavior of 1,3-dioleoyl-2-palmitoyl *sn*-glycerol (OPO)– Methyl Stearate Binary System[3]

4.1 Introduction

Various factors including fossil fuel depletion and environmental concerns have resulted in an increasing demand for renewable and environmentally responsible fuels [1]. Biodiesel derived from vegetable oils or animal fat is one of the most promising alternatives to petroleum based diesel [2]. Definition and detailed specifications of biodiesel are outlined in standards such as ASTM D 6751 in the United States and the EN 14214 of the European Committee for Standardization. Biodiesel is attractive as it has many of the conventional diesel characteristics and can be used neat or in blends with petroleum diesel in unmodified existing diesel engines [3]. Its advantages and disadvantages are very well documented [4].

A critical inherent problem of biodiesel which limits its wide-spread usage is its poor performance during cold weather as indicated by relatively high cloud point (CP) and pour point (PP) [4]. The gelling of the fluid and subsequent operability problems, such as plugging of filters, is essentially dependent upon the amount and size of the solids

---

[3] A version of this chapter has been accepted in Energy: Mohanan, A., l. Bouzidi, and S. Narine, S., (2015) "Mitigating Crystallization of Saturated FAMES in Biodiesel: 4. The Phase Behavior of 1,3-dioleoyl-2-palmitoyl Glycerol– Methyl Stearate Binary System"

crystallizing. The actual temperatures at which the operability of biodiesel is compromised are defined by standards (e.g., the cold-filter plugging point (CFPP; EN 116, IP-309, ASTM D-6371)).

The overall thermal behavior of biodiesel is particularly affected by the relative concentration of its saturated and unsaturated fatty acid methyl esters (FAMEs) components. The highest melting components of biodiesel, the saturated FAMEs such as methyl stearate (MeS) and methyl palmitate (MeP), disproportionately affect its cold flow properties even at low concentration [5].

A number of approaches have been investigated to mitigate the cold flow issues of biodiesel. The strategies employed are not only aimed at lowering the freezing point (onset of crystallization, cloud point (CP)) of constituents in biodiesel but also at controlling the solids (size and amount) crystallizing at low temperatures. The proposed solutions include the use of additives, winterization, dilution, and blending with petrodiesel and/or other fuels such as kerosene [3]. The diversification and genetic modification of the feedstock aimed at providing advantageous composition/profile of the fuels are also suggested [6, 7]. Alcohols other than methanol are used for the synthesis of biodiesel in order to obtain chemical compositions which provide the same advantages and improved cold temperature performance [4]. Nonetheless, these strategies are applied with varying degrees of success and come mostly at the detriment of other properties, or are not cost effective [4].

Fundamentally, the objective, if not to prevent, would be to adequately disrupt the crystallization process at both the nucleation and growth stages in order to lower the onset temperature of crystallization and decrease the number and size of the crystals. In this

regard, a better understanding of the phase behavior of the biodiesel components and the potential "improver" of cold flow or any other property is of critical importance.

The cold flow issue is primarily a multifaceted problem of crystallization (of saturated FAMEs) in solution (unsaturated FAMEs) which can be approached from several angles. Studies of the phase behavior of the individual FAMEs and mixtures constituting the biodiesel have already been used as a means to better understand the thermodynamics and kinetics of phase change in biodiesel [8]. Phase diagrams of FAME systems are particularly investigated and modeled to gain insights into the molecular interactions involved, intersolubility and special transformations, such as eutectics, peritectics and compound formation, that can occur [9, 10].

The present work is part of a series of investigations triggered by promising cold flow results obtained by the addition of self-metathesized soybean oil MSBO to commercial biodiesels [11]. It has been found that particular components of MSBO such as TAGs and oligomers of TAGs with two fatty acids in the *cis-* configuration and a saturated fatty acid or a fatty acid in the *trans-* configuration are highly functional in depressing the onset of crystallization of biodiesel [12]. The most effective stereospecificity is when the *trans/saturated* fatty acid is at the *sn-*2 position. This suggests that the particular geometry of these molecules, while promoting a first packing via the straight fatty acid chain with the linear saturated FAMEs (MeP and MeS), prevents further crystallization due to the steric hindrance presented by the two kinked chains.

We have conducted binary phase behavior studies of the molecules having the greatest effect on the crystallization behavior of biodiesel (OPO, OSO, Dimer) and the two major saturated components of common North American biodiesel (MeS and MeP).

The present paper, the fourth in the series, reports on the phase behavior of OPO and MeS binary system. The system was chosen to investigate the effect of chain length mismatch (CLM) between the common structural elements of the TAG and FAME, i.e., the straight chains, on the transformation path of TAG/FAME mixtures. The crystal structure, microstructure, crystallization and phase development of the mixtures were tested using, X-Ray diffraction (XRD), polarized (PLM) and Differential Scanning Calorimetry (DSC) respectively. The DSC thermograms were used to construct detailed kinetic phase diagrams, encompassing the various thermal transformations on both cooling and heating. The liquidus line in the phase diagram of the binary systems obtained upon heating was modeled using so-called Bragg-William approximation, a thermodynamic model based on the Hildebrand equation and taking into account non-ideality of mixing.

4.2   Experimental Methods

4.2.1   Materials

OPO was synthesized and purified in our laboratory according to known procedures [13]. MeS was purchased (Aldrich Chemical Co. Inc. Oakville, Ontario). Their purities were greater than 99% as determined by high performance liquid chromatography (HPLC). The purified OPO and MeS were mixed in the desired molar fractions (X_{OPO}, molar fraction being X= 0, 0.11, 0.25, 0.40, 0.50, 0.55, 0.60, 0.65, 0.70, 0.75, 0.85, 0.95 and 1.00), then heated at 80 °C and stirred for 5 min to ensure complete homogeneity. Special care was taken for the overall handling and storage (4 °C) of the samples.

4.2.2 Differential Scanning Calorimetry

The solid–liquid phase behavior of the OPO/MeS mixtures was investigated by means of differential scanning calorimetry (DSC) under cooling as well as heating protocols. The DSC measurements were carried out under a nitrogen flow of 50 mL/min on a Q200 model (TA Instruments, New Castle, DE). Sample of approximately 0.4 to 0.6 (± 0.1) mg in a hermetically sealed aluminum DSC pan was first equilibrated at 80 ℃ for 5 min, a temperature and a time over which crystal memory was erased, and cooled with a constant rate (5 K/min) down to -40 °C. The sample was subsequently held at -40 °C for 5 min then reheated to 80 ℃ at a constant rate of 2.0 K/min to obtain the melting profiles. The "TA Universal Analysis" software was used to analyze the data and extract the main characteristics of the peaks. The reported values and uncertainties are the average and standard deviation of at least three runs, respectively.

4.2.3 Thermodynamic Analysis of the Boundaries in the Phase Diagram

The pseudo-equilibrium phase diagram was constructed using the data generated in the DSC heating experiments. The liquidus line was generated using the offset temperature of melting. This point is suitable for studying equilibrium properties because it is determined by the most stable crystal [14]. The phase boundaries in the phase diagram was simulated using a simple thermodynamic model based on the Hildebrand equation [15] coupled with the Bragg-William approximation for non-ideality of mixing [16]. This model is a powerful tool commonly used to investigate the miscibility of the components in the study of lipid mixtures [17-21].

The Bragg-Williams approximation attributes the origin of the non-ideality of mixing to the enthalpy term of the free energy of mixing and assumes the same entropy term as in

the ideal mixing case [22]. The deviation from an ideal behavior is described by a non-ideality of mixing parameter, ρ (J/mol), defined as the difference in the energy of mixed-pairs (AB) and the average pair interaction energy between like pairs (AA and BB) formed in the mixture:

$$\rho = z\left(u_{AB} - \frac{u_{AA} + u_{BB}}{2}\right) \tag{4.1}$$

where z is the first coordination number, u_{AB}, u_{AA} and u_{BB} are the interaction energies for AB, AA and BB pairs, respectively.

According to this approximation, the two branches of an equilibrium liquidus line are described by the following equations depending on whether the composition is smaller or larger than the eutectic composition X_E [21]:

$$\ln X_A + \frac{\rho(1 - X_A)^2}{RT} = -\frac{\Delta H_A}{R}\left(\frac{1}{T} - \frac{1}{T_A}\right) \tag{4.2}$$

$$\ln X_B + \frac{\rho(1 - X_B)^2}{RT} = -\frac{\Delta H_B}{R}\left(\frac{1}{T} - \frac{1}{T_B}\right) \tag{4.3}$$

where, R is the gas constant. X_A represents the mole fraction of A, ΔH_A and T_A are the molar heat of fusion and the melting point of component A, respectively. X_B, ΔH_B and T_B are those of component B.

For ideal mixing, the intermolecular interaction of like-pairs is equal to that of mixed-pairs and consequently $\rho = 0$ and the Hildebrand equation is obtained. A negative ρ is obtained when the formation of AB pairs is energetically more favorable than AA or BB

pairs and reflects a tendency for order. A positive ρ is obtained when mixed-pair formation is energetically less favorable, and reflects a tendency of like molecules to cluster, which beyond some critical value leads to phase separation [21].

4.2.4 Polarized Light Microscopy

A polarized light microscope, PLM, (Leica DM2500P, Leica Microsystems, Wetzlar, Germany) fitted with a Leica (DFC420C) digital camera was used for image capture. The samples were thermally processed in a temperature - controlled stage (Linkam LS 350, Linkam Scientific Instruments, Tadworth, Surrey, UK) fitted to the PLM. A small droplet of material was carefully pressed between a moderately preheated glass microscope slide and cover-slip ensuring a uniform thin layer of sample. The sample was melted at 80 ºC for 5 min to delete all crystal memory, then cooled at 1 K/min down to -40 °C. The development of the microstructure was monitored as the sample was cooling using the automatic multi-time image capture available in the PLM. The temperature at which the first "white spot" appeared in the PLM was recorded as the induction temperature (T_{ind}). Note that the smallest structures observable in a light microscope are of the order of 0.5 μm, due to the limitation induced by light diffraction. Therefore, structures detected by the light microscope are significantly larger than nuclei.

4.2.5 X-Ray Diffraction

The XRD measurements were performed on a Panalytical Empyrean X-ray diffractometer (PANalytical B.V., Lelyweg, The Netherlands) equipped with a filtered Cu-K_α radiation source and a PIXcel^{3D} detector. The XRD patterns were recorded between 1 and 50° (2θ) in 0.013 ° steps, at 45 kV and 40 mA. The sample was thermally processed in

the XRD chamber, similarly to PLM, using a 700 Series Cryostream Plus cooling system (Oxford Cryosystems, Oxford, UK) fitted to the diffractometer. The temperature was controlled to better than ±0.5 °C. The data were processed and analyzed using the Panalytical's X'Pert HighScore V3.0 software.

4.2.6   X-Ray Data Analysis and Polymorphism

The main subcell hydrocarbon-chain packing modes of TAGs are commonly denoted as the α, β' and β polymorphs [23]. The chain packing of the α- polymorph is hexagonal with non-specific chain-chain interactions. The common subcell packing of the β'-polymorph is orthorhombic, and the hydrocarbon chains of the β-polymorph are ordinarily packed parallel to each other in a triclinic or monoclinic subcell ($T_{//}$). The β- polymorph is the most stable crystal form, with the highest melting temperature, and the α-polymorph is the least stable crystal form, with the lowest melting temperature [24, 25]. The hydrocarbon chain layering is responsible for the characteristic small-angle x-ray diffraction (SAXD, long-spacing). Note that the first order reflection (d_{001}) of the SAXD represents the thickness of the molecular layers [26] and the higher order reflections indicate regular periodic structures, and represent the periodical sequence of electronic density differences in multiple layers [27, 28]. The period of layers observed for TAG structures is usually proportional to the acyl chain length by a factor of two or three, suggesting a double-chain length (DCL) or a triple-chain length (TCL) packing [26, 29].

4.3   Results and Discussion

4.3.1   Kinetic Phase Properties – Crystallization Behavior

Figure 4.1(a and b) shows the DSC cooling thermograms of the OPO/MeS mixtures at 5 °C/min. Figure 4.1c displays the corresponding crystallization temperatures. Note that the phases obtained at 5 °C/min are not the most stable, and would not therefore represent the equilibrium state for the system. For example, the DSC cooling trace of OPO obtained at 5 °C/min is very similar to what was obtained with a more rapid cooling (15 °C) by Bayes-Garcia et al., [30].
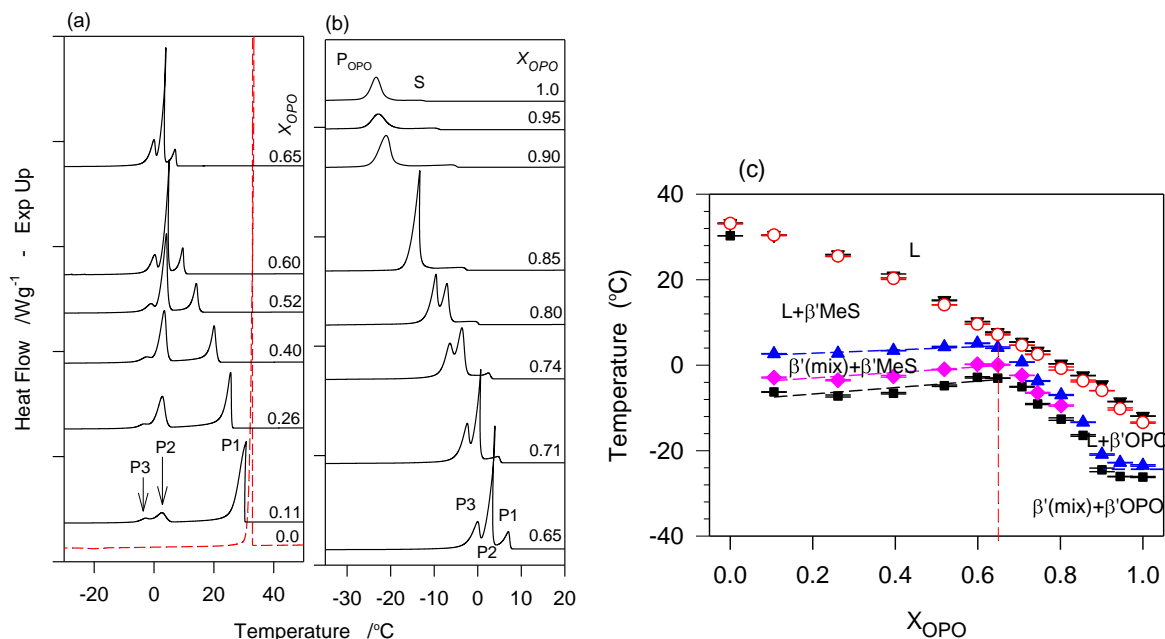
Figure 4.1. (a and b) DSC cooling (5 °C/min) thermograms of OPO/MeS mixtures. (c) Characteristic temperatures obtained from the thermograms of Figs. 4.1a and b. L: liquid

As can be seen, MeS crystallized with a sharp exotherm (Figs. 4.1a) whereas OPO and OPO-rich mixtures transformed with a small leading exotherm (S in Fig. 4.1b for mixtures $X_{OPO} > 0.80$) indicating a two-step crystallization process. The peak temperatures

of the main exotherms of MeS (T_{MeS} at 31.0 °C) and OPO (T_{OPO} at -23.3 °C) correspond to the crystallization of their respective β'-phases (the crystal structure of these phases was identified by XRD, see Section 3.4). S was small and wide, indicating the slow formation of small lamellar structures. The fact that the height of S remained almost constant as the temperature was decreased suggests that the nucleation was dominated by a relatively extended and continuous process. Note that the enthalpy of S is less than 10% of the total enthalpy of crystallization, indicating that the first solid phase was dispersed in a large liquid material. The narrow and intense exotherm that followed S in these mixtures is associated with crystals of a pure OPO or OPO-rich phase that crystallized rapidly, either from the small entities or from new nuclei. The overall span of crystallization of this phase suggest that the OPO molecules experienced complex conformational adjustments along the crystallization path.

MeS crystallized with a sharp exotherm (P1 in Fig. 4.1a) and as soon as OPO was added to MeS two extra exotherms (P2 and P3 in Fig. 4.1a and b) appeared in the DSC thermograms, indicating the formation of an OPO/MeS mixed phase. As OPO was added, the crystallization peak of MeS shifted to lower temperatures and its intensity decreased dramatically (P1 in Fig. 4.1a and b). For mixtures with $X_{OPO} > 0.65$, P1 could not be distinguished from the leading peak S. In the case of the mixtures with $X_{OPO} \leq 0.65$, P1 is assigned to the crystallization of a phase made predominantly, if not exclusively, of MeS. For larger OPO content, it can be safely associated with MeS taking part in the formation of OPO-MeS mixed lamellas.

The liquidus line constructed using the onset of crystallization (▼ in Fig. 4.1c) and the leading peak P1 (○ in Fig. 4.1c) exhibits two monotectic phases, distinguishable by a singularity at 0.65_{OPO}. The peak temperatures of P2 and P3 delimit the boundaries of two different transitions in the system just below the liquidus line (▲ and ◆ in Fig. 4.1c). The third peak that appeared for the 0.10_{OPO} to 0.85_{OPO} mixtures (P3 in Figs. 4.1a-b) is associated with an OPO-rich phase. As can be seen in Fig. 4.1c, both presented constant transformation lines (~3.8 °C and -2.5 °C) in the 0.10_{OPO} to 0.65_{OPO} range and an abrupt decrease at the singular point 0.65_{OPO}. The transformation line can be assigned to the crystallization of a mixed OPO/MeS phase with the MeS phase (Liquid +MeS → MeS + OPO/MeS) below the singularity, and a mixed OPO/MeS phase with the OPO phase above the singularity (Liquid +OPO → OPO + OPO/MeS).

The analysis of the enthalpy change of the individual phase transformations supports and further explains the phase diagram. The enthalpy data of P1-3 are provided in the Appendix in Fig. A2. The enthalpies of P2 and P3 plotted as a function of OPO concentration show "Tamman-triangle like" plots which suggest particular transformation points such as eutectics or peritectics and also delimit the biphasic regions in the phase diagram [31]. The Tamman triangle of P2 peaked at 0.60_{OPO}, and P3 increased only slightly up to 0.50_{OPO}, then displayed a Tamman triangle with an edge at 0.85_{OPO}, suggesting two different special transformations. Furthermore, these singularities are also observed in the span of crystallization versus X_{OPO} (not shown), highlighting their importance in the phase diagram. Note that the enthalpy of P2 increased linearly concomitant with a linear decrease of the enthalpy of P1 indicating the formation of a MeS-

OPO mixed phase at the detriment of a MeS phase. The nature of these singularities will be further clarified with the heating cycles, where the transformation paths are much more defined.

4.3.2 Melting Behaviour and Phase Development

The DSC heating thermograms of selected OPO/MeS mixtures are shown in Fig. 4.2a. Figure 4.2b shows the transition temperatures of all the examined mixtures. Figure 4.2b is in fact the phase diagram of the OPO/MeS binary system. The offset temperature of melting (T_{Off}, ▼ in Fig. 4.2b) was used to determine the liquidus line, as typically done in the study of binary lipid mixtures [20, 32, 33]. Peak temperature of the other peaks represent the solid-solid transition lines after correction for the transition widths of the pure components [34]. Note that the effect of heating rate was systematically checked on select mixtures and the protocol with a heating rate of 5 °C/min that provides optimal peak separation and peak intensity was chosen for the mixtures. The DSC thermograms of all the examined mixtures and the enthalpy analysis of the main endotherms are provided in the Appendix in Fig. A3 and Fig. A4, respectively.

The phase development of the OPO-rich mixtures is reminiscent of that of pure OPO. The transformation path of the mixtures seems to be mainly driven by multiple "recrystallizations" spanning over ~ 37.0 °C. Note that no exotherms were recorded for the mixtures with molar percentages less than 85% OPO. As illustrated with the heating trace of OPO in Fig. 4.2a, the transformation path of OPO-rich mixtures ($X_{OPO} > 0.80$) was a succession of at least two direct solid-solid transformations from the pre-existing phase(s) into more stable phases that subsequently melt. The heat flow recorded for the exothermic

transformations did not significantly weaken with added MeS, suggesting that it is the OPO

phase that was still developing.
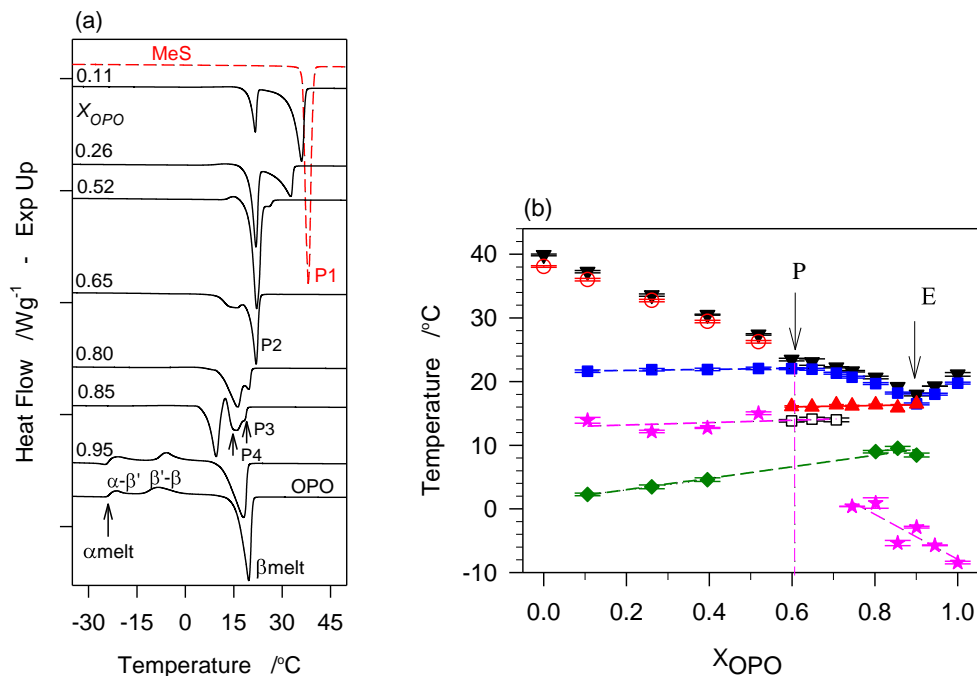
Figure 4.2. (a) DSC heating traces (2 °C/min) obtained subsequent to cooling (5 °C/min)

of selected OPO/MeS mixtures, (b) Characteristic temperatures of the examined OPO/MeS

mixtures: offset of melting ($\blacktriangledown$, T_{Off}); recrystallization ($\star$); peritectic ($\blacksquare$); eutectic ($\blacktriangle$).

Arrows P and E point to the peritectic and eutectic points, respectively. Vertical dashed

line: incongruent 1:1 molecular compound. (Goodness of fits: R^2=0.9020 for blue line,

R^2=0.8060 pink line, and R^2=0.9720 for green line. All fits have significance level=0.05).

The high temperature endotherms of OPO peaking at T_P = 20 °C and 16 °C are the

recording of the melting of the β -phase of OPO in its β_1- and β_2 -subforms, respectively

[35]. These endotherms remained strong and sharp (FWHM ~ 2.3 °C) even with 10% MeS,

indicating that at high levels, the OPO most stable crystal phase was still very well-

organized and was resilient to the influence of MeS. As exemplified with the thermogram of pure OPO in Fig. 4.2a, the β_1- form transformed through crystallization mediated by melt from the β'-form (12 °C) which itself crystallized from α (-18 °C), the least stable form of OPO. These results are in agreement with the work of Minato et al. [35].

MeS melted with a single endotherm (P1 in Fig. 4.2a, T_{P1} ~38 °C). The effect of OPO on the transformation path of MeS was dramatic even at small concentration. The addition of OPO induced an increase of the number of transitions available for the system, and subsequently a dramatic broadening of the span of melting. The intensity of P1 decreased dramatically and disappeared for mixtures with $X_{OPO} > 0.50$, suggesting that it is associated with a MeS-rich phase.

The increase in OPO concentration caused an abrupt decrease of T_P of the last endotherm and offset temperature of melting forming an apparent eutectic at $\sim 0.90_{OPO}$ (arrow E in Fig. 4.2b). Beside the eutectic, a singularity in the liquidus line separating two monotectic regions can be noticed at 0.65_{OPO} (arrow P in Fig. 4.2b). The constant transformation line running from 0.11_{OPO} to the singularity (line at ~22 °C, squares in Fig. 2b) indicate a peritectic transformation with a peritectic point at 0.65_{OPO} [35]. The enthalpy of P2, the endotherm associated with the peritectic transformation, displayed a typical "Tamman triangle" with an edge at 0.50_{OPO} (see Fig. A2) indicating the formation of a 1:1 molecular compound (MC) from the reaction of a liquid and a crystal [36, 37]. The melting temperature of the MC is the same as that of the β_1- form of OPO. Note that

the heating data discussed above reflect the data of the cooling phase diagram presented in section 4.3.1 above.

A eutectic line at ~ 16.16 ± 0.19 °C running from 0.60_{OPO} to 0.90_{OPO} can be clearly distinguished (▲ in Fig. 4.2b, peak temperature of P3 of Fig. 4.2a). The endotherm associated with the eutectic line is similar to the melting of the β-form of OPO. The transition at 14 °C (P4 in Fig. 4.2a and ■ in Fig. 4.2b) showing below the eutectic line was probably due to the melting of a slightly lower stability phase. Note that the combined enthalpy of these two peaks increased linearly from a value of 6 ± 2 J/g when it first appeared at 0.50_{OPO} forming a Tamman triangle edging at 0.85_{OPO} (data presented in the Appendix in Fig. A4). The Tamman plot confirms the eutectic nature of the transformation and delimits its boundaries. Note that a slightly sloped low temperature solid-solid transformation was also detected in the heating phase diagram (♦ in Fig. 4.2b). The transition temperature obtained for this line in the OPO-rich mixtures was ~ 10 °C, which matches the melting temperature of the β'- form of OPO. The incline is due to kinetic effects.

4.3.3   Thermodynamic Analysis of the Liquidus Line

The calculated liquidus line in the phase diagram is presented in Fig. 4.3. The parameters T_A, T_B, ΔH_A and ΔH_B used to simulate the liquidus line are provided in the Appendix listed in Table A5. The standard method of least squares was used to obtain the best fit and subsequent value of ρ.

The calculated liquidus line assuming an ideal mixture ($\rho = 0$ in Eq. (4.2) or Eq. (4.3)) did not reproduce the experimental data and is not shown. The experimental liquidus line has been satisfactorily reproduced by considering the two eutectic branches and the peritectic branch separated by the peritectic point at 0.65_{OPO}. The simulated three segments of the liquidus line (labeled I to III) are represented by solid lines in Fig. 4.3. The singularity has been confirmed at 0.62_{OPO} and the eutectic point obtained by the intersection of the two eutectic segments was confirmed at 0.92_{OPO}.
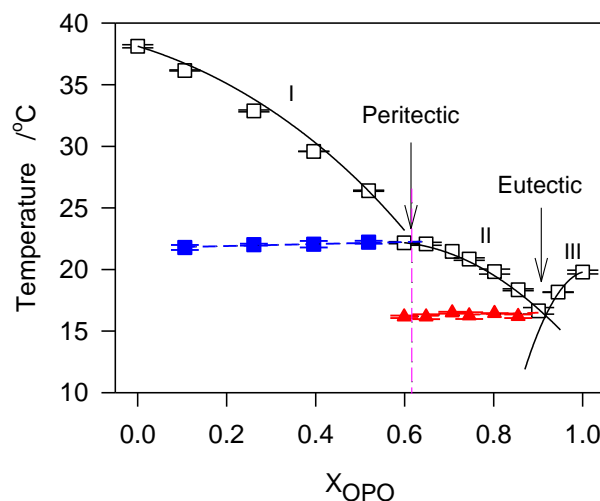
Figure 4.3. Experimental ($\square$) and calculated (solid line) liquidus line of the MeS/OPO binary system. $\blacksquare$, peritectic line; $\blacktriangle$, eutectic line. Vertical dashed line: incongruent transformation.

The simulation yielded negative values of ρ for all segments. The value of ρ obtained for region I (the peritectic region) was very small (~3 kJ/mol., see Table A6) and indicates a mixing behavior close to ideal. On the eutectic region, and for both branches (Region II and III in Fig. 4.3) the fit yielded large negative ρ-values (-30 kJ/mol. and -97

kJ/mol., respectively) reflecting a tendency for order [21]. These data indicate strong OPO-MeS molecular interactions tending to favour the formation of mixed pairs in the liquid state. Note that ρ obtained for Region III is 3 times that of Region II, indicating that the tendency for order is greater in OPO-richer mixtures. Note that the calculated ρ-values (listed in Table A6) are comparable to published values for other binary lipid systems [20].

4.3.4 Crystal Structure of OPO/MeS

The WAXD spectra of the OPO/MeS mixtures measured at -40 °C after cooling from the melt at 1 °C/min are shown in Fig. 4.4a.
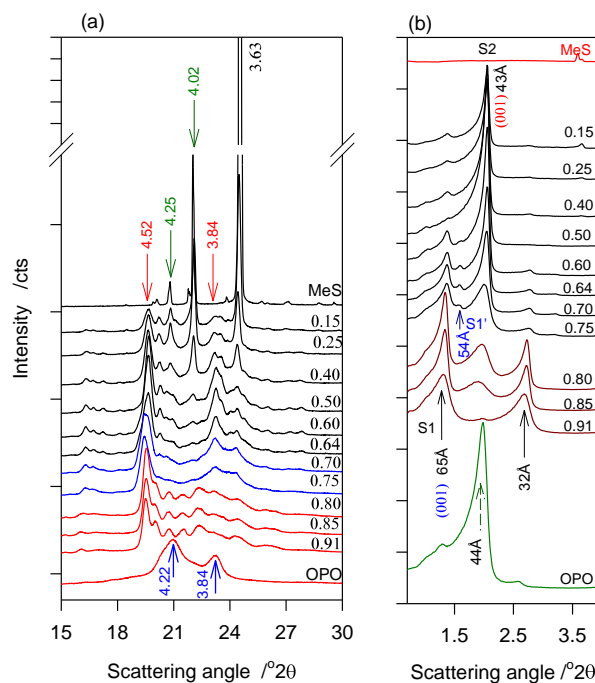
Figure 4.4. (a) WAXD and (b) SAXD spectra of OPO/MeS mixtures measured at -40 °C after cooling (1 °C/min) from the melt. OPO molar ratio is reported on the right side above the patterns

The corresponding SAXD spectra including the first order reflection (d_{001}) are shown in Fig. 4.4b. The d-spacing and corresponding Miller indices are provided in the Appendix listed in Table A6. The SAXD spectra including the higher order reflections are provided in the Appendix in Fig. A6.

Wide Angle X-Ray Diffraction and Subcell Structure

As can be seen in Fig. 4.4a, even at low temperature (-40 °C), the crystal peaks are superimposed to a wide background halo indicating the persistence of a liquid phase. This is particularly noticeable in the WAXD patterns of OPO-rich mixtures. The analysis of the WAXD crystal peaks was carried out after the removal of the background and liquid phase contributions. An accurate qualitative as well quantitative description of the crystal phases was obtained.

The XRD pattern obtained for MeS matched perfectly its diffraction powder file (PDF, reference No 00-032-1764) published by the International Centre for Diffraction Data (ICDD) and assigned to a monoclinic crystal structure (β_M). The signature reflections of the β'-phase of OPO (peaks at 4.22 and 3.84 Å in Fig. 4.4a) were only detected in pure OPO and in the binary mixtures with more than 0.75_{OPO}. The characteristic reflections of a triclinic subcell (4.52 Å and 3.84 Å peaks in in Fig. 4.2a) appeared in all the binary mixtures studied. This phase is labeled β_{II}-phase. β_{II} coexisted with and grew at the detriment of the monoclinic phase of MeS in the mixtures with 0.60_{OPO} or less. New reflections at 4.55, 4.13, 4.42, and 3.99 Å of a second triclinic form (labeled β_I) started to appear at 0.60_{OPO}, particularly prominently in OPO rich mixtures ($> 0.80_{OPO}$). The β_I-

phase replaced gradually the β_{II}-phase in the mixtures involved in the eutectic transformation.

The β_{II}-phase increased linearly reaching a maximum at $\sim 0.60_{OPO}$. Concomitantly, the monoclinic phase of MeS decreased linearly with increasing OPO content, up to 0.60_{OPO}, at which point it almost disappeared, supporting our analysis of the thermal data (see section 3.1 above). The range of concentration where the β_{II}-phase was detected coincided with the mixtures of the peritectic transformation revealing the triclinic nature of the peritectic solid. Furthermore, similarly to the enthalpy of the peritectic, the intensity of the signature peaks versus X_{OPO} of the β_{II}-phase formed typical Tamman triangles edging at 0.60_{OPO} that indicate clearly the boundaries of this transformation (data not shown but provided in the Appendix in Fig. A5a). Also, the β_{I}-phase content formed a Tamman triangle which peaks at the eutectic concentration (data also provided in the Appendix in Fig. A5b) clarifying the eutectic transformation and confirming its boundaries.

The mixtures in the peritectic and eutectic regions of the phase diagram of Fig. 4.3 presented a delicate balance between the different coexisting phases. The peritectic region spanning from above pure MeS to 0.64_{OPO}, presented a MeS phase in the monoclinic subcell structure and a mixed OPO - MeS peritectic phase in the β_{II}-triclinic subcell structure. The eutectic region from 0.64_{OPO} to pure OPO was a delicate balance between the triclinic phase of the peritectic solid (β_{II}), the OPO-rich triclinic phase (β_{I}) and the orthorhombic phase of OPO (β'). This phase configuration is consistent with the

compound forming a eutectic with the OPO-rich triclinic phase coexisting with a small β' -phase of OPO.

Small Angle X-Ray Diffraction and Lamellar Packing

MeS displayed a doublet series of sharp SAXD peaks with repeat units of 49.2 Å and 48.3 Å, indicative of a tilted subcell in a DCL structure. These data also match the PDF No 00-032-1764 of the crystal structure of MeS. The DCL structure is consistent with the formation of dimers due to hydrogen-bonding between carboxyl groups as is known in fatty acids [38]. The pure OPO displayed a series of reflections with $d_{001} = 44.15$Å of a DCL structure, in agreement with previously reported data for the β'- phase of OPO [30, 35]. A schematic model of the β' structure is shown in Fig. 4.5a. There were two other distinct series, with fundamental reflections at ~65 and 43 Å (S_1 and S_2 in Fig. 4b, respectively). The intensity versus X_{OPO} curves of the (001) fundamental reflections (65 Å, 44 Å and 43 Å of Fig. 4.4a) and that of $(002)_M$ at 22 Å, the second harmonic of the β_M -phase, are provided in the Appendix in Fig. A6c.

Firstly, the SAXD reflections associated with monoclinic MeS decreased exponentially and disappeared for the mixture having an OPO concentration larger than 50% (see Fig. A6), confirming that the monoclinic phase was present in the mixtures involved in the peritectic transformation only.

The intensity of the reflection at 43 Å presented a triangular shape with an edge at 0.50_{OPO}, mirroring the trend observed for the 3.84 reflection of β_{II}. The variation of the intensity of the peaks is also reminiscent of the Tamman plot observed for its melting

enthalpy. This supports the formation of a peritectic compound in the β_{II}-form in the DCL structure with a lamellar thickness of ~43 Å. A tentative schematic of the model double layer structure of the β_{II}-form of the compound is shown in Fig. 4.5b. Note that in this model, MeS packs close to the straight palmitic acid in order to achieve the double layer structure of a 1:1 molecular compound.
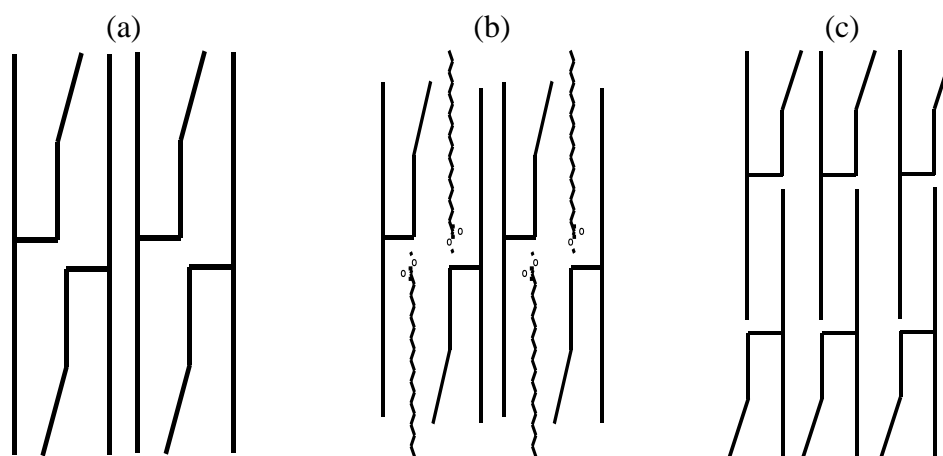
Figure 4.5. Schematic representation of the (a) β'-form of OPO in the DCL structure ($d_{001} = 44.5$ Å); (b) β_{II}-form of the 1:1 molecular compound in the DCL structure ($d_{001} = 43$ Å) (c) β_I-form of OPO in the TCL structure ($d_{001} = 65$ Å). The models are depicted based on the lamellar distances obtained with XRD

The 65 Å-series was detected in the SAXD pattern of all the mixtures except OPO and the 0.50_{OPO} mixture. Furthermore, disregarding the 0.50_{OPO} mixture, the intensity of the 001 reflection increased exponentially with OPO concentration and peaked at 0.80_{OPO} (see Fig. A6c). This series is directly related to the β_I-phase which involved both OPO and MeS in its packing. This chain length is close to the value of 67 Å previously published

for the β_I-phase of OPO in the TCL structure [39], indicating their very close similarity. The data in fact indicate that the OPO:MeS pairs have been accommodated so to pack in the TCL structure similarly to OPO. MeS is therefore shown to pair with OPO closely enough to not disturb dramatically the β_I subcell packing of the OPO mother phase. A schematic of the model triple layer structure of the β_I form is shown in Fig. 4.5c.

4.3.5   Microstructure of the OPO/MeS Mixtures

OPO/MeS mixtures displayed very complex microstructures that developed in several steps. They presented a variety of fat networks with distinctive crystal shapes and sizes, and a variety of spatial distributions of the solid phases. Selected snapshots from the time-temperature resolved PLM of the different mixtures are provided in the Appendix in Fig. A8.

The first and only crystal of pure MeS showing in the PLM slide started to appear at a relatively high temperature (36.0 ± 0.5 °C). The crystal developed radially into a very large palm leaf-like spherulitic structure (>6000 μm) very rapidly, forking along the growth directions. Only one crystal was detected in the PLM slide, suggesting that it developed from a single nucleus. As expected, the nucleation and growth of OPO crystals were very different from MeS. The first crystals of OPO showed at ~-9.5 ℃ and developed into a dense network of a large number of small spherulites (~200 μm). Crystal growth of OPO was very slow compared to MeS.

The addition of OPO altered the microstructure of the FAME dramatically at very low loading. OPO participated in the formation of a variety of microstructures that are more or less closely related to MeS and/or OPO microstructures. Although varying in size

and distributed differently, four types of crystals were singled out in the OPO/MeS mixtures (Type I to IV, Fig. 4.6). These microstructures have developed from apparent successive (primary, secondary and, ternary) nucleation processes and are related to the different phases unveiled by DSC and XRD.

(a) Pure MeS   (b) Pure OPO   (c) Type I

(d) Type II   (e) Type III   (f) Type IV
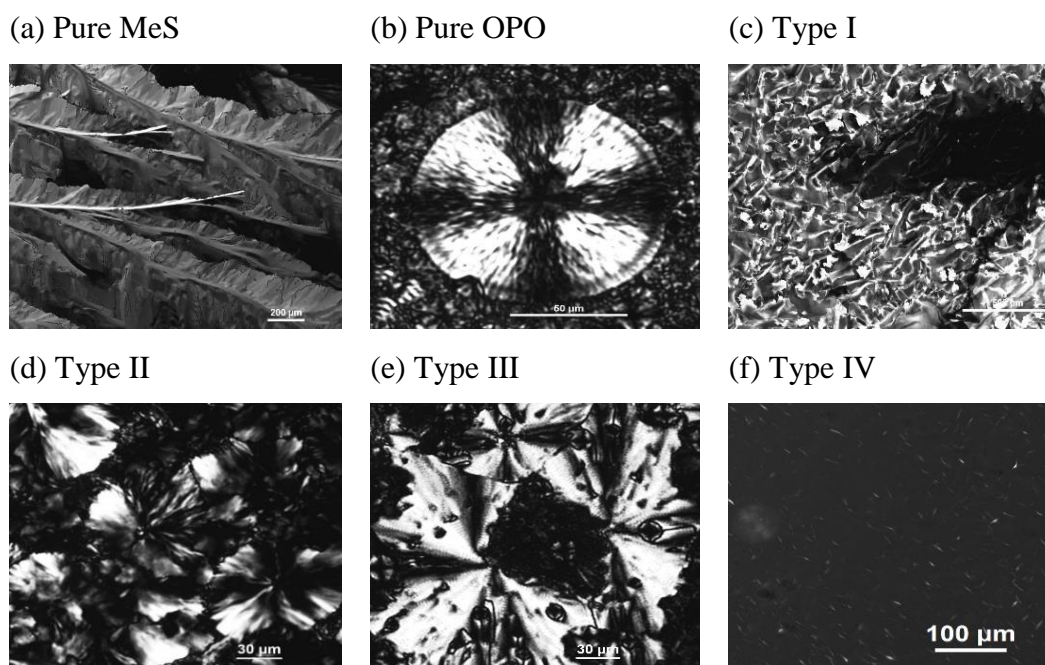
Figure 4.6. Microstructures formed in OPO/MeS mixtures. (a) Pure MeS; (b) Pure OPO; (c - f) Type I-IV

The induction temperatures of crystallization (T_{ind}) recorded at the appearance of the first "white spot" in the PLM for each nucleation are represented in Fig. 4.7a. The corresponding final crystal size represented in Fig. 4.7b. As can be seen in Fig. 4.7a, the trends observed for T_{ind} mirrored those of the in DSC transition lines, indicating a strong correlation between the evolution of the microstructure and the different thermal transformation occurring in the OPO/MeS binary system. Not only T_{ind} matched perfectly the DSC onset temperature of crystallization, it also reflected the peritectic transformation

line at ~11 °C spanning from 0.15_{OPO} to 0.64_{OPO} (down triangles in Fig. 4.7a), showing the

link between the microstructures and the phases forming upon cooling.
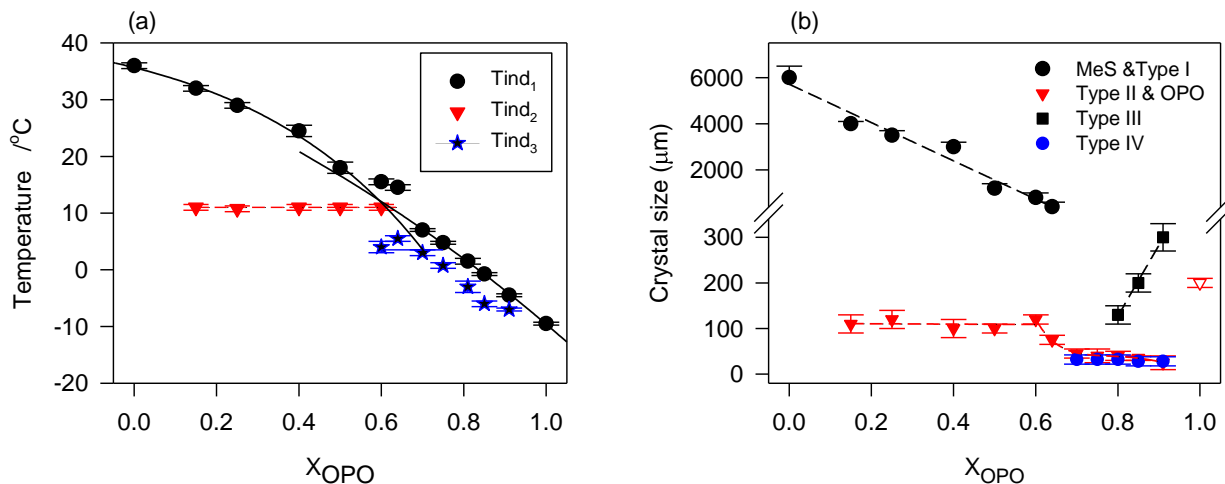
Figure 4.7. (a) Induction temperature of crystallization (T_{ind}) of OPO/MeS mixtures as

recorded at the appearance of the first "white PLM spot", (b) corresponding crystal size

(Goodness of fits: R^2=0.9662 and 0.9662 for black line, R^2=0.9987 for the red line. All fits

have significance level=0.05)

Beside the typical long leaflet-like MeS crystals (Fig. 4.6a) and the well-defined

small Maltese Crosses of OPO (Fig. 4.6b), a disrupted leaflet-like type (Type I, Fig. 4.6c)

appeared in the primary stage of the crystallization of the mixtures with $X_{OPO} < 0.64$. These

crystals developed similarly to MeS crystals in a spherulitic and forked manner, and

although much smaller, remained relatively large indicating that their growth was

controlled by MeS. Due to the large microstructure size, particularly in MeS rich mixtures

($< 0.40_{OPO}$), only a part of the crystal was visible in 100X PLM. Note that with increasing

OPO content, Type I crystals decreased in size and grew along increasingly blurred forking

lines, altering their regular form and homogeneity dramatically.

Type II crystals were relatively small (~100 μm) fuzzy Maltese Crosses (Fig. 4.6d) that developed in the mixtures with X_{OPO} of less than 0.64 in an apparent secondary nucleation on top of Type I microstructure. Type II crystals appeared first at ~11.3±0.5 ºC in all of these mixtures. Type III crystals are spherulites (Fig. 4.6c) which grew in OPO-rich mixtures ($>0.80_{OPO}$) after a ternary nucleation. As can be seen, they share a similar but fuzzier Maltese cross shape with the crystals formed by pure OPO. Their size was relatively large compared to OPO crystals. Also Type III crystals were very heterogeneously distributed, due to a rapid sporadic nucleation. Type IV crystals (Fig. 4.6d) are very small (~30 μm) fibril-like entities that appeared in the primary stage of development of the mixtures with $X_{OPO} > 0.70$.

The mixtures of the peritectic region ($X_{OPO} \leq 0.64$) presented Type I and II microstructures that have grown following a primary and secondary nucleation. Type I crystals grew from the primary nuclei relatively rapidly, highlighting the role of MeS in the development of the microstructure of the peritectic mixtures. However, the rate of growth as well as the size of Type I crystals decreased significantly with increasing OPO. For example, these crystals took ~30-60 s in mixtures $<0.40_{OPO}$ and 2-3 min in the mixtures $>0.40_{OPO}$ and $<0.64_{OPO}$ in order to reach their final size. The number of type I crystals observed with 100X magnification increased from 1 in mixtures with $<0.40_{OPO}$ to 5-10 in the mixtures with $<0.64_{OPO}$, indicating a dramatic change in the nucleation rate. Type II crystals were formed following a secondary nucleation. New white spots started to appear at the temperature of the peritectic transformation, i.e., ~11.3 ± 0.5 ºC, in all the mixtures with $X_{OPO} < 0.64$. These crystals developed completely in a very short period of time,

indicating an instantaneous nucleation and a very high rate of growth. The trends observed in the development of the microstructure of the $[0.40_{OPO} - 0.64_{OPO}]$ mixtures match very closely the XRD data collected for the monoclinic structure. It is therefore reasonable to infer that these crystals are monoclinic and that their growth followed a disturbed MeS development path.

Type IV, fibril-like very small crystals (~30 µm) were the first to form in the 0.70_{OPO} to 0.91_{OPO} mixtures. These mixtures also displayed a secondary nucleation after which they developed Type II-like crystals. These crystals were similar in shape to those found in mixtures $<0.64_{OPO}$ but smaller in size. The rate of nucleation as indicated by the number of Type II crystals was higher in these mixtures than in the peritectic mixtures $(<0.64_{OPO})$. Note that the small Type II crystals were very inhomogeneously distributed.

The variation of the average size of the different crystals, shown in Fig. 4.7b, mirrored the cooling thermal transformation lines, indicating their strong correlation. For example, the increase in the number of Type I crystals was accompanied with a significant decrease of their size (circles in Fig. 4.7b). Although the number of Type II crystals increased significantly with increasing OPO content, they reached almost the same size (~100 ± 20µm) and presented the same shape in all the mixtures of this group (down triangles in Fig 4.7b). These data are consistent with the peritectic reaction observed by DSC. Type II crystals are therefore associated with the peritectic phase in the β_{II}-crystal structure.

4.3.6 Discussion

The nucleation and growth stages of the crystallization were controlled by a delicate balance between MeS and OPO. The nucleation rate of the different phases of the OPO-MeS mixtures depended on the probability of interaction between similar and dissimilar molecules. Because of a common structural feature, saturated straight chains, and a large size difference, the OPO-MeS contacts are favored first despite that in the earlier stages of nucleation (the metastable fluid phase), and in the presence of supercooling, MeS is the entity that starts developing gel-like clusters. OPO attaches to the MeS with its saturated chain and accommodates into a lattice via rotations of the kinked oleic acid, preventing phase separation. The particular position of the palmitic moiety at the *sn-2* position provided equal opportunity for the rotation of the oleic chains for an easy rearrangement of OPO and MeS into a molecular compound. The best configuration for minimum energy of such a pair would be an OPO molecule in the chair configuration accommodating a MeS molecule parallel and close to the palmitic chain (see Fig. 4.6b).

With increasing OPO content in the mixture, the probability of MeS-compound interactions increases dramatically reducing the diffusion of MeS through the melt. This induces the formation in the melt of several molecular clusters which seed a large number of nuclei. The average microstructure size is therefore reduced. As the concentration of OPO increases above the 50% level, the number of compound molecules as well as MeS-MeS pairs decrease, and the probability of both compound-OPO and OPO-OPO contacts increases. OPO molecules rearrange to accommodate the compound pairs and form a mixed phase (β_I) resembling the β_I-phase of OPO (Fig. 4.6c). At this point, the interactions of OPO with the compound limit the formation of nuclei of a pure compound

phase, and delays crystallization further. This explains the singularity in the liquidus line and the steeper drop in melting temperature as illustrated by the first eutectic segment. In the region of concentrations richest in OPO, i.e., the second eutectic segment, the compound molecules act as nucleating agents that reduce the free energy of nucleation of a pure OPO phase, and hence increase the crystallization temperature.

The size of the crystals is determined by both the nature of the molecules present in the system and the particular polymorph that is forming. MeS-rich compositions displayed relatively large microstructures that are associated with a monoclinic subcell. The compound phase is associated with a DCL triclinic form (the β_{II} structure), and the compound-OPO mixed phase with a β_I-like phase of OPO (β_I). The microstructure of pure OPO phase presented homogeneously distributed small spherulites that are associated with the orthorhombic subcell of OPO.

The study indicate unambiguously that the involvement of the additive in the nucleation process and early stages of crystallization was the chief factor that dictated the overall transformation process and phase behavior. The continuous and competing involvement along the transformation path was inherent to the dual straight/kinked structure of OPO which handles relatively weakly the balance between nucleation and growth rates, limiting the extent at which temperature can be depressed and the material gelled. Fortunately, additives composed of such structures will impact very favorably the flow behavior of biodiesel because of the type, size and number of crystals that they promote during crystallization. These are important findings that also point to the limits

as cold flow improver (CFI) of two-feature structure additives and to the significance of a proper balance of the interactions at the molecular level.

4.4 Conclusions

A complete phase diagram of the OPO/MeS binary system encompassing the thermal transitions, polymorphism and crystal structures as well as detailed microstructure development was achieved (Fig. 4.8).
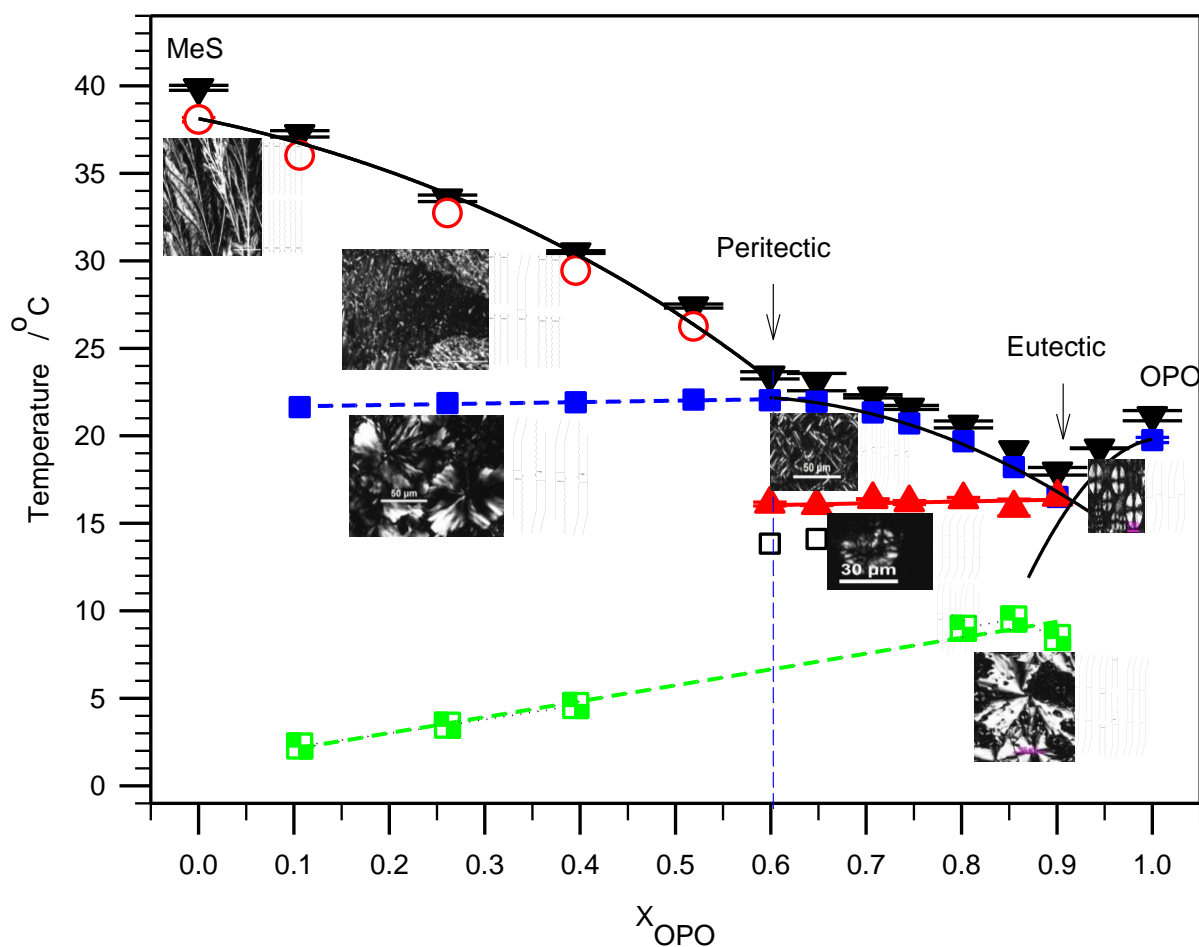
Figure 4.8. Phase diagram of OPO/MeS binary system including thermal transitions, crystal structures and PLM microstructures (100X)

The knowledge gathered at such different length scales is a gateway to understanding and therefore possibly custom-engineering biobased formulations for cold flow additives. The construction of the phase diagram allowed the identification of the transformation points which are desirable in the context of improving the cold flow performance of biodiesel, such as the eutectic and the peritectic. The peritectic transformation for example was revealed by the DSC on cooling and heating and involved the MeS-richest mixtures (up to 0.65_{OPO}), indicating that it is a common transformation for the stable as well as metastable crystals. The eutectic point was measured at 16 °C, a drop in temperature from MeS of ~24 °C.

The peritectic and eutectic concentrations for example, can be adjusted to the actual amount of saturated FAMEs of biodiesel. Soybean biodiesel which comprises ~15% of saturated FAME, would need about 1.2% to 10 % additive to achieve the molar fraction range of the peritectic of the system at hand. The eutectic is not so favorable if OPO is used alone as it would require 12 % to impact the MeS of the biodiesel by the maximum 24 °C depression.

This depression which was obtained for the most stable crystals evidence the effectiveness of OPO to disrupt the transformation behavior of MeS through colligative effects also. The ideal mixing behaviour of the peritectic mixtures and the tendency for order in the eutectic region, as revealed by the Bragg-William thermodynamic model, highlights the prevailing effect of the peritectic compound on the solubility behaviour of the FAME. No metatectic transformation was observed. This is of significant interest as

the presence of a metatectic reaction is responsible for the formation of higher number of large solids below the cloud point than a simple eutectic or peritectic system.

The crystallization process was disrupted at the nucleation as well as growth stages altering the phase trajectories significantly, and also resulting in successive nucleation processes and hence development of different types of microstructures, all of which are much more favorable for the easier flow of the material. OPO by promoting increasingly larger numbers of nuclei and reduced crystal size transforms also the filterability of the mixtures favorably at increasingly lower temperature. Noticeably, the size of the microstructures varied similarly to the temperature of transformation of each phase. The direct correlation of crystal size with the induction temperature of crystallization provides the means for the fine tuning of additive load. Furthermore, the microstructure phase composition was linked with the crystal phase composition allowing a rational use of processing conditions so to avoid or at least mitigate the problems of metastable states.

The finding of the present work and the underlying understanding of the specific interactions at play along the whole transformation path is a powerful tool in the hand of the formulator to designing very efficient biobased, biodiesel specific cold flow improvers (CFI). The work is a staple study on selecting molecules of the next generation of CFI by rational design through the choice of specific structural elements that can be involved favorably in the early stages of crystallization and provide at some stage of growth a suitable selective solid-liquid interface that would prevent the acceleration of growth and keep the biodiesel fluid for extended periods of time. It is expected that cocktail additives made of vegetable oil derivatives that would target specific FAMEs of biodiesel and the right concentration would improve greatly the cold flow behavior of actual biodiesel.

The study demonstrates clearly that a rigorous structure-function relationships approach is creditable of a fundamental understanding that can be applied straightforwardly. This can come also in the form of giving the formulator judicious tools for designing additives with very high molecular specificity. Such tools are tantamount to, if not more important than, providing a specific CFI. The findings of the study indicate that one can achieve a significant depression on both CP and PP of biodiesel, with a judicious selection of additives.

The practical application of OPO and other vegetable derivatives as additive in small concentration (2-4% by wt.) in biodiesel won't be detrimental to the fuel as prescribed by ASTM. An indication is that some of the work involving vegetable oil derivatives, specifically metathesized oils, have been shown to have the qualities required in alternative fuels [40].

4.5   References

[1] Fazal MA, Haseeb A, Masjuki HH. Biodiesel feasibility study: An evaluation of material compatibility; performance; emission and engine durability. Renew Sust Energ Rev. 2011;15(2):1314-24.

[2] Hoekman SK, Broch A, Robbins C, Ceniceros E, Natarajan M. Review of biodiesel composition, properties, and specifications. Renew Sust Energ Rev. 2012;16(1):143-69.

[3] Misra RD, Murthy MS. Blending of additives with biodiesels to improve the cold flow properties, combustion and emission performance in a compression ignition engine-A review. Renew Sust Energ Rev. 2011;15(5):2413-22.

[4] Dunn RO. Cold-Flow Properties of Soybean Oil Fatty Acid Monoalkyl Ester Admixtures. Energy Fuels. 2009;23(8):4082-91.

[5] Chastek TQ. Improving cold flow properties of canola-based biodiesel. Biomass Bioenergy. 2011;35(1):600-7.

[6] Knothe G. Improving biodiesel fuel properties by modifying fatty ester composition. Energy Environ Sci. 2009;2(7):759-66.

[7] Soriano NU, Migo VP, Sato K, Matsumura M. Crystallization behavior of neat biodiesel and biodiesel treated with ozonized vegetable oil. Euro J Lipid Sci Techn. 2005;107(9):689-96.

[8] Knothe G. Dependence of biodiesel fuel properties on the structure of fatty acid alkyl esters. Fuel Process Technol. 2005;86(10):1059-70.

[9] Rocha SA, Guirardello R. An approach to calculate solid-liquid phase equilibrium for binary mixtures. Fluid Phase Equilib. 2009;281(1):12-21.

[10] Costa MC, Boros LAD, Coutinho JoAP, Krähenbühl MA, Meirelles AJA. Low-Temperature Behavior of Biodiesel: Solid–Liquid Phase Diagrams of Binary Mixtures Composed of Fatty Acid Methyl Esters. Energy Fuels. 2011;25(7):3244-50.

[11] Christensen SA, DiBiase SA, Rizvi SQA. Cold flow additives. In: EPO, editor. C10L 1/19 (2006.01); C10L 1/224 (2006.01) ed2012.

[12] Mohanan A, Bouzidi L, Li S, Narine SS. Mitigating crystallization of saturated FAMES in biodiesel: 1. Lowering the crystallization temperature via addition of metathesized soybean oil. Upublished- Submitted to Energy.

[13] Bentley PH, McCrae W. Efficient synthesis of symmetrical 1,3-diglycerides. J Org Chem. 1970;35(6):2082-3.

[14] Chiavaro E. Differential Scanning Calorimetry: Applications in Fat and Oil Technology: CRC Press, 2014.

[15] Hildebrand JH. Solubility XII. Regular solutions. J Am Chem Soc. 1929;51:66-80.

[16] Bragg WL, Williams EJ. The effect of thermal agitation on atomic arrangement in alloys. Proc R Soc. 1934;145(855):699-730.

[17] Inoue T, Hisatsugu Y, Yamamoto R, Suzuki M. Solid-liquid phase behavior of binary fatty acid mixtures 1. Oleic acid/stearic acid and oleic acid/behenic acid mixtures. Chem Phys Lipids. 2004;127(2):143-52.

[18] Costa MC, Rolemberg MP, Boros LAD, Krahenbuhl MA, de Oliveira MG, Meirelles AJA. Solid-liquid equilibrium of binary fatty acid mixtures. J Chem Eng Data. 2007;52(1):30-6.

[19] Abes M, Bouzidi L, Narine SS. Crystallization and phase behavior of fatty acid esters of 1,3 propanediol III: 1,3 propanediol dicaprylate/1,3 propanediol distearate (CC/SS) and 1,3 propanediol dicaprylate/1,3 propanediol dipalmitate (CC/PP) binary systems. Chem Phys Lipids. 2008;151(2):110-24.

[20] Boodhoo MV, Bouzidi L, Narine SS. The binary phase behavior of 1, 3-dipalmitoyl-2-stearoyl-sn-glycerol and 1, 2-dipalmitoyl-3-stearoyl-sn-glycerol. Chem Phys Lipids. 2009;160(1):11-32.

[21] Lee AG. Lipid Phase-Transitions and Phase-Diagrams .2. Mixtures Involving Lipids. Biochim Biophys Acta. 1977b;472(3-4):285-344.

[22] Moore WJ. Physical Chemistry 4th ed. Englewood Cliffs, New Jersey: Prentice-Hall, 1972.

[23] Larsson K. Physical Properties - Structural and Physical Characteristics. In: Gunstone FD, Harwood JL, Padley FB, editors. The Lipid handbook. London: Chapman and Hall; 1986. p. 335-77.

[24] Ghotra BS, Dyal SD, Narine SS. Lipid shortenings: a review. Food Research International. 2002;35(10):1015-48.

[25] Timms RE. The Confectionary Fats Handbook: Properties, Production, and Application. Chapter 2: Physical Chemistry. Bridgewater, England: The Oily Press, 2003.

[26] Fahey DA, Small DM, Kodali DR, Atkinson D, Redgrave TG. Structure and polymorphism of 1,2-dioleoyl-3-acyl-sn-glycerols - 3-layered and 6-layered structures. Biochem. 1985;24(14):3757-64.

[27] Dorset D. The crystal structure of waxes. Acta Crystallogr, Sect B: Struct Sci. 1995;51(6):1021-8.

[28] Dorset DL. From waxes to polymers - crystallography of polydisperse chain assemblies. Struct Chem. 2002;13(3):329-37.

[29] Mykhaylyk OO, Smith KW, Martin CM, Ryan AJ. Structural models of metastable phases occurring during the crystallization process of saturated/unsaturated triacylglycerols. J Appl Crystallogr. 2007;40(s1):s297-s302.

[30] Bayes-Garcia L, Calvet T, Cuevas-Diarte MA, Ueno S, Sato K. In situ synchrotron radiation X-ray diffraction study of crystallization kinetics of polymorphs of 1,3-dioleoyl-2-palmitoyl glycerol (OPO). Cryst Eng Comm. 2011;13(10):3592-9.

[31] Chernik GG. Phase equilibria in phospholipid-water systems. Adv Colloid Interface Sci. 1995;61(C):65-129.

[32] Inoue T, Hisatsugu Y, Ishikawa R, Suzuki M. Solid–liquid phase behavior of binary fatty acid mixtures: 2. Mixtures of oleic acid with lauric acid, myristic acid, and palmitic acid. Chem Phys Lipids. 2004;127(2):161-73.

[33] Costa MC, Rolemberg MP, Boros LAD, Krähenbühl MA, de Oliveira MG, Meirelles AJA. Solid−Liquid Equilibrium of Binary Fatty Acid Mixtures. J Chem Eng Data. 2006;52(1):30-6.

[34] Inoue T, Motoda I, Hiramatsu N, Suzuki M, Sato K. Phase-behavior of binary mixture of palmitoleic acid (cis-9-hexadecenoic acid) and asclepic acid (cis-11-octadecenoic acid). Chem Phys Lipids. 1993;66(3):209-14.

[35] Minato A, Ueno S, Yano J, Smith K, Seto H, Amemiya Y, et al. Thermal and structural properties of *sn*-1,3-dipalmitoyl-2-oleoylglycerol and *sn*-1,3-dioleoyl-2-palmitoylglycerol binary mixtures examined with synchrotron radiation x-ray diffraction. J Am Oil Chem Soc. 1997;74(10):1213-20.

[36] Barbosa DF, de Alcântara Pessôa Filho P. On the description of the liquidus line of systems presenting peritectic reactions. Fluid Phase Equilib. 2013;337:379-83.

[37] Slaughter DW, Doherty MF. Calculation of solid-liquid equilibrium and crystallization paths for melt crystallization processes. Chem Eng Sci. 1995;50(11):1679-94.

[38] Sangwal K, Mielniczek-Brzoska E. Effect of impurities on metastable zone width for the growth of ammonium oxalate monohydrate crystals from aqueous solutions. J Cryst Growth. 2004;267(3):662-75.

[39] Minato A, Ueno S, Yano J, Smith K, Seto H, Amemiya Y, et al. Thermal and structural properties of sn-1,3-dipalmitoyl-2-oleoylglycerol and sn-1,3-dioleoyl-2-palmitoylglycerol binary mixtures examined with synchrotron radiation X-ray diffraction. Journal of the American Oil Chemists Society. 1997;74(10):1213-20.

[40] Jenkins RW, Sargeant LA, Whiffin FM, Santomauro F, Kaloudis D, Mozzanega P, et al. Cross-metathesis of microbial oils for the production of advanced biofuels and chemicals. ACS Sustain Chem Eng. 2015.

5.   Mitigating Crystallization of Saturated FAMES in Biodiesel 6:

The Binary Phase Behavior of 1, 2-dioleoyl-3-stearoyl sn-glycerol (SOO)

– Methyl Stearate (MeS)[4]

5.1   Introduction

Biodiesel is a renewable engine fuel considered as a viable alternative to fossil fuels [1]. It can be derived from any crop oil or animal fat, and legally used if it meets specifications mandated by national or regional standards such as ASTM D6751 in the United States or EN14214 standards in Europe. Its advantages and disadvantages are well documented [2]. Because of poor performance at low temperature, its use and viability are particularly limited in countries where cold weather is prolonged.

The cold flow problems of biodiesel are essentially related to its long saturated fatty methyl ester (FAME) components, such as methyl ester stearate (MeS) and methyl ester palmitate (MeP), common in North American biodiesel. The temperature characteristics of biodiesel are usually described by standardized measurements that are correlated to field operability temperatures such as the cloud point (CP), the pour point (PP), the cold filter plugging point (CFPP) and the low-temperature flow test (LTFT). Common biodiesels present CP and PP that are much higher than petro-diesel. For example, soybean oil and

---

[4] A version of this chapter has been submitted to "Energy": Mohanan, A.; Bouzidi, L; and S. Narine, S.; (2015)-" 5   Mitigating Crystallization of Saturated FAMES in Biodiesel VI: The Binary Phase Behavior of 1, 2-dioleoyl-3-stearoyl sn-glycerol (SOO) – Methyl Stearate (MeS).

palm oil biodiesels present CPs of ~0 °C and 15 °C, respectively, whereas, No. 1 diesel has a CP of about -40 °C. Furthermore, biodiesel tend to have a narrow range of temperatures between CP and PP, adding to its cold flow problems. Heaters and insulators may be installed along the fuel line and storage facilities to allow its use at temperatures lower than the CP or PP, but this incurs additional costs.

Several approaches have been tried to improve the cold-weather performance of biodiesel. They are fundamentally targeted at modifying composition or/and structure, or at altering the crystallization behavior of the biodiesel by additives [3]. The appropriate adjustment of the molecular composition of biodiesel is in principle a straightforward method that would beneficially impact the crystallization parameters. For example, although at the cost of a yield loss, CP and/or PP can be significantly reduced by simple processing methods, such as "winterization" which reduces the long chain FAMEs content, the main culprit for the early crystallization of biodiesel [4]. Also, a biodiesel that is relatively rich in low melting temperature compounds can be produced by chemically reacting the lipid feedstock with an alcohol producing fatty acid esters other than methanol [5]. These modification methods however are either generally not efficient or expensive, or both.

Application of cold flow improver (CFI) additives is the most popular approach used to treat biodiesel [6-17]. CFI additives are designed to lower the temperature characteristics of biodiesel such as CP and PP by disrupting the crystallization process at as many length scales as possible from nucleation and crystalline growth to agglomeration [12]. The existing CFI additives can be classified into two large categories: i) crystallization modifiers which affect one or more phases of the crystallization process

[18], and ii) pour point depressants (PPDs) which function as crystal growth limiters [7, 19, 20]. Unfortunately, no one single approach has yet been able to simultaneously address both PP and CP effectively [18]. Additives that are capable of altering both nucleation and growth are preferred as they can delay crystallization and reduce the size of the crystals [21].

The overriding trend that emerges from the studies corroborates our finding that in order to be effective, the additive must have a structural element that initiates association with the FAMEs of the biodiesel and at least another structural element that prevents further growth or organization of the initial crystals [22]. This supports previous knowledge that for an additive to work, it has to possess a structural similarity with the host material (biodiesel for instance) that favors the formation of initial entities with the additive rather than itself, and a dissimilarity that prevents further crystallization and growth [23]. Notice that most commercially available additives are designed specifically for petro-diesel and do not work as well for biodiesel because of this specificity requirement [24].

This study into lipid-based CFI additives was triggered by findings that the addition of small amounts (<4%) of metathesized soybean oil (MSBO) significantly lowers the crystallization of commercial biodiesel [25]. The compounds in MSBO that are most effective in this function were identified as was the mechanism of their action (Chapter 2). TAGs and oligomers of TAGs with two fatty acids in the *cis-* configuration and a fatty acid in the *trans-* configuration or a *saturated* fatty acid were shown to be the structures at the origin of the effect. The most effective stereospecificity was shown to be when the *trans/saturated* fatty acid is at the *sn-*2 position (Chapter 2). This particular geometry suggested a simple mechanism of action of the molecules wherein while the straight chain

moiety promotes a first packing with the linear saturated FAMEs, the kinked chains prevent further crystallization due to geometric steric hindrances.

The present work is part of a series examining the phase behavior of model systems made of selected molecules from those which had the largest effect on the crystallization of biodiesel (OPO, OSO, SOO, dimer of OPO) and the main saturated FAMEs of common North American biodiesel (MeS and MeP). Specific binary systems with given structural features were selected to determine the effect of molecule type, chain length and chain length mismatch (CLM) on the phase trajectories at the different stages and length scales involved in the transformation process and determine their role in the mechanism of the disruptive action. These include TAG/FAME with matching structural features (MeS/OSO [22] and MeP/OPO (Chapter 3), and TAG/FAME with mismatching structures (MeS/OPO-Chapter 4).

The SOO/MeS binary system of the present study was chosen in contrast to the OSO/MeS binary system [22] in order to determine the effect of positional isomerism. Similar to the previous studies of TAG/FAME systems, the phase behavior of SOO/MeS was examined in detail with x-ray diffraction (XRD), polarized light microscopy (PLM) and differential scanning calorimetry (DSC). Also, a complete phase diagram including phase transition boundaries, polymorphism and phase structures, and microstructure development was established for the SOO/MeS system. The liquidus line in the phase diagram obtained upon heating was modeled using so-called Bragg-William approximation, a thermodynamic model based on the Hildebrand equation and taking into account non-ideality of mixing.

5.2   Materials and Methods

5.2.1   Materials

Methyl stearate (MeS, purity of 99%) was purchased from Sigma-Aldrich (Oakville, Ontario). SOO was synthesized in our laboratory according to known procedures [26, 27] with a purity exceeding 99%. The purity of MeS was confirmed by GC-FID. The sample was run as is in chloroform, using a Zebron Capillary GC (ZB-5HT Inferno) column (Phenomenex, Torrance, CA, USA). SOO purity was determined by a Waters HPLC system (Alliance e2695 Milford, MA) fitted with a Waters ELSD 2424 evaporative light scattering detector. SOO and MeS were mixed in the desired molar fractions ($X_{SOO} = 0$, 0.05, 0.10, 0.20, 0.30, 0.40, 0.50, 0.60, 0.70, 0.80, 0.90 and 1.00), then heated to 80 °C and stirred for 5 min to ensure complete homogeneity. The samples were stored at 4 °C.

5.2.2   Differential scanning calorimetry

The thermal transition behavior of the SOO/MeS mixtures was investigated by differential scanning calorimetry (DSC). The measurements were carried out on a Q200 model (TA Instruments, New Castle, DE) under a nitrogen flow of 50 mL/min. The sample (~4.0 to 6.0 ± 0.1 mg) in a hermetically sealed aluminum pan was first equilibrated at 90 ºC for 5 min, a temperature and a time over which crystal memory was erased, and then cooled at 5 ºC/min down to -90 °C. The sample was held at -90 °C for 5 min then subsequently reheated to 90 ºC at 5.0 ºC/min to obtain the melting profiles. All measurement temperatures are reported to a certainty of better than ± 0.5 °C. The "TA Universal Analysis" software was used to analyze the data and extract the main characteristics of the peaks. The positions of non-resolved thermal events were estimated

using the first and second derivatives of the differential heat flow, and their other characteristics were simply estimated using the software elements.

5.2.3 Thermodynamic analysis of the boundaries in the phase diagrams

The pseudo-equilibrium phase diagram of the SOO/MeS binary system was constructed using the data generated in the DSC heating experiments. The liquidus line was generated by the offset temperature of melting, a point that is suitable for studying equilibrium properties because it is determined by the most stable crystal [28] It was simulated using a simple thermodynamic model based on the Hildebrand equation [29] coupled with the Bragg-William approximation for non-ideality of mixing [30]. The Bragg-William approximation is commonly used to investigate the miscibility of lipid mixtures [31-39]. In this model, the deviation from an ideal behavior is described by a non-ideality of mixing parameter, ρ (J/mol), defined as the difference in the energy of mixed-pairs (A–B) and the average pair interaction energy between like pairs (A–A and B–B) formed in the mixture:

$$\rho = z\left(u_{AB} - \frac{u_{AA} + u_{BB}}{2}\right)$$

(5.1)

where z is the first coordination number, u_{AB}, u_{AA} and u_{BB} the interaction energies for AB, AA and BB pairs, respectively.

The Hildebrand equation is simply modified by introducing an extra energy term, which accommodates the extra entropy in mixing due to non-ideality of mixing (Eq 2), [37, 40]:

$$\ln X_S + \frac{\rho(1-X_S)^2}{RT} = -\frac{\Delta H_S}{R}\left(\frac{1}{T} - \frac{1}{T_S}\right)$$
(5.2)

For ideal mixing, the intermolecular interaction of like-pairs is equal to that of mixed-pairs and consequently $\rho = 0$ and the Hildebrand equation is obtained. A negative ρ is obtained when the formation of AB pairs is energetically more favorable than AA or BB pairs and reflects a tendency for order. A positive ρ is obtained when mixed-pair formation is energetically less favorable and reflects a tendency of like molecules to cluster, which beyond some critical value leads to phase separation [37, 39]. A more detailed description is reported in a previous Chapters, 3 and 4.

5.2.4 Polarized light microscopy

A Leica DM2500P (Leica Microsystems, Wetzlar, Germany) fitted with a Leica DFC420C digital camera was used for the microstructure studies. A Linkam LS 350 temperature-controlled stage (Linkam Scientific Instruments, Tadworth, Surrey, UK) fitted to the PLM was used to process thermally the samples. A small droplet of material was carefully pressed between a preheated glass microscope slide and cover-slip ensuring a uniform thin layer of sample. The sample was melted at 90 ℃ for 5 min to delete all crystal memory then cooled down to -90 °C at 1 ℃/min. The temperature at which the first "white spot" was observed in the PLM was recorded as the induction temperature of crystallization (T_i). Temperature resolved images were measured at 100X magnification during cooling using the automatic multi-time image capture feature available in the PLM. The final crystal network was imaged at 50X, 100X and 500X magnification.

5.2.5 X-ray diffraction

X-ray diffraction measurements were performed on a PANalytical Empyrean apparatus (PANalytical B.V., Lelyweg, The Netherlands) equipped with a filtered Cu-K_α radiation source and with the PANalytical PIXcel^{3D} detector used in line-scanning mode. The XRD patterns were recorded between 1 and 60° (2θ) in 0.013° steps, at 45 kV and 40 mA. The procedure was automated and controlled by PANalytical Data Collector (V 3.0c) software. The sample was processed in the XRD chamber, similarly to PLM as described in section 2.2.3, using a 700 Series Cryostream Plus cooling system (Oxford Cryosystems, Oxford, UK) fitted to the diffractometer. The temperature was controlled to better than ± 0.5 °C. The data were processed and analyzed using the PANalytical X'PertHighScore V3.0 software. We refer to the range $2\theta = [0\text{-}15]°$ and $[15\text{-}30]°$ as the small- and wide-angle scattering regions (SAXD and WAXD), respectively.

5.2.6 X-ray data analysis and polymorphism

The main subcell hydrocarbon-chain packing modes are commonly denoted as the α, β' and β polymorphs [41]. The chain packing of the α - polymorph is hexagonal with non-specific chain-chain interactions. The common subcell packing of the β' - polymorph is orthorhombic, and the hydrocarbon chains of the β-polymorph are ordinarily packed in a triclinic (or monoclinic, if the angles α and γ are 90 °) parallel subcell ($T_{//}$). The β-polymorph is the most stable crystal form, with the highest melting temperature, and the α-polymorph is the least stable crystal form, with the lowest melting temperature [42, 43]. The hydrocarbon chain layering is responsible for the characteristic small-angle (long-spacing) reflections. The period of layers normally observed for TAG

structures is usually proportional to the acyl chain lengths by a factor of two or three, suggesting a double-chain length (DCL) or a triple-chain length (TCL) packing [44, 45].

Note that the first order reflection (d_{001}) represents the thickness of the molecular layers [44] and the higher order reflections (d_{00l}, l= 2, 3,..) indicate regular, periodic structures, and represent the periodical sequence of electronic density differences in multiple layers [46, 47].

5.3   Results and Discussion

5.3.1   Crystal structure of SOO/MeS mixtures

Wide angle x-ray diffraction and subcell structure

The WAXD patterns of the SOO/MeS mixtures measured at -40 °C after cooling from the melt at 1 ºC/min are shown in Fig. 5.1a. The intensity of selected reflections in the WAXD region are presented in Fig. 5.1b. As can be seen, a background halo indicative of the presence of a liquid or amorphous phase was still present in the patterns even at -40 °C, particularly in the SOO-rich mixtures. This contribution was systematically subtracted before the analysis of the patterns and determination of the crystal phases.

The XRD pattern of MeS perfectly matched the diffraction powder file of its monoclinic structure (labeled β_M) published by the International Centre for Diffraction Data (ICDD) and assigned to a monoclinic crystal structure (PDF, reference No 00-032-1764). The peaks at 4.25 Å, 4.03 Å and 3.63 Å of pure MeS are assigned to the ($\bar{6}11$), ($\bar{10}11$) and (121) planes, respectively.
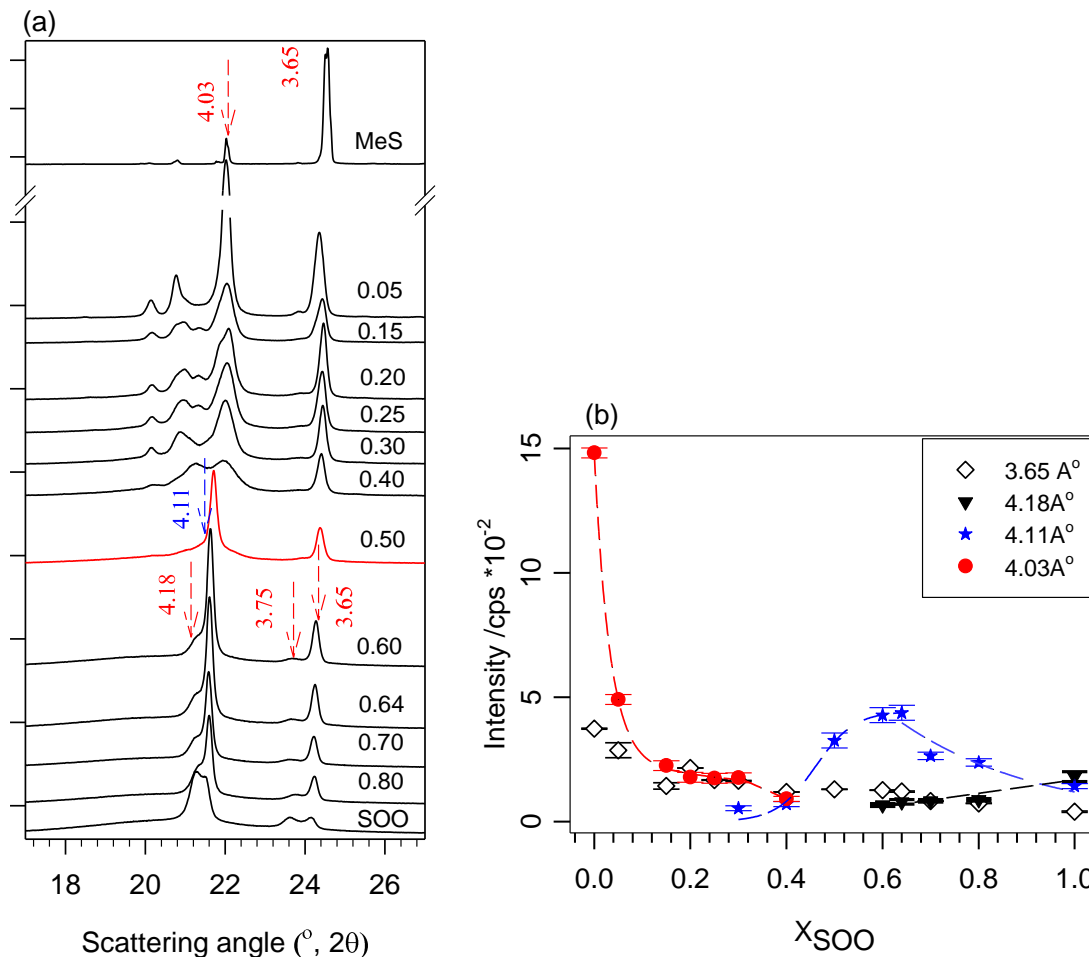
Figure 5.1: (a) WAXD spectra of SOO/MeS mixtures measured at -40 °C, after cooling (1 °C/min) from the melt, and (b) intensity of selected reflections characteristic of the different phases occurring in the SOO-MeS mixtures. The selected peaks are specified with their d-spacing (in Å) and indicated with arrows in Fig. 5.1a

Pure SOO presented four peaks in the WAXD pattern (at 4.18 Å, 4.11 Å, 3.75 Å and 3.65 Å in Fig. 5.1a) indicative of two orthorhombic subcell structures. The coexistence of such dual phases is common in asymmetric unsaturated TAGs like SOO [48]. Temperature resolved WAXD (TR-WAXD, not shown) of SOO cooled at 1 °C/min revealed that a first phase is a very loose hexagonal structure (very wide peak at 4.18 Å) reminiscent of the

least stable phase known for SOO, the α_2-phase [49], which started to crystallize at ~ 5 °C. This phase transformed gradually into a more stable orthorhombic structure (appearance of the 200 peak at 3.85 Å) at -1 °C. The crystal grew and ordered upon cooling further, as indicated by the steady increase of the intensity of the reflection from (200) plane and decrease of its d-spacing (3.75 Å in the most organized crystal). This phase of SOO is known as the α_1-phase [49]. The second phase also started at ~-1 °C in the hexagonal subcell structure with a shoulder peak at 4.11 Å indicative of the α_2-phase of SOO, and then transformed below -9 °C to an orthorhombic phase having a 200 reflection at 3.65 Å characteristic a β'-phase rather than a pseudo α-phase [49].

The addition of SOO to MeS triggered the formation of new phases at very low loading. As soon as SOO was added, new reflections at 4.11, and 4.18 Å started to appear at the detriment of those of the pure MeS phase. The presence of these reflections along with the peak at 3.65 Å is indicative of the formation of new orthorhombic phases. They are attributed to mixed MeS/SOO phases. Their peaks were relatively wider than those of pure SOO indicating that the phases induced by SOO were less ordered and have smaller coherence lengths. In fact, as indicated by the intensity of the signature peaks of MeS (see the 4.03 Å curve, circles in Fig. 5.1b), the pure MeS phase decreased exponentially and disappeared completely in the 0.50_{SOO} mixture.

Interestingly, the 0.50_{SOO} mixture presented peaks of a well-ordered orthorhombic subcell structure, indicating the formation of a 1:1 molecular compound (MC). The crystallization (1 °C/min) of the 0.5_{SOO} mixture followed by TR-XRD (Fig. 5.2a) showed that this mixture started crystallizing from the melt at 21.5 °C in the hexagonal subcell

structure (characteristic reflection at 4.11 Å in Fig. 5.2a) and then transformed at 17.5 °C into an orthorhombic phase (signature peaks at 4.18 Å and 3.85 Å at 17.5 °C transformed gradually to 4.14 Å and 3.68 Å in the last scan in Fig. 5.2a). This latter phase is very close to the β'-form of SOO and is therefore labelled β'_{MC}.
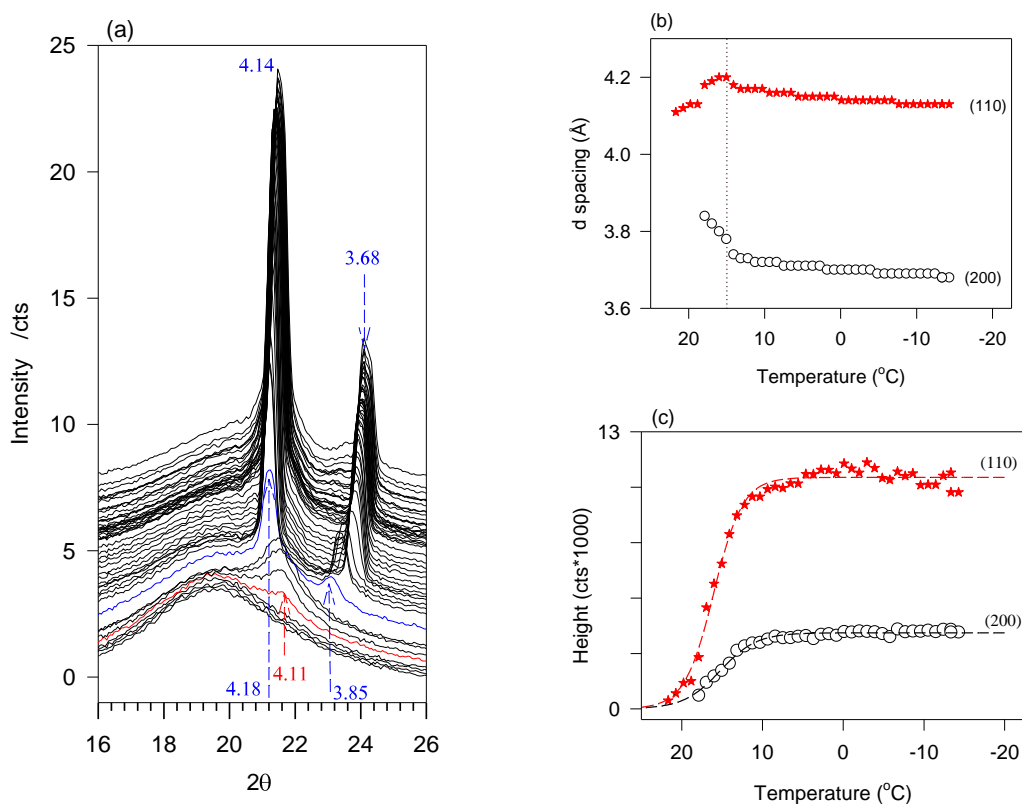
Figure 5.2: (a) Temperature resolved (from 27 °C to -20 °C) WAXD of 0.50_{SOO} obtained while cooling from the melt at 1 °C/min, (b) d spacing and (c) intensity versus temperature curves of the WAXD peaks

As the sample was cooled from 21.5 °C to 15.0 °C during the polymorphic transformation, the (100) lateral d-spacing (d_{100}) of the α-form increased from 4.11 to 4.20 Å to accommodate the (110) and (200) planes of the new β'-structure (Fig. 5.2b).

The accommodation (d_{100} increase) coincided with the rapid decrease of d_{200} (vertical dotted line in Fig. 5.2b), indicating that the transformation involved the closest neighbouring molecules. After this rapid adjustment of the molecules to make the new crystal structure, the subcell ordered isotropically relatively slowly to reach its equilibrium values at -20 °C (d_{200} = 3.68 Å and d_{110} = 4.14 Å in Fig. 5.2b). The intensity of the reflections of the orthorhombic phase increased with cooling following a sigmoidal function and reached 95% of its plateau at ~ 8 °C (Fig. 5.2c) indicating that the accommodation and the formation of the MC in its final form was achieved in a relatively small temperature range (in less than 5 °C).

In all the SOO rich mixtures, the 4.11 Å and 3.65 Å peaks of the β'_{MC}-form were presented superimposed to the 4.18 Å and 3.75 Å reflections of SOO (0.60_{SOO} - 0.80_{SOO} mixtures in Fig. 5.1a). This indicates that the β'_{MC}-phase coexisted with both the α_1-phase and β'-phase of SOO. Note that as the mixtures became richer in SOO, the peaks of β'_{MC} decreased while those of the α_1-phase increased, understandably because less MeS-SOO pairs were available to form MC crystals.

Small angle x-ray diffraction and lamellar packing

The SAXD patterns of SOO/MeS mixtures measured at -40 °C are displayed in Fig. 5.3a and 5.3b. The intensity of selected SAXD peaks are shown Fig. 5.3c.

MeS displayed a doublet series of sharp SAXD peaks ($00l$ = 2, 4, 6 and 8) with repeat units d_{001} of 49.2 Å and 48.3 Å, indicative of a DCL structure of a tilted subcell. The pure SOO displayed one series of reflections with d_{001} = 61 Å of a TCL structure, in agreement

with previously reported data for the orthorhombic phase of SOO [49, 50]. The SAXD of

the mixtures can be categorized into two groups separated at the 0.50_{SOO} mixture.
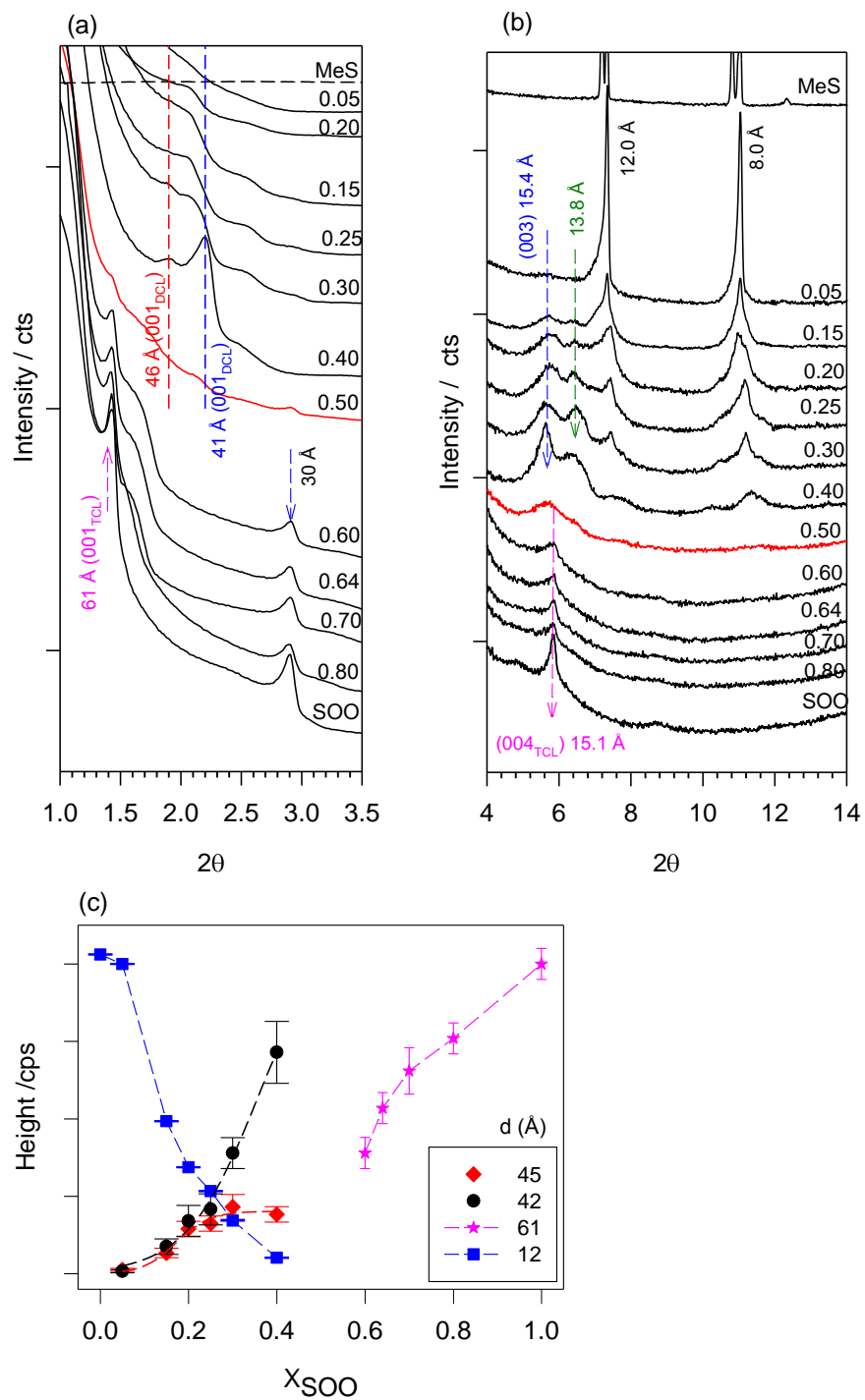
Figure 5.3: (a-b) The SAXD of SOO/MeS mixtures taken at -40 °C, after cooling from the

melt at 1 °C/min and (c) intensity of selected SAXD reflections

The first group of mixtures ($<0.50_{SOO}$) presented the DCL packing structure of MeS (d_{001} = 49 Å) and two other different DCL structures attributed to mixed phases (fundamental reflections at d_{001} = 46.0 Å and 42.0 Å in Fig. 5.3a) with corresponding (003) reflections at 15.5 Å, 13.8Å, respectively, as well as other higher order reflections (Fig. 5.3b). The decrease with increasing SOO concentration of the intensity of the 00l reflections associated with the MeS monoclinic phase (exemplified by 12 Å (004)-curve in Fig. 5.3c) was concomitant with the increase of the intensity of the reflections of the mixed phases (46 and 42 Å in Fig. 5.3c). The 46.0 Å and 42.0 Å reflections are associated with the orthorhombic phases involving SOO. As the concentration approached the compound composition, the (00l) reflections with fundamental repeat unit of 42 Å became narrower and their intensity higher than those of the 46-Å reflections indicating the prevalence of the MC at the detriment of the MeS phase. The 42-Å reflection was therefore associated with the MC in the β'-form, and the 46-Å reflection was associated with a smaller mixed MeS-rich phase, both in the DCL structure. There was no pure SOO phase developed in the mixtures of this group since no peaks of its characteristic TCL packing were detected. It is reasonable to think that the small (001) repeat length (46 Å and 42 Å) was due to the MeS unit cell (packed in 49-Å units) accommodating SOO molecules in a 1:1 MC (in a 42-Å units) and in MeS-rich/SOO mixed (in a 46-Å units) structures.

The second group of mixtures ($\geq 0.50_{SOO}$) displayed a TCL packing structure similar to SOO with 001, 002 and 003 reflections at 61.0 Å, 30.0 Å and 15 Å, respectively (Fig. 5.3a and 5.3b). This indicates that the β'-phase of pure SOO and the pseudo α-phase of SOO/MeS mixed phase as well as the β'_{Mc}-phase were packed in similar TCL structures.

Such crystal structures were initiated by SOO templates which accommodated the MeS molecules in either the MC or the mixed SOO-rich phases. The similarity in chain length between the three structures can be explained by SOO providing sufficient space to host MeS. Note that there was no pure MeS phase detected in this group of mixtures.
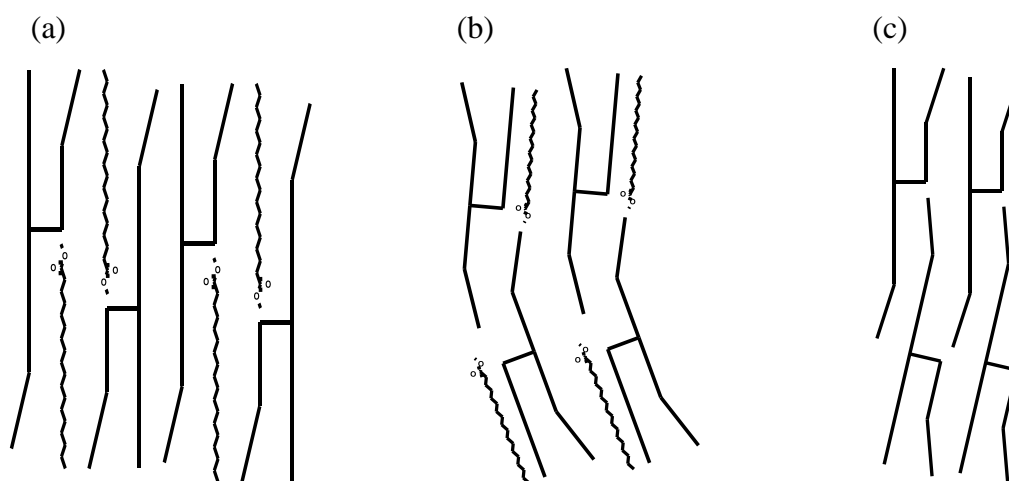
Figure 5.4: Suggested lamellar structures of SOO/MeS compound and TCL structure of SOO. (a) SOO/MeS molecular compound (MC) in the DCL, (b) SOO/MeS MC in the TCL and (c) pure SOO in the TCL structure

The switch at the 0.50_{SOO} mixture of the crystal structure from subcells initiated by MeS to subcells initiated by SOO is attributable to the chain length structure of SOO which is practically double that of MeS, coupled with the geometric steric hindrances due to the asymmetric nature of SOO. It is suggested that once TCL SOO pairs are formed, it is easier for MeS to join in the packing but not when SOO is dissolved in MeS, in which case SOO pairs with MeS to form the MC directly. A proposed structure of MC of SOO/MeS is provided in Fig. 5.4a and 5.4b. A TCL structure of pure SOO is also provided in Fig. 5.4(c).

5.4   Crystallization and melting behaviors

5.4.1   Crystallization behavior

The DSC cooling thermograms of the SOO/MeS mixtures are displayed in Fig. 5.5a.

The cooling phase diagram of the binary system including T_{on}, T_P and T_{off} of

crystallization is presented in Fig. 5.5b. MeS presented a single sharp and intense exotherm

at ~33.3 °C (P_o in Fig. 5.5a) with a loop due to the exothermic energy not being dissipated

by the DSC in sufficient time for the signal to be temporally resolved. Such a signal is

typical of the rapid growth of a very energetic single phase. SOO presented an extended

and relatively weak leading peak at ~ 7 °C followed by a large exotherm at ~-7 °C (P1 and

P3 in Fig. 5.5a, respectively) indicating a complex crystallization process.   This

transformation path is similar to what was previously reported for SOO [51] wherein, the

nucleation and slow growth of the low stability α_2 -phase of OPO was followed by a rapid

polymorphic transformation into the α_1 -phase as well as the nucleation and strong growth

of a higher melting temperature crystal phase, β'.

The effect of SOO on the crystallization of MeS was strong even at the lowest

composition. SOO not only reduced the magnitude of the initial heat flow, it also shifted

the onset temperature steadily to lower temperatures and triggered new transformations,

thereby increasing the span of crystallization dramatically. The MeS-rich mixtures (X_{SOO}

≤ 0.40) presented three notable exotherms (P_M , P_L, and P_3' in Fig. 5.5a) having constant

T_P indicative of lines of transformations spanning to 0.40_{SOO} (lines T_M , T_L , and T_{SOO} in

Fig. 5.5b). With increasing SOO, the intensity of the first peak (P_0 in Fig. 5.5a) which is

associated to the crystallization enthalpy of pure MeS, decreased linearly ($R^2 = 0.8979$,

empty circle in Fig. 5.5b) while the enthalpy of P_M, the closest peak which appeared at ~23.0 °C just upon the addition of SOO (stars in Fig. 5.5b), increased linearly ($R^2 = 0.94985$, stars in Fig. 5.5c). This indicate the formation of a well-defined MeS-SOO mixed phase whose content increases at the detriment of the MeS phase.

The phase transformation indicated by P_3' at -5.5 °C, appeared in concurrence with the MeS/SOO mixed phase, and the enthalpy corresponding to this peak also increased linearly with increasing SOO content ($R^2 = 0.9187$, filled squares in Fig. 5.5c), but at a much lower rate: 21.4 kJ/mol for P_3' compared to 60 kJ / mol for P3. The intermediary peak (P_L in Fig. 5.5a) was located at 10 °C, and was paired with P_3' in the same manner as was the leading peak of pure SOO (P_1) with its P_3 counterpart. The intensity of P_L (filled triangle in Fig. 5.5c) increased in the same manner as P_3'. P_L and P_3' are therefore associated with the formation of another well-defined mixed phase whose phase trajectory mirrors the crystallization of SOO. Note that P_L and P_3' are only slightly higher than the P_1 and P_3 peaks of pure SOO.

The SOO-rich mixtures ($X_{SOO} > 0.40$) presented relatively more complex transformation traces compared to the MeS-rich mixtures. The crystallization of these mixtures occurred with four notable exotherms (P_1, P_L, P_2 and P_3 in Fig. 5.5a) in a much smaller temperature range than the MeS-rich mixtures. P_M, the peak of the mixed phase, was notably absent in the thermograms of these mixtures. Furthermore, the peak temperatures of their exotherms varied with concentration contrary to those of the MeS-rich mixtures. When these peak temperatures were graphed with those of the MeS-rich

mixtures (Fig. 5.5a), clear singularities appeared at the 0.40_{SOO} mixture. Also, except for P_3, the peak associated with the crystallization of SOO and which increased substantially as the molar ratio of SOO was increased, their intensity did not vary substantially.
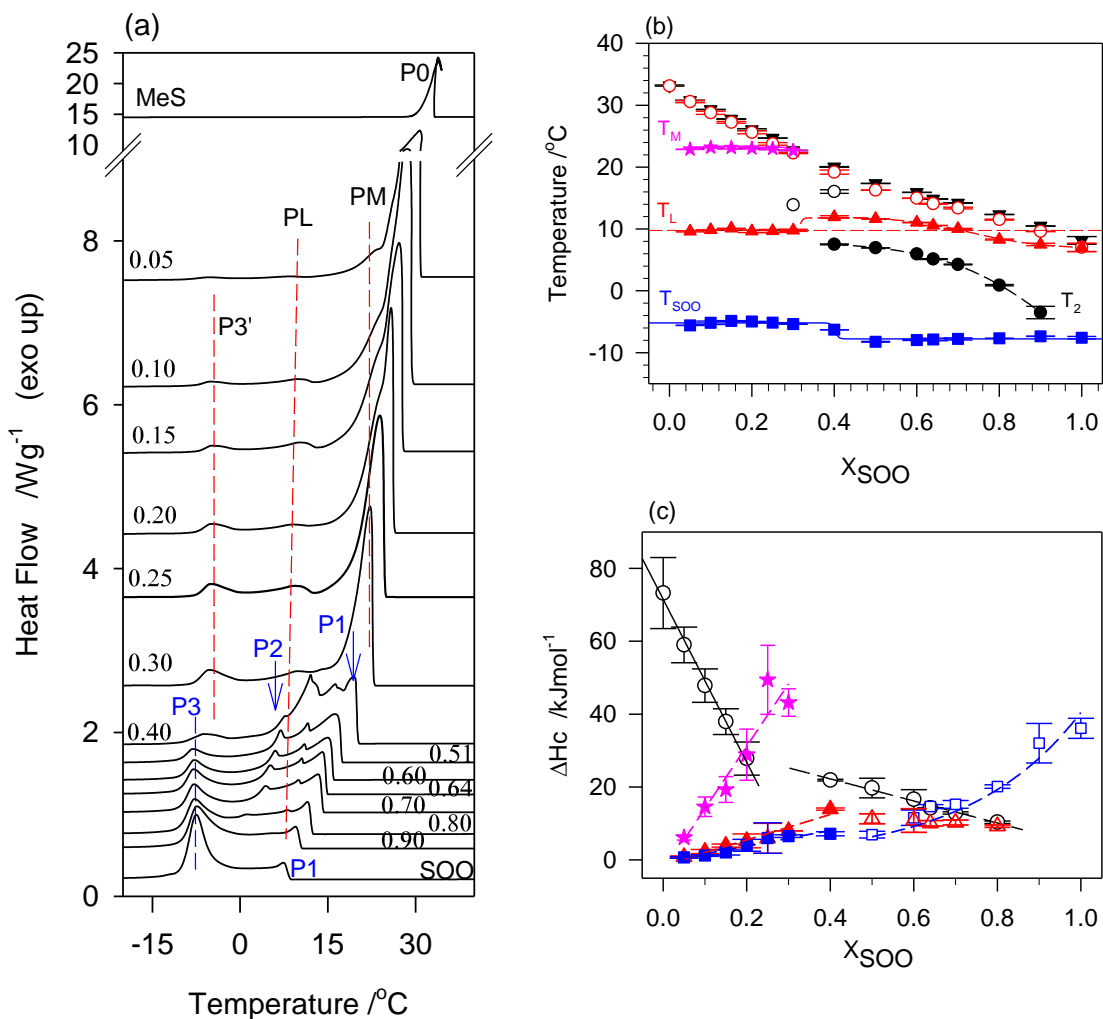
Figure 5.5: (a) Cooling (5 °C/min) thermogram of SOO/MeS mixtures (b) characteristic temperatures of crystallization, and (c) enthalpy associated with individual exotherms (P0 to P3). (Onset temperature of crystallization: T_{On}, offset temperature of crystallization T_{Off} and Peak temperature: T_P). Open circles, P0 and P1; stars: PM; up triangles: PL; squares: P3'; empty triangles: P2; empty squares: P3.

The liquidus line in the crystallization phase diagram (T_{On} or T_P of the leading peak in Fig. 5.5b) is marked by a singularity at 0.30_{SOO} coupled with a horizontal transformation line expanding from 0.05_{SOO} to 0.30_{SOO} indicating a peritectic transformation.

The different crystallization behaviors delimited at the 0.40_{SOO} as illustrated with the thermograms of Fig. 5.5a and quantified in Figs. 5.5b and 5.5c, are correlated with the XRD findings. The polymorphism of MeS-rich and SOO-rich mixtures is directly related to the transformation revealed by DSC, with a close match of the intensity of the XRD characteristic reflections with the enthalpy of corresponding peaks. The decrease of P_0 intensity and subsequent increase of P_M intensity with increasing SOO concentration correlate very well with the increase of the orthorhombic phase content at the expense of the monoclinic phase of pure MeS. Hence the peritectic compound is associated with the MeS-rich mixed phase in the orthorhombic and DCL structure without any ambiguity. The exotherms P_L and the $P_3^{'}$ in mixtures $\leq 0.40_{SOO}$ are associated with the MC and the compound/SOO mixed phases, respectively, both in the orthorhombic form and DCL structure. Note that the position of $P_3^{'}$ and P_L shifted to lower temperatures indicating a decrease in crystal stability. P_3 is associated with pure SOO in the β'-form and TCL structure. The intensity of P_3 increased with increasing SOO but its position remained unaffected indicating that it crystallized in the same stability form despite the presence of MeS or mixed phases. P_2 is associated with the compound in the orthorhombic form and TCL structure. This phase grew at the detriment of the α_1-phase of pure SOO, and as expected showed a maximum at 0.50_{SOO}.

5.4.2 Melting behavior

The DSC heating profiles of the SOO/MeS mixtures are shown in Fig. 5.6a. The corresponding kinetic phase diagram comprising the transition temperatures are presented in Fig. 5.6b. The liquidus line in the phase diagram is represented by the peak and offset temperature of the most stable crystals. As can be seen, two group of melting traces delimited by the 0.50_{SOO} mixture are presented in Fig. 5.6(a), mirroring what was observed in the crystallization thermograms.
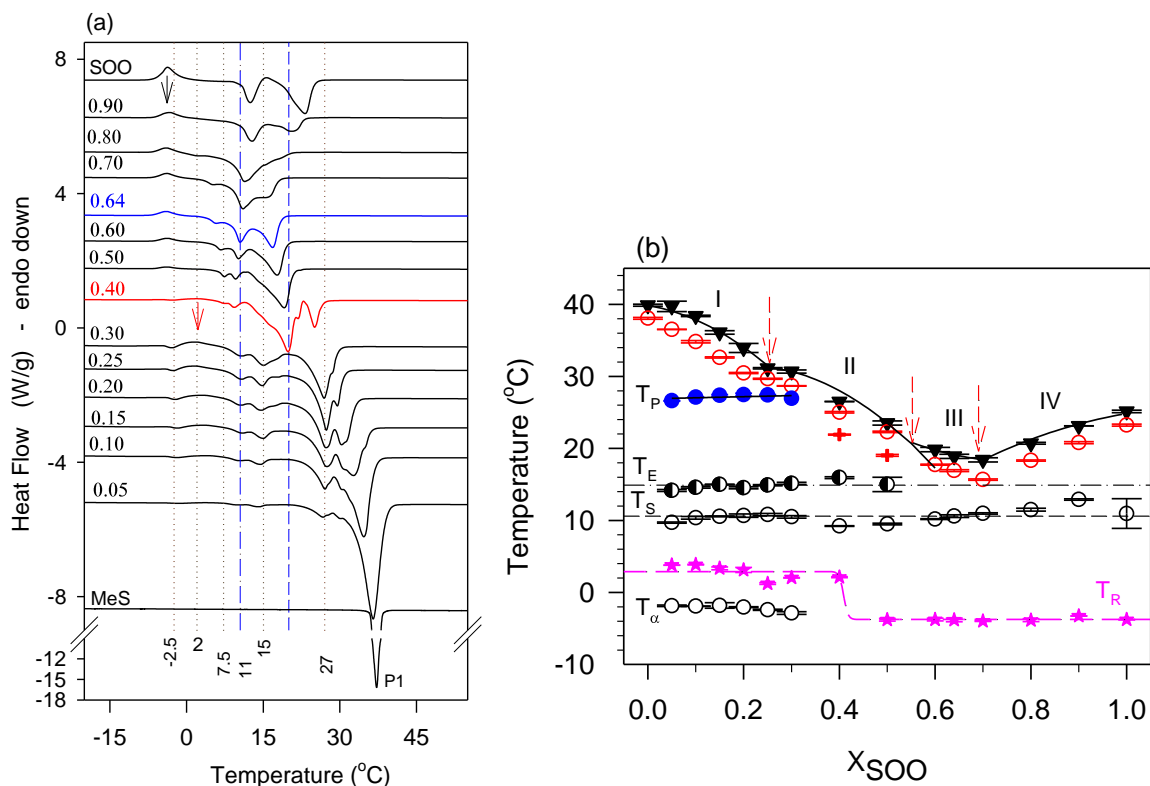
Figure 5.6. **(a)** Heating (5 ºC/min) thermograms of SOO/MeS mixtures. SOO molar fraction is reported on the left side of each curve. **(b)** Characteristic transition temperatures. Symbols represent: offset temperature of melting, T_{off}: ▼, Peak temperature of last endotherm, T_{P1}: ○, and peak temperature of intermediary transformations T_P: ○, and recrystallization temperature: ★.

The mixture with $X_{SOO} \geq 0.50$ started with a strong exothermic event followed by a series of thermal transitions and complete melting all before 27 ºC, the melting temperature of SOO. Although the presence of MeS in this group of mixtures resulted in extra phase transformations, the overall melting profiles resembles that of SOO. Note that the strong crystallization mediated by melt of SOO at ~15 °C was hindered in the other mixtures of the group, probably because it was weaker than the overlapping melting events.

For the mixtures with $X_{SOO} < 0.50$, and from the single endotherm of pure MeS, the addition of SOO induced a significant increase of the number of transitions (as much as 7 between exotherm and endotherms) and broadened the temperature transformation window. All the heating thermograms of these mixtures started with a small melting event at ~ -2.5 ºC followed by a broad exotherm at ~2 ºC (T_R in Fig. 5.6b) and ended with an increasingly weakening endotherm. This last endotherm decreased very rapidly with increasing SOO content and disappeared in the mixtures with more than 40% SOO (P1 in Fig. 5.6a).

A notable transformation line was presented at ~ 29 ºC spanning from $X_{SOO} > 0$ to 0.30, the concentration at which a singularity was observed in the liquidus line (arrow 1 in Fig. 5.6b). This is a clear indication of a peritectic transformation. These features in the heating phase diagram coincided with the peritectic transformation observed in the cooling phase diagram and indicate the reversibility of the transition. The peritectic transformation is usually induced by specific unlike-pair intermolecular interactions and is accompanied by the formation of so-called peritectic compound.

From the SOO side of the phase diagram, one can see that MeS significantly affected the transformation behavior of SOO, particularly in its ability to form the most stable crystals. The exotherm appearing in SOO at ~15.7 °C was overwhelmed as soon as MeS was added (Fig. 5.6a), and the $\beta_1^{'}$-form of SOO (melting at 23 °C) was reduced dramatically and completely suppressed in the 0.70_{SOO} mixture. The melting point of the most stable phase was also shifted to a minimum, indicating strong colligative effects. These effects were illustrated in the liquid-solid boundary of the kinetic phase diagram by a sharp eutectic (eutectic concentration $X_E = 0.70$) and a eutectic line (eutectic temperature $T_E = 15$ °C in Fig. 5.6b). The eutectic is formed between SOO and the 1:1 MC rather than MeS.

Other solid-solid transformation lines in the kinetic phase diagram below the peritectic and eutectic lines are also visible in both sides of the stoichiometric 50/50 mixture (T_S, T_R and T_α in Fig. 5.6b). Note that the mixtures with X_{SOO} below 0.20 presented a small peak above the peritectic at ~33 °C (indicated by the upward arrow in Fig. 5.6a) forming a line that indicate a possible metatectic transformation (not reported in Fig. 5.6b).

5.4.3   Thermodynamic analysis of the liquidus line

The liquidus line in the binary phase diagram was constructed with T_{off} (offset temperature of melting) as typically done in the study of lipid mixtures [31, 34-36, 38, 52, 53]. Four segments, delimited by the singularities in experimental liquidus line, i.e., the peritectic point, the MC and the eutectic point, were considered for the fit to Eq. 3.2. The calculated and experimental liquidus lines are shown in Fig. 5.6b. The results of the fit are listed in Table 5.1. The fit was excellent with R^2 values all higher than 0.99875, residuals

smaller than 3%, and RMSD less than 0.5. The peritectic, MC and eutectic points have

been confirmed at 0.25_{SOO}, 0.54_{SOO} and 0.70_{SOO}, respectively.

The fit yielded the highest negative value for ρ in the MeS rich region where the

peritectic transformation occurred, indicating that the formation of unlike molecular pairs

was most favourable in this region of the phase diagram. The value of ρ for the SOO-

rich eutectic segment, which although also negative was ~4 times smaller than that of the

MeS-rich peritectic segment, indicating that the formation of unlike pairs with the MC was

much less favourable. One can notice that close to the eutectic region where the MC

dominates (segment III), the value of ρ was slightly positive indicating weak repulsive

forces between unlike molecules, and a miscibility dominated by a behavior close to ideal.

The negative value of ρ in segment II also indicates that unlike pair formation is

favourable in this region of the phase diagram but not as much as in the peritectic mixtures.

Table 5.1: Temperature and enthalpy parameters T_s and ΔH_s used to simulate the liquidus

line (Eq.3.3), and resulting non-ideality of mixing parameter ρ.

Segment	Region	T_s (K)	ΔH_s (kJ/mol)	ρ (kJ/mol)
I	$0 \leq X_s \leq 0.25$	313.5 ± 0.5	72	-23.0
II	$0.25 \leq X_s \leq 0.50$	308.5 ± 0.5	61	-7.5
III	$0.55 \leq X_s \leq 0.70$	294.0 ± 0.3	65	4.0
IV	$0.70 \leq X_s \leq 1.0$	298.3 ± 0.3	65	-6.0

5.5   Microstructure development of the SOO/MeS mixtures

The final microstructures of the SOO/MeS mixtures captured by PLM at -90 °C are displayed in Fig. 5.7. The induction temperatures determined at the observation of the first white spot in the PLM are shown in Fig. 5.8. Note that the smallest structures observable in the PLM (~0.5 μm) are significantly larger than nuclei due to the limitation induced by light diffraction. Also because of differences in the size and shape of the samples, PLM induction temperatures can be compared to but are not the same as the DSC onset of crystallization. Nonetheless, the singularities that are observed at 0.20_{SOO}, and 0.50_{SOO} in the PLM induction temperature versus SOO molar ratio (arrows 1 and 2, respectively, in Fig. 5.8) correspond to the peritectic and MC singularities of the liquidus line in the DSC cooling phase diagram.

Pure MeS started crystallizing at relatively high temperature (36.0 ± 0.5 °C), and crystallized completely within a fraction of a second. Only one crystal was detected in the PLM slide, suggesting that it developed from a single nucleus. The very large crystal of MeS (> 6000 μm) developed radially from the nucleus into a palm leaf-like structure, forking along the growth direction. The crystallization of pure SOO was very slow compared to MeS. SOO started to form small fibril like microstructures at ~ 8.5 ±0.5 ºC and completed its crystallization at very low temperatures (~ -70 ℃).

The typical microstructure of MeS was dramatically altered by the addition of SOO. As the concentration of SOO was increased, the number, shape, size, homogeneity and distribution of the microstructures were dramatically changed. Similar to SOO, all the SOO/MeS mixtures displayed different microstructures at different steps of crystallization.

The MeS-rich mixtures ($<0.40_{SOO}$) displayed two types of microstructures. The crystallization of these mixtures started with the formation and rapid (30 s or 0.5 °C drop in temperature) development of entities whose nucleation and spherulitic growth mode was reminiscent of the large leaf-like microstructures of MeS, followed within 30 s to 1 min by the formation of fibril-like microstructures. This secondary nucleation was continuous and fast. The fibrils developed fully within 2 to 3 min after they appeared.

(a) MeS (b) 0.10 (c) 0.20 (d) 0.25

(e) 0.30 (f) 0.40 (g) 0.50 (h) 0.60

(i) 0.64 (j) 0.70 (k) 0.80 (l) SOO
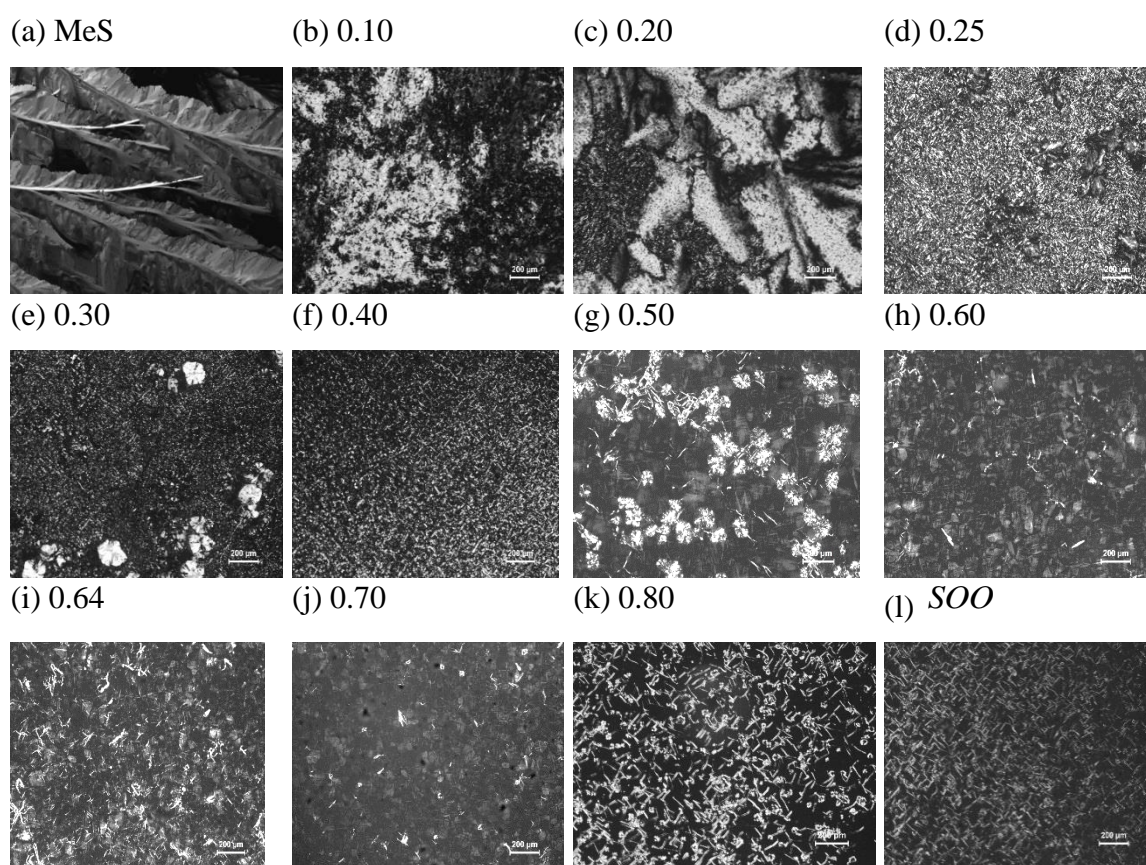
Figure 5.7. PLM of SOO/MeS binary mixtures taken at -90 °C. The SOO molar ration is reported on the top of the PLM images.

Interestingly, the neat and smooth appearance of the leaflets of the MeS microstructures was lost (see for example PLM of the 0.10_{SOO} mixture in Fig. 5.7b), their

size decreased and their number increased (PLM of the 0.20_{SOO} mixture in Fig. 5.7b) indicating a strong effect of SOO on the nucleation and growth rate of the crystals of the MeS-rich phase. For example, three- to four distorted spherulitic microstructures filling about 80% of the PLM slide were observed in the 0.10_{SOO} mixture. The growth of these spherulites was complete in about one minute. The PLM of the 0.25_{SOO} to 0.40_{SOO} mixtures (Fig. 5.7d-f) was different because of the dramatic drop in the number and size of the spherulitic microstructures. For example, these crystals were dispersed in 15 to 20% of the whole PLM slide area in the 0.25_{SOO} mixture (Fig. 5.7d) and did not appear in the 0.40_{SOO} mixture (Fig. 5.7f). The PLM data indicate that along the increasing nucleation rate, the growth rate of these entities was reduced as SOO was added.
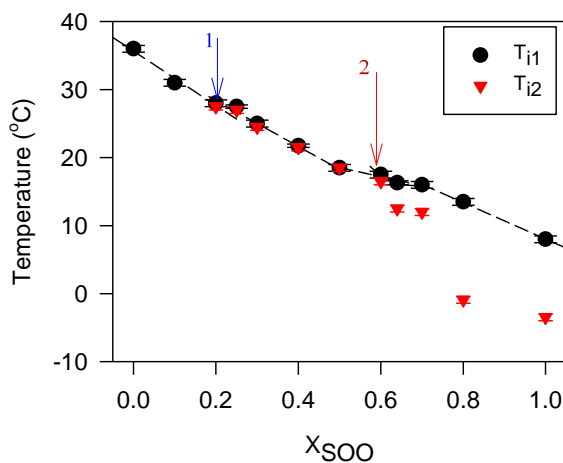
Figure 5.8. PLM induction temperature of different mixtures obtained upon cooling from the melt at 1 °C/min. T_{i1} and T_{i2} are the temperature at which the first and second microstructures were observed first. The dashed line is a guide for eye.

The formation of spherulitic and fibril-like microstructures in the MeS-rich mixtures can be related respectively to the DSC crystallization peak of the MeS phase (P_0) and the shoulder peak (P_M) of a well-defined MeS-SOO mixed phase which followed very shortly. The number of fibril-like microstructures increased with increasing SOO at the detriment of the spherulitic microstructure in accordance to the variation of P_M and P_0, respectively. Furthermore, the presence of the spherulites coincided with the monoclinic phase of MeS, confirming the above association.

The 0.50_{SOO} mixture displayed two types of microstructures, fibril-like entities developed in the primary stage (at ~19 °C) and small spherulites formed later (~ 13 °C). These two different microstructures share the same orthorhombic subcell structure as it was the only form that was detected for this composition at the completion of the crystallization. This very interesting finding can be explained with the temperature/time resolved WAXD (Fig. 5.2a) which revealed that the 0.50_{SOO} mixture started crystallizing in the hexagonal form (α-form) then slowly transformed into the higher stability orthorhombic form (β'-form). The time-lapse PLM showed that the spherulitic crystals developed from the melt at a temperature where the intensity of the characteristic peaks of the orthorhombic subcell increased dramatically (between 16-10 °C). Furthermore, both fibril-like and spherulitic microstructures continued to develop during cooling in this temperature range. Therefore, it is possible that the orthorhombic crystals which transformed from the hexagonal phase (solid-solid transformation) retained the initial fibril like microstructure, and the spherulitic microstructure were formed by an orthorhombic phase which developed directly from the melt. The two crystal developments could not be discriminated directly in the TR-XRD of

the 0.50_{SOO} mixture because the XRD peaks of the same crystal phase occur at the same position. It is also possible that it was only at the lower temperature where the spherulites were observed that nano-sized single domains have enough energy to form these new microstructures. The mixtures in the $0.50 > X_{SOO} < 0.80$ range displayed similar fibril-like microstructures irregularly dispersed over a cloudy background (Fig. 5.7g-k). The SOO-richer mixtures ($X_{SOO} > 0.80$) displayed only fibril like microstructures (Fig. 5.7l). This indicates that the material was still not fully crystallized at low temperature as was observed in the XRD. The number of these microstructures increased in mixtures with X_{SOO} higher than 0.80, indicating their close relation to SOO.

5.6 Effect of asymmetry of TAG on FAME/TAG phase behavior

Symmetry and stereospecificity is known to be an important structural element for the selection of the phase trajectory and polymorphism of TAGs. The symmetry of the TAG additive is therefore expected to be a significant parameter in the phase behaviour of TAG/FAME binary systems. The effect of symmetry of the TAG on the transformation path, polymorphism and microstructure of TAG/FAME binary systems can be understood in light of the differences in the phase behavior between the two TAGs and by contrasting the present work with the findings of the previous MeS/OSO study [22]. SOO is known to nucleate and form crystals faster than OSO but takes longer to reach equilibrium [51]. SOO packs predominantly in pseudo-hexagonal phases and also in β'-phases both in the TCL structure; whereas, OSO crystallizes equally in pseudo-α and β'-subcells, both in the DCL structure. Under the same thermal treatment, SOO displayed a similar fibril like microstructure to SOO, but in a denser network.

SOO as well as OSO formed a 1:1 MC with MeS. However, the OSO/MeS compound formed a eutectic with both pure MeS ($X_{E1} = 0.49_{OSO}$) and pure OSO ($X_{E2} = 0.84_{OSO}$) when SOO/MeS compound formed one eutectic with pure SOO ($X_E = 0.70_{SOO}$) and a peritectic with pure MeS ($X_P = 0.25_{SOO}$). The striking phase behaviour of SOO/MeS mixtures is related to the distinctiveness of the SOO:MeS compound, which was developed because of the asymmetry of SOO. During crystal packing, because of this asymmetry, the unsaturated fatty acid on the *sn*-2 position comes close to the saturated fatty acid on the *sn*-1 position and aligns in a way so to reduce the repulsion due to the geometric steric hindrance presented by the kink and optimize crystal energy. The most stable phase available for the SOO:MeS compound was the orthorhombic subcell structure contrary to the OSO:MeS compound which achieved a triclinic subcell packing, because of the much less hindrance because of the availability of its stearic moiety at the *sn*-2 position for tighter packing.

The peritectic transformation that occurred with SOO and not OSO can also be explained by symmetry considerations, i.e., the disposition of the oleic moieties about the ester group. In the MeS-rich mixtures and in the liquid state, because of the asymmetry, SOO presents its unsaturated oleic acids on both sides of its glycerol backbone and accommodates the MeS-MeS dimers to form the lamellae that seed a peritectic transformation. Note the formation of dimers of fatty acid esters in the liquid phase was evidenced previously [54]. On the other hand, the dimers of MeS face two unsaturated fatty acids on one side and two saturated fatty acids on the other side of an OSO/MeS compound, triggering strong enough repulsion from the two unsaturated fatty acids so that the formation of MeS lamellae in the MeS-rich mixtures are more favorable than mixed

MeS/OSO other than the compound, leading to colligative effects that may explain the formation of a eutectic between the compound and MeS.

The difference in position of the oleic acids about the stearic moiety also explain the differentiated effect of concentration on the crystal chain packing structure on the SOO:MeS and OSO:MeS compounds. Due to these structural features, the stacking of the SOO:MeS compound was much more easily influenced by its molecular environment (MeS and SOO) than the OSO:MeS compound by MeS and OSO. In the SOO/MeS system, the DCL structure of the MC was promoted in the MeS rich side of the phase diagram, and the TCL in the SOO-rich side, indicating a critical difference in interaction under different environments. Similar influences were not observed on the chain length stacking of the OSO:MeS compound where similar DCL packing was achieved independently of concentration.

The formation of two types of chain length structure for the SOO/MeS compound (a DCL in the MeS rich region and TCL in SOO-rich mixtures) is suggested as a cause of the occurrence of a peritectic and a eutectic transformation. Similar considerations of chain length structure in the OSO/MeS system, in which the compound displayed a DCL packing in both MeS-rich and OSO-rich regions, can explain the two eutectics.

Both SOO/MeS and OSO/MeS systems displayed similar microstructure developments, driven primarily by the influence of the TAG. In the MeS-rich mixtures of both systems, the TAG distorted the large spherulites of the monoclinic phase of MeS and dramatically reduced their size, and in the TAG (OSO or SOO)-rich region both systems displayed fibril like microstructures. However, the number density of the crystals

(spherulites or fibrils) was much larger and their size much smaller in the SOO/MeS mixtures than in the OSO/MeS counterparts, resulting in denser solid networks. A surprising effect of symmetry manifested in the microstructure of the MCs of the systems. Because of the way the SOO:MeS compound nucleated from the melt into its orthorhombic phase, it formed both fibril-like and spherulitic microstructures; whereas the OSO:MeS compound formed fibril like microstructures only.

5.7   Conclusions

A complete phase diagram of SOO/MeS binary system encompassing thermal transitions, crystal structure and microstructure is constructed for the first time. The SOO/MeS mixtures presented a SOO:MeS molecular compound (MC) which participated with MeS and SOO in the formation of a peritectic and a eutectic, respectively. In fact, the phase behavior of the SOO/MeS system is directly related to the asymmetry of SOO and the resulting distinct structure of the MC. The peritectic line occurred in the MeS rich side 12 °C below the melting point of pure MeS but resulted in relatively large crystals although much smaller than the MeS microstructures. The phases at the eutectic point presented a depression in the crystallization and melting points as large as 25 °C, and a microstructure with very small crystals, all desirable attributes for an improved low temperature flow. The deep eutectic in the SOO rich side was promoted by strong colligative effects. Also one can notice that close to the eutectic region where the MC dominates, the miscibility behavior was close to ideal with weak repulsive forces between unlike molecules contrary to peritectic MeS-rich side where the formation of unlike molecular pairs were favored.

A significant body knowledge encompassing different length scales in the phase development of structured TAG/FAME model mixtures, never reported before, was

developed. Furthermore, this fundamental knowledge is not specific to cold flow improver

(CFI) additives, but can be used to understand the action of other properties modifiers.

Straightforwardly, the findings can be used to formulate additive blends incorporating SOO

with judiciously selected biobased, biodiesel specific CFI structures that can substantially

improve the cold flow performance of biodiesel.

5.8   References

[1] Dunn RO, Knothe G. Alternative diesel fuels from vegetable oils and animal fats. J Oleo Sci. 2001;50(5):415-26.

[2] Erhan SZ, Dunn RO, Knothe G, Moser BR. Fuel Properties and Performance of Biodiesel. In: Hou CT, Shaw J-F, editors. Biocatalysis and Bioenergy. Hoboken, NJ: John Wiley & Sons, Inc; 2008. p. 3-58.

[3] Smith PC, Ngothai Y, Dzuy Nguyen Q, O'Neill BK. Improving the low-temperature properties of biodiesel: Methods and consequences. Renew Energ. 2010;35(6):1145-51.

[4] Lee I, Johnson L, Hammond E. Reducing the crystallization temperature of biodiesel by winterizing methyl soyate. J Amer Oil Chem Soc. 1996;73(5):631-6.

[5] Lee I, Johnson L, Hammond E. Use of branched-chain esters to reduce the crystallization temperature of biodiesel. J Am Oil Chem Soc. 1995;72(10):1155-60.

[6] Makarevičienė V, Kazancev K, Kazanceva I. Possibilities for improving the cold flow properties of biodiesel fuel by blending with butanol. Renew Energ. 2015;75(0):805-7.

[7] Wang J, Cao L, Han S. Effect of polymeric cold flow improvers on flow properties of biodiesel from waste cooking oil. Fuel. 2014;117, Part A(0):876-81.

[8] Zhang X, Rong J, Chen H, He C, Wang Q. Current Status and Outlook in the Application of Microalgae in Biodiesel Production and Environmental Protection. Front Energy Res. 2014;2:32.

[9] Ali OM, Yusaf T, Mamat R, Abdullah NR, Abdullah AA. Influence of Chemical Blends on Palm Oil Methyl Esters' Cold Flow Properties and Fuel Characteristics. Energies. 2014;7(7):4364-80.

[10] Cao L, Wang J, Liu C, Chen Y, Liu K, Han S. Ethylene vinyl acetate copolymer: A bio-based cold flow improver for waste cooking oil derived biodiesel blends. Applied Energy. 2014;132(0):163-7.

[11] Cao L, Wang J, Liu K, Han S. Ethyl acetoacetate: A potential bio-based diluent for improving the cold flow properties of biodiesel from waste cooking oil. Applied Energy. 2014;114:18-21.

[12] Ribeiro NM, Pinto AC, Quintella CM, da Rocha GO, Teixeira LS, Guarieiro LL, et al. The role of additives for diesel and diesel blended (ethanol or biodiesel) fuels: a review. Energy Fuels. 2007;21(4):2433-45.

[13] Dunn RO, Shockley MW, Bagby MO. Improving the low-temperature properties of alternative diesel fuels: Vegetable oil-derived methyl esters. J Am Oil Chem Soc. 1996;73(12):1719-28.

[14] Sorate KA, Bhale PV. Biodiesel properties and automotive system compatibility issues. Renew Sust Energ Rev. 2015;41(0):777-98.

[15] Srivastava SP, Hancsók J. Fuel Additives. Fuels and Fuel-Additives: John Wiley & Sons, Inc; 2014. p. 177-269.

[16] Liu G. Development of low-temperature properties on biodiesel fuel: a review. Int J Energ Res. 2015;DOI: 10.1002/er.3334(Published Online March 2015).

[17] Dunn RO, Ngo HL, Haas MJ. Branched-Chain Fatty Acid Methyl Esters as Cold Flow Improvers for Biodiesel. J Amer Oil Chem Soc. 2015;92(6):853-69.

[18] Knothe vG. Krahl, The biodiesel handbook. National Center for Agricultural Utilization Research Agricultural Research Service US Department of Agriculture Peoria, Illinois, USA, Department of Mechanical Engineering Iowa State University Ames, Iowa, USA, University of Applied Sciences Coburg, Germany. 2005:123-58.

[19] Chandler JE, Horneck FG, Brown GI. The Effect of Cold Flow Additives on Low Temperature Operability of Diesel Fuels. San Francisco, CA: Society of Automotive Engineers, 1992.

[20] Sern CH, May CY, Zakaria Z, Daik R, Foon CS. The effect of polymers and surfactants on the pour point of palm oil methyl esters. Eur J Lipid Sci Technol. 2007;109(4):440-4.

[21] Joshi H, Moser BR, Toler J, Smith WF, Walker T. Ethyl levulinate: A potential bio-based diluent for biodiesel which improves cold flow properties. Biomass Bioenergy. 2011;35(7):3262-6.

[22] Baker M, Bouzidi L, Narine SS. Mitigating crystallization of saturated FAMEs (fatty acid methyl esters) in biodiesel: 2. The phase behavior of 2-stearoyl diolein–methyl stearate binary system. Energy. 2015;83:647-57.

[23] Hamada H, Kato H, Ito N, Takase Y, Nanbu H, Mishima S, et al. Effects of polyglycerol esters of fatty acids and ethylene-vinyl acetate co-polymer on crystallization behavior of biodiesel. Eur J Lipid Sci Technol. 2010;112(12):1323-30.

[24] Shrestha DS, Van Gerpen J, Thompson J. Effectiveness of cold flow additives on various biodiesels, diesel, and their blends. Transactions of the ASABE. 2008;51(4):1365-70.

[25] Christensen SA, DiBiase SA, Rizvi SQA. Cold flow additives. In: EPO, editor. C10L 1/19 (2006.01); C10L 1/224 (2006.01) ed2012.

[26] Bentley PH, McCrae W. Efficient synthesis of symmetrical 1,3-diglycerides. J Org Chem. 1970;35(6):2082-3.

[27] Chandran DV, Bhatnagar RK. A method for synthesis of α-monoricinolein. J Amer Oil Chem Soc. 1968;45(8):581-2.

[28] Chiavaro E. Differential Scanning Calorimetry: Applications in Fat and Oil Technology: Taylor & Francis, 2014.

[29] Hildebrand JH. Solubility XII. Regular solutions. J Am Chem Soc. 1929;51:66-80.

[30] Bragg WL, Williams EJ. The effect of thermal agitation on atomic arrangement in alloys. Proc R Soc. 1934;145(855):699-730.

[31] Abes M, Bouzidi L, Narine SS. Crystallization and phase behavior of 1,3-propanediol esters II. 1,3-Propanediol distearate/1,3-propanediol dipalmitate (SS/PP) and 1,3-propanediol distearate/1,3-propanediol dimyristate (SS/MM) binary systems. Chem Phys Lipids. 2007;150(1):89-108.

[32] Abes M, Bouzidi L, Narine SS. Crystallization and phase behavior of fatty acid esters of 1,3 propanediol III: 1,3 propanediol dicaprylate/1,3 propanediol distearate (CC/SS) and 1,3 propanediol dicaprylate/1,3 propanediol dipalmitate (CC/PP) binary systems. Chem Phys Lipids. 2008;151(2):110-24.

[33] Boodhoo MV, Bouzidi L, Narine SS. The binary phase behavior of 1,3-dicaproyl-2-stearoyl-*sn*-glycerol and 1,2-dicaproyl-3-stearoyl-*sn*-glycerol. Chem Phys Lipids. 2009;157:21-39.

[34] Boodhoo MV, Bouzidi L, Narine SS. The binary phase behavior of 1, 3-dipalmitoyl-2-stearoyl-sn-glycerol and 1, 2-dipalmitoyl-3-stearoyl-sn-glycerol. Chem Phys Lipids. 2009;160(1):11-32.

[35] Boodhoo MV, Kutek T, Filip V, Narine SS. The binary phase behavior of 1,3-dimyristoyl-2-stearoyl-sn-glycerol and 1,2-dimyristoyl-3-stearoyl-sn-glycerol. Chem Phys Lipids. 2008;154(1):7-18.

[36] Höhne G, Hemminger W, Flammersheim H-J. Differential scanning calorimetry. 2nd ed ed. Berlin, Heidelberg, New York: Springer–Verlag; 2003. p. 298.

[37] Lee AG. Lipid Phase-Transitions and Phase-Diagrams .2. Mixtures Involving Lipids. Biochim Biophys Acta. 1977b;472(3-4):285-344.

[38] MacNaughtan W, Farhat I, Himawan C, Starov V, Stapley A. A differential scanning calorimetry study of the crystallization kinetics of tristearin-tripalmitin mixtures. J Amer Oil Chem Soc. 2006;83(1):1-9.

[39] Lee AG. Lipid Phase-Transitions and Phase-Diagrams .1. Lipid Phase-Transitions. Biochim Biophys Acta. 1977a;472(2):237-81.

[40] Tenchov BG. Non-uniform lipid distribution in membranes. Prog Surf Sci. 1985;20(4):273-340.

[41] Larsson K. Physical Properties - Structural and Physical Characteristics. In: Gunstone FD, Harwood JL, Padley FB, editors. The Lipid handbook. London: Chapman and Hall; 1986. p. 335-77.

[42] Ghotra BS, Dyal SD, Narine SS. Lipid shortenings: a review. Food Res. Int. 2002;35(10):1015-48.

[43] Timms RE. The Confectionary Fats Handbook: Properties, Production, and Application. Chapter 2: Physical Chemistry. Bridgewater, England: The Oily Press, 2003.

[44] Fahey DA, Small DM, Kodali DR, Atkinson D, Redgrave TG. Structure and polymorphism of 1,2-dioleoyl-3-acyl-*sn*-glycerols - 3-layered and 6-layered structures. Biochem. 1985;24(14):3757-64.

[45] Mykhaylyk OO, Smith KW, Martin CM, Ryan AJ. Structural models of metastable phases occurring during the crystallization process of saturated/unsaturated triacylglycerols. J Appl Crystallogr. 2007;40(s1):s297-s302.

[46] Dorset D. The crystal structure of waxes. Acta Crystallogr, Sect B: Struct Sci. 1995;51(6):1021-8.

[47] Dorset DL. From waxes to polymers - crystallography of polydisperse chain assemblies. Struct Chem. 2002;13(3):329-37.

[48] Mykhaylyk OO, Martin CM. Effect of unsaturated acyl chains on structural transformations in triacylglycerols. Eur J Lipid Sci Technol. 2009;111(3):227-35.

[49] Bouzidi L, Tessier MJ, Narine aSS. Time and Temperature – resolved phase trajectories of stearic and oleic acid tags during non-isothermal crystallization. 2015.

[50] Norris R. the Physical Properties of Triacyglycerols in Relation to Milk Fat: Massey University, 1977.

[51] Baker M, Bouzidi L, Garti N, Narine S. Multi-Length-Scale Elucidation of Kinetic and Symmetry Effects on the Behavior of Stearic and Oleic TAG. II: OSO and SOO. J Amer Oil Chem Soc. 2014;91(10):1685-94.

[52] Inoue T, Hisatsugu Y, Ishikawa R, Suzuki M. Solid–liquid phase behavior of binary fatty acid mixtures: 2. Mixtures of oleic acid with lauric acid, myristic acid, and palmitic acid. Chem Phys Lipids. 2004;127(2):161-73.

[53] Costa MC, Rolemberg MP, Boros LAD, Krähenbühl MA, de Oliveira MG, Meirelles AJA. Solid−Liquid Equilibrium of Binary Fatty Acid Mixtures. J. Chem. Eng. Data. 2006;52(1):30-6.

[54] Inoue T, Hisatsugu Y, Yamamoto R, Suzuki M. Solid–liquid phase behavior of binary fatty acid mixtures: 1. Oleic acid/stearic acid and oleic acid/behenic acid mixtures. Chem Phys Lipids. 2004;127(2):143-52.

6.   Mitigating Crystallization of Saturated FAMES in Biodiesel: 5. The Unusual Phase Behavior of a Structured Triacylglycerol Dimer and Methyl Palmitate Binary System[5]

6.1   Introduction

The increasing demand for energy is fuelled by population growth, modernization and rapid development in many countries. The search for sustainable alternatives to fossil fuels is due to the finite nature of petroleum and environmental concerns over petroleum usage and related escalating climate change [1]. Biodiesel is currently considered as a sustainable alternative fuel and is increasingly used worldwide [2]. Biodiesel is generally produced by the transesterification of vegetable oil or animal fats with an alcohol in the presence of an acid or alkali catalyst [3]. It is mainly composed of saturated and unsaturated mono-alkyl fatty acid esters, mainly methyl oleate (MeO), methyl linoleate (MeL), methyl stearate (MeS) and methyl palmitate (MeP).

Biodiesel has low toxicity and is readily biodegradable and non-flammable, making it safe to store and handle. Compared to conventional fuels, biodiesel has lower smoke opacity, polycyclic aromatic hydrocarbon and other regulated emissions [4-7]. The most

---

challenging problems associated with biodiesel are its poor long-term storage stability characteristics and poor performance in cold conditions [8]. Its high cloud point (CP) and pour point (PP) can lead to fuel starvation and result in engine failure during cold conditions. For example, the cloud point and pour point of soybean-based methyl esters, the most common biodiesel in the United States of America, are ~ 0 °C and ~ -5 °C, respectively [9]. As overnight temperatures during three seasons of the year can fall into this range, the saturated fatty acid methyl esters (FAMEs) present in the biodiesel nucleate and form crystals in the fuel [10].

Several approaches have been tested to modify commercial biodiesel so as to improve its cold flow properties, including additives, feedstock and biodiesel modification such as winterization, and blending with conventional diesel fuel or with FAMEs which have low crystallization temperature [11-13]. Branched chain esters and bulky substituents in the chains have also been suggested to improve the cold flow properties of biodiesel [14, 15].

The crystallization of biodiesel at low temperatures is primarily due to the high melting point of its saturated FAMEs [16]. The removal of these compounds from biodiesel may be a way to reduce the crystallization temperature. However, the process is non-trivial and expensive [4]. It also significantly decreases the oxidative stability and cetane number [17], and further worsens the combustion performance and exhaust emissions of the biodiesel [10, 18]. The current most popular approach is the use of additives to suppress the crystallization and lower the rate of nucleation and/or crystal growth [13]. The additive is usually designed to disrupt the arrangement of the linear saturated FAMEs [19]. The changes in the crystallization behavior of biodiesel due to the

additives can be appreciated at different length scales through the modification introduced to the crystal structure, polymorphism, and microstructure.

The present work was motivated by promising cold flow results obtained with self-metathesized soybean oil (MSBO) additives to commercial biodiesel [20]. It was observed that MSBO stripped of olefins depresses the onset of crystallization of methyl soyate (biodiesel) at loadings as low as 1%. The compounds in MSBO responsible for this behaviour were unclear, as was the mechanism. A number of approaches were therefore utilized to determine the compounds in MSBO responsible for this behaviour and to provide an understanding of the underlying mechanism. GPC, HPLC and MS methods were developed for analysing MSBO compositions. Families of compounds present in MSBO and a large number of pure molecules of MSBO were tested on biodiesel and the most effective compounds were determined. The constituent "molecular families" of MSBO as well as and a series of model compounds representing the constituents prevalent in metathesized soybean oil were tested in order to determine the structures most effective in depressing crystallization onset [21]. TAGs with two unsaturated and a saturated/*trans*-fatty acids and their oligomers were found to be highly effective in depressing onset of crystallization with the most effective stereospecificity being when the *trans-/saturated* fatty acid is at the *sn*-2 position. It was hypothesized that these compounds, because of their particular structure and conformation, disrupts the regular packing of the linear saturated FAMEs, thereby delaying nucleation and mitigating crystal growth.

Phase behavior studies of model binary systems made of the pure molecules that most depressed the crystallization of commercial biodiesel and the two major saturated FAMEs of common biodiesel (MeS and MeP) were therefore conducted to uncover the fundamental

mechanisms of disruption of the packing of the saturated FAMEs and to examine the extent to which it can delay nucleation and affect crystal growth and crystal size, and consequently the transformation behavior of biodiesel. (E)-1-(1-(oleoyloxy)-3-(stearoyloxy)propan-2-yl)18-(1-(oleoyloxy)-3-(stearoyloxy) propan-2-yl) octadec-9-enedioate (D), the dimer of the present work is an oligomer of unsaturated TAG, found to be particularly effective in lowering the crystallization temperature of commercial biodiesel [21]. Its effect was also puzzling as the addition of 1% by wt. of D into biodiesel depressed the crystallization onset temperature by 2.8 °C whereas 4% by wt. depressed it by 1.7 °C only. The hypothesis was that the chemical structure of D (shown in Scheme.6.1) would explain this behavior. As can be seen in Scheme 6.1, the structure of D has two saturated moieties similar to MeP and *cis-* double bonds in two of its carbon chains that can provide a structural element that would promote an initiation of packing with the straight FAME, and another that would prevent further crystallization due to the steric hindrance presented by the two kinked chains, which would explain its general effectiveness, but is also large enough to behave somehow like a small polymer additive, a feature that would explain its higher effectiveness at small loading compared to high concentration [22, 23].

The TAG dimer, is interesting as it is a component of the metathesis of vegetable oil, a reaction that is increasingly used to produce fine chemicals and modified triacylglycerol (TAG). The self-metathesis of TAGs, such as soybean oil, results in a complex mixture comprising linear oligomers (from dimer to pentamer), macrocyclic structures, cross-linked polymers, as well as trans-/cis isomers [24]. The actual composition of a metathesis product is highly dependent on the reaction conditions, such as such as starting materials, temperature, type of catalyst, etc., giving the possibility to control the product composition

[25-28]. The catalysts used for the self-metathesis of soybean oil were Grubbs' catalysts. Grubbs' Catalysts are a series of transition metal carbene complexes. MSBO was composed of 6% olefins, and oligomers of the TAG structures of the natural oil, soybean oil (8% monomers, 30% dimers, 50% trimers and quatrimers and 2% of other higher level oligomers) [21]. The compounds have saturated fatty acids (~14% in total) as well as unsaturated fatty acids in the cis- and trans- configuration with a trans-/cis ratio from 4.4 to 8.
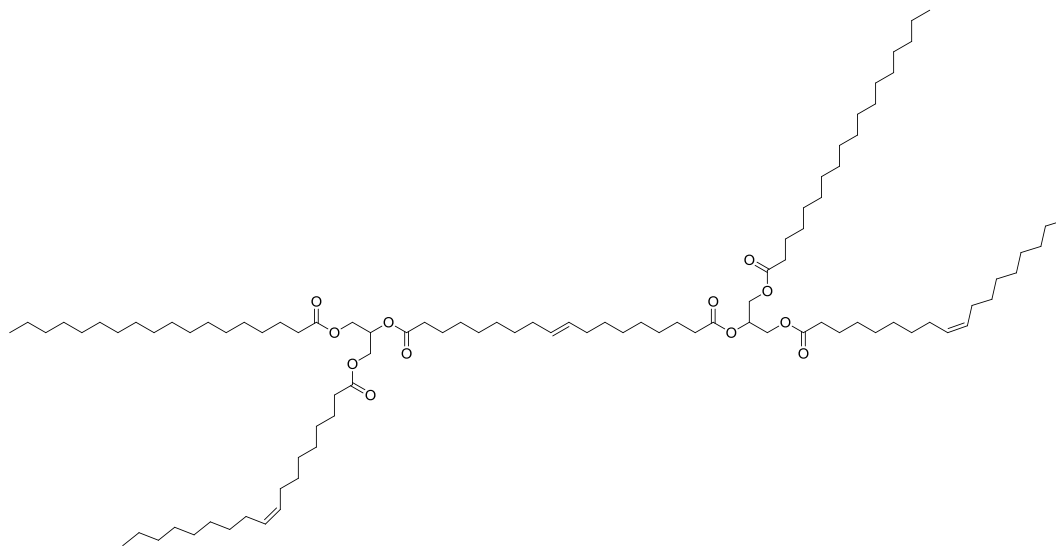
Scheme 6.1. Structure of the dimer (D), IUPAC name: (E)-1-(1-(oleoyloxy)-3-(stearoyloxy) propan-2-yl) 18-(1-(oleoyloxy)-3-(stearoyloxy) propan-2-yl) octadec-9-enedioate.

To the best of our knowledge, no such feedstock nor any oligomer of TAG has been studied or applied as a cold flow modifier to biodiesel. Ozonized soybean oil, a transformed vegetable oil, was tried as a cold flow additive, but failed to improve the cold flow properties of biodiesel [29], outlining the limits of a serendipitous approach to searching for effective additives of biodiesel.

The thermal transformation properties of thirteen (13) D/MeP mixtures were investigated using differential scanning calorimetry (DSC). Crystal structure and microstructure of selected mixtures were examined by X-ray diffraction (XRD) and polarized light microscopy (PLM), respectively.

6.2   Materials and Methods

6.2.1   Materials

Methyl palmitate (MeP) purchased from Sigma-Aldrich (Oakville, Ontario) at a claimed purity of 96% was further purified in our laboratory to a purity greater than 99%. The purity of MeP was determined by GC-FID. The sample was run as is in chloroform, using a Zebron Capillary (ZB-5HT Inferno) Column (Phenomenex, Torrance, CA, USA). The dimer (D) was synthesized in our laboratory (see section 2.3.) with a purity of more than 99%. The purity of D was determined by a Waters Alliance (Milford, MA) e2695 HPLC system fitted with a Waters ELSD 2424 evaporative light scattering detector.

N, N'-dicyclohexylcarbodiimide (DCC), 4-dimethylaminopyridine (DMAP), stearoyl chloride (98%), Grubbs generation II catalyst and sodium borohydride were purchased from Sigma-Aldrich. 2,3- dihydroxypropyl oleate and 1,18-otadec-9-enedioic acid were prepared in our laboratory as reported in a previous work [30]. Chloroform was purified by distillation over calcium hydride.

D and MeP were mixed in the desired molar fractions then melted and homogenised using a mechanical stirrer. Special care was taken for the overall handling and storage (0 °C) of the samples. The molar fractions, X_D, used are 0, 0.025, 0.05, 0.1, 0.2, 0.3, 0.40, 0.50, 0.60, 0.70, 0.80, 0.90 and 1.00.

6.2.2 Nuclear Magnetic Resonance (^{1}H- and ^{13}C-NMR)

One dimensional ^{1}H- and ^{13}C-NMR spectra were recorded on a Bruker Advance III 400 spectrometer (Bruker BioSpin MRI GmbH, Karlsruhe, Germany) at a frequency of 400 MHz and 100 MHz respectively, using a 5 mm BBO probe. ^{1}H-NMR Spectra were acquired at 25 ℃ over a 16-ppm spectral window with a 1 s recycle delay, 32 transients. ^{13}C-NMR spectra were acquired at 25 ℃ over a 240-ppm spectral window with a 0.2 s recycle delay, 2048 transients. Both NMR spectra were Fourier transformed, phase corrected, and baseline corrected. Window functions were not applied prior to Fourier transformation. Chemical shifts were referenced relative to residual solvent peaks.

6.2.3 High Performance Liquid Chromatography (HPLC)

HPLC was carried out on a Waters Alliance (Milford, MA, USA) e2695 HPLC system fitted with a Waters ELSD 2424 evaporative light scattering detector. The HPLC system includes an inline degasser, a pump and an auto-sampler. The temperature of the column (C18, 150mm × 4.6 mm, 5.0 μm, X-Bridge column, Waters Corporation, MA, USA) was maintained at 35 °C by a Waters Alliance column oven. The ELSD nitrogen flow was set at 25 psi with nebulization and drifting tubes maintained at 12 ℃ and 55 ℃, respectively. Gain was set at 500. The mobile phase was chloroform: acetonitrile (50:50)v run for 30 min at a flow rate of 0.2 mL/min. 1 mg/mL (w/v) solution of sample in chloroform was filtered through single step filter vial from Thomson Instrument Company (Oceanside, CA, USA) and 0.5 mL of sample was passed through the C18 column by reversed- phase in isocratic mode. All solvents were HPLC grade and obtained from VWR International (Mississauga, ON, Canada).

6.2.4 Differential Scanning Calorimetry

A Q200 model DSC (TA Instruments, New Castle, DE) was used to investigate the thermal properties of the samples. The DSC measurements were carried out under a nitrogen flow of 50 mL/min. Samples of approximately 0.3 to 0.5 (± 0.1) mg in a hermetically sealed aluminum DSC pan were subjected to the same thermal protocol to allow for comparison. The sample was first equilibrated at 90 °C for 10 min, a temperature and a time over which crystal memory was erased, then cooled with a constant rate (1 K/min) down to -90 °C, point at which the crystallization was deemed complete. The sample was held at -90 °C for 10 min then reheated to 90 °C at the same rate of 1.0 K/min to obtain the melting profiles. All measurement temperatures are reported to a certainty of better than ± 0.5 °C. The "TA Universal Analysis" software together with a method developed by our group [31] was used to analyze the data and extract the main characteristics of the peaks (peak temperature, T_p; onset temperature, T_{On}; offset temperature, T_{Off}; enthalpy, ΔH; and full width at half maximum, FWHM). The temperature window over which a thermal event occurs is defined as the absolute value of the difference between T_{Off} and T_{On} of that event. The positions of non-resolved thermal events were estimated using the first and second derivatives of the differential heat flow, and their other characteristics were simply estimated using the software elements.

6.2.5 Polarized Light Microscopy

A polarized light microscope, PLM, (Leica DM2500P, Leica Microsystems, Wetzlar, Germany) fitted with a Leica digital camera (DFC420C) was used for image capture. A Linkam LS 350 temperature – controlled stage (Linkam Scientific Instruments, Tadworth, Surrey, UK) fitted to the PLM was used to process the samples. A small droplet of material

was carefully pressed between a preheated glass microscope slide and cover-slip ensuring a uniform thin layer of sample. The sample was melted at 90 ºC for 10 min to erase all crystal memory then cooled at 1 K/min down to -90 °C. Time resolved images (0.5 min or 0.5 °C) were taken at 500X magnification starting from the liquid state until the crystallization was complete. Images of the fully crystallized material were recorded at 50X, 100X and 500X magnification.

6.2.6   X-Ray Diffraction

A Panalytical Empyrean x-ray diffractometer (PANalytical B.V., Lelyweg, The Netherlands) equipped with a filtered Cu- K_α radiation source ($\lambda = 0.1542$ nm) and a PIXcel^{3D} detector was used in line-scanning mode (255 lines over 3.347° wide detector). The XRD patterns were recorded between 1.2 and 70° (2θ) in 0.0131° steps, at 45 kV and at 40 mA. The procedure was automated and controlled by PANalytical's Data Collector (V 3.0c) software. The samples were processed in the XRD chamber using the 700 Series Cryostream Plus cooling system (Oxford Cryosystems, Oxford, UK) fitted to the diffractometer. The sample was heated to 90 °C, hold at that temperature for 10 min to delete all crystal memory then cooled down to -60 °C at 1 K/min. The temperature was controlled to better than ± 0.5°C. The data were processed and analyzed using X'Pert HighScore V3.0 software (PANalytical). We refer to the range $2\theta = [0.3 - 15]$° and [15 - 70]° as the small- and wide-angle x-ray diffraction regions (SAXD and WAXD), respectively.

6.2.7   Synthesis and Characterization of the Dimer

The synthesis route of the D is shown in Scheme 6.2. D was prepared from 1-oleyol-3-stearoyl-2-hydroxyl propane (**2**) and 1,18-Otadec-9-enedioic acid (**3**).   1-oleyol-3-

stearoyl glycerol (**2**) was synthesized from 2,3- dihydroxypropyl oleate (**1**) and stearoyl chloride in the presence of pyridine.
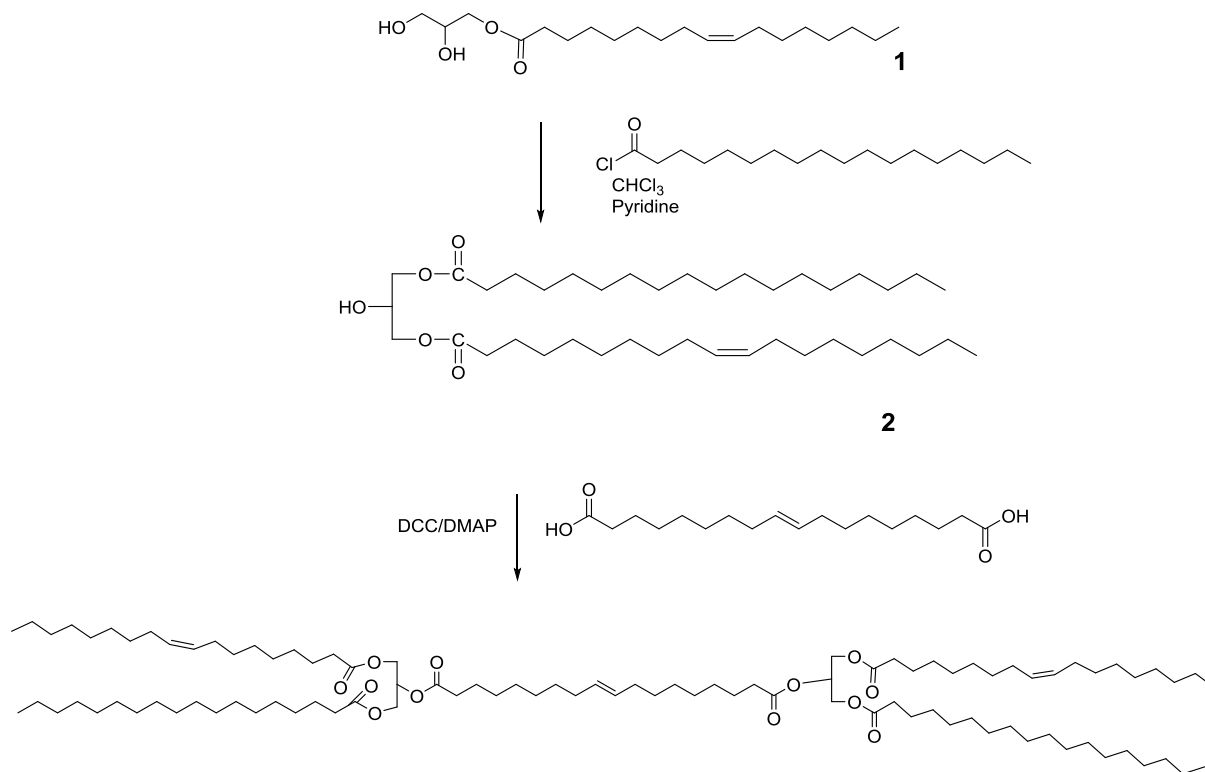
Scheme 6.2. Synthesis route of (E)-1-(1-(oleoyloxy)-3-(stearoyloxy)propan-2-yl) 18-(1-(oleoyloxy)-3-(stearoyloxy)propan-2-yl) octadec-9-enedioate (D)

To a solution of (32.4 mmol) 2,3- dihydroxypropyl oleate (**1**) in 200 mL chloroform, stearoyl chloride (32.4 mmol) was added. Then (48.6 mmol) pyridine was added to the reaction solution drop-wise. The reaction mixture was stirred at room temperature overnight. The reaction mixture was diluted with another 160 mL chloroform. The organic layer was washed with water (3×300 mL), followed sequentially by 5% HCl (2×300 mL), water (2×300 mL), 4% NaHCO$_3$ (2×300 mL), and then water (3×300 mL). The organic

layer was dried on Na_2SO_4. After chloroform was removed, the residue was purified by column chromatography with hexanes/ethyl acetate=20:1. The yield was 73%.

6.2.8 Synthesis of (E)-1-(1-(oleoyloxy)-3-(stearoyloxy)propan-2-yl)18- (1-(oleoyloxy)-3-(stearoyloxy)propan-2-yl) octadec-9-enedioate (dimer)

To a solution of (1 mmol) 1-oleyol-3-stearoyl-2-hydroxyl propane (**2**) and (1 mmol) diacid in 10 mL $CHCl_3$ under the protection of N_2, 0.2 mmol DMAP was added, followed by 1.2 mmol DCC. The reaction was carried out at room temperature overnight. The precipitated dicyclohexylurea was removed by filtration. The organic phase was diluted with 10 mL chloroform, then washed sequentially with water (3×20 mL), 4% aqueous $NaHCO_3$ (2×200 mL) and brine (3×200 mL), and then dried over Na_2SO_4. After filtration, the filtrate was concentrated using a rotary-evaporator, and the residue was purified by column chromatography with ethyl acetate / hexanes =1:20. The yield was 70.9% and purity was 99.9%.

6.3 Results and Discussion

6.3.1 Crystal Structure

The WAXD and SAXD spectra of the mixture with $X_D = [0, 0.10]$, 0.50_D and MeP are shown in Fig. 6.1a and Fig. 6.1b, respectively. The relevant d-spacing and Miller indices are reported in Table 6.1. One can see that only the orthorhombic form (β'-polymorph) was detected as shown unmistakably by its characteristic $(\bar{1}10)$ and (200) reflections (Table 6.1). The appearance of a doublet (4.04 Å (020) and 4.10 Å $(\bar{1}10)$-lines) for the mixtures with $X_D \leq 0.10$ indicates that more than one β'- phase were involved in the crystallization process.
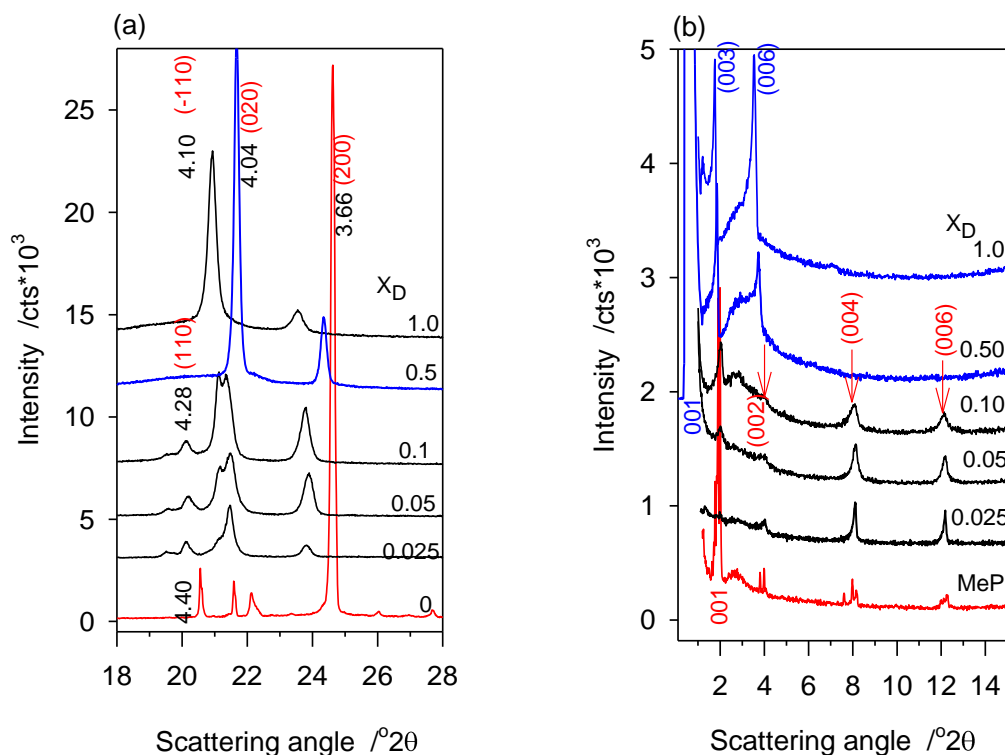
Figure 6.1. (a) Wide angle x-ray diffraction (WAXD) and (b) small angle x-ray diffraction (SAXD) spectra of the mixture with $X_D \leq 0.10$, 0.50_D and MeP.

As can be seen in Fig. 6.1a, the MeP phase as represented by the intensity of its signature peak (4.40 Å) almost disappeared as soon as D was added. The 4.40 Å peak decreased sharply and retained only a 10th of its initial value for the 0.025_D mixture. It remained very weak for the mixtures measured and did not appear for D nor for 0.50_D, indicating that a very small pure MeP phase persisted only in the mixtures with the lowest D content. The disappearance of the MeP phase was confirmed by the similar and more dramatic decrease, if not disappearance, of the most intense reflection of pure MeP (line 3.67 Å, Fig. 6.1a). This peak was 40 times stronger than the (200) peak observed at 3.65 Å in mixtures containing D ($X_D \geq 0.025$). This indicates that despite being close, the two

peaks did not originate from the same phase. The latter is obviously tied principally to phases involving D. A very small MeP phase, however, may still be present with a very weak superimposed peak.

The intensity of the (200) peak increased practically exponentially from 0.025_D to 0.10_{D3} and then dropped to a third of its value, indicating that it originated from a D phase. The 4.28 Å-line which appeared for the D/MeP mixtures but not for any of the pure components, increased exponentially with increasing D, and supporting the presence of an increasing D/MeP mixed phase. The intensity of both the 4.04 Å- and 4.10 Å-peaks increased with increasing X_D but at a different rate. The intensity of 4.04 Å (020) increased much more rapidly than 4.10 Å $(\overline{1}10)$ and did not appear for D. The 4.10 Å line increased exponentially to a reach a maximum for D ($R^2= 0.9958$; critical D molar ratio of 0.30). The peculiar variation of these two lines as a function of X_D provides further support for the presence of a D/MeP mixed phase in the mixtures having a D molar ratio lower or equal to 0.10. It indicates that while the 4.10 Å line may be associated with a D family of planes, the 4.04 Å originated from a mixed phase, adequately located at the (020) position, i.e., the centre of the subcell.

The repeat unit of the chain packing of D ($d_{001}= 149.10$ Å) and all mixtures with $X_D > 0.10$ is 3 times larger than those obtained for mixtures with $X_D < 0.10$. This length can accommodate 3 dimers stacked along the c- axis. The fact that only the odd harmonics were presented indicates that the packing was different from what was initiated by MeP and suggests that units of D/MeP were the building blocks of the crystal structure.

Table 6.1. Wide- and small-angle x-ray diffraction data. Miller indices are those of the orthorhombic crystal structure (β'-form).

X_D		(110)	$(\bar{1}10)$	(020)	(200)
0.0	4.39		4.08	4.06	3.67
0.025	4.42	4.28	4.09	4.03	3.65
0.05	4.39	4.27	4.09	4.03	3.64
0.10	4.39	4.29	4.09	4.04	3.65
	4.40 ± 0.01	4.28 ± 0.01	4.09 ± 0.01	4.03 ± 0.01	3.65 ± 0.01
0.50	NA	NA	4.10	NA	3.66
1.0	NA	NA	4.13	NA	3.68

X_D		001	002	004	006
0.0		43.99	21.81	10.88	7.25
0.025		42.96	21.85	10.88	7.25
0.05		43.86	21.95	10.88	7.27
0.10		43.19	22.30	10.95	7.29
	Average	43.50 ± 0.51	21.98 ± 0.22	10.89 ± 0.03	7.26 ± 0.01
	001	003	006	0012	--
0.50	142.71	47.26	23.60	--	--
1.0	149.10	49.50	24.85	12.47	--

6.3.2 Crystallization Behavior

The DSC cooling thermograms are displayed in Fig. 6.2 (a, b & c). The corresponding characteristic temperatures are presented in Fig. 6.2d. The thermograph of pure MeP showed one main peak at ~24 °C (P1 in Fig. 6.2a,b & c) indicating a single phase transition, whereas pure D presented two relatively large peaks at ~ 16 °C and 13 °C, and

a small peak at ~-7 °C, indicative of a longer crystallization process with successive phase transitions. The addition of D to MeP was marked by an obvious extra peak at the high temperature side (P2, Fig. 6.2a) and twin peaks (P3 and P4, Fig. 6.2c) at the low temperature side of the thermograms. Note that between P1 and P2 a resolved peak appeared for the 0.10_D and 0.20_D mixtures, and at least one non-resolved peak can be observed for the other mixtures. As D concentration was increased, P1 shifted to lower temperature, dramatically first (-69.9 ± 23.1 K/mol) to 17.20 ± 0.05 °C at $X_D = 0.15$, then very gradually (-1.2 ± 0.1 K/mol) to 16.16 ± 0.07 °C for $X_D = 1.0$ (Fig. 6.2d). A similar trend was observed for the small twin peaks P3 and P4. Obviously, the effect of D on the onset of crystallization was optimum at the low 0.15_D concentration. The peak appearing closest to the MeP exotherm (P2 in Fig. 6.1a & b) grew larger and closer to P1 up 0.15_D at which point it shifted back to lower temperature.

A plot of the enthalpy of the individual peaks (Fig. 6.2e) presented a typical Tamman triangle with a base spanning from $X_D = 0$ to 0.30 and an edge at ~ $X_D = 0.15$, indicating the occurrence of a particular reaction, possibly a eutectic transformation. The same plot shows two other singularities at X_D ~ 0.40 and X_D ~ 0.75 (arrows in Fig. 6.2d), which may be related to particular reactions. The enthalpy of the twin peaks (P3 and P4) also presented Tamman – like plots (not shown) with the triangle peaking at $X_D = 0.30$ for both exotherms, indicating that the reactions implicating the low temperature phases of D are different from those involving the phases at higher temperature.
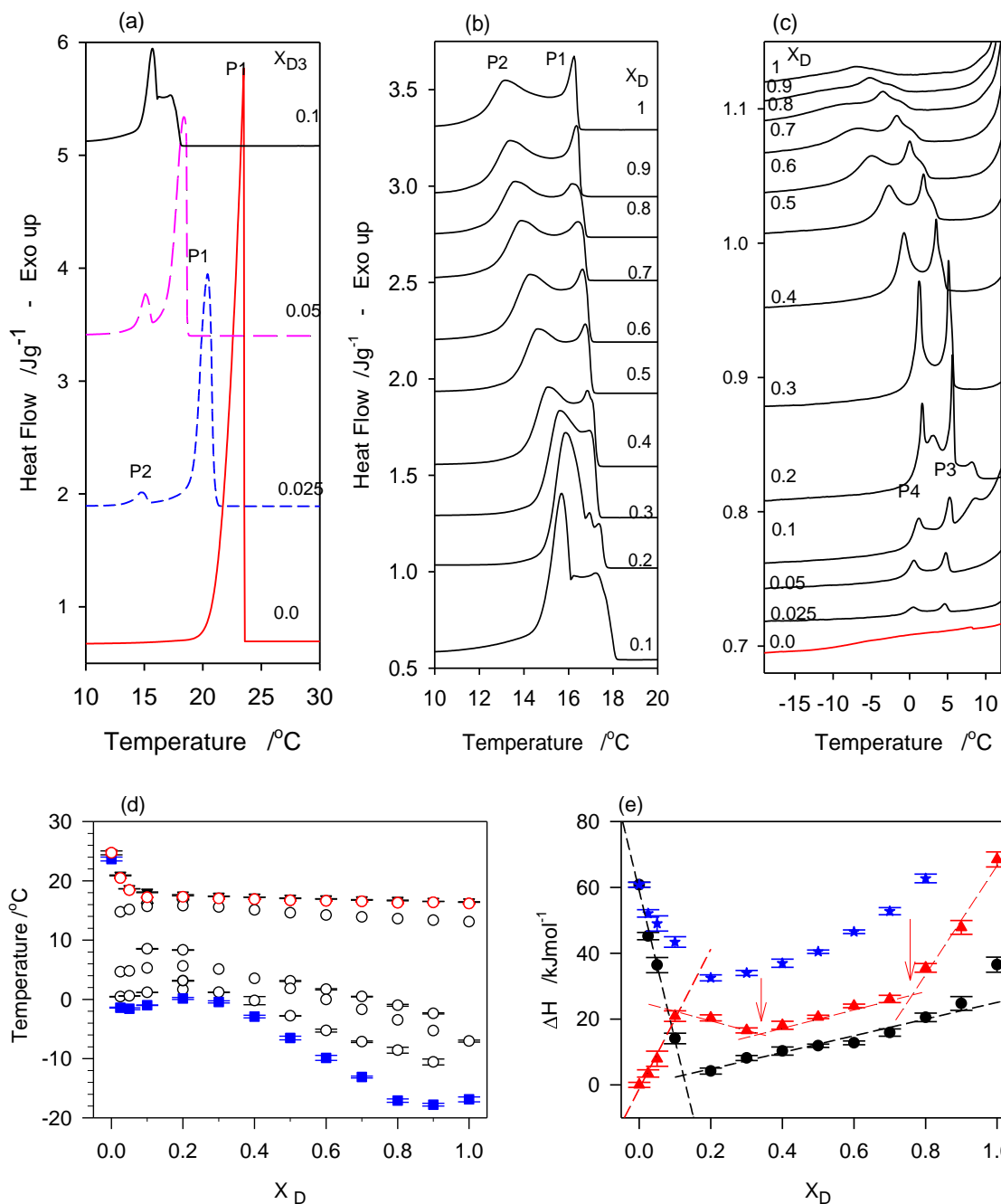
Figure 6.2. (a, b and c) Cooling (1 °C /min) thermograms of D/MeP mixtures; (d) corresponding characteristic transition temperatures (▼: Onset temperature of crystallization (T_{On}), ○: peak Temperature (T_P), ■: Offset temperature of crystallization (T_{Off}), (e) Enthalpy of crystallization of peaks P1 (●, ΔH_1), P2 (▲, ΔH_2) and total enthalpy of crystallization (★, ΔH_c)

Because D presented only one of these peaks, one can confidently affirm that at least one of the twin peaks, if not both, is associated with a mixed D/MeP phase. It is interesting to note that even if the peak positions of the D thermogram are slightly shifted to higher temperature with increasing MeP content, the overall shape of the thermogram of D did not change dramatically up to 0.10_D, as if MeP molecules merged within this oligomer by packing on its different branches. A possible scenario for the crystal packing for the D-rich mixtures is the alignment of MeP with the saturated branches and with the C18 *trans*-bridge of the D, yielding a relatively loose buildup of D-MeP units, carrying 1 to 3 MeP straight chains each. The relative diversity of these units while allowing for a slight change in crystallization temperature would not change the overall transformation path of the D molecules. It appears as if D was associated with the MeP molecules starting from the melt to form the phases of the mixture with D concentrations higher than 15%. This parasitic – like association must have been initiated in the liquid phase promoted by unhindered D chain rotations, and favorable mass transfer for easy MeP diffusion.

The drastic change in the temperature of P1 (MeP peak) that was observed for the mixtures having a concentration of D between 0.00 to 0.2 indicates that the two *cis*-branches of D perturbed the packing of MeP as soon as there was not enough D molecules to accommodate all the MeP chains in straight moieties. This is attributable to a growing tendency of the MeP molecules to form lamellae rather than associate with D, due to mean free path considerations. Note that the shape of the thermograms of the 0.10_D and 0.20_D mixtures are also reminiscent of D, suggesting that the D/MeP "parasitic" association was ongoing for some of the D molecules even at low MeP content. The competition between MeP lamellae formation and MeP-D association mechanisms seems to have been most

active for the mixtures between 0.10_D and 0.40_D, included, as suggested by the relative changes observed in the shape of P1 and P2, and the thermal events observed between them.

The peculiar variation of the intensity of the different peaks show that such a packing is possible. MeP may be the interstitial molecule that is probed by the (020) reflection of the orthorhombic cell, the only crystal form detected by XRD for all the mixtures. Furthermore, the value of the (001) d-spacing (50 Å) for D and the D- rich mixtures can account for the packing of the units made of the "associated" MeP in D. The peculiar variation of the intensity of the 4.04 Å and 4.10 Å peaks in the [0.00 to 0.2] concentration range may be related to the balance between MeP lamellar formation and MeP-D association.

6.3.3   Melting Behavior and Phase Development

The heating thermograms of the D/MeP binary system are relatively complex (Fig. 6.3a, b, c & d). The phase development inferred from the heating cycles depended strongly on D concentration and mirrored fully the cooling cycles. As clearly illustrated by the heating thermogram of the 0.025_D mixture (Fig. 6.3a), several extra thermal events appeared as soon as D was added to MeP. Overall, one can single out three major endothermic events between 10 and 35 °C (P1, P2 and P3 in Fig. 6.3b). The melting peak of pure MeP (P1 of curve 0.0 in Fig. 6.3a) decreased dramatically with increasing D concentration and disappeared for mixtures with $X_D > 0$. P2 appeared for all mixtures containing D; whereas, P3 was only observed for 0.30_D and D-richer mixtures. Also, similarly to the cooling thermograms, twin peaks are observed in the heating thermograms

(P3 and P4 in Fig. 6.3c). These are probably the recording of the melting of the low temperature phases that are associated with the twin exotherms observed in the cooling cycles (P3 and P4 in Fig. 6.2c).

The endotherm P1 was followed by a wide exothermic peak centered at ~25.24 ± 0.86 °C in the mixtures with $X_D \geq 0.10$ (Fig. 6.3d). The exotherm was followed by two endotherms having exactly the same total enthalpy (Fig. 6.3f). This indicates that two separate phases of higher stability have recrystallized from the melt. Because of their close melting temperatures, the recrystallized phases are probably in the same crystal form but made of different constituents. The nature and composition of these two phases have not been determined here as they are out of the scope of the study.

The complexity of the transformation behavior of the D/MeP binary system is well represented by the phase diagram constructed using the peak temperature of the resolved peaks of the heating cycles (Fig. 6.3e). The liquidus line in the phase diagram as represented by T_{Off} of melting is highly unusual. It displays a minimum at 0.05_D suggesting an apparent eutectic and a singularity at 0.40_D. It also presents two plateaus (T_{off} ~ 35.9 °C from 0.15_D to 0.30_D and T_{off} ~ 43.4 °C from 0.50_D to 0.70_D) and a linear increase for the D- richer mixtures. Each plateau is a liquid-solid transformation line representing the melting of the same crystal phase, probably with the same constituents. The jumps in melting temperature observed at 0.10_D, 0.40_D and 0.70_D indicates a stepped increase in the stability of the available crystal forms. These data show that phases with well-defined stablility are available in well-defined D/MeP concentration ranges. The discontinuous levels of stability of the phases available for the D/MeP system is a strong

indicator of the inertia of the bulky D. The increase in phase stability with increasing D content, particularly for mixture with $X_D > 0.70$, stresses that D is the ultimate driver of the phase behavior of the D/MeP binary system.

The kinetic phases of this binary system can be located below the offset temperature of melting (T_{off1}, ▼ in Fig. 6.3e) of the main melting peaks (P2 and P3 in Fig. 6.3a, b, c & d). As can be seen in Fig. 6.3e, the melting temperature of these phases decreased gradually until the 0.50_D mixture where it plateaued. Note that T_p of the peaks below T_{off1} also plateaued at 0.50_D. The transformations described by these peaks are solid-solid transformations which can be explained by the relatively easier diffusion of MeP molecules compared to the bulky D. The plateau observed after the 50% mixture may be related to a dramatic limitation of this diffusion due to increased interaction hindrances by D.

The enthalpy of P1 decreased very dramatically and that of P2 showed a Tamman-like trend with a maximum at 0.20_D, plateaued for 0.30_D to 0.70_D and then increased again to reach its maximum for pure D (Fig. 6.3f). The endotherm P3, which appeared at 0.30_D, also increased almost linearly to reach a maximum for pure D. The maximum observed in the Tamman-like plot at 0.20_D did not match the apparent eutectic observed in the liquidus line at 0.05_D suggesting that the reaction may be of a more complex nature than a simple eutectic.
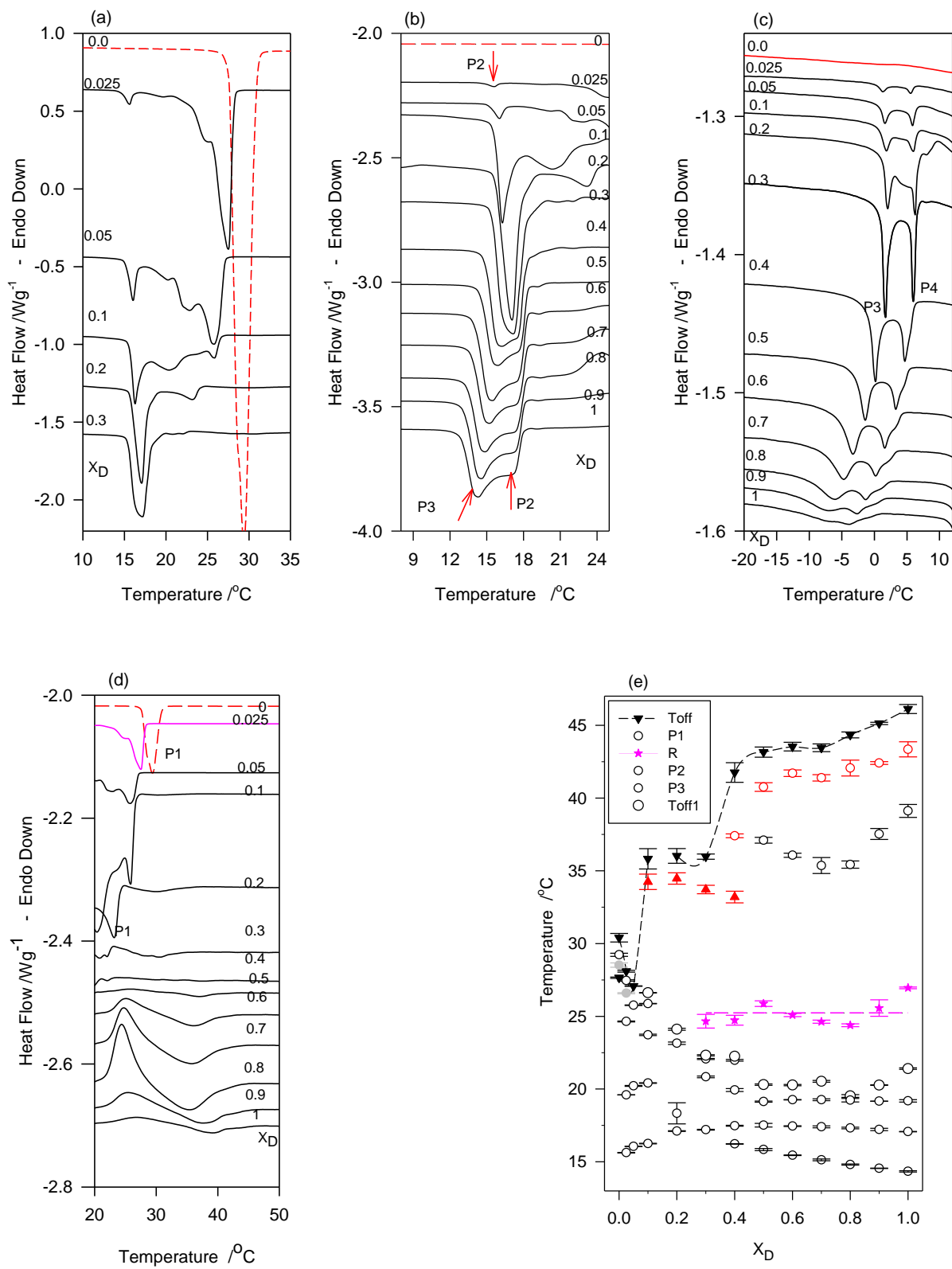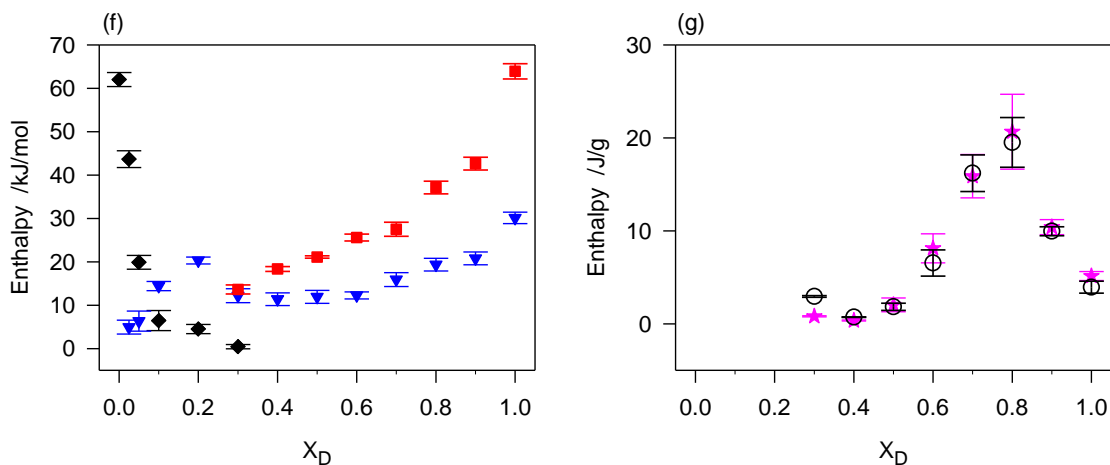
Figure 6.3. (a, b, c & d) DSC heating (1 °C /min) thermograms of D/MeP mixtures. D molar ratio is indicated above the curves; (e) corresponding characteristic temperatures (▼: Offset of melting (T_{Off}); ○: peak (T_P); and ★: recrystallization), (f) enthalpy of melting of peaks P1 (◆, ΔH_1), P2 (▼, ΔH_2) and P3 (■, ΔH_3), and (g) enthalpy of the recrystallization exotherm (★), and enthalpy of its subsequent endotherms (○)

6.3.4 Microstructure

To better understand the microstructural changes occurring in the D/MeP system, two mixtures (0.05_D and 0.10_D) were studied in detail. The microstructural characterization of pure D and MeP crystals provided a baseline for comparison. PLM images (500X) of fully crystallized D, 0.10_D and 0.05_D mixtures, and PLM images (100X) of MeP are shown in Fig. 6.4a – d, respectively. The first crystals of pure D appeared at 15.5 °C as small entities appeared as small "white spots" (indicated by arrows in Fig. 6.5a), then continued to grow into relatively long platelet-like crystals (Fig. 6.5b). The platelets aggregated to form a dense fibrillar network (Fig. 6.4a). Note that the rate at

which new crystals appeared was relatively low as it took approximately 12 min (corresponding to 12 °C) to fill the PLM slide. This temperature window can be related directly to the width of the main two exotherms observed in the cooling DSC thermogram of this compound.

(a) Dimer

(b) 0.10_D
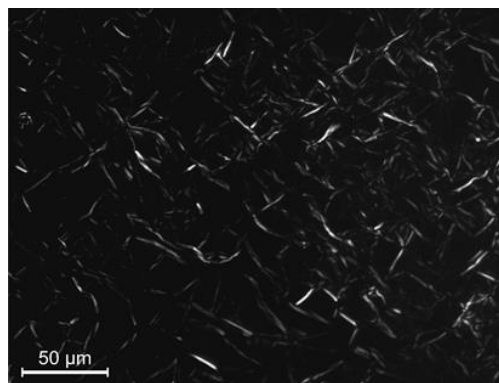
(c) 0.05_D
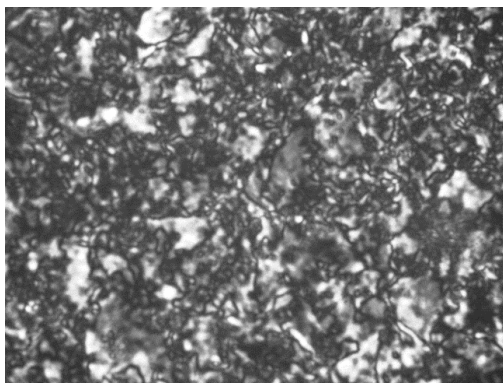
(d) MeP
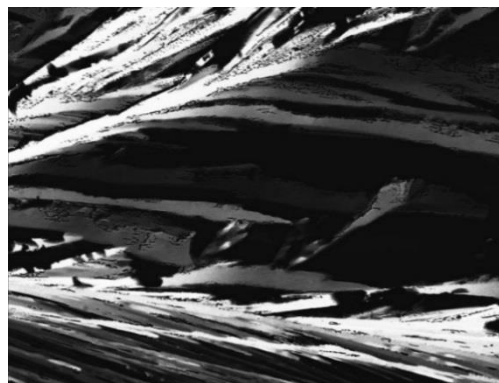
Figure 6.4. PLM images (taken at -60 °C, 500X, scale bar= 50 μm) of fully crystallized (a) dimer D, (b) 0.10_D and (c) 0.05_D, and (d) PLM images (obtained at -10 °C, 100X, scale bar= 200 μm) of MeP. Samples were cooled from the melt at 1 °C /min

(a) D at 15.5 °C   (b) D at 14.5 °C   (c) D at 3 °C   (d) D at -30 °C
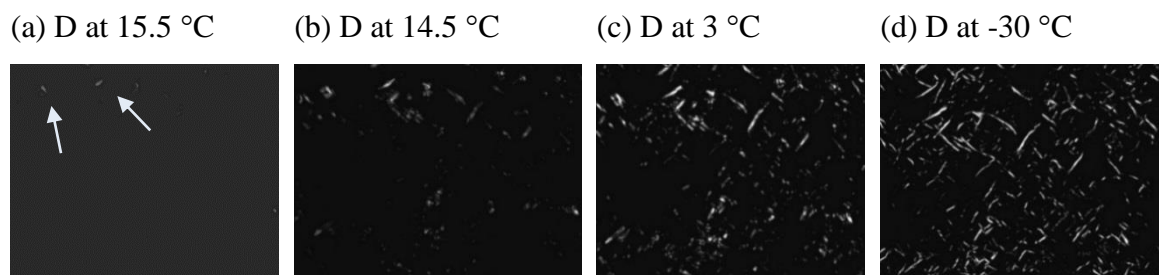
Figure 6.5. PLM images (500X) of the pure dimer D obtained at selected temperatures after cooling from the melt at a constant rate of 1 °C /min.

(a) 0.05_D at 20 °C   (b) 0.05_D at -19 °C   (c) 0.05_D at -30 °C
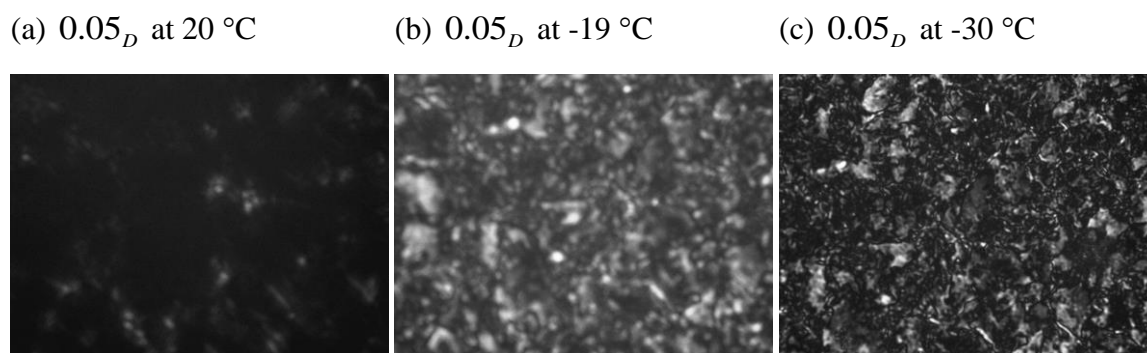
Figure 6.6. PLM images (500X) of 0.05_D mixtures obtained at selected temperatures after cooling from the melt at a constant rate of 1 °C /min.

(a) D at -90 °C   (b) 0.10_D at -90 °C
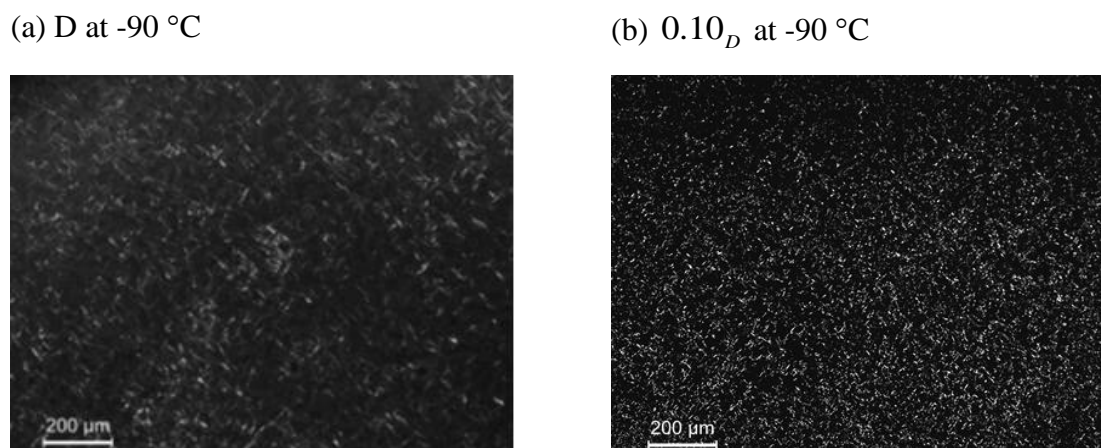
Figure 6.7 .PLM images (100X) of fully crystallized (a) D and (b) 0.10_D mixture obtained after cooling from the melt at a constant rate of 1 °C /min

The crystal network of the 0.05_D sample started with the appearance at 20 °C of several bright spherulitic crystallites (Fig. 6.6a) which increased and grew very rapidly (~19 °C) into a network of large aggregates in which smaller structures, platelet-like crystals and a few Maltese crosses, were observed (Fig. 6.6b). The small entities evolved towards better aggregation and resolution without fundamentally changing the shape of the crystal network (Fig. 6.6c). The crystals of the 0.05_D mixture continued to grow and formed aggregates very quickly, as shown in the PLM taken at 19 °C (Fig. 6.6b).

The 0.10_D sample showed its first crystals at 18.3 °C and presented a nucleation and a growth behavior similar to D. It formed a similar homogenous but relatively denser fibrillar network made of smaller fibrils (Figs. 6.7a and b). MeP microstructure formed very rapidly from one nucleus in the slide which grew radially into a very large leaflet-like crystallite (Fig. 6.4c). As indicated by the PLM of the 0.05_D mixture (Fig. 6.4c), the microstructural characteristics of MeP were lost as soon as D was added, outlining the dramatic effect of D on the growth of the FAME at very small loading. Note that the microstructure of the 0.05_D mixture contrast also with 0.10_D and pure D.

The microstructure shown by these mixtures may be related to their DSC melting behavior. One can notice first that the onset temperature of crystallization determined by PLM is higher than its DSC counterpart by ~1 °C only, a difference that might be explained by the way this latter is extracted from the signal. The mixture which presented a dominant MeP peak (P1 in Fig. 6.3a) have probably grown a large MeP dominant phase which showed in the form of large aggregates in pure MeP and 0.05_D. The dramatic decrease of

P1 and concomitant increase of P2 with D concentration (Fig. 6.3a), can be related to the disappearance of the large aggregates due to MeP and the increasing predominance of the fibrillar entities formed by D. Note that P1 did not completely disappear for the 0.10_D sample but is small enough to explain why no aggregate was observed under the PLM for this mixture. The DSC data for mixtures with more than 0.40_D show a clearly defined extra peak (P3 at approximately 15–16 °C) beside the transitions observed between ~20–25 °C, in addition to the clearly defined melting peak of D (Fig. 6.3b). The microstructure of the phase associated with endotherm P3 is very similar to that of pure D because even with a substantial increase of P3 enthalpy with increasing D content, no change in the microstructure of D has been observed in the PLM of any of the mixtures where P3 was detected. The intermediate DSC melting peak shown at ~ 20 to 25 °C (Fig. 6.3a) in samples with $X_D \leq 0.20$ are probably mixed phases hypothesized to act as linking domains between the crystals of D phase and MeP phase.

6.4 Conclusions

The phase behavior of a model binary system made of methyl palmitate (MeP) and (E)-1-(1-(oleoyloxy)-3-(stearoyloxy)propan-2-yl)18-(1-(oleoyloxy)-3-(stearoyloxy) propan-2-yl) octadec-9-enedioate (D), a triacylglycerol dimer which can be produced safely and inexpensively by metathesis of vegetable oil, was investigated using DSC, XRD and PLM. The XRD data revealed that the solid phases formed after a relatively slow cooling (1 °C/min) were in the orthorhombic crystal subcell structure. The crystal packing was shown to be guided by the bulky D molecules at concentration levels as low as 10%.

The phase diagram obtained using the DSC cooling traces presented a singularity at the 0.10_D mixture for all the characteristic transition temperatures. At this level of loading, the onset of crystallization of MeP was reduced by ~6 °C. For richer mixtures, D had practically no apparent effect on the induction of crystallization. Particular reaction at ~ 0.15_D, 0.40_D and 0.75_D ~ 0.75 were indicated by typical Tamman plots of the enthalpy, confirming the possible eutectic observed in the liquidus line of the cooling phase diagram and other particular reactions which were not observed in the liquidus line for kinetic reasons.

The phase diagram of the D/MeP system constructed using the DSC heating data is very complex and unusual. It revealed that beyond the apparent eutectic formed at ~5% of D, the most stable phases available for the system form in three stepped levels of stability. The variation of the melting temperature and stability of the kinetic phases was explained by the association, via van der Waals interactions, of D and MeP molecules to form D/MeP units in which the D carries the MeP molecules on its saturated moieties and bridge. This association was revealed to start from the liquid state where mobility of MeP and free rotation of the D branches are most favorable. The disruptive effect of D on the packing of the saturated FAME was effective only at low concentrations ($X_D < 0.15$) because there is not enough D carriers to form the D/MeP composite units.

The results of the present work in terms of reduction of crystallization temperature of biodiesel, can be compared to the results obtained by Soares et al., [32] with esters such as (trimetylol) propanal dodecanoate, which with 0.08mol/100g biodiesel, reduced cloud point of biodiesel by 5.7 °C [32], or the results reported by Moser et al., [33] for branched

diester, which reduced the cloud point of biodiesel by 0.7 °C and 3.2 °C with 1% by vol. and 5% by vol. respectively [33]. Although the finding of the present work go beyond the particular merits of the D itself, these data and those reported in [21] about its effect on commercial biodiesel suggest that D may be used as a crystallization depressants that would be effective at both nucleation and growth stages of crystallization at concentrations that are lower than 5%.

6.5   References

[1] Costa MC, Boros LAD, Coutinho JAP, Kraehenbuehl MA, Meirelles AJA. Low-temperature behavior of biodiesel: solid-liquid phase diagrams of binary mixtures composed of fatty acid methyl esters. Energy Fuels. 2011;25(7):3244-50.

[2] Lopes DdC, Steidle Neto AJ, Martins PAR. Economic simulation of biodiesel production: SIMB-E tool. Energ Econ. 2011;33(6):1138-45.

[3] Demirbas A. Biodiesel production from vegetable oils via catalytic and non-catalytic supercritical methanol transesterification methods. Progress Energ Combust. 2005;31(5–6):466-87.

[4] Dunn RO. Cold-flow properties of soybean oil fatty acid monoalkyl ester admixtures. Energy Fuels. 2009;23(8):4082-91.

[5] Ong HC, Mahlia TMI, Masjuki HH, Norhasyima RS. Comparison of palm oil, Jatropha curcas and Calophyllum inophyllum for biodiesel: A review. Renew Sust Energ Rev. 2011;15(8):3501-15.

[6] Knothe G, Sharp CA, Ryan TW. Exhaust emissions of biodiesel, petrodiesel, neat methyl esters, and alkanes in a new technology engine. Energy Fuels. 2006;20(1):403-8.

[7] Bajpai D, Tyagi VK. Biodiesel: Source, production, composition, properties and its benefits. J Oleo Sci. 2006;55(10):487-502.

[8] Dunn RO. Effect of temperature on the oil stability index (OSI) of biodiesel. Energy Fuels. 2007;22(1):657-62.

[9] Chiu CW, Schumacher LG, Suppes GJ. Impact of cold flow improvers on soybean biodiesel blend. Biomass Bioenerg. 2004;27(5):485-91.

[10] Dunn RO. Effects of minor constituents on cold flow properties and performance of biodiesel. Progress Energ Combust. 2009;35(6):481-9.

[11] Knothe G. Dependence of biodiesel fuel properties on the structure of fatty acid alkyl esters. Fuel process technol. 2005;86(10):1059-70.

[12] Misra RD, Murthy MS. Blending of additives with biodiesels to improve the cold flow properties, combustion and emission performance in a compression ignition engine—A review. Renew Sust Energ Rev. 2011;15(5):2413-22.

[13] Smith PC, Ngothai Y, Dzuy Nguyen Q, O'Neill BK. Improving the low-temperature properties of biodiesel: Methods and consequences. Renew Energ. 2010;35(6):1145-51.

[14] Moser BR, Erhan SZ. Synthesis and evaluation of a series of alpha-hydroxy ethers derived from isopropyl oleate. J Am Oil Chem Soc. 2006;83(11):959-63.

[15] Moser BR, Erhan SZ. Branched chain derivatives of alkyl oleates: Tribological, rheological, oxidation, and low temperature properties. Fuel. 2008;87(10-11):2253-7.

[16] Jeong G-T, Park J-H, Park S-H, Park D. Estimating and improving cold filter plugging points by blending biodiesels with different fatty acid contents. Bioresour Technol. 2008;13(4):505-10.

[17] Park J-Y, Kim D-K, Lee J-P, Park S-C, Kim Y-J, Lee J-S. Blending effects of biodiesels on oxidation stability and low temperature flow properties. Bioresour Technol 2008;99(5):1196-203.

[18] Imahara H, Minami E, Saka S. Thermodynamic study on cloud point of biodiesel with its fatty acid composition. Fuel. 2006;85(12–13):1666-70.

[19] Knothe G, Dunn RO. A Comprehensive Evaluation of the Melting Points of Fatty Acids and Esters Determined by Differential Scanning Calorimetry. J Am Oil Chem Soc. 2009;86(9):843-56.

[20] Christensen SA, DiBiase SA, Rizvi SQA. Cold flow additives. In: EPO, editor. C10L 1/19 (2006.01); C10L 1/224 (2006.01) ed2012.

[21] Mohanan A, Bouzidi L, Li S, Narine SS. Mitigating crystallization of saturated FAMES in biodiesel: 1. Lowering the crystallization temperature via addition of metathesized soybean oil. Unpublished - Submitted to Energy. 2014.

[22] Boshui C, Yuqiu S, Jianhua F, Jiu W, Jiang W. Effect of cold flow improvers on flow properties of soybean biodiesel. Biomass Bioenergy. 2010;34(9):1309-13.

[23] Chastek TQ. Improving cold flow properties of canola-based biodiesel. Biomass Bioenergy. 2011;35(1):600-7.

[24] Refvik M, Larock R. The chemistry of metathesized soybean oil. J Am Oil Chem Soc. 1999;76(1):99-102.

[25] Li SJ, Hojabri L, Narine SS. Controlling Product Composition of Metathesized Triolein by Reaction Concentrations. J Am Oil Chem Soc. 2012;89(11):2077-89.

[26] Pillai SK, Abidli A, Belkacemi K. Triacylglycerol self-metathesis over highly chemoselective methyltrioxorhenium supported on ZnCl2-promoted mesoporous alumina. Appl Catal A-Gen. 2014;479:121-33.

[27] Tian QP, Larock RC. Model studies and the ADMET polymerization of soybean oil. J Am Oil Chem Soc. 2002;79(5):479-88.

[28] Biermann U, Metzger JO, Meier MAR. Acyclic Triene Metathesis Oligo- and Polymerization of High Oleic Sun Flower Oil. Macromol Chem Phys. 2010;211(8):854-62.

[29] Soriano Jr NU, Migo VP, Matsumura M. Ozonized vegetable oil as pour point depressant for neat biodiesel. Fuel. 2006;85(1):25-31.

[30] Li S, Bouzidi L, Narine SS. Synthesis and Physical Properties of Triacylglycerol Oligomers: Examining the Physical Functionality Potential of Self-Metathesized Highly Unsaturated Vegetable Oils. Ind Eng Chem Res. 2013;52(6):2209-19.

[31] Bouzidi L, Boodhoo M, Humphrey KL, Narine SS. Use of first and second derivatives to accurately determine key parameters of DSC thermographs in lipid crystallization studies. Thermochim Acta. 2005;439(1-2):94-102.

[32] Soares VL, Nascimento RS, Albinante SR. Ester-additives as inhibitors of the gelification of soybean oil methyl esters in biodiesel. J Therm Anal Calorim. 2009;97(2):621-6.

[33] Moser BR. Preparation and evaluation of multifunctional branched diesters as fuel property enhancers for biodiesel and petroleum diesel fuels. Energy Fuels. 2014;28(5):3262-70.

7.   Harnessing the Synergies between Lipid Based Crystallization Modifiers and a Polymer Pour Point Depressant to Improve Cold Flow Properties of Biodiesel[6]

7.1   Introduction

Biodiesel is an alternative engine fuel made from renewable materials such as plant oils and animal fat. Its use has increased over recent years but is limited in cold climates due to its inherent cold flow issues. Most of the cold flow problems of common biodiesel are associated with the relatively high crystallization temperature of its saturated fatty acid methyl ester (FAME) components [1, 2]. The cold flow characteristics of biodiesel are described by standardized measurements of temperatures related to field operability such as the cloud point (CP, ASTM D2500), the cold filter plugging point (CFPP, ASTM D6371) and the pour point (PP, ASTM D97). The CP, CFPP and PP are directly correlated to particular points in the crystallization process. CP is defined as the temperature at which fuel starts to appear cloudy, i.e., once the crystals become visible. CFPP is the lowest temperature at which the growing crystals can pass through a standard (45 μm) filter. The PP is reached when the fuel is prevented from flowing. This occurs when the fluid is viscous enough to be immobilized or when the crystals form a three dimensional solid network capable of trapping the liquid.

---

[6] A version of this chapter has been filed for a patent (Patent #- 62250577): S. Narine, A Mohanan and L. Bouzidi (2015)-"Pour Point Depressants and Natural Oil Based Crystallization Modifiers for Biodiesel"

Among the several approaches taken to improve the cold flow performance of biodiesel [3, 4], application of cold flow improver (CFI) additives is the most popular [5, 6]. Generally CFI additives are designed to interrupt the crystallization of the biodiesel at the nucleation, growth or aggregation stages [7]. All the studies present convincing evidence that the action of the additives is controlled by similar dominating mechanisms despite the variety and complexity of their chemical structures. High selectivity as well as effectiveness can be traced to the presence of structural elements that allow the disruption of the crystallization process at given stages and given length scales. The overriding trend that emerges from the studies corroborates the finding that in order to be effective, the additive must possess a structural similarity that initiates association with the host material (the FAMEs of the biodiesel for instance) rather than undergoing self-association and a structural dissimilarity that would obstruct and delay, if not prevent, further growth or organization and aggregation of the initial crystals (Chapter 2-6).

The cloud point depressants (CPD) work principally by disturbing the crystallization process at small length scales, principally at the nucleation and early stages of growth [8]. The growth and aggregation of FAME crystals can follow quite rapidly, drastically limiting the effectiveness of the additive on the PP. For example [6] reported that at 5% vol. loading, a glycerol derivative, glycerol butanal acetal, depressed the CP of animal fat biodiesel by ~5 °C but achieved a PP that was just 1 °C below the CP.

The pour point depressants (PPDs) are designed to aid pumpability, and as a result affect CP and filterability of biodiesel marginally [9-11]. PPDs are typically composed of low-molecular-weight copolymers and function as crystal growth limiters [12, 13]. They are essentially crystal morphology modifiers which may participate in the early steps of

crystallization of the saturated components of biodiesel, even after nucleation, but are able to provide a barrier to further growth, therefore reducing crystal size and limiting crystal aggregation [14]. Ozonized vegetable oil is an example of an efficient PPD found to not interfere in the crystallization of saturated FAMEs, but works by modifying the crystal morphology of the unsaturated FAMEs of biodiesel [15, 16].

Unfortunately, until the work described in this chapter was completed, no single approach has yet been able to simultaneously address both PP and CP depression effectively. The achievement of significant depression in both CP and PP and a large difference between the PP and the CP simultaneously would be the winning combination for the viability of common biodiesel in the cold climates of North America and Europe. For a single CFI to achieve such a task, the additive must delay nucleation, prevent growth of the crystals and hinder their aggregation. This is quite understandable because such a CFI which has to modify crystallization at very different stages must develop specific interactions at each length scale involved. Although such an additive may be possible and maybe discovered serendipitously, the actual fundamental knowledge of the mechanism(s) at such wide length scales is not sufficient to design a universal single additive which would congruently incorporate the structural features of a CPD and a PPD in one compound.
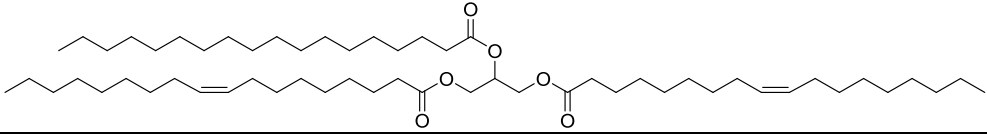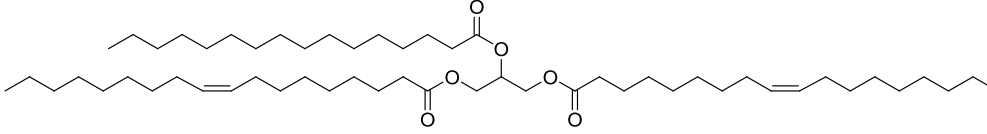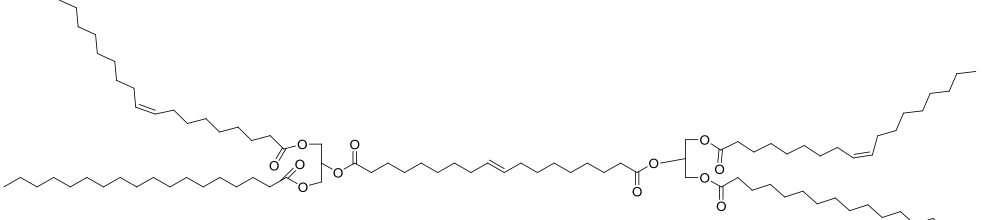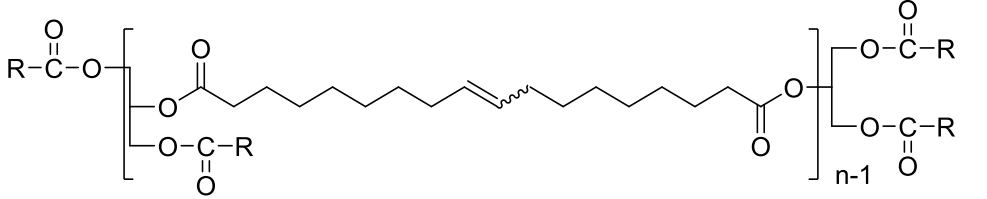
The present work was aimed at finding an alternate solution where these effects can be achieved through synergistic actions of a CPD and a PPD. The hope was that the combination would work concurrently and more efficiently than the individual additive, by for example laying the grounds for each to work more efficiently than alone. It follows a series of investigations of vegetable oil based crystallization modifiers (VOCMs) sourced from self-metathesized soybean oil (MSBO). MSBO and components of MSBO such as
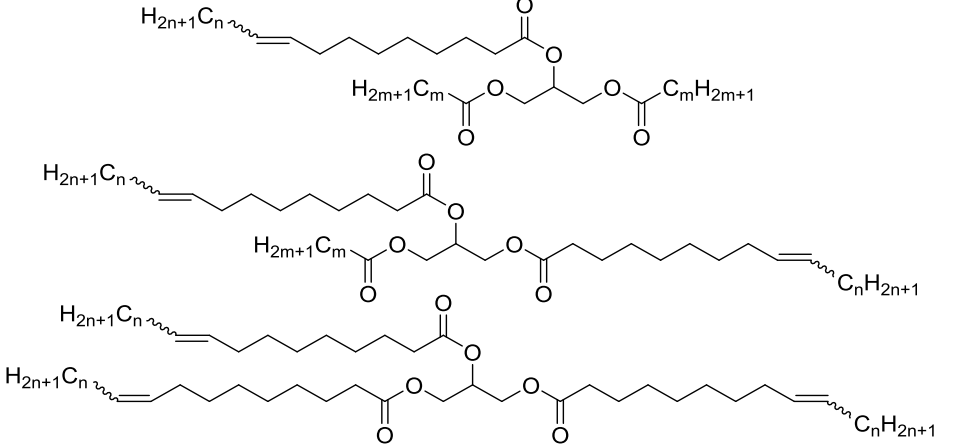
TAGs and oligomers of TAGs with two fatty acids in the *cis-* configuration and a saturated fatty acid or a fatty acid in the *trans-* configuration were found to be highly functional crystallization depressors (Chapter 2). These VOCMs although highly effective in lowering the onset of crystallization of biodiesel and decreasing crystal size, did not significantly alter the PP.

Poly lauryl methacrylate (PLMA), a polymer which has been shown to decrease the PP of canola oil biodiesel by 30 °C [4] was chosen as the PPD to be tested in combination with VOCMs selected from the most effective compounds determined in Chapter 2. The IUPAC names and chemical structure of the VOCMs used in this study are listed in Table 7.1. PLMA was expected to work in soybean biodiesel as well as canola oil biodiesel because of similar FAME composition to the oils [17]. The VOCMs include pure compounds such as 1,3 dioleoyl 2-stearoyl *sn*-glycerol (OSO), 1,3 dioleoyl 2-palmitoyl *sn*-glycerol (OPO), and (E)-1-(1-(oleoyloxy)-3-(stearoyloxy)propan-2-yl) 18-(1-(oleoyloxy)-3-(stearoyloxy) propan-2-yl) octadec-9-enedioate, a dimer of OPO (Dimer, D), and complex mixtures such as self-metathesized soybean oil (MSBO) and cross-metathesized palm oil (PMTAG). Each VOCM was tested individually and in combination with PLMA. A method inspired by ASTM D97 and ASTM D2500 was specially designed to measure CP and PP of the biodiesel mixtures much more precisely (see Section 2.2.1). In order to uncover the mechanism of action and the role of concentration or particular structural features that favor synergetic effects, the mixtures were also investigated with DSC and PLM.

Note that measurement of PP and CP of biodiesel with methods other than ASTM D97 and ASTM D2500 is not unusual [4, 18, 19]. Some of these methods are reported to be even better than the ASTM method [19, 20].

Table 7.1. IUPAC names and chemical structure of vegetable oil derived crystallization modifiers (VOCMs) used in this study.

Selected VOCMs	IUPAC names and general Structure of VOCMs
1,3 dioleoyl 2-stearoyl *sn*-glycerol (OSO)	9-Octadecenoic acid (Z)-, 2-[(1-oxooctadecyl) oxy]-1, 3-propanediyl ester
(1,3 dioleoyl 2-palmitoyl *sn*-glycerol OPO)	9-Octadecenoic acid (Z)-, 2-[(1-oxohexadecyl)oxy]-1,3-propanediyl ester
Dimer of OPO-(Dimer, D)	E)-1-(1-(oleoyloxy)-3-(stearoyloxy)propan-2-yl) 18-(1-(oleoyloxy)-3-(stearoyloxy) propan-2-yl) octadec-9-enedioate, a D of OPO
self-metathesized soybean oil (MSBO)	General structure of triacylglycerols (TAGs) monomers and TAG-oligomers[a,b] of metathesized soybean oil (MSBO) [a] n represents oligomer level (n=1: TAG monomer; n= 2: dimer; n= 3: trimer; n= 4: quatrimer; etc.).

	[b] RCOOH= stearic acid (S), palmitic acid (P), linolenic acid (L), oleic acid (O), linoleic acid (Ln). Double bonds in R include *cis-* and *trans-* configurations such as in elaidic acid (E) R in MTO is from oleic acid, and R in MSBO is mainly from oleic acid, linoleic acid, linolenic acid, stearic acid or palmitic acid
cross-metathesized palm oil (PMTAG)	 General Structure of cross metathesized palm oil. n is the number of carbons.

7.2   Materials and Methods

7.3   Materials

Soy 1500 is a mixture of FAMEs derived from soybean oil, donated by AG Environmental products, L.L.C, USA. The fatty acid methyl ester (FAME) composition of Soy1500 as determined by GC is presented in Table 2.1. The non-polymer additives were all derived from vegetable oil. Their IUPAC names and structures are provided in Table 7.1. They are referred to as vegetable oil crystallization modifiers (VOCMs). The structured TAGs OSO, OPO, and the dimer of OPO (D), were synthesized in our laboratory according to known methods [21, 22]. Self-metathesized soybean oil (MSBO), and metathesized palm oil (PMTAG) were provided by Elevance Renewable Sciences (ERS, Bolingbrook, IL, USA). MSBO is the product of self-metathesis of soybean oil, and PMTAG is the product of cross-metathesis of palm oil with 1-butene, both stripped of short

aliphatic olefinic components. MSBO consists of structured TAGs such as OSO, OPO, SOO, etc. and oligomers of these TAGs such as dimers and quatrimers (Chapter 2) PMTAG consists of the saturated unmodified TAGs of palm oil and modified TAGs including shortened TAGs at the level of the double bond as well as trans- isomers [23]. PMTAG polyol was synthesized by epoxidation and hydroxylation [23]. PLMA, the polymer additive, was purchased from Scientific Polymer Products, Ontario, New York, USA, as a solution in toluene. Toluene was removed from PLMA using rotary evaporation followed by vacuum drying for a week.

The mixtures were prepared by weighing the required amount of additives in a glass vial and then adding them to Soy1500. When PLMA was present, it was weighed first. Because PLMA does not dissolve in the biodiesel at room temperature, the mixtures containing PLMA were heated to 50 °C for 5 min then homogenized with Soy 1500 using a digital vortex mixture (Fisher Scientific, Pittsburgh, PA, USA) for 5 min. The other mixtures were homogenized at room temperature using the vortex mixture for 2 min. Six (06) different mixtures with loadings between 0 and 2% by wt. (%w/w) were prepared for each individual additive. Note that because the concentration of the additives is expressed in weight% throughout the text, reference to weight in the designation of the mixtures will be omitted from the remainder of the chapter.

7.4   Methods

7.4.1   Pour Point and Cloud Point Measurement

Pour point and cloud point of samples, were measured using a setup designed in our laboratory. The equipment was developed based on ASTM D-97 and ASTM D-2500 and

uses similar methods to measure CP and PP. The system is also similar to a method reported previously [4].

7.4.1.1   The Apparatus

The apparatus is shown in Fig.7.1. It consists of a temperature controlled cooling/ heating circulator (Julabo F50-ME, Julabo USA Inc., Allentown, PA, USA) used as a cooling bath, and complies with ASTM D97 recommendations. The sample jar is a 1.5 × 15 cm glass test tube (Pyrex, SciLabware, Stoke-on-Trent, UK) fitted with a type K thermocouple attached to a data logger (Temp-300 Dual-Input, OAKTON Instruments, Vernon Hills, IL, USA) that records the temperature of the sample continuously. The thermocouple is placed at mid fill level and maintained rigidly in place by a rubber cork. Another thermocouple also attached to the data logger was immersed in the cooling bath to record its temperature. A stand was specially designed to allow for the quick and smooth testing operations. A vertical metallic bar securely fixed to the heavy base of the stand was fitted with two tight but easily released claps to hold the sample tube with the thermocouple still during the thermal processing of the sample and quick release and replacement for measurement. A regular thermometer was used to double check the temperature of the bath regularly. Ice point (set point of -0.5 °C for the thermometer used) was checked prior to each experiment. The precision of the sample and bath temperature was determined to better than ± 0.1 °C.
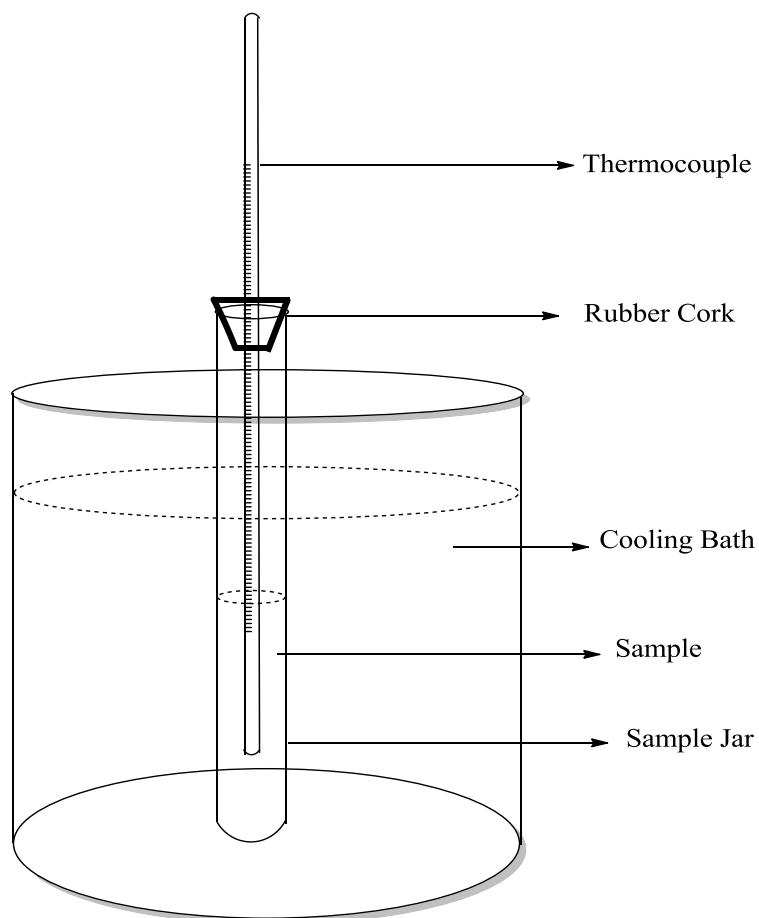
Figure 7.1. Apparatus for cloud point and pour point measurement.

7.4.1.2   The Cloud Point and Pour Point Measurement Procedure:

A sample of 8 ml in the test jar is cooled directly in the circulating thermal bath. The

sample is equilibrated at 25 °C for 5 min to erase the thermal history than cooled at ~0.3

°C/min. Such a slow cooling ensured crystallization conditions closer to equilibrium and

a homogeneous distribution of the temperature in the sample. The direct contact of the test

jar with the thermal bath ensured a better control of the sample temperature than what is

obtained with the jacketed system of ASTM D97. The present method also avoids some

of the common sources of errors in the ASTM methods such as those due to the fluctuations

in the air density and humidity.

As exemplified with the cooling profiles of the cooling bath and Soy1500 supplemented with 0.2%w/w PLMA and 2.5% w/w OSO presented in Fig. 7.2, the temperature of the sample decreases fairly linearly and closely follows the bath temperature. The monitoring of the temperature was excellent. One can even notice the singularity in the sample temperature at the point where it started to crystallize (arrow in Fig. 7.2).
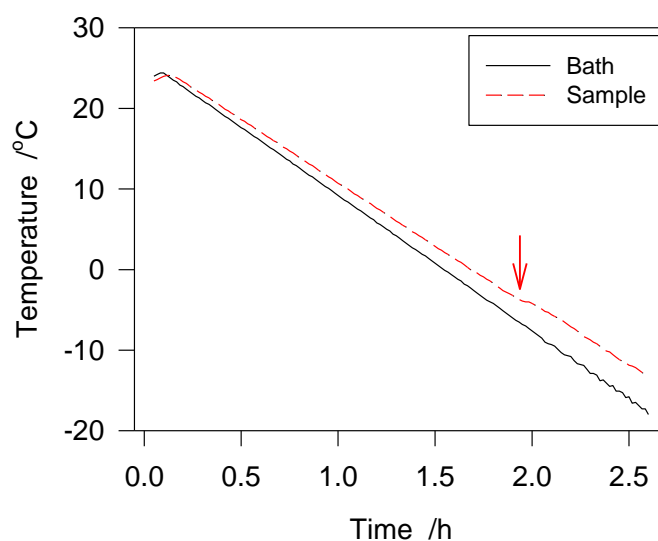
Figure 7.2. Temperature versus time curves of the cooling bath and sample (Soy1500 + 0.2% w/w PLMA + 2.5% w/w OSO) measured simultaneously

The sample is visually examined for the presence of any crystal at least 10 °C above the expected CP of the material. The sample tube is quickly removed from the bath and checked and then placed back. The whole process is performed in less than five (5) seconds and is repeated every 1 °C. The CP is recorded as the temperature at which the first crystal is observed. At this stage the sample jar is tilted horizontally and the sample checked for flow. The process is repeated until no movement is observed. The PP is recorded as the

temperature at which the sample showed the latest movement. Note that as recommended by the ASTM procedure, the sample is kept undisturbed while inspecting the presence of crystals, and the sample jar is not tilted until CP was recorded. The precision of the measurement temperature was determined to better than $\pm$ 0.5 °C.

7.4.2 Polarized Light Microscopy

Microstructure analysis of selected mixtures was conducted using a polarized light microscope (PLM, Leica DM2500P, Leica Microsystems, Wetzlar, Germany) fitted with a Leica (DFC420C) digital camera. A temperature – controlled stage (Linkam LS 350, Linkam Scientific Instruments, Tadworth, Surrey, UK) fitted to the PLM was used to process the samples thermally. A small droplet of material was carefully pressed between a preheated glass microscope slide and cover-slip ensuring a uniform thin layer of sample. The sample was melted at 25 °C for 5 min to delete all crystal memory then cooled at 3 °C/min down to -50 °C. Temperature / time resolved images of the sample were collected using the automatic multi-time image capture available in the PLM. The appearance of the first "white spot" in the PLM was recorded as the start temperature of crystallization or induction temperature (T_{ind}).

7.5 Results and Discussion

7.6 Effect of the Additives on the Cloud Point of Soy1500 Biodiesel

The CP of biodiesel supplemented singularly with additives is displayed in Fig. 7.3. The maximum depression of CP values obtained with single treatment of additives are provided in Table 7.2.
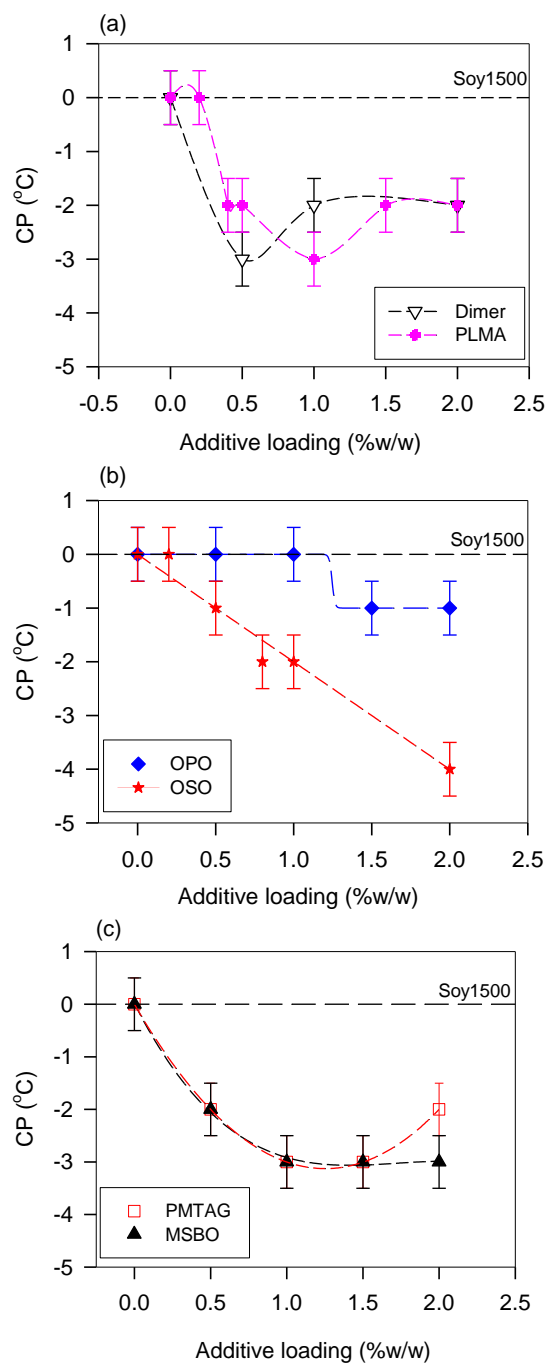
Figure 7.3. Cloud point (CP) versus concentration of polymer and VOCMs additives added singularly in Soy 1500 biodiesel. (a) D and PLMA; (b) OSO and OPO; and (c) MSBO and PMTAG; Dashed lines are guides for the eye. Horizontal dotted line shows the CP of Soy1500 biodiesel. Error bars are the standard errors associated with the measurements..

As can be seen in Fig. 7.3, the presence of additives all lowered the CP of Soy1500. The CP of Soy1500 versus loading curves presented a minimum at -3 °C, corresponding to a depression of 3 °C at 1% w/w for PLMA, PMTAG and MSBO (Fig. 7.3a and 7.3c) and 0.5% w/w for D (Fig. 7.3a). OSO depressed the CP of Soy1500 linearly (-2.09°C per %, R^2= 0.9747), achieving a depression of 4 °C at 2% w/w loading. OPO affected CP of Soy1500 only marginally, starting at a minimum threshold concentration of 1.5% w/w loading with a small depression of 1 °C. The depression in CP of biodiesel caused by the VOCMs used here compares favorably with those observed for other CFI additives reported in the literature [24]. Depression in CP achieved using 2% w/w OSO compares favorably with the results obtained using complex lipid based structures such as branched diesters [24]; CP was reduced by 0.7 to 5.3 °C, at loadings between 1% and 10% by volume.

Table 7.2. Depression in cloud point (CP) of Soy obtained with selected additives. ΔCP is the difference between CP of the sample and CP= 0 °C of neat biodiesel.

Additive	ΔCP (± 0.5 °C)
1.5% w/w OPO	1.0
2.0% w/w OSO	4.0
0.5% w/w D	3.0
1.0% w/w MSBO	3.0
1.5% w/w PMTAG	3.0
1.0% w/w PLMA	3.0
0.2% w/w PLMA+1.5% w/w OPO	1.0
0.2% w/w PLMA+0.5% w/w D	3.0
0.2% w/w PLMA+2% w/w PMTAG	3.0
0.2% w/w PLMA+2% w/w MSBO	4.0
0.2% w/w PLMA+2% w/w OSO	4.0

The CP of Soy1500 supplemented with a cocktail made of the VOCMs at their most effective concentrations and 0.2% w/w PLMA was measured in order to determine possible compounding effects. The results are presented in Fig. 7.4. The corresponding depressions are listed in Table 7.2. As shown in Fig. 7.4, except with PMTAG and MSBO where a small decrease (1 °C) was observed, PLMA combined with other VOCMs did not change CP of Soy1500. The effect of PLMA on the CP was small when present and does not seem to affect the way the VOCMs function. The effect was not investigated further as it was not germane to the study at hand, and very small for the complex mixtures.
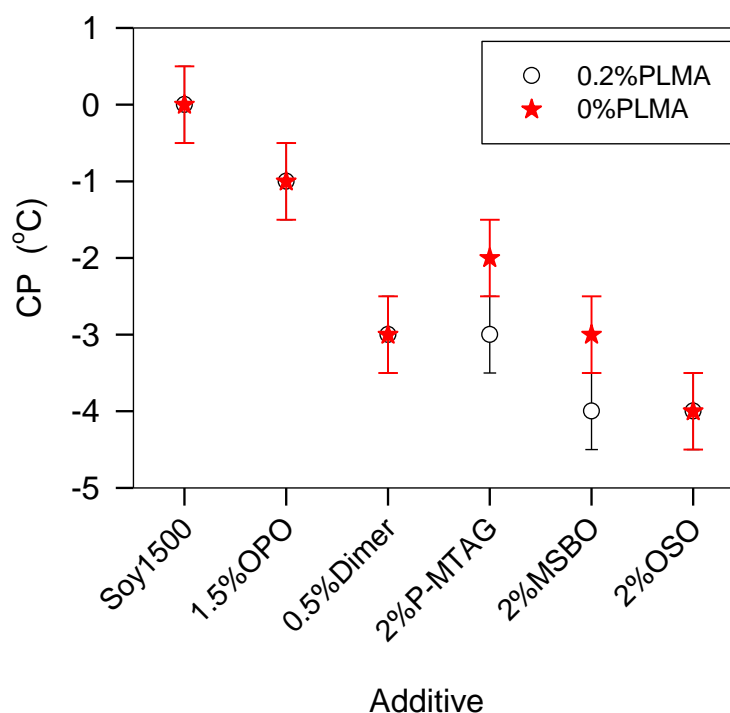
Figure 7.4. Cloud point (CP) of Soy1500 supplemented with selected concentration of vegetable oil based crystallization modifiers (VOCMs) additives without PLMA (0% w/w PLMA, stars) and with 0.2% w/w PLMA (empty circles). Error bars are the standard errors associated with the measurements.

7.7 Effect of the Additives on the Pour Point of Soy1500

7.7.1 Effect of Individual Additives on the Pour Point of Soy1500

The effect of the individual VOCMs (MSBO, OSO, OPO and PMTAG) on PP of Soy1500 is shown in Fig. 7.5a. The effect of the D and PLMA is presented in Fig. 7.5b. The latter two are singled out in different panels to highlight their peculiar behavior. The PP and the depression of PP for biodiesel with selected concentrations of additives are also provided in Table 7.3.
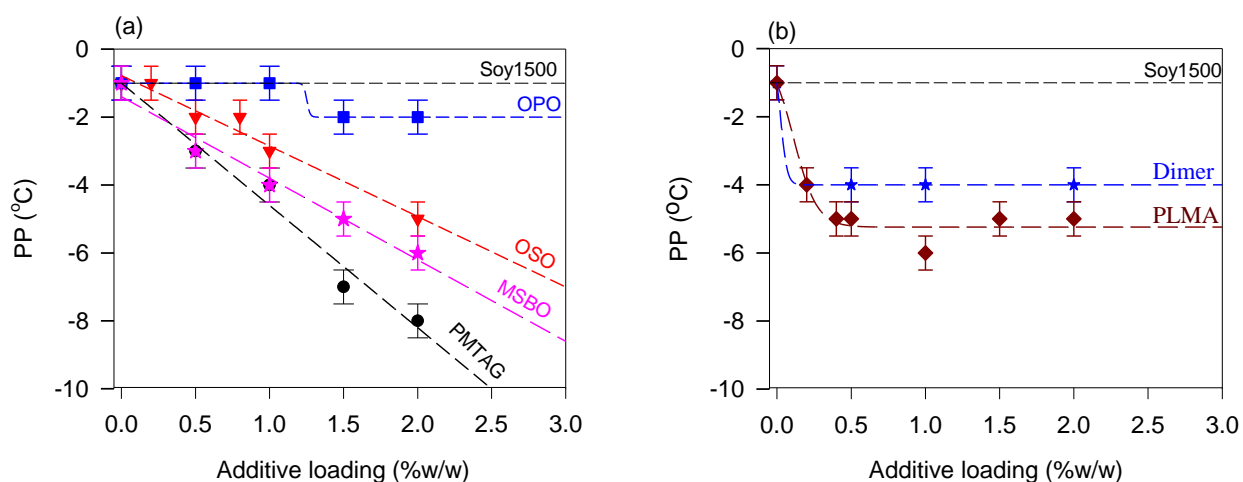
Figure 7.5. Pour point (PP) of Soy1500 versus concentration curves of (a) PMTAG, MSBO, OSO and OPO; and (b) the D and PLMA. Dashed lines are guides for the eye. Error bars are the standard error associated with the measurements.

All of the additives depressed the PP of the biodiesel significantly. The magnitude of depression, however, depended on the nature and concentration of the additive. Addition of PMTAG, MSBO and OSO up to 2% w/w reduced PP of Soy1500 linearly ($R^2 > 0.9755$, dashed lines in Fig. 7.5a). At any given concentration, PMTAG affected PP the most with a depression of 3.6 °C per %w/w, followed by MSBO with 2.4 °C per %w/w and OSO with 2.1 °C per %w/w. OPO affected PP of Soy1500 only marginally, starting at 1.5%

w/w loading with a small reduction of 1 °C (i.e., from -1°C to -2 °C). The effectiveness of PLMA and the D was limited to very low loadings (Fig. 7.5b). The polymer additive, PLMA, achieved its highest effect on the PP of Soy1500 with a depression in PP of 4 °C, from -1 °C to -5 °C, at a loading of 0.4% w/w, then plateaued afterwards. The D followed the same trend with a depression of 3 °C, from -1 °C to -4°C, at 0.5% w/w loading. This close similarity in action on PP mirror the similarity observed in CP (see section 7.6) and suggests that the attributes of a pour point depressant (PPD) in terms of its action on biodiesel may start with a dimeric structure. This particular D showed a very peculiar phase diagram with methyl palmitate, wherein it displayed a eutectic at very low concentration and a stepwise increase in its most stable phases for higher concentrations (Chapter 6). Note that at corresponding low loadings, the D and PLMA were more effective than all the other additives.

The VOCMs used in this study achieved comparable or better performance than other bio-based PPDs found in literature. At a loading of 2% w/w PMTAG displayed a depression in the PP of Soy1500 similar to 1.5% w/w of ozonized sunflower oil in soybean oil biodiesel [25]. Other bio-based PP additives depressed PP at significantly higher concentrations, such as ethyl levulinate which depressed the PP of cotton seed biodiesel and poultry fat biodiesel by 4 °C at 20% by vol. [26] or ethyl acetoacetate which depressed the PP of cotton seed biodiesel by 4 °C at the same loading of 20% by vol. [27].

Note that, PMTAG although derived from palm oil, had a significantly greater effect on the PP of Soy1500 than MSBO, a product derived from soybean oil. This suggests that the selectivity criteria drawn by Soriano et al. from the comparison of the effect of ozonized vegetable oil additives on biodiesel derived from different vegetable oils [15] are specific

to ozonide products and that the interactions at play between the additive and the biodiesel are much more complex than what a simple structure match would provide.

7.7.2 Effect of PLMA Combined with Individual Additives on the Pour Point of Soy1500

In order to test for synergy effects between PLMA and the VOCMs, cocktail mixtures made with 0.2% w/w PLMA, the smallest efficacious load observed for the PPD alone, and the VOCMs at the concentrations which achieved the largest PP depression, i.e., 1.5% w/w OPO, 0.5% w/w D, 2% w/w MSBO, 2% w/w OSO and 2% w/w PMTAG (see Fig. 7.5a) were tested on Soy1500 for PP. Figure 7.6 shows the data comparing the effect on PP of Soy1500 of the individual VOCMs and cocktail additives made of 0.2% w/w PLMA and VOCM.

Overall, the additive which showed the highest effect on PP without PLMA showed also the highest effect with PLMA. As can be seen in Fig. 7.6, the combination of 0.2% w/w PLMA with OPO did not enhance the efficacy of either additives. The PP of Soy1500 in this case was that obtained with 0.2% w/w PLMA alone, as if OPO did not take part in the disruption process. The polymer probably interfered with the crystallization process after the formation of OPO/biodiesel crystals, when all OPO was spent. MSBO, and the D at a lesser extent, also did not present synergistic effects with 0.2% w/w PLMA. It is probable that these levels of PLMA loadings were not sufficient to add to the effect of these VOCMs. The synergy with OSO and PMTAG was very marked. For both VOCMs, the combination with PLMA resulted in a further drop in PP of Soy1500 by 5 °C. When combined with 0.2 % w/w PLMA, 2% w/w OSO decreased the PP of Soy1500 to -10.5 °C, i.e., a depression of 9.5 °C, much higher than the 4.0 °C depression achieved by 2% w/w

OSO alone. Also, the 0.2% w/w PLMA+2% w/w PMTAG, decreased the PP of Soy1500 to -13.0 °C, which is a 5.0 °C improvement to the depression of 7 °C that was achieved by PMTAG alone.
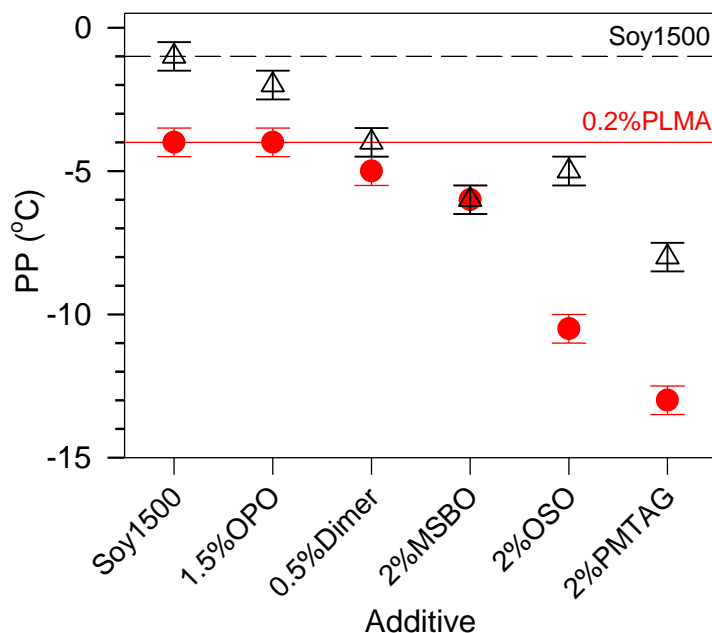
Figure 7.6. Pour point (PP) of Soy1500 supplemented with vegetable oil based crystallization modifiers (VOCMS) alone (up triangles), and with cocktails of 0.2% w/w PLMA and the VOCM additives (solid circles). The error bars are the standard errors associated with the measurements.

The data from experiment supports that the concentration of the polymer that would achieve the optimal synergistic effect is dependent on the type of VOCM and its concentration. Efforts were therefore made to optimize the cocktails that showed the largest synergetic effect, i.e., PLMA and OSO, and PLMA and PMTAG.

7.7.3 Optimization of PLMA Combined with Individual Additives: I

In order to investigate the combined effect of polymer and non- polymer additives, PLMA was combined with the selected VOCM (OSO and PMTAG) in a systematic manner. In the preliminary investigations, the VOCM concentration was fixed and PLMA concentration was varied to determine the optimal PLMA loading. This was done keeping in mind that polymer additives such as PLMA have an optimal effect at relatively very low concentrations [14, 28]. The pure TAG, i.e., OSO, was selected for more extensive preliminary investigation instead of PMTAG to avoid probable interference effects that might occur with complex compositions. Figure 7.7a shows the effect on the PP of Soy1500 of cocktail mixture of OSO at fixed concentration (1% w/w and 2% w/w shown) and varying PLMA concentration.

As evident from Fig. 7.7a, the combination of PLMA with 1% w/w OSO plateaued at 0.4% w/w - 0.5% w/w PLMA with a depression in PP of 5 °C. PLMA worked most efficiently with 2% w/w OSO, the concentration that achieved the highest depression in PP when OSO was used individually. As can be seen also in Fig. 7.7a, the optimal PLMA concentration was 0.2% w/w with a maximum depression of 9.5 °C. Such an optimum in the action of PLMA is not surprising as polymer additives are known to be less effective at high loading [14, 28].

A similar approach was followed to find the optimal PLMA loading in combination with PMTAG. 2% w/w PMTAG was chosen as the fixed VOCM because it achieved the highest PP depression in the experiments which investigated the effect of individual additives (see Fig. 7.7a). The results of the effect of 2% w/w PMTAG and varying PLMA concentration are shown in Fig. 7.7b. As can be seen in the figure, an optimum was

obtained at 0.5% w/w PLMA, a value quite different from what was obtained with OSO.

Furthermore, a much larger depression of 25 °C in the PP (from -1 °C to -26 °C) of Soy1500

was obtained with this combination. Note that the depression in PP of about 10 °C achieved

by the optimum mixture in the case of OSO (0.2% w/w PLMA and 2% w/w OSO) was

lower even than what was achieved with the 0.2% w/w PLMA and 2% w/w PMTAG

cocktail mixture (12 °C).
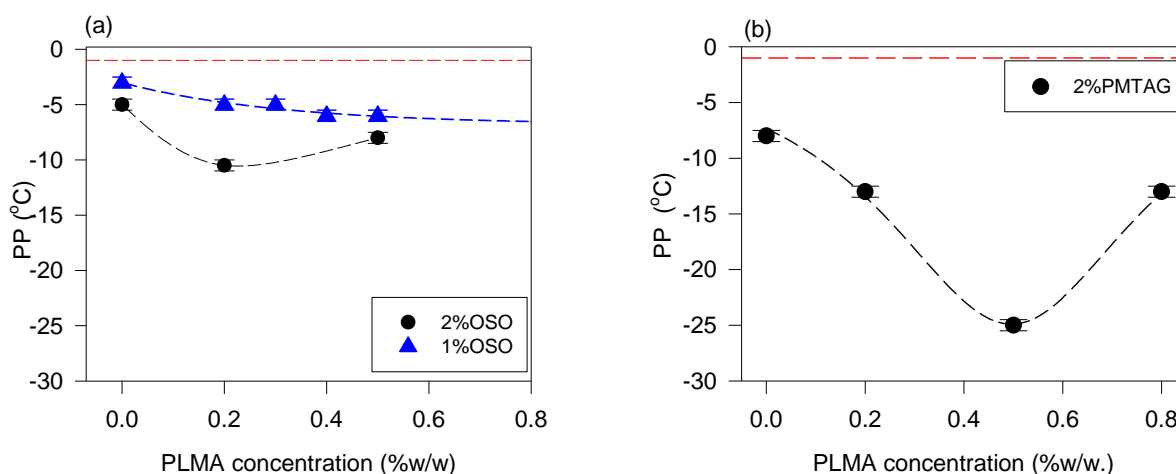
Figure 7.7. Pour point (PP) of Soy1500 supplemented with (a) PLMA and OSO cocktail

additives. Loading of OSO fixed at 1% w/w and 2% w/w and varying PLMA concentration,

(b) PLMA and PMTAG cocktail additives. Loading of PMTAG fixed at 2% w/w and

varying PLMA concentration. Upper horizontal line is the PP of Soy1500 biodiesel, and

dashed lines passing through the data points are guides for the eye. The error bars are the

standard errors associated with the measurements.

7.7.4   Optimization of PLMA Combined with Individual Additives: II

In a second set of experiments, PLMA concentration was fixed at the optimal values

determined previously, and the concentration of the VOCM was varied from 0 to 6% w/w.

The PP of Soy1500 results obtained by adding OSO with 0.2% w/w PLMA are shown in

Fig. 7.8a, and those with PMTAG and 0.5% w/w PLMA are shown in Fig. 7.8b. The PP of biodiesel was depressed very dramatically by both combinations. OSO combined with 0.2% w/w PLMA decreased PP to as low as -16 °C (a depression of 15 °C) for OSO concentrations between 3% w/w and 5% w/w, after which CP increased to -10 °C, a depression of 9 °C, with 6% w/w OSO. This indicates that although very strong synergies were obtained, a limiting effect, similar to what was obtained with PLMA alone, occurred with the combination of PLMA with OSO. This suggests that the polymer has limited effectiveness also in the presence of the VOCM. We therefore suggest that the action of PLMA is maximized on crystals already modified by the VOCM.
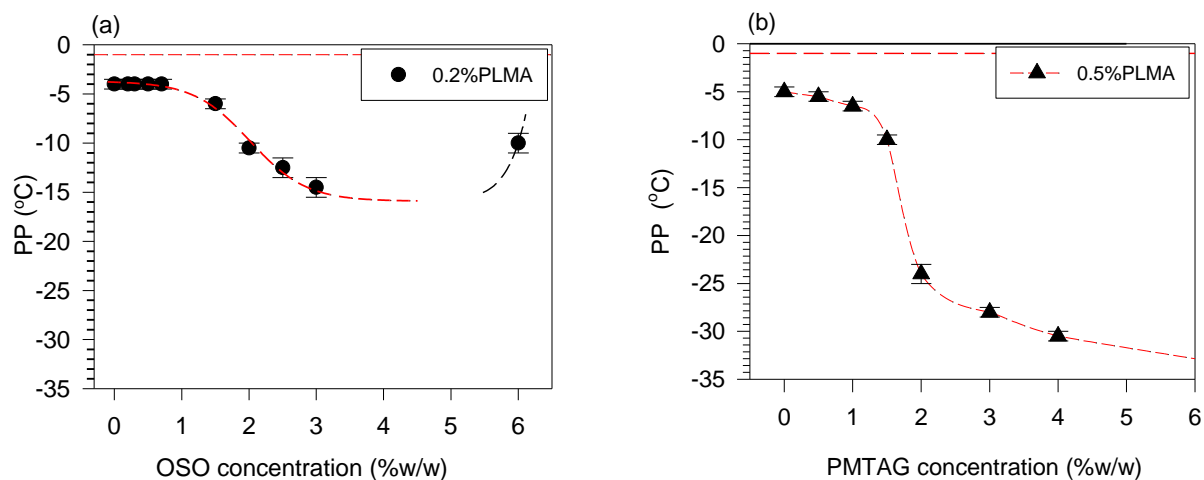
Figure 7.8. Pour point of Soy1500 supplemented with (a) PLMA and OSO cocktail additives with loading of PLMA fixed at 0.2% w/w and varying OSO concentration, (b) PLMA and PMTAG cocktail additives with PLMA loading fixed at 0.5% w/w and varying PMTAG concentration. Upper horizontal line is PP of Soy1500 biodiesel, and dashed lines passing through the data points are guides for the eye. The uncertainty attached is the standard error associated with the measurement.

The metathesized product of palm oil achieved a much more dramatic decrease in the PP of Soy1500, where a rather exceptional depression of -30 °C was obtained with the mixture of 4% w/w PMTAG and 0.5% w/w PLMA.

The trend observed in the depression (inverse of the trend shown in Fig. 7.8a and 8b) are those of multiplicative effects. It is characterized by an elongated S-shaped, or sigmoid curve typical of so-called "population growth rate" trends, followed by a capping effect. It is very similar to an "augmentation" pattern of population density that increases slowly initially, then increases rapidly, approaching an exponential rate; but then, as limiting factors are encountered, declines in a negative acceleration phase until a limit is approached asymptotically. This type of growth is termed density-dependent. The point of stabilization, or zero rate, is termed the saturation value (symbolized by K) or carrying capacity of the environment for that entity. K represents the upper asymptote of the sigmoidal or S-shaped curve. A tentative fit to a sigmoidal function of the S-shaped segment of the PP depression curve due to OSO with PLMA yielded a saturation value K= 15.8 °C (R^2= 0.99693). The capping of the effect at 6% w/w OSO can be attributed to "increasing environmental resistance" analogous to "population killers".

The tentative fit to one sigmoidal function of the S-shaped segment of the PP depression curve due to PMTAG with PLMA was not successful, understandably, as it obviously shows the superposition of more than one sigmoid. Its fit to two superimposed sigmoidal functions yielded saturation values K= 19.0 °C and 33.6 °C (R^2= 0.99993). The estimation obtained with the available data indicates that with the 0.5% w/w PLMA+PMTAG cocktails one can achieve a depression 4 °C larger if not more than what was obtained with the 0.5% w/w PLMA+4% w/w PMTAG.

We do not discuss further the implications of this model, particularly in terms of rate and acceleration, because more data are needed to avoid unsupported speculations.

Table 7.3. Pour point (PP) of the most effective samples. ΔPP is the difference between PP of the sample and PP of pure biodiesel (-1 ℃).

Additive	CP (±0.5 ℃)	ΔPP (±0.5 ℃)
1.5% w/w OPO	-2.0	1.0
2.0% w/w OSO	-5.0	4.0
0.5% w/w D	-4.0	3.0
2.0% w/w MSBO	-6.0	5.0
2.0% w/w PMTAG	-8.0	7.0
1.0% w/w PLMA	-6.0	5.0
0.2% w/w PLMA+1.5% w/w OPO	-4.0	3.0
0.2% w/w PLMA+0.5% w/w D	-5.0	4.0
0.2% w/w PLMA+2% w/w PMTAG	-13.0	12.0
0.5% w/w PLMA+2% w/w PMTAG	-24.0	23.0
0.5% w/w PLMA+4% w/w PMTAG	-30.5	29.5
0.2% w/w PLMA+2% w/w MSBO	-6.0	5.0
0.2% w/w PLMA+2% w/w OSO	-10.5	9.5
0.2% w/w PLMA+3% w/w OSO	-15.0	15.0

7.8 Microstructure Development of Mixtures of Biodiesel with Different Additives

7.8.1 Effect of Single Additives on the Microstructure of Biodiesel

The time resolved PLM (provided in the Appendix in Fig. A8) shows that pure Soy1500 developed fibril like entities from a centre of nucleation which grew radially, very rapidly, into a very large distorted crystal (~1500 μm) as the temperature was decreased.

This microstructure development is reminiscent of the crystallization of pure saturated FAMEs; MeS in (Chapter 4), and MeP in (Chapter 3) . While cooling, several branches grew from these fibrils, forming a network in which the remaining liquid phase was trapped. The trapped fuel started crystallizing within the network below -10 °C as small granules on the fibrils. The microstructure observed for Soy1500 was the result of a rapid crystallization of the saturated FAMEs forming a continuous solid network in which the trapped liquid unsaturated FAMEs crystallized as the temperature was decreased.
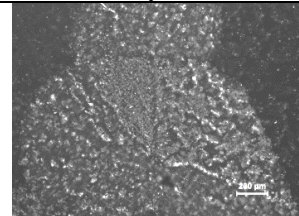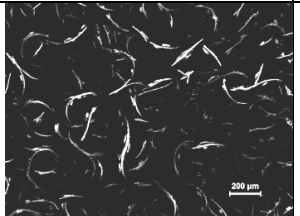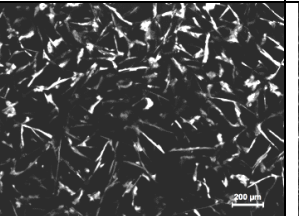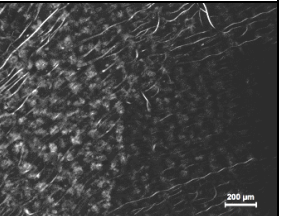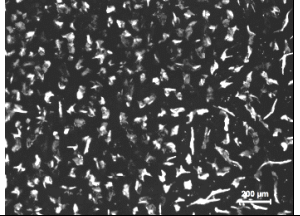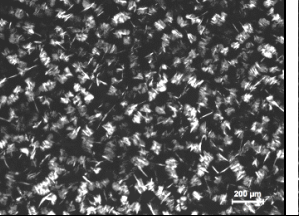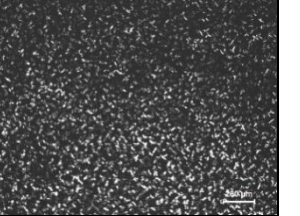
(a) Soy1500		(b) 0.2% w/w PLMA		(c) 0.5% w/w D		(d) 1.5% w/w OPO	
1500 ±500	1500 ±500	125 ±25	15 ±5	250 ±50	25 ±5	1500 ±50	700 ±5
		(e) 2% w/w MSBO		(f) 2% w/w OSO		(g) 2% w/w PMTAG	
		120 ±20	20 ±10	150 ±50	70 ±5	30 ±10	10 ±5

Figure 7.9. PLM of mixtures of Soy1500 and selected additives taken at -50 °C after cooling from the melt at 3 °C /min. The concentration of additives is provided on the top of each image. The average characteristic dimensions of the microstructures (in μm) are provided below the images. The uncertainty attached is the standard deviation from all the distinguishable microstructures of the slides of at least two runs.

Figure 7.9 shows the final microstructure of biodiesel with selected concentrations of VOCMs. As can be seen, the additives dramatically altered the microstructure of the

crystallized biodiesel and considerably reduced the crystal size (crystal size of the mixtures is provided below the images of Fig. 7.9). The original fibrils were reduced into elongated worm-like or platelet-like entities. As illustrated clearly in the PLMs of Fig. 7.9, the type, shape and size of the microstructures depended on the type and concentration of additive.

7.8.1.1   Effect of the Structured TAGs on the Microstructure

The time resolved PLM of Soy1500 with 1.5% w/w OPO (Fig. 7.10a) revealed that OPO affected the microstructure of the fuel at the earliest stages of crystallization. OPO in fact prevented the radial growth of the crystals and allowed the development of long thin fibrils indicating a strong directional growth. Furthermore, OPO prevented the branching of the fibrils contrary to what was observed in Soy1500 alone. The remaining liquid phase in the system started to crystalize at -9 °C giving small granular microstructures and leading to a final microstructure that was similar in many aspects to that of pure Soy1500. The growth rate of the fibrils was similar to that of the radial microstructure of Soy1500, indicating that it was the saturated FAMEs that were involved in this development. The PLM reveals that OPO was involved primarily with the saturated FAMEs of Soy1500 as early as the nucleation stage, locking any lateral growth probably via geometric steric hindrance of its kinked oleic moieties. The PLM explains why although OPO disrupts the crystallization of the fuel at both the nucleation and growth stages, particularly its saturated FAMEs, it does not favorably impact the PP. In fact, the solid network that was formed, although different, was formed as rapidly as the one formed by Soy1500 alone.

Time lapse PLMs of the Soy1500 with 2% w/w OSO mixture (Fig. 7.10b) revealed a different microstructure development than with OPO. In this case, the fuel was not only prevented from crystallizing in the lateral directions but also severely constrained in the

longitudinal direction. As a result, a large number of small platelet-like microstructures were formed, distributed homogeneously in the liquid phase. More importantly, these entities grew very slowly with decreasing temperature, allowing for the slow crystallization of granular entities on their walls. The development of a critical mass for these entities was necessary to build a gelling network. The delay observed between the formation of the early crystals and a binding solid network explains the large decrease in PP due to OSO. The action of OSO was different from OPO, particularly in supressing the growth in all directions as indicated by the formation of small platelets instead of long fibrils
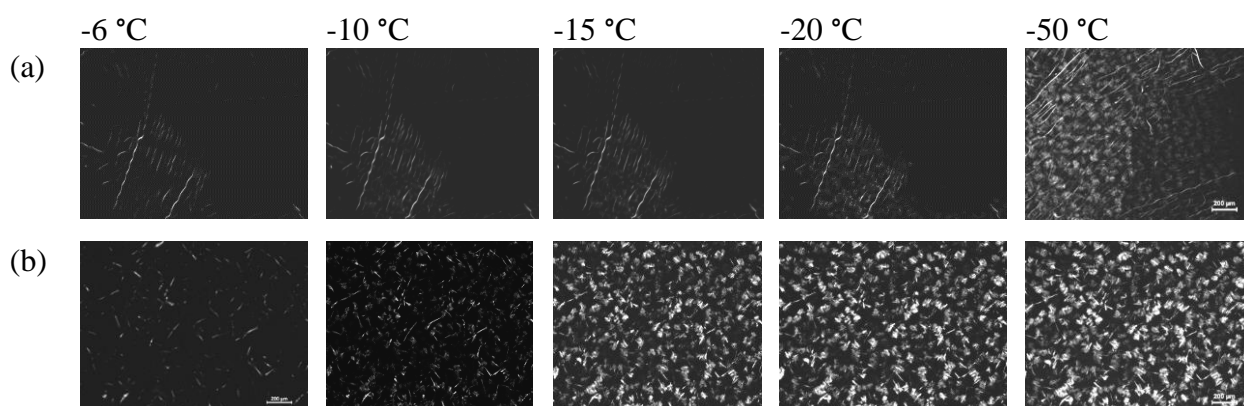
Figure 7.10. Microstructure development of Soy1500 biodiesel supplemented with (a) 1.5% w/w OPO and (b) 2% w/w OSO. Images were taken at different temperatures while cooling from the melt at a rate of 3 °C/min. The temperatures were reported on the top of each image.

7.8.1.2 *Effect of MSBO and PMTAG on the Microstructure*

Microstructure of Soy1500 was also disrupted significantly by the metathesized vegetable oils, MSBO and PMTAG. The microstructure of Soy1500 with MSBO displayed platelet like microstructures (Fig. 7.11a), randomly distributed in the liquid

phase. The microstructure of Soy1500 with PMTAG (Fig. 7.11b) however displayed very small (30 µm) and dense granular microstructure.
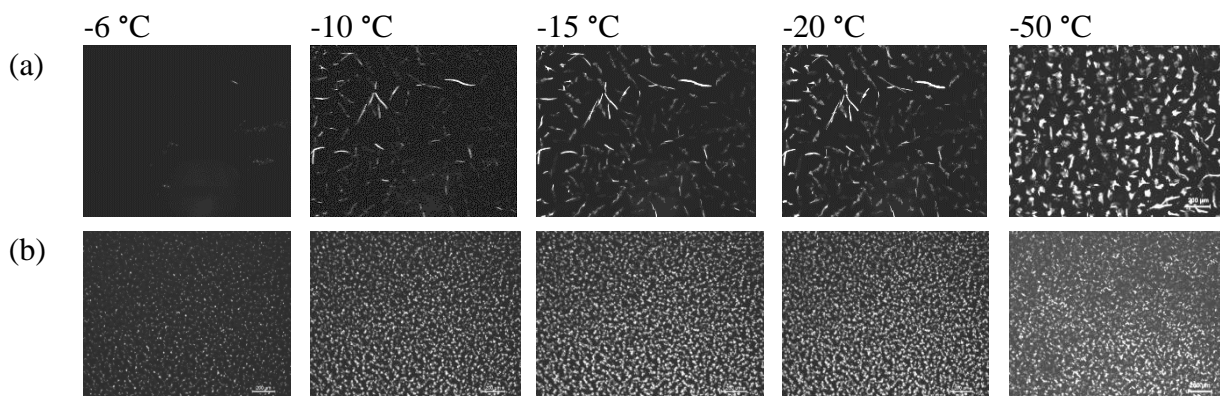
Figure 7.11. Microstructure development of Soy1500 biodiesel supplemented with (a) 2% w/w MSBO and (b) 2% w/w PMTAG. Temperature of images capture during cooling (3 °C/min) from the melt provided on top of the images.

7.8.1.3 *Effect of the TAG Dimer and Polymer on the Microstructure*

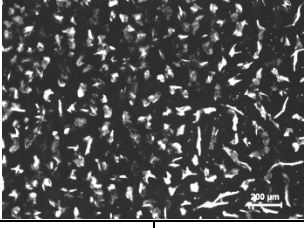Time-resolved PLM of the samples with PLMA (Fig. 7.12a) indicate a continuous nucleation and growth of fibrils first, followed by the formation of very small grainy crystals on the walls of the fibrils. The growth of the fibrils was very rapid reminiscent but relatively slower than the radial growth of the biodiesel or saturated FAMEs. The growth of the fibrils completed at -6 °C, just 2 °C below the appearance of the first crystal. The directional growth continued until the small crystals started to appear, indicating that the fastest directional growth, although being slowed down compared to what was observed in the radial growth of the biodiesel, was not totally inhibited by PLMA. The nucleation of the secondary small entities was continuous and their growth was slow.

The correlation between the numbers of fibrils with concentration of PLMA (See Appendix in, Fig. A9) and the related decrease in the length of the fibrils with the fact that saturated FAMEs content was constant support a two-step crystallization process arbitrated by PLMA. It is safe to assume that the saturated FAMEs were the molecules that were forming the fibrils and that PLMA was anchored to the other growing surfaces, allowing the directional growth until all the saturated FAMEs of the biodiesel are spent. The nucleation and growth of the small crystals on the walls of the fibrils is associated with the unsaturated FAMEs of the biodiesel. The PLM data indicate that the nucleation and growth rate of these entities was effectively controlled to a large extent by PLMA.
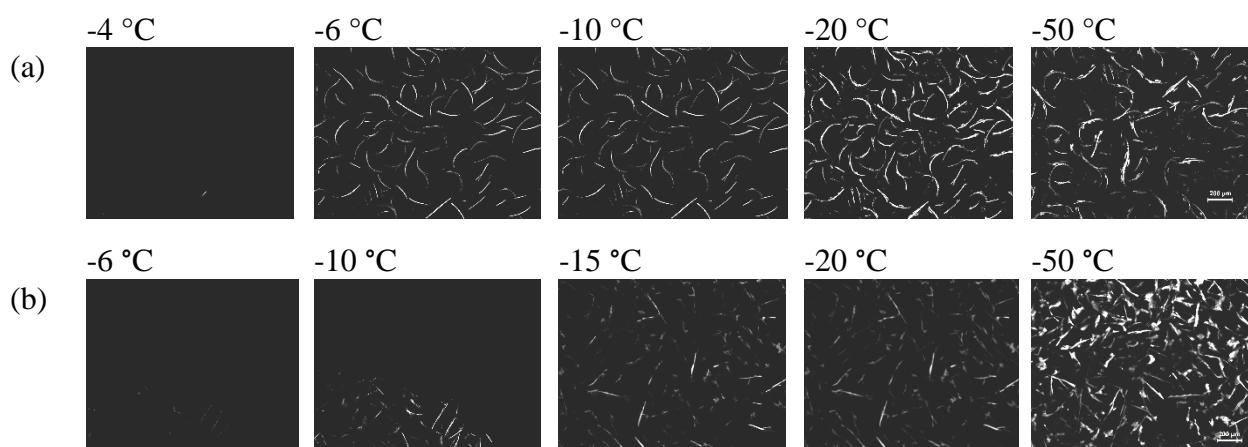
Figure 7.12. Time-resolved PLM of (a) Soy1500 biodiesel with 0.5% w/w PLMA and (b) Soy1500 with 0.5% w/w D. Images were taken at different temperatures while cooling from the melt at a rate of 3 °C/min. The temperatures were reported on the top of each image.

As the time resolved PLM shows, Soy1500 with the D mixture also displayed short fibril-like microstructures (Fig. 7.12b). The effect of the D on the microstructure of Soy1500 resembles that of PLMA, suggesting similar mechanisms of action. Similarly, as

the sample was cooling, small crystals appeared at the walls of the fibrils but at significantly smaller rates. These entities remained very small even at -50 °C. This shows that, PLMA and the D additives inhibited the growth of both saturated and unsaturated FAMEs in the system.

7.8.1.4 *Effect of Concentration of VOCMs on the Microstructure*

The microstructure development of Soy1500 depended on the concentration of the additive also. The additive concentration primarily influenced the length of the fibrils and the rate at which the secondary crystals appeared and grew on the walls of the fibrils. The effect of concentration of VOCMs on the microstructure is illustrated very well by the experiments with PMTAG. The microstructures obtained at -50 °C for the samples of Soy1500 supplemented with different amounts of PMTAG are shown in Fig. 7.13. As can be seen in the figure, long fibrils were obtained with the low concentration of 0.5% w/w PMTAG (Fig. 7.13a). The fibrils shortened dramatically as the concentration was increased to 1% w/w PMTAG, (Fig. 7.13b) then became small platelets for 2% w/w PMTAG (Fig. 7.13c).

(a) 0.5%PMTAG   (b) 1%PMTAG   (c) 2%PMTAG
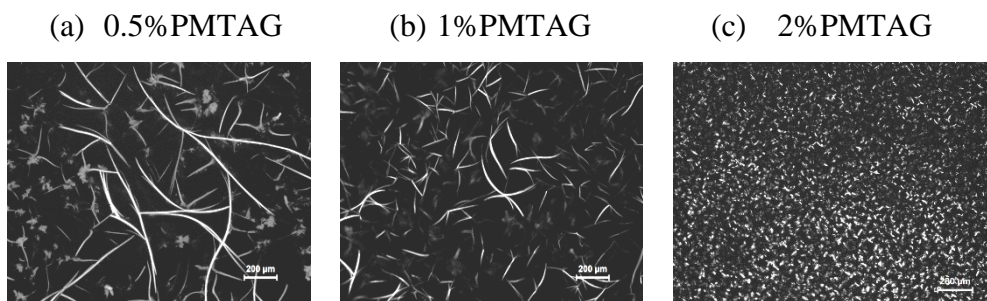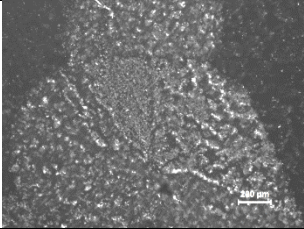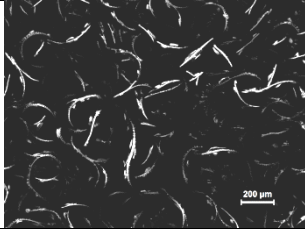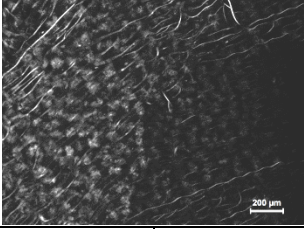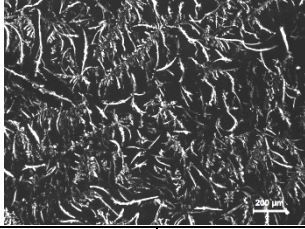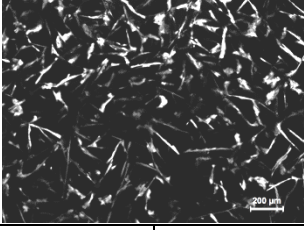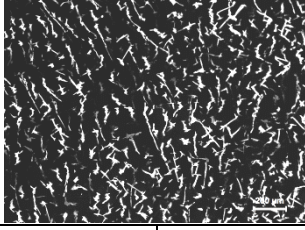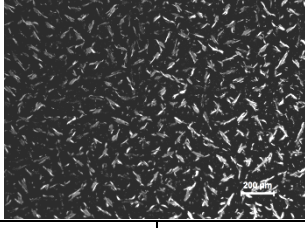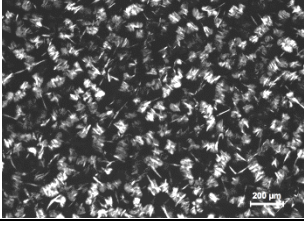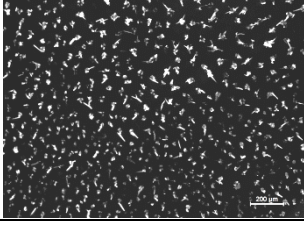
Figure 7.13. Microstructure development of Soy 1500 biodiesel supplemented with 0.5, 1.0 and 2% w/w PMTAG concentration. Images were taken at -50 °C after cooling from the melt at 3 °C/min.

7.8.2 Effect of Cocktail Additives on the Microstructure of Biodiesel

The effect of the combination of OSO, OPO, D, MSBO and PMTAG with PLMA on the final microstructure of Soy1500 is shown in Figs. 7.14a-f. The combination of PLMA with the VOCM additive resulted in a significant decrease of both the length and breadth and number density of the microstructures compared to the effects of the VOCM alone.

	VOCM alone		VOCM+0.2% w/w PLMA	
(a) Soy1500				
Length/Breadth	1500 ±500	1500 ±500	125 ±25	15 ±5
(b) 1.5% w/w OPO				
Length/Breadth	1500 ±50	700 ±5	500 ±20	200 ±5
(c) 0.5% w/w D				
Length/Breadth	250 ±50	25 ±5	200 ±50	10 ±5
(d) 2% w/w MSBO				
Length/Breadth	120 ±20	20 ±10	80 ±20	15±10
(e) 2% w/w OSO				
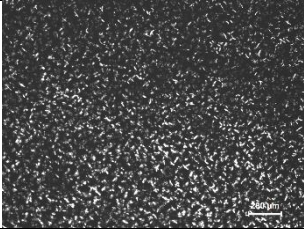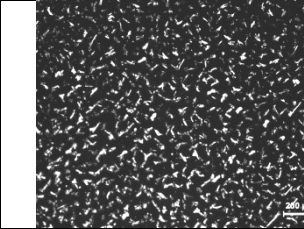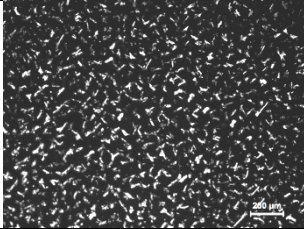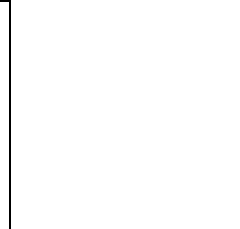
Length/Breadth	150 ±50	70 ±5	100 ±20	20 ±10
(f) 2% w/w PMTAG				
Length/Breadth	30 ±10	10 ±5	30 ±10	10 ±5

Figure 7.14. PLM taken at -50 °C after cooling from the melt at 3 °C/min of Soy1500 biodiesel with VOCM additives alone and with the VOCM and PLMA. The concentration of the VOCM additive is provided on the left side of the PLM images. The average characteristic dimensions of the microstructures (in µm) are provided below the images. The uncertainty attached is the standard deviation from all the distinguishable microstructures of the slides of at least two runs.
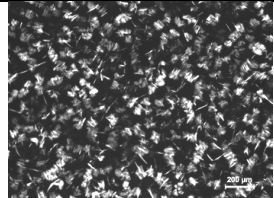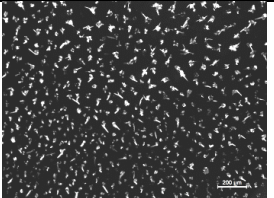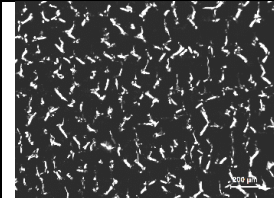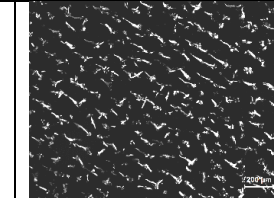
	+ 0.2% w/w PLMA		
(a) 2%OSO	(b) 2% w/w OSO	(c) 2.5% w/w OSO	(d) 3% w/w OSO

Figure 7.15. PLM images of Soy1500 with binary cocktails of 0.2%PLMA and OSO taken at -50 °C. Soy1500 mixed with (a) 2% w/w OSO alone, (b) 0.2% w/w PLMA and 2% w/w OSO, (c) 0.2% w/w PLMA and 2.5% w/w OSO; and (d) 0.2% w/w PLMA and 3% w/w OSO. The samples were cooled at 3 °C/min.

The VOCM concentration was also a factor in the changes in the microstructure of Soy1500 with the VOCM/PLMA cocktail additives. As exemplified in Fig. 7.15a-d for the typical case of OSO with 0.2% w/w PLMA, the increase of OSO concentration from

2% w/w to 3% w/w, significantly reduced the microstructure density allowing for a very large oil phase even at very low temperature, such as at -50 °C (Fig. 7.15a-d).

7.9 PP and Average Microstructure Size Correlations

The PP and average microstructure size shown in Fig. 7.16, correlate very well.

The plot of average crystal size versus CP, except OPO for which the crystal size was not measured accurately, yielded linear relationships (Fig. 7.16b; a= 1.6±0.2 and y_0= 7.6±1.3, R^2= 0.9125, W Statistic= 0.9357 and Significance Level = 0.0500) indicating a strong correlation between the two parameters.
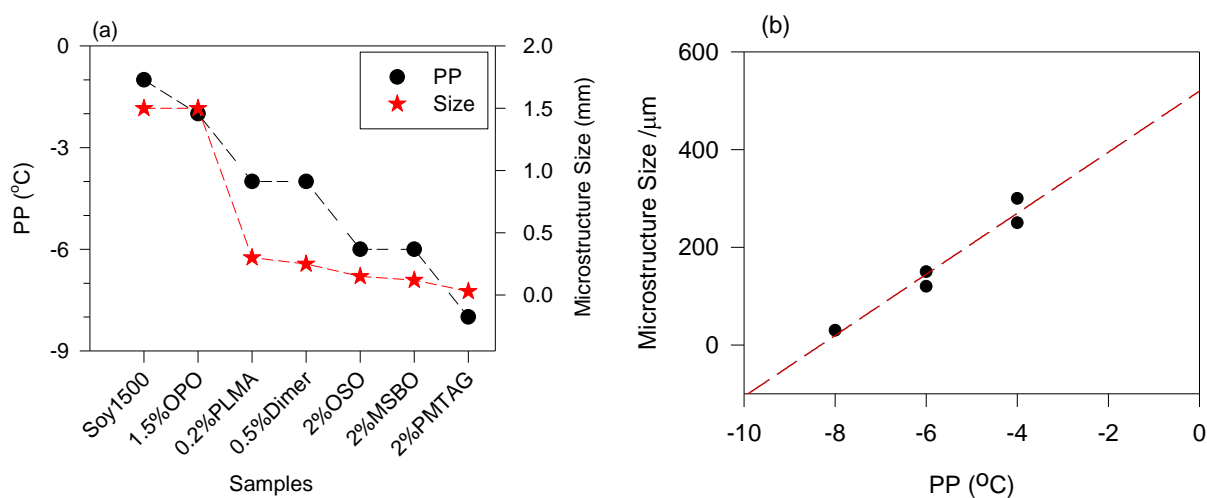
Figure 7.16. (a) Pour point, and average microstructure size determined using PLM for selected mixtures, and (b) Pour point versus average microstructure size

7.10 Mechanism of Action of the Additives and Synergy

The combination of a VOCM with a PPD in a cocktail perform more effectively than any single additive, the effect being more pronounced on PP than CP. The effect of the additives manifested by a strong directional inhibition of growth, dramatically reducing the

size of the microstructures and delaying the formation of a binding network. The structural features of the additive as well as concentration determined the extent to which the microstructure of the biodiesel was altered and hence the magnitude of CP and PP depressions. The effectiveness of the cocktail additives is directly correlated to their ability to work synergistically at different length scales, (a) delaying nucleation, (b) preparing the nuclei for an alteration of the microstructure, typically a dramatic reduction of crystal size, and then (c) slowing down the formation of bridges between growing crystals. The right amount of one additive is needed so all the saturated FAMES of the fuel, MeS and MeP in the case of Soy1500 are spent into forming the smallest crystals possible, and right amount of the other additives to provide the necessary barrier to growth and aggregation of these crystals. Note that although very structure specific, the particular contribution of the VOCM or PPD is not restricted to one of these actions. The ultimate result is the delaying of the formation of a gelling network.

The action of the VOCMs depend on the type of molecular lamellas that they initiate with the saturated FAMEs of the fuel and on the following interactions with its unsaturated molecules. The chain length mismatch (CLM) between the interacting moieties is a determining factor as it determines the methyl end chain interactions at the terrace level for further growth [29]. With a CLM= 0, when growth is not hindered spherulitic microstructures are formed easily. When there is a CLM, due to the missing of atoms there will be a void created on the terrace site of the lamellae, which reduces the lattice cohesion energy [30]. This may interrupt the formation of large microstructures. The results obtained with OPO and OSO TAGs is very telling in this regard.

The addition of OSO to Soy1500 resulted in a much more significant depression of PP or CP than OPO despite a strong directional inhibition of growth. This is related to the relative action of OPO and OSO on specific FAMEs composing Soy1500. The usual mere similarity/dissimilarity criteria that explain the disturbance of crystallization as explained in Chapter 2 is obviously not sufficient to justify such stark differences between the actions of OSO and OPO as both present similar linear features at the *sn*-2 position compatible with the straight saturated FAMEs and two kinks that prevent further packing. Obviously, CLM between the TAG and the FAMEs play a critical role. In Soy1500 supplemented with OPO or OSO, the one-directional growth was promoted at the detriment of the spherulitic growth which was completely suppressed. In the case of OPO, the directional growth of long thin fibrils was probably facilitated by advantageous methyl-end chain interactions due to chain length mismatch considerations.

The effect of PMTAG on PP can be explained in terms of CLM and position of the double bond considerations. PMTAG consists of modified TAGs of palm oil, in which about 28% of the C18 oleic and linoleic acids were converted into C10 and C12 moieties (9-decenoic acid and 9-dodecenoic acid). In addition to the large CLM, these modified TAGs have terminal double bonds, which are much more strained than the internal double bonds, making a methyl end terrace inadequately suited for an efficient surface of growth. These factors, particularly if in a large collection of molecules with varied structural features, are usually the origin of weak interactions and lead to the formation of small microstructures [30, 31]. PMTAG was the most effective VOCM because it is composed of a large number of molecules having an array of structural features that could address appropriately all the FAMEs of the biodiesel.

MSBO, on the other hand, although also a complex mixture, did not perform as well. Unlike PMTAG, MSBO comprises a large number of oligomers of the TAGs of its starting soybean oil that are much less effective than the modified TAGs of PMTAG at arresting growth. MSBO manifested more like PLMA and the D with long curved fibrils, indicating that it functions as more of a weak PPD than an effective VOCM.

The peculiar action of PLMA and at a lesser extent, the D and MSBO can be understood in light of the mechanism of action formulated for polymer additives. The mechanism as supported by experiments [13, 32] and theoretical molecular modeling [12] is based on the locking of the active growth faces to further growth by the adsorption of the polymer to the growing surface [13, 32, 33]. This mechanism is most efficient when along with a structural similarity a moderate CLM between the monomer of the polymer and the crystallizing entities was present. In the case of PLMA, the lauric acid moiety is structurally similar to and present small CLMs (4 and 2, respectively) with the MeS and MeP, the saturated FAMEs of Soy1500.

The different additives disrupted different levels of biodiesel crystallization. OPO, OSO, and PMTAG were able to disrupt the crystallization from nucleation and during growth to different extents; whereas, PLMA and D acted as directional growth modifiers. The latter two adsorbed on preferential growing surfaces of the crystals. In the combination VOCM and PLMA additives, the VOCM increased the nucleation rate and number of crystals, and acted as a template for crystallization. This provided increased surface area for the action of the polymer additive, resulting in further disruption of growth and crystal aggregation. The combination was most effective when the VOCM disrupted the crystallization most and induced the smallest crystals, and the PPD in optimal

concentration to adsorb in all active surfaces such with PMTAG and PLMA for example. The action of PLMA on growing surfaces of FAME crystals hence depressed the growth further and kept the fuel fluid for larger ranges of temperature even after the first crystals were observed.

At this point the fundamental mechanism for synergistic functioning of the VOCMs and PPDs cannot be accurately ascertained. However, whether it was a delay in nucleation, a disruption of the growth or inhibition of aggregation, it has been revealed that the effect of the cold flow additives were significant only when these fundamental actions resulted in a significant reduction in microstructure size. More clearly, any additive that can result in affecting FAME crystallization at the microscale is able to affect the pour point of biodiesel. The cloud point would affected as well but at lower magnitudes. A particular structural feature common to all the VOCM additives that resulted in a significant reduction of the crystal size of biodiesel was the presence of a chain length mismatch between the additive molecule and the saturated FAMEs.

7.11 Conclusions

The problems inherent to the low temperature flow of biodiesel are shown to be greatly mitigated by a judicious choice of cold flow improver (CFI) additives sourced from vegetable oils and their derivatives. A setup especially designed based on ASTM methods provided very accurate measurements of the cloud point (CP) and the pour point (PP) of biodiesel that can be directly compared to industrial field operability standardized measurements. The series of compounds investigated in the study were obtained using green and economical chemistries such as metathesis and comprise pure compounds such

as TAGs and oligomers of TAGs as well more complex mixtures such as self-metathesized soybean oil (MSBO) and cross-metathesized palm oil (PMTAG).

The single additives provided depressions in the PP of biodiesel as large as 10 °C. The compounds that were found to be most effective presented high specificity to the molecules of biodiesel, targeting its saturated FAMEs. However, although having prevented the early crystallization and dramatically reduced the size of the crystals of biodiesel, these compounds did not prevent the aggregation of the crystals and therefore did not sufficiently address lowering of the PP. These vegetable oil derivatives are basically vegetable oil crystallization modifiers (VOCMs) most effective at the nucleation and growth stages of the crystallization process where they induce dramatic changes to the type and rate of nucleation, and significantly impact the rate and direction of growth, reducing crystal size dramatically.

The combination of a pure as well as mixtures of VOCMs with a pour point depressant (PPD), namely PLMA, achieved impressive results. Depressions in PP as large as 30 °C were achieved for example in the case of PLMA with PMTAG. The cocktail additive is shown to work most effectively when the VOCM delays the crystallization onset substantially enough and then forms crystals with surface characteristics most favorable for adsorbing the PPD. Provided the right molecular structure and optimal or critical concentration used to restrain the saturated FAMEs of biodiesel, the PPD-VOCM cocktails achieved exceptional synergistic effects that not only affected the nucleation and crystal growth but also provided barriers to agglomeration and transformed the solid-liquid interface characteristics that prevented the gelling of the biodiesel for an extended temperature range. Note that although very structure specific, the particular contribution of

the VOCM or PPD is not restricted to one of these actions but rather worked in unison. The ultimate result was the delaying of the formation of a gelling network along all the length scales involved during the cooling process.

The cocktail additives investigated herein can be readily tested at an industrial scale and straightforwardly used with biodiesel and its blends to lower the CP and PP in a manner never achieved before. They are so effective that they can be used all year long even in the coldest climates. The study indicates that with a judicious selection of already tested crystallization modifiers from vegetable oils and their derivatives such as TAGs and the products of metathesis of vegetable oils, and polymer pour point depressants, that exceptional depression on both CP and PP of biodiesel can be achieved. More importantly, the valuable knowledge gathered on the specificity required, the synergistic effects and the mechanism of action of biobased additives in harmony with PPDs can be used for the design of more functional and economical cold flow improver (CFI) additives that are biodiesel specific.

7.12   References

[1] Dunn RO. Crystallization behavior of fatty acid methyl esters. J Am Oil Chem Soc. 2008;85(10):961-72.

[2] Knothe G. Dependence of biodiesel fuel properties on the structure of fatty acid alkyl esters. Fuel Process Technol. 2005;86(10):1059-70.

[3] Steppuhn H, Stumborg MA, McDonald T, Dunn R. Biodiesel Fuel Quality of Canola Feedstock Grown on Saline Land2009.

[4] Chastek TQ. Improving cold flow properties of canola-based biodiesel. Biomass Bioenergy. 2011;35(1):600-7.

[5] Dunn R, Moser B. Cold flow properties and performance of biodiesel. The Biodiesel Handbook, 2nd edn, AOCS Press, Urbana. 2010:147-203.

[6] Silva PH, Gonçalves VL, Mota CJ. Glycerol acetals as anti-freezing additives for biodiesel. Bioresour Technol. 2010;101(15):6225-9.

[7] Knothe G, Van Gerpen J, Krahl J. The Biodiesel Handbook. Champaign, IL: AOCS Press; 2005. p. 286.

[8] Ribeiro NM, Pinto AC, Quintella CM, da Rocha GO, Teixeira LS, Guarieiro LL, et al. The role of additives for diesel and diesel blended (ethanol or biodiesel) fuels: a review. Energy Fuels. 2007;21(4):2433-45.

[9] Chandler JE, Horneck FG, Brown GI. The Effect of Cold Flow Additives on Low Temperature Operability of Diesel Fuels. San Francisco, CA: Society of Automotive Engineers, 1992.

[10] Sern CH, May CY, Zakaria Z, Daik R, Foon CS. The effect of polymers and surfactants on the pour point of palm oil methyl esters. Eur J Lipid Sci Technol. 2007;109(4):440-4.

[11] Wang J, Cao L, Han S. Effect of polymeric cold flow improvers on flow properties of biodiesel from waste cooking oil. Fuel. 2014;117, Part A(0):876-81.

[12] Wu C, Zhang J-l, Li W, Wu N. Molecular dynamics simulation guiding the improvement of EVA-type pour point depressant. Fuel. 2005;84(16):2039-47.

[13] Zhang J, Wu C, Li W, Wang Y, Han Z. Study on performance mechanism of pour point depressants with differential scanning calorimeter and X-ray diffraction methods. Fuel. 2003;82(11):1419-26.

[14] Boshui C, Yuqiu S, Jianhua F, Jiu W, Jiang W. Effect of cold flow improvers on flow properties of soybean biodiesel. Biomass Bioenergy. 2010;34(9):1309-13.

[15] Soriano NU, Migo VP, Matsumura M. Ozonized vegetable oil as pour point depressant for neat biodiesel. Fuel. 2006;85(1):25-31.

[16] Soriano NU, Migo VP, Sato K, Matsumura M. Crystallization behavior of neat biodiesel and biodiesel treated with ozonized vegetable oil. Eur J Lipid Sci Technol. 2005;107(9):689-96.

[17] Schuster D, Irani C. Understanding The Pour Point Depression Mechanism-II Microfiltration Analysis of Crude Oils. Preprints of papers. 1985;30:169.

[18] Knothe G. Analyzing biodiesel: standards and other methods. Am Oil Chem Soc. 2006;83(10):823-33.

[19] Khan HU, Dilawar SVK, Nautiyal SP, Srivastava SP. New methods determine pour point more accurately than ASTM D-97. Oil Gas J.. 1993:Medium: X; Size: Pages: 74-6.

[20] Claudy P, Létoffé J-M, Neff B, Damin B. Diesel fuels: determination of onset crystallization temperature, pour point and filter plugging point by differential scanning calorimetry. Correlation with standard test methods. Fuel. 1986;65(6):861-4.

[21] Chandran DV, Bhatnagar RK. A method for synthesis of α-monoricinolein. J Am Oil Chem Soc. 1968;45(8):581-2.

[22] Bentley PH, McCrae W. Efficient synthesis of symmetrical 1,3-diglycerides. J Org Chem. 1970;35(6):2082-3.

[23] S. Pillai PK, Bouzidi L, Li S, and Narine SS. 1-Butene Metathesized Palm Oil & Its Polyol Derivatives: Structure, Chemical Composition and Physical Properties. 2015.

[24] Moser BR. Preparation and evaluation of multifunctional branched diesters as fuel property enhancers for biodiesel and petroleum diesel fuels. Energy Fuels. 2014.

[25] Soriano Jr NU, Migo VP, Matsumura M. Ozonized vegetable oil as pour point depressant for neat biodiesel. Fuel. 2006;85(1):25-31.

[26] Joshi H, Moser BR, Toler J, Smith WF, Walker T. Ethyl levulinate: A potential bio-based diluent for biodiesel which improves cold flow properties. Biomass Bioenergy. 2011;35(7):3262-6.

[27] Cao L, Wang J, Liu K, Han S. Ethyl acetoacetate: A potential bio-based diluent for improving the cold flow properties of biodiesel from waste cooking oil. Applied Energy. 2014;114(0):18-21.

[28] Chastek TQ. Improving cold flow properties of canola-based biodiesel. biomass and bioenergy. 2011;35(1):600-7.

[29] Marangoni AG, Acevedo N, Maleky F, Peyronel F, Mazzanti G, Quinn B, et al. Structure and functionality of edible fats. Soft Matter. 2012;8(5):1275-300.

[30] Fairley P, Krochta JM, German JB. Crystal morphology of mixtures of tripalmitin and butterfat. Journal of the American Oil Chemists' Society. 1995;72(6):693-7.

[31] Narine SS, Marangoni AG. The difference between cocoa butter and salatrim® lies in the microstructure of the fat crystal network. J. Am. Oil Chem. Soc.. 1999;76(1):7-13.

[32] Zhang J, Wu C, Li W, Wang Y, Cao H. DFT and MM calculation: the performance mechanism of pour point depressants study. Fuel. 2004;83(3):315-26.

[33] Zhang H, Liu H, Wang S. A new alternating copolymerized derivative as a cold flow improver for diesel fuel. Petroleum Science. 2009;6(1):82-5.

8.   Conclusions

The study conducted in this thesis provided a significant amount of the fundamental understanding essential for the rational design of effective cold flow improvers for biodiesel. All of the objectives and hypotheses outlined for this thesis have been met and addressed. The most important conclusions formulated from the study are provided in the following section.

8.1   General Conclusions and Implications

This study showed that very effective cold flow improvers (CFIs) can be sourced from vegetable oils. The metathesis of vegetable oils was demonstrated to be a relevant platform for the synthesis of compatible biodiesel-specific CFIs. Structural "families" of the complex feedstock generated from metathesis can be isolated with appropriate economical methods such as fractionation (demonstrated to be feasible in the case of MSBO) and some of these families, including MSBO itself, were demonstrated to be effective biodiesel CFIs.

As was hypothesized (Hypothesis I), MSBO comprises compounds which have the structural elements that disrupt the crystallization of biodiesel. In fact, as postulated in Hypothesis Ia, only particular components and families of compounds of MSBO were effective and resulted in the depression of the onset temperature of crystallization of biodiesel. The structural architecture which significantly disrupts the crystallization of biodiesel and improve its cold flow performance is typified by structured triacylglycerol (TAG) molecules and TAG dimers which comprise a saturated fatty acid moiety or a *trans*-unsaturated chain similar to the straight chain of the saturated FAMEs of biodiesel, along

with dissimilar kinked moieties (*cis*-unsaturated fatty acids). This corroborates Hypothesis Ib which stated that the effective molecules of MSBO possess specific structural elements that help the interaction with biodiesel molecules in such a way to prevent the packing of the saturated FAMEs of biodiesel. The optimal effect was obtained when the straight chain of the additive was in the *sn*-2 position and the kinked chains in the *sn*-1 and *sn*-3 position. This finding verifies Hypothesis Ic which related the effectiveness of the additives on particular structural architectures, specified in terms of size, number of *cis*/*trans* unsaturated fatty acids and saturated fatty acids, and their positional configuration.

As hypothesized also (Hypothesis II), the most effective components of MSBO disrupt the crystallization of biodiesel starting at the nucleation stages through a mechanism that is determined by the uniqueness of their structure. The effect is explained by the participation of the straight chain of the additive in the early crystallization of the saturated FAME, forming strong unlike pairs which, because of steric hindrances introduced by the kinks of the additive, alter the normal nucleation of biodiesel and prevent further growth, delaying the onset of crystallization.

The effect of the additives at the nucleation and growth stages was reflected measurably in the crystal structure and the microstructure of the biodiesel (Hypothesis IIa). The most effective additives resulted in much smaller microstructures, further favorably impacting the cloud point. However, even though the disruptive effect of these structures was extensive and measurably impacted the CP, it did not extend to preventing the growth and agglomeration necessary to also impact the PP. In fact all the vegetable oil derived additives affected the crystallization stages of biodiesel relevant to the CP, i.e., nucleation and growth, but only marginally those relevant to the PP (essentially aggregation).

The dimer of OPO, an oligomer of an effective CP depressor, was however different because it caused a depression of the crystallization temperature as well as the PP of biodiesel, but only in small concentrations similar to what is usually observed with polymer additives. Its disruptive effect manifested in the formation of very small crystals but did not extend to lowering the temperature of their aggregation. The dimer in fact reflects some of the crystallization modification capabilities of the structured TAGs and some of the obstruction to growth of polymers, two effects which seem to be competing. The results indicate that an oligomer consisting of two functional structured TAGs is too small to provide enough of a barrier to prevent a sufficient agglomeration of crystals, but provides valuable insight into the requirements of a single additive which could both impact CP and PP simultaneously.

Binary phase diagrams encompassing the thermal transitions, polymorphism and crystal structures, and microstructure of model structures and saturated FAMEs of biodiesel proved to be an effective means to study the additive effect on CP capable of revealing the drivers and mechanism of action of particular structures at different length scales along the crystallization path. The phase diagrams allowed the identification of transformation behavior which are desirable to reduce the crystallization temperature of biodiesel (and therefore CP), such as the eutectic and peritectic relationships, as well as those that are undesirable such as the metatectic governed transformations. Furthermore, the phase diagrams and their thermodynamic modeling revealed the effect of structural elements such as mass, chain length mismatch, oligomerization, and positional isomerism on the interactions driving the action of the additives at the different stages and length scales of fatty acid methyl ester (FAME) crystallization. The study of the model binary

systems revealed that the melting temperature as expressed with the liquidus line and as determined by PLM is strongly correlated with the crystal size, and that the transformations below the melting point which are associated with a diversity of microstructures and crystal structures were driven by the action of the different structural elements of the additives. The results of these binary phase behavior studies confirmed the hypothesis that the interaction between the additives and the FAMEs determines the solubility behavior in the liquid and solid states (Hypothesis IIb), and established predictable structure-function relationships, particularly the structural features such as chain length, chain length mismatch, symmetry and molar mass or oligomerization level of the additives. As hypothesized, quantifiable changes were measured in the polymorphism, phase trajectory, phase composition and microstructure development of the additive biodiesel mixtures.

The application of a PPD (PLMA in our case) in combination with a vegetable oil derived crystallization modifier (VOCM) resulted in impressive depressions in both CP and PP. As hypothesized in Hypothesis III, the study evidenced important synergistic effects that impacted the nucleation, the growth and agglomeration of FAME crystals beyond what the additives can singly achieve. The effectiveness of the cocktails depended strongly on the structure of the VOCM. The details of the structural compatibility between the VOCM and the PPD such as the chain length mismatch (CLM) between the interacting moieties were the determining factors of the growth rate as they shape the interactions at the level of the growing surface.

The participation of the VOCM in the crystallization of the saturated FAMEs provided the PLMA with a suitable adsorption surface for an optimized barrier action to aggregation. When a VOCM with a suitable molecular structure is combined with the PPD

at the optimal or critical concentration, the resulting cocktail provided synergies that achieved exceptional depressions in the PP of biodiesel, such as in the case of a 2%PMTAG (cross metathesized palm oil) and 0.5%PLMA mixture which depressed PP by more than 30 ℃, or the case of the 2%OSO and 0.2%PLMA mixture which depressed PP by more than 15 ℃. This is probably one of the most promising prospects for an economical, sustainable and environment friendly solution of the flow problems of biodiesel proposed so far.

The present study confirms that the crystallization of saturated FAMEs is the cause of the high CP and PP of biodiesel, and proves that the affinity of the liquid unsaturated FAMEs towards the growing solid crystal surface also matters. The best PP results were obtained with particular structures can be associated with a particular preparation of the biodiesel growing solid surface by the VOCM because the affinity of liquid oil towards a solid crystal surface depends on the properties of the surface [1].

Importantly, the cocktail mixtures tested in the study can be added directly to common biodiesel to ensure its use all year long, even in the coldest climates. Furthermore, the present work is clear evidence that a rigorous structure-function relationships approach is creditable of a fundamental understanding that can be applied straightforwardly. This approach is essential for selecting molecules of the next generation of cold flow improvers (CFI) by rational design through the choice of specific structural elements. These results and the underlying understanding of the specific interactions at play along the whole transformation path are powerful tools in the hands of the formulator for designing additives with specific molecular attributes that can be involved in the early stages of crystallization and provide at some stage of growth a suitable selective solid-liquid

interface that would prevent the acceleration of growth and keep the biodiesel fluid for extended temperatures and periods of time.

The knowledge gathered here is a gateway to understanding and therefore possibly custom-engineering lipid-based formulations for other high end applications which bear similar problematics as the cold flow of biodiesel. The fundamental knowledge that emerged from this study can be used to control and supress the crystallization of any lipid derived products such as lubricants.

8.2 Future work

The scope of the present research although very extended was limited to the effect of additives on the cold flow properties of biodiesel. The changes to other properties of biodiesel such as cetane number, kinematic viscosity, oxidative stability etc., were not considered. Also, storage studies, and engine and field tests of the additives, all important for the practical use of the created knowledge, are still to be done. A more in depth theoretical modeling would provide a more detailed fundamental understanding of the synergies between the VOCMs and the PPD. A higher level of understanding of the molecular interactions in the additive-biodiesel mixtures may be obtained by complementary experimental techniques such as atomic force microscopy and synchrotron-XRD, and more sophisticated thermodynamic models such as the Margules-type models.

8.3 References

[1] Razul MSG, MacDougall CJ, Hanna CB, Marangoni AG, Peyronel F, Papp-Szabo E, et al. Oil binding capacities of triacylglycerol crystalline nanoplatelets: nanoscale models of tristearin solids in liquid triolein. Food & function. 2014;5(10):2501-8.

Appendix

A1   Synthesis of Structured TAGs

Materials

Stearoyl chloride (98%), palmitoyl chloride (98%), linoleic acid (99%), elaidic acid (99%), linolenic acid (99%), oleoyl chloride (85%), 1, 3-dihydroxyacetone (99%), glycerol (99%), solketal (99%), pyridine (99%), N, N'-dicyclohexylcarbodiimide (DCC), 4-dimethyl aminopyridine (DMAP), and sodium borohydride were purchased from Sigma-Aldrich. Chloroform was purified by distillation over calcium hydride.

Synthesis Routes of Triacylglycerols

The different structures of the TAGs presented here are shown in **Scheme A1**. Depending on the fatty acid moiety, TAGs can be classified as **Type I** where $R_1 \neq R_2 \neq R_3$, **type II** where $R_1 \neq R_2 = R_3$, **type III**, where $R_1 = R_3 \neq R_2$, and **type IV**, where $R_1 = R_3 = R_2$.
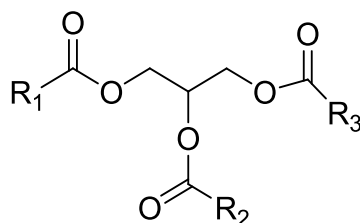
Scheme A 1. Structure of triglycerides. Type I: $R_1 \neq R_2 \neq R_3$; Type II: $R_1 \neq R_2 = R_3$; Type III: $R_1 = R_3 \neq R_2$; Type IV: $R_1 = R_3 = R_2$

Type I TAGs were prepared as shown in **Scheme A2.** One fatty acid (R1COOH) or its chloride was reacted with 1, 3 -dihydroxyacetone with DMAP as catalyst and DCC

as the condensing agent (or in the presence of pyridine), giving the hydroxyl substituted glyceroloxypropan-2-one (**I-a**), which was reacted to another fatty acid (R3COOH) or its chloride to give 1,3-Di-substituted glyceroloxypropan-2-one (I-b), followed by a reduction reaction with NaBH$_4$, yielding 1,3- glycerol. The **type I** TAGs were synthesized from 1, 3 −glycerol and fatty acids (R2COOH) or their chloride.
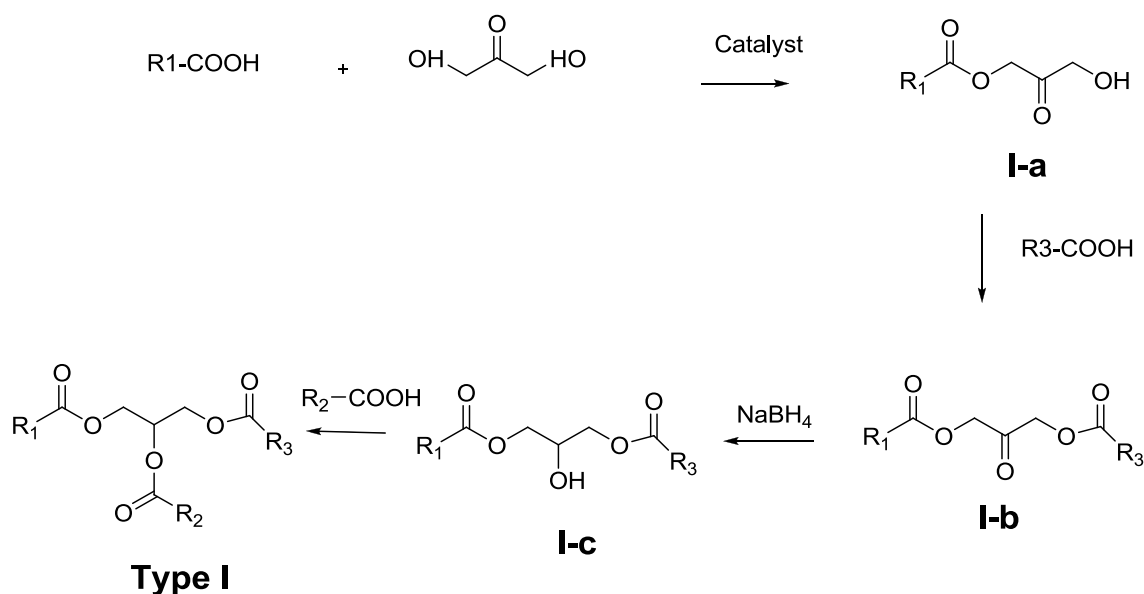
Scheme A 2. General synthesis of asymmetrical triglycerides with $R_1 \neq R_2 \neq R_3$ (Type I triglycerides)

$R_{1,2,3}$COOH= stearic acid, palmitic acid, linolenic acid, oleic acid, linoleic acid, elaidic acid

Type II TAGs were synthesized from an intermediate (2,3-dihydroxy-1-substituted propane (**II-b**)) and fatty acids as shown in Scheme A3. 1,2-Isopropylidene-3-substituted glycerol (**II-a**) was synthesized by esterification of solketal and fatty acids (or their chloride) with DMAP as catalyst and DCC as the condensing agent (or in the presence

of pyridine). 2,3-dihydroxy-1- substituted propane (**II-b**) was prepared by removing the protection group with concentrated HCl in dioxane [1][1][87][1] from **II-a.**
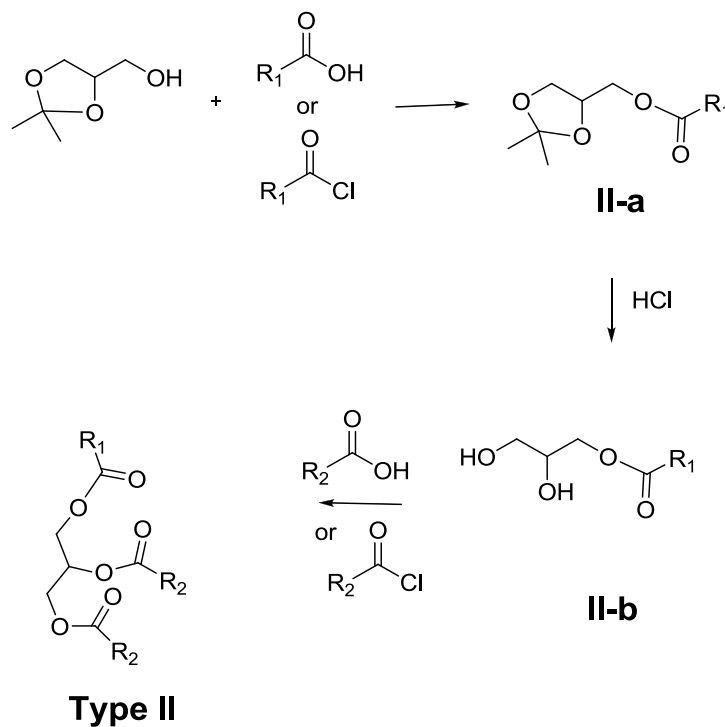
Type II

Scheme A 3. General synthesis of asymmetrical triglycerides with $R_1 \neq R_2 = R_3$ (Type II triglycerides)

$R_{1,2}COOH$= stearic acid, palmitic acid, linolenic acid, oleic acid, linoleic acid, elaidic acid

Type III TAGs were prepared as shown in Scheme A4. An intermediate, 1, 3-substituted-2-oxopropane (**III-a**) was prepared from 1, 3-dihydroxylacetone and fatty acids (or chlorides) with DMAP as catalyst and DCC as the condensing agent (or in the presence of pyridine). The resultant ketone was reduced by $NaBH_4$ in a solution of THF.
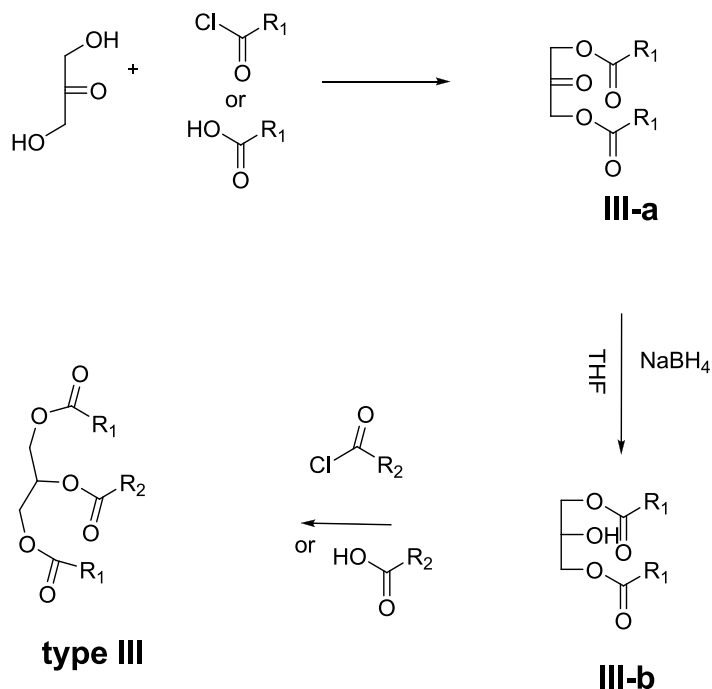
Scheme A 4. General synthesis of symmetrical triglycerides with $R_1= R_3 \neq R_2$ (Type III triglycerides). $R_{1,2}COOH=$ stearic acid, palmitic acid, linolenic acid, oleic acid, linoleic acid, elaidic acid

Type IV TAGs were synthesized by the etherification of glycerol and fatty acids (or chloride), as shown in Scheme A5.
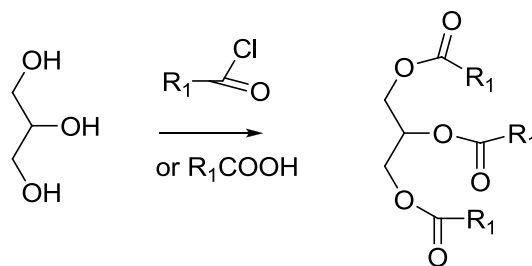
Scheme A 5. General synthesis of symmetrical triglycerides with $R_1= R_3= R_2$ (Type IV triglycerides). $R_1=$ stearic acid, palmitic acid, linolenic acid, oleic acid, linoleic acid, elaidic acid

A2   Synthesis of Oligomers

Materials

Stearoyl chloride (98%), palmitoyl chloride (98%), linoleic acid (99%), elaidic acid (99%), linolenic acid (99%), oleoyl chloride (85%), oleic acid (90%), 1, 3-dihydroxyacetone (99%), glycerol (99%), solketal (98%), pyridine (99%), N, N'-dicyclohexylcarbodiimide(DCC), 4-dimethylaminopyridine (DMAP), Grubbs generation II catalyst and sodium borohydride were purchased from Sigma-Aldrich. Chloroform was purified by distillation over calcium hydride.

Syntheses of Dimers and Quatrimers

A series of dimers and quatrimers (as showed in Scheme A6) with steric selected saturated (or trans-unsaturated) and cis-unsaturated fatty acid chain were synthesized from 2,3 –dihydroxyl-1-substituted-acetone (**1**) ,1,3-disubstituted-2-hydroxypropane (**A₁, B₁ or C₁**) and an unsaturated dicarboxylic acid (1, 18-Octadec-9-enedioic acid(**2**)) by Steglich esterification [2], where 4-dimethylaminopyridine (DMAP) was used as catalyst and N,N'-dicyclohexylcarbodiimide (DCC) as the condensing agent.

The unsaturated dicarboxylic acid here, 1, 18-Octadec-9-enedioic acid (**2**) was produced by self-metathesis of oleic acid using Grubbs catalyst. The double bond on the alkyl chain of the diacid used has a trans- geometry [3].

1,3-disubstituted -2-hydroxypropane (**A₁, B₁ or C₁**) was synthesized following a reported procedure [4]. An intermediate, 1, 3-disubstituted - 2-oxopropane was prepared from 1, 3-dihydroxylacetone and fatty acid (or chloride) with DMAP as catalyst and DCC

as the condensing agent (or in the presence of pyridine). The resultant ketone was reduced

by NaBH₄ in a solution of THF.
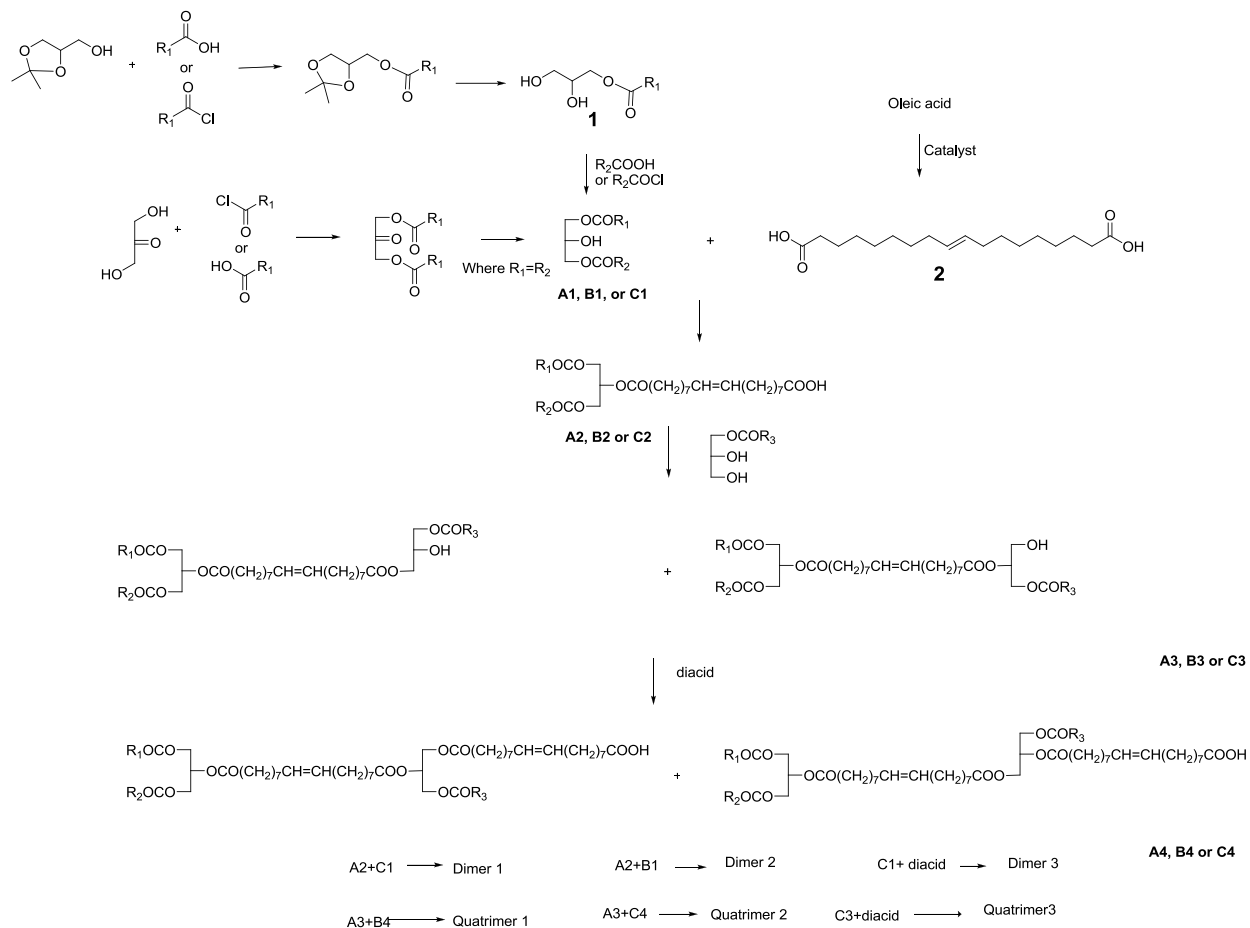
Scheme A 6. General synthesis routes of dimer and Quatrimer.

A1(2, 3, or 4): R₁COOH=R₂COOH=Oleic acid, linolenic acid, linoleic acid

B(2, 3, or 4): R₁COOH=R₂COOH= stearic acid, palmitic acid, elaidic acid

C(2, 3, or 4): R₁COOH=Oleic acid, linolenic acid, linoleic acid; R₂COOH=stearic acid, palmitic acid, elaidic acid

1,2-Isopropylidene-3-substituted glycerol was synthesized by esterification of solketal and fatty acid (or chloride). 1-substituted -2, 3-dihydroxypropane (**1**) was prepared by deprotecting 1,2-Isopropylidene-3-substituted glycerol with concentrated HCl in dioxane [1]. Increasing reaction time in the deprotection step leads to the hydroxylation of the ester group. The optimized reaction time was suggested around 2-5 hours.

The mono-ols (**A$_3$**, **B$_3$** or **C$_3$**) were prepared from mono-acids (**A$_2$**, **B$_2$** or **C$_2$**) and 1-substituted -2,3-dihydroxypropane by controlling their ratios. The mono- acids (**A$_2$**, **B$_2$** or **C$_2$**) were prepared separately from 1,3-disubstituted-2-hydroxypropane (**A$_1$, B$_1$ or C$_1$**) and 1, 18-Octadec-9-enedioic acid by controlling their ratios.

All the reactions presented here were carried out at room temperature to avoid the conversion of *cis-* geometry into *trans-* geometry which would occur at a higher reaction temperature [5].

A3 Structure of TAGs and Oligomers

Table A 1. Structures of the main alkenes present in MSBO.

Diene

Triene

Tetraene
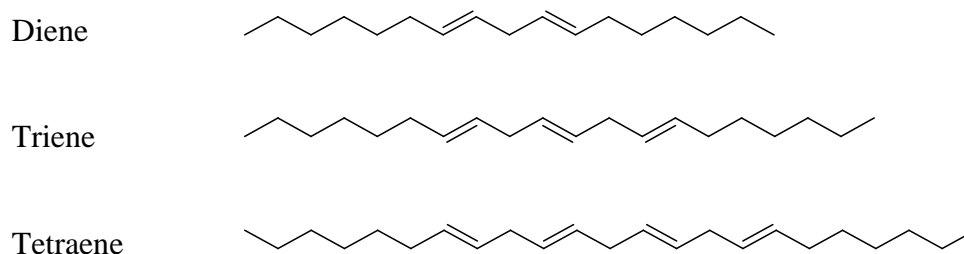
Table A 2. Model structures of the fractions collected from column chromatography of metathesized triolein (MTO) neat

Fraction	Component	Structures
MTO-F3	Triolein	OCO(CH₂)₇CH=CH(CH₂)₇CH₃ OCO(CH₂)₇CH=CH(CH₂)₇CH₃ OCO(CH₂)₇CH=CH(CH₂)₇CH₃ **Note: Containing Cis- and trans-**
MTO-F4	Dimer	OCO(CH₂)₇CH=CH(CH₂)₇CH₃ ┌ OCO(CH₂)₇CH=CH(CH₂)₇CH₃ OCO(CH₂)₇CH=CH(CH₂)₇COO ─┤ OCO(CH₂)₇CH=CH(CH₂)₇CH₃ └ OCO(CH₂)₇CH=CH(CH₂)₇CH₃
MTO-F5	Trimer	OCO(CH₂)₇CH=CH(CH₂)₇CH₃ ┌ OCO(CH₂)₇CH=CH(CH₂)₇CH₃ OCO(CH₂)₇CH=CH(CH₂)₇COO ─┤ ┌ OCO(CH₂)₇CH=CH(CH₂)₇CH₃ OCO(CH₂)₇CH=CH(CH₂)₇CH₃ └ OCO(CH₂)₇CH=CH(CH₂)₇COO ─┤ └ OCO(CH₂)₇CH=CH(CH₂)₇CH₃
MTO-F6	Quatrimer	OCO(CH₂)₇CH=CH(CH₂)₇CH₃ ┌ OCO(CH₂)₇CH=CH(CH₂)₇CH₃ OCO(CH₂)₇CH=CH(CH₂)₇COO ─┤ ┌ OCO(CH₂)₇CH=CH(CH₂)₇CH₃ OCO(CH₂)₇CH=CH(CH₂)₇CH₃ └ OCO(CH₂)₇CH=CH(CH₂)₇COO ─┤ ┌ OCO(CH₂)₇CH=CH(CH₂)₇CH₃ └ OCO(CH₂)₇CH=CH(CH₂)₇COO ─┤ └ OCO(CH₂)₇CH=CH(CH₂)₇CH₃

Table A 3. Triacylglycerols (TAGs) used in this work. S: Stearic acid; P: Palmitic acid; Ln: Linolenic acid; O: Oleic acid; L: Linoleic acid; E: Elaidic acid

IUPAC Name and Structure
TAGs Type I
SOO 9-Octadecenoic acid (9Z)-, 1-[[(1-oxooctadecyl)oxy]methyl]-1,2-ethanediyl ester
POO 9-Octadecenoic acid (9Z)-, 1,1'-[1-[[(1-oxohexadecyl)oxy]methyl]-1,2-ethanediyl] ester
SLL 9,12-Octadecadienoic acid (Z,Z)-, 1-[[(1-oxooctadecyl)oxy]methyl]-1,2-ethanediyl ester

SLnLn (9Z,9'Z,12Z,12'Z,15Z,15'Z)- 9,12,15-Octadecatrienoic acid, 1-[[(1-oxooctadecyl) oxy] methyl]-1,2-ethanediyl ester

EOO (9Z,9'Z)-,9-Octadecenoic acid, 1-[[(9E)-1-oxo-9-octadecen-1-yl]oxy]-2,3-propanediyl ester

EEO (9Z)-3-(oleoyloxy)propane-1,2-diyl bis(octadec-(9E)-enoate)

SSO (Z)-3-(oleoyloxy)propane-1,2-diyl distearate

TAGs Type II

OSO 9-Octadecenoic acid (Z)-, 2-[(1-oxooctadecyl) oxy]-1, 3-propanediyl ester

OPO 9-Octadecenoic acid (Z)-, 2-[(1-oxohexadecyl)oxy]-1,3-propanediyl ester

LSL 9, 12-Octadecadienoic acid (Z,Z)-, 2-[(1-oxooctadecyl)oxy]-1,3-propanediyl ester

LnSLn (9Z,9'Z,12Z,12'Z,15Z,15'Z)- 9,12,15-Octadecatrienoic acid, 1,1'-[2-[(1-oxooctadecyl)oxy]-1,3-propanediyl] ester

EOE (Z)-2-((E)-octadec-9-enoyloxy)propane-1,3-diyl dioleate
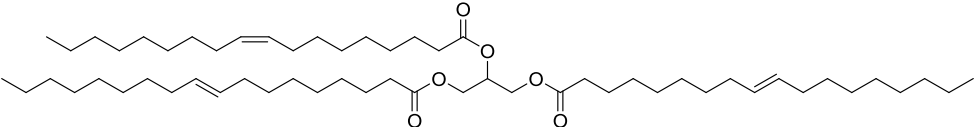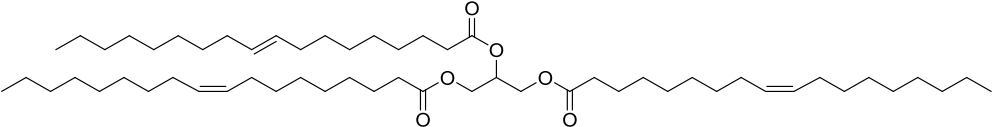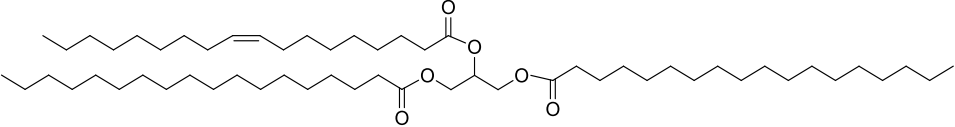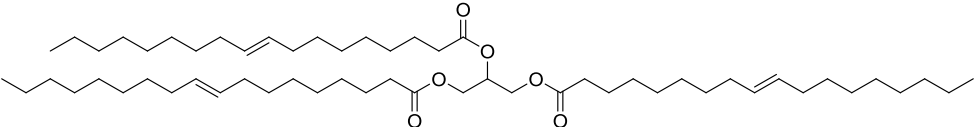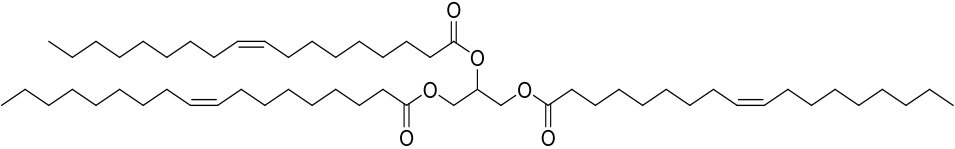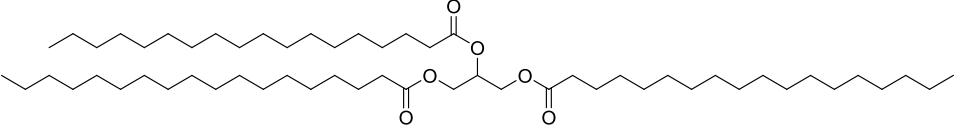
OEO (Z)-2-((E)-octadec-9-enoyloxy)propane-1,3-diyl   dioleate

SOS (Z)-2-(oleoyloxy)propane-1,3-diyl distearate

TAGs Type III

EEE (9E,9'E,9''E)-9-Octadecenoic-1-13C acid, 1,1',1''-(1,2,3-propanetriyl-1,2,3-) ester

OOO 9-Octadecenoic acid (Z)-, 1,2,3-propanetriyl ester

SSS Octadecanoic acid, 1,1',1''-(1,2,3-propanetriyl) ester

Table A 4. Structure of triacylglycerol oligomers (TAG-oligomers) used in this work

Oligomer	Structure
Dimer 1	1-(1, 3-bis (oleoyloxy) propan-2-yl) 18-(1-(oleoyloxy)-3-(stearoyloxy) propan-2-yl) octadec-9-enedioate

Dimer 2	1-(1, 3-bis (oleoyloxy) propan-2-yl) 18-(1, 3-bis (stearoyloxy) propan-2-yl) octadec-9-enedioate

Dimer3	-(1-(oleoyloxy)-3-(stearoyloxy) propan-2-yl) 18-(1-(oleoyloxy)-3-(stearoyloxy) propan-2-yl) octadec-9-enedioate

Quatrimer 1	1-(2, 23-bis ((oleoyloxy) methyl)-4, 21, 26, 43, 48-pentaoxo-45-((stearoyloxy) methyl)-3, 22, 25, 44, 47-pentaoxapentahexaconta-12, 34-dien-1-yl) 18-(1, 3-

bis   (oleoyloxy)   propan-2-yl)   octadec-9-enedioate
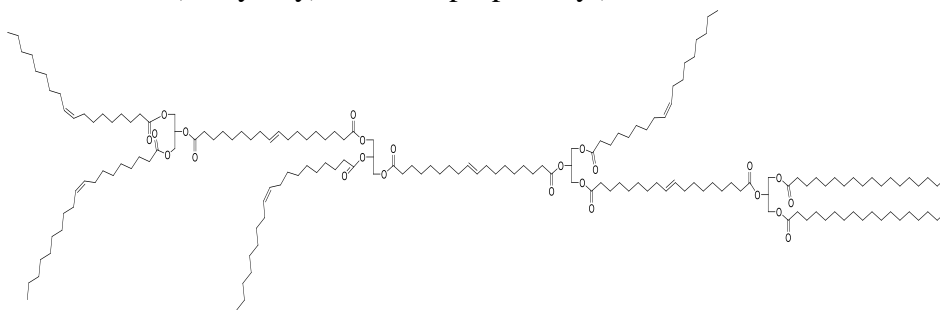
Quatrimer2   1-(2, 23-bis ((oleoyloxy) methyl)-4, 21, 26, 43, 48-pentaoxo-45-((stearoyloxy) methyl)-3, 22, 25, 44, 47-pentaoxapentahexaconta-12, 34, 56-trien-1-yl) 18 - (1,   3-bis   (oleoyloxy)   propan-2-yl)   octadec-9-enedioate
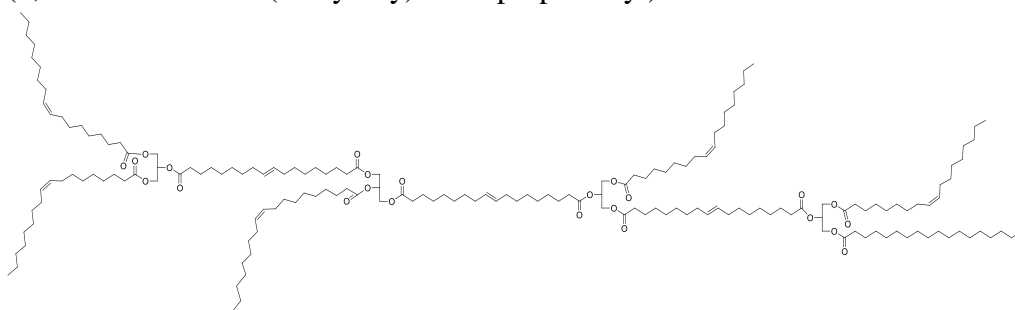
Quatrimer 3   bis (1-(oleoyloxy)-3-(stearoyloxy) propan-2-yl) O'1, O1-(((octadec-9-enedioyl) bis (oxy)) bis (3-(oleoyloxy) propane-2, 1-diyl)) bis (octadec-9-enedioate)
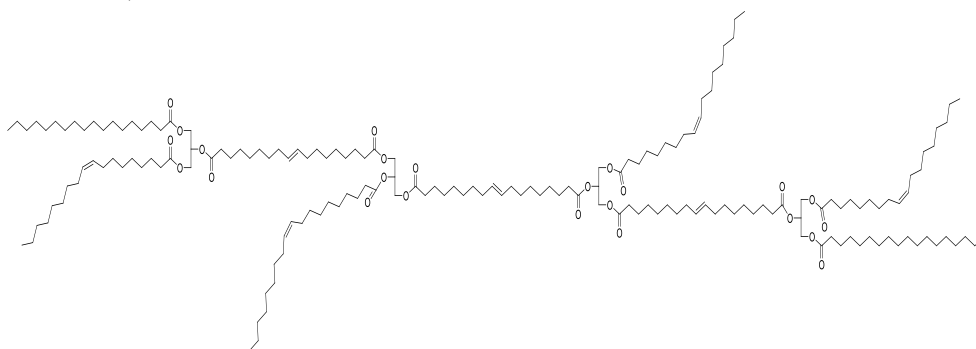
Quatrimer 4   bis (1, 3-bis (oleoyloxy) propan-2-yl) O'1, O1-(((octadec-9-enedioyl) bis (oxy)) bis (3-(oleoyloxy) propane-2, 1-diyl)) bis (octadec-9-enedioate)
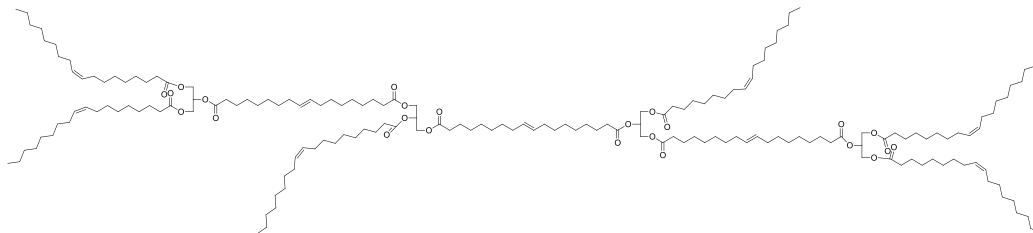
Figure A 1. ^{1}H-NMR spectra of MSBO and MSBO column chromatography fractions. a: MSBO; b: MSBO-F1; c: MSBO-F3a; d: MSBO-F3b; e: MSBO-F3c; f: MSBO-F4

Fig. A1a
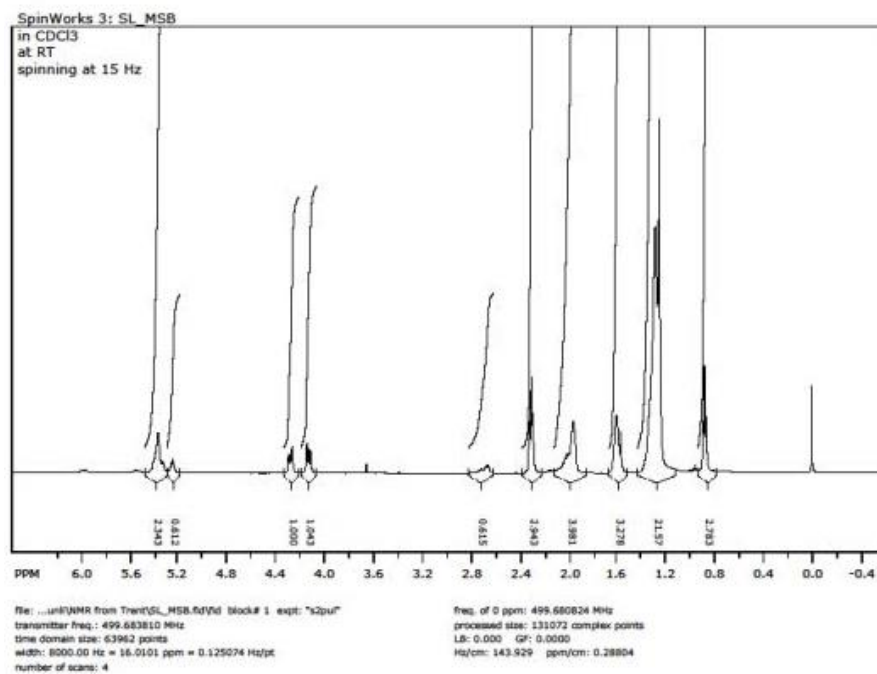
Fig. A1b

Fig. A1c

Fig. A1d

Fig. A1e

20110519-8400_NMRLQ_S4712_x_MSBO-fr-11_Li_apg_Proton
MSBO-Fr-11 in CDCl3, NMRLQ-54712x
Trent University, Shaojun Li

operator: Dr. A. Golombek
tel: 416 978-0448
email: adina.golombek@utoronto.ca
chem_Proton_Day CDCl3 /opt/data service 35

Fig. A1f

NMRLQ_R4702_SLi_MSBO_PC
sample: MSBO_PC, solvent: CDCl3
Operator: Dr. D.C. Burns
University of Toronto, Department of Chemistry, NMR Facility
e-mail: darcy.burns@utoronto.ca
phone: (416)-978-0448

Sample Name:
  NMRLQ_R4702_SLi_MSBO_PC
Archive directory:
  /export/home/vnmr1/vnmrsys/data
Sample directory:

FidFile: 20110418-NMRLQ_R4702_SLi_MSBO_PC_Proton-002

Pulse Sequence: Proton (s2pul)
Solvent: cdcl3
Data collected on: Apr 18 2011

A4   Phase behaviour of OPO/MeS System

Table A 5: Parameters used in the Bragg – William approximation to calclate the different segments of the liquidus line and corresponding values of the non-ideality of mixing parameter, ρ. ΔH_A: enthalpy of melting, and T_A: temperature of melting

Segment	Region	T_A (K)	ΔH_A (kJ/mol)	ρ (kJ/mol)	χ^2
I	$0 \leq X_A \leq 0.65$	311.13 ± 0.13	72.89	-3.5	1.1295
II	$0.65 \leq X_A \leq 0.90$	295.18 ± 0.12	195.69	-29.8	0.1930
III	$0.90 \leq X_A \leq 1.0$	292.80 ± 0.15	122.33	-97.1	0.1857

Table A 6. WAXD data measured at -40 °C of OPO/MeS mixtures cooled from the melt at 1 °C/min: d-spacing of resolved lines and corresponding Miller indices. Uncertainty= ± 0.02.

X_{OPO}	$(010)_\beta$	$\overline{6}11_{\beta M}$	$110_{\beta'}$	$0\overline{1}1_\beta$	$\overline{1}011_{\beta M}$	102_β	$\overline{1}10_\beta$	$200_{\beta'}$	100_β
(MeS)	--	--	4.29	--	--	4.02	--	--	3.62
0.15	--	4.52	4.26	--	--	4.03	--	3.84	--	3.63
0.25	--	4.52	4.27	--	--	4.03	--	3.84	--	3.64
0.40	--	4.51	4.24	--	--	4.00	--	3.83	--	3.65
0.50	--	4.51	4.23	--	--	4.03	--	3.82	--	3.65
0.60	4.54	4.51	4.23	--	--	4.01	--	3.82	--	3.65
0.64	4.58	4.52	4.24	--	--	4.04	--	3.82	--	3.63
0.70	4.59	4.52	--	4.30	--	4.04	--	3.83	--	6.65
0.75	4.57	4.52	--	4.26	--	4.04	--	3.83	--	3.66
0.80	4.57	4.52	--	4.27	4.14	--	3.99	--	3.84	3.66
0.85	4.56	--	--	4.27	4.13	--	3.96	--	3.85	3.65
0.95	4.55	--	--	4.28	4.12	--	3.99	--	3.85	3.61
OPO	--	--	--	4.22		--	--	--	3.84	--

Table A 7. SAXD data of OPO/MeS mixtures: d-spacing and corresponding Miller indices. Samples were cooled from the melt at a rate of 1 °C/min. Patterns measured at -40 °C. Uncertainty= ± 0.10.

	(001)	(002)	(004)	(006)	(008)
MeS	--	24.62	12.27	8.17	6.48
	--	24.22	12.03	8.05	6.13
	--	21.91		8.01	6.03

	(001)			(002)			(003)	
X_{OPO}	S1	S2	MeS	S1	S2	MeS	S2	MeS
0.15	64.14	42.82	24.2	33.03	21.18	12.04	14.19	7.99
0.25	64.25	42.47	24.1	32.00	21.27	12.01	14.17	8.00
0.40	63.25	42.86	24.1	31.76	21.31	12.01	14.16	8.00
0.50	--	42.66	--	--	21.17	12.02	14.14	
	(001)			(002)			(003)	
	S1	S2	OPO	S1	S2 or (003) of S1	OPO	S2	OPO
0.60	64.20	42.69	--	31.85	21.33	--	14.16	--
0.64	63.99	43.05	--	31.88	21.19	--	14.27	--
0.70	63.96	43.01	--	32.02	21.23	--	14.30	--
0.75	65	43.08	--	32.06	21.39	--	14.33	--
0.80	65.60	--	45.45	32.59	--	21.55	--	14.54
0.85	66.10	--	46.70	32.79	--	21.61	--	14.60
0.90	67.32	--	44.79	33.00	--	21.51	--	13.69
OPO	--	--	44.15		--	21.94	--	14.51
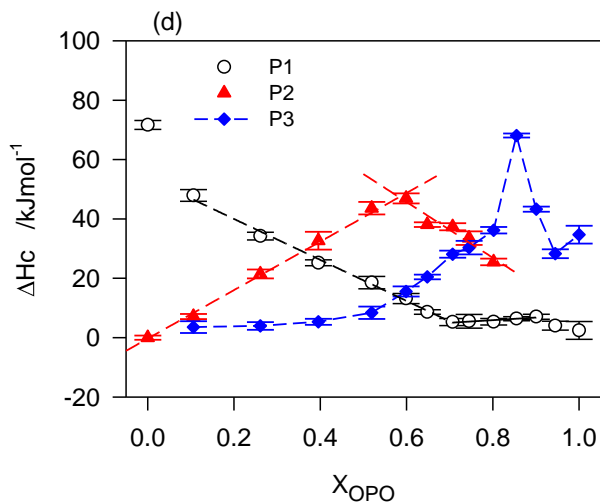
Figure A 2. (d) Enthalpy of the transitions associated with exotherms P1, P2 and P3 of Figs. 1a and b versus OPO molar ratio (○, P1, ▲, P2 and ◆, P3). (Goodness of fits R^2=0.9947 for black line, R^2=0.9281 and 0.9959 for the red lines. All fits have significance level=0.05)
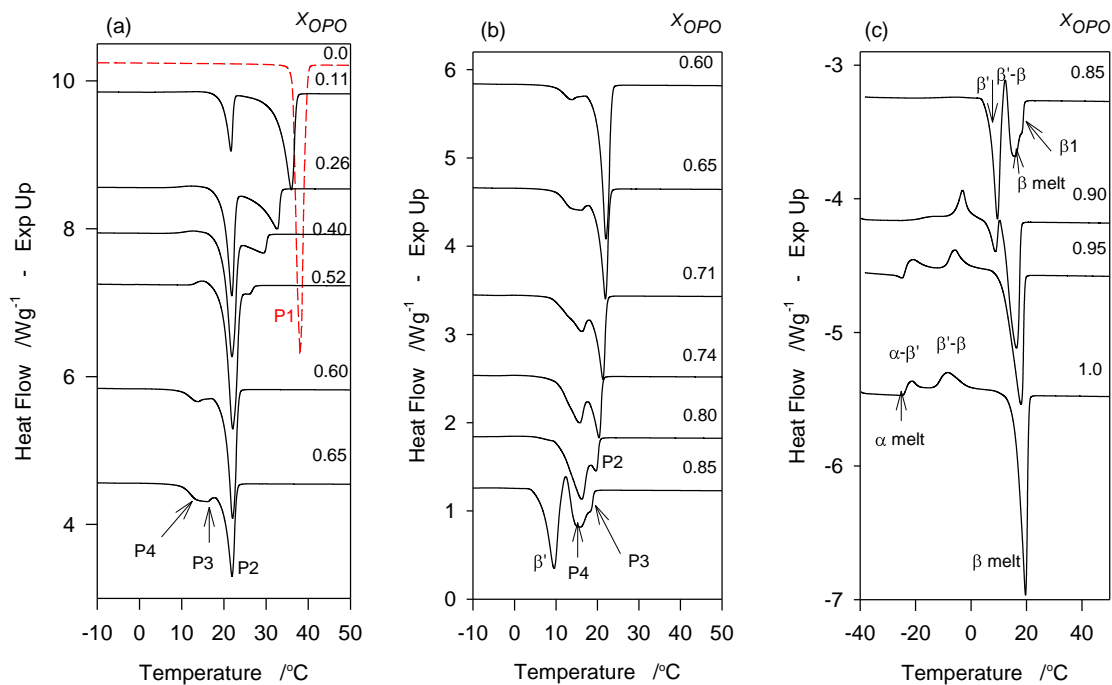
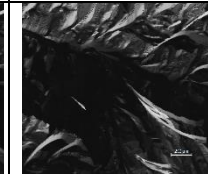**Figure A 3** (a, b and c) DSC heating traces (2 °C/min) obtained subsequent to cooling (5 °C/min) of OPO/MeS mixtures
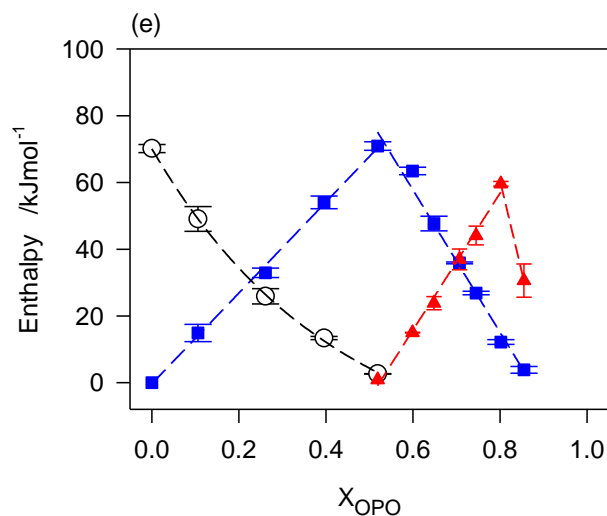
Figure A 4. Enthalpy of melting of P1 (○), P2 (■) and P3-4 (▲) of Fig. 2a plotted as a function of OPO molar ratio. (Goodness of fits: R^2=0.9980 for black line, R^2=0.9933 and 0.9999 for the red lines and R^2=0.9933 and 0.9999, and R^2=0.9856 and 0.9980 for the blue lines. All fits have significance level=0.05)
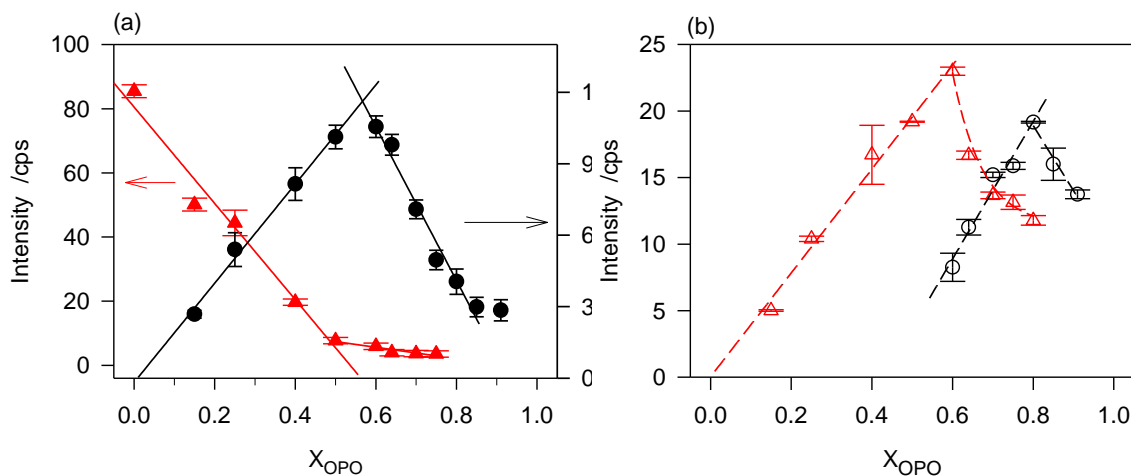
Figure A 5. Intensity versus OPO molar fraction of (a) the β_M-phase (monoclinic phase,

▲: peak at 4.03 Å) and β_{II}- triclinic phase (●: peak at 3.84 Å), . (Goodness of fits: R^2=0.9741 for red line line, R^2=0.9931 and 0.9958 for the black lines. All fits have significance level=0.05) and (b) the β_I-triclinic phase (△: Peak at 4.52 Å), and β_{II}-triclinic phase (○: peak at 4.55 Å). (Goodness of fits: R^2=0.9873 for red line, and R^2=0.9668 and 0.9783 for the black lines and R^2=0.9933 and 0.9999, and R^2=0.9856 and 0.9980 for the blue lines. All fits have significance level=0.05)
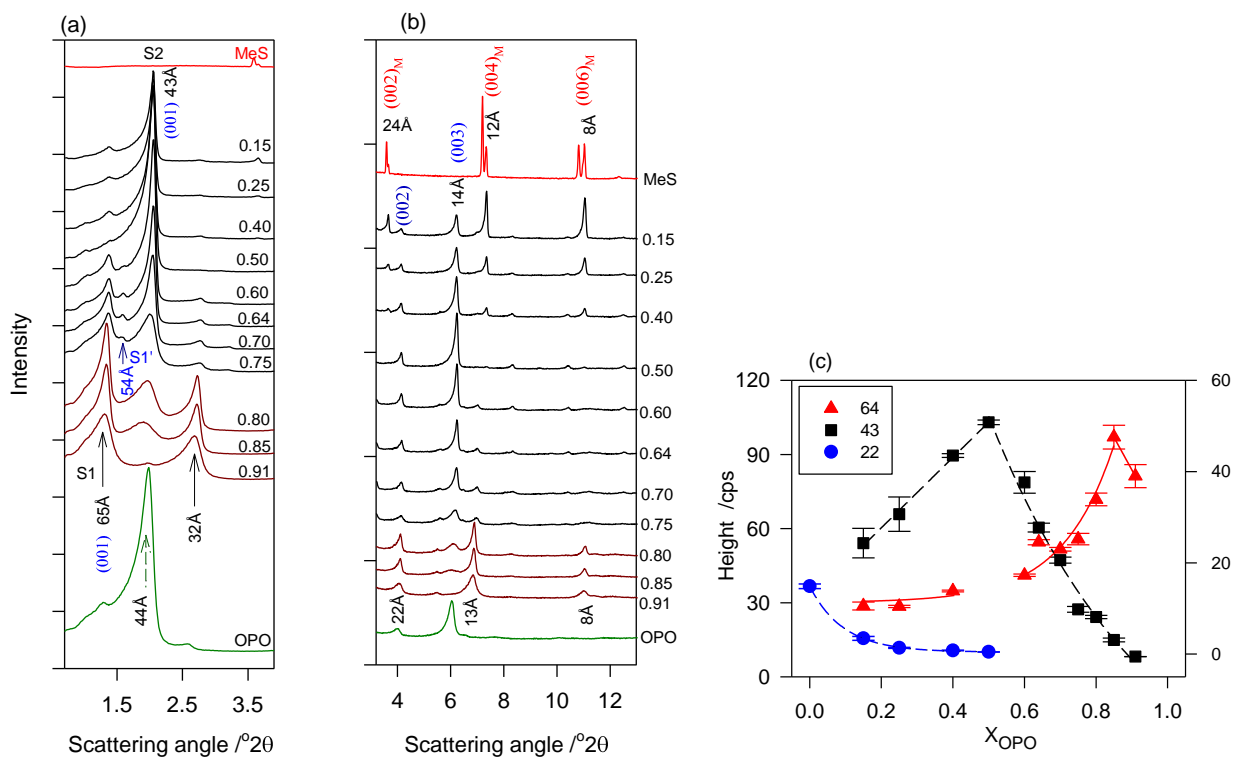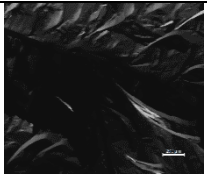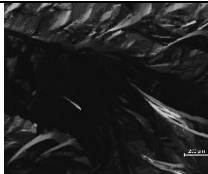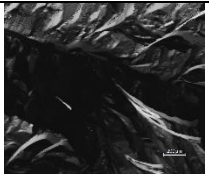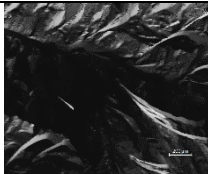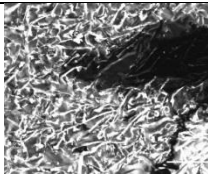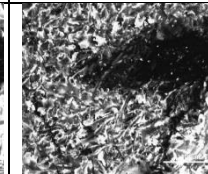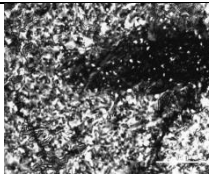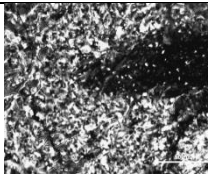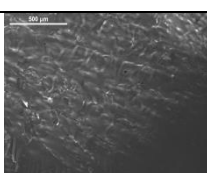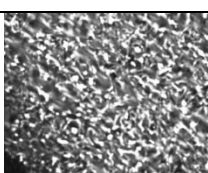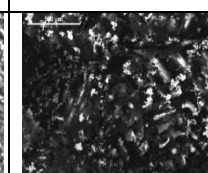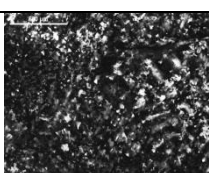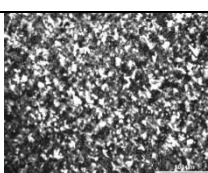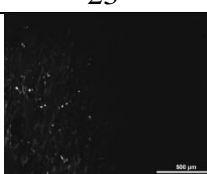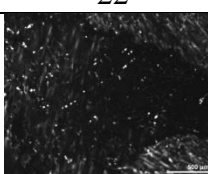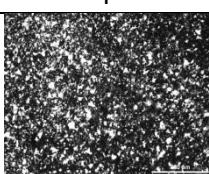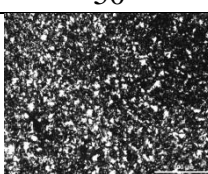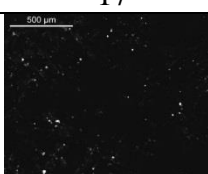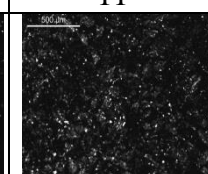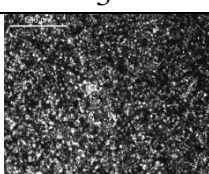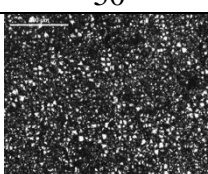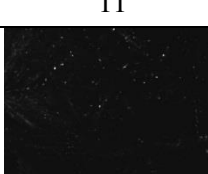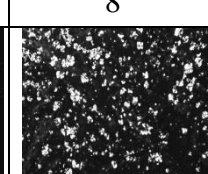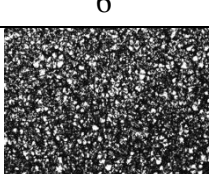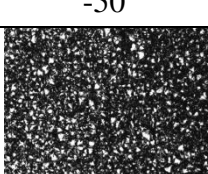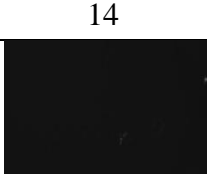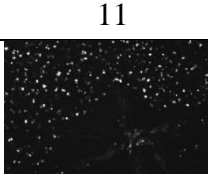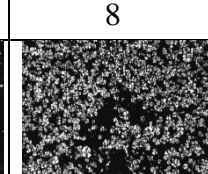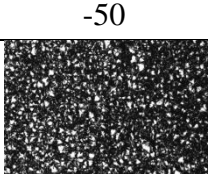
Figure A 6. (a and b) SAXD spectra of OPO/MeS mixtures measured at -40 °C after cooling from the melt at 1 °C/min. OPO molar ratio is reported on the right side of the patterns. (c). Variation of the intensity of SAXD reflections as a function of OPO molar ratio. (Goodness of fits: $R^2=0.9662$ and 0.9862 for black line, $R^2=0.9580$ for the red lines, and $R^2=0.9997$ for the blue lines. All fits have significance level=0.05)

	X_{OPO}	PLM (100X) taken at temperature (°C)				
		(a) 1st Formed	(b)	(c)	(d)	(e)
A	0.0	36	34	10	0	-50
B	0.15	32	31	10	0	-50
D	0.25	29	21	10	4	-50
D	0.40	23	22	10	4	-50
E	0.50	19	17	11	3	-50
F	0.60	15	11	8	6	-50
G	0.64	14	11	8	3	-50
H	0.70	6	5	4	-4	-50

276

		4	2	1	3	-50
I	0.75					
		1	-2	-3	4	-50
J	0.80					
		-3	-4	-6	-8	-50
K	0.85					
		-5	-7	-11	-18	-50
L	0.91					
		-10	-11	-13	-18	-50
M	1.0					

Figure A 7. Selected snapshots from the time-temperature resolved PLM (100X) of OPO/MeS mixtures. Samples were cooled from the melt at 1 °C/min.

A5   Harnessing the Synergies between Lipid Based Crystallization Modifiers and a Polymer Pour Point Depressant to Improve Cold Flow Properties of Biodiesel

0 °C   -6 °C   -10 °C   -20 °C   -50 °C
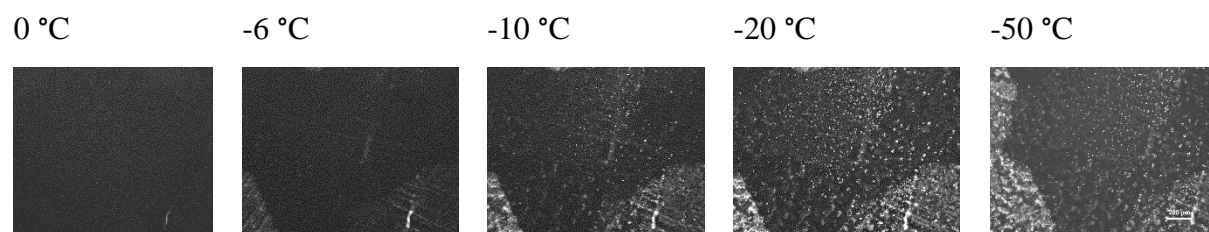
Figure A 8. Microstructure development of pure Soy1500. The images were taken while cooling the sample from the melt at 3 °C /min.
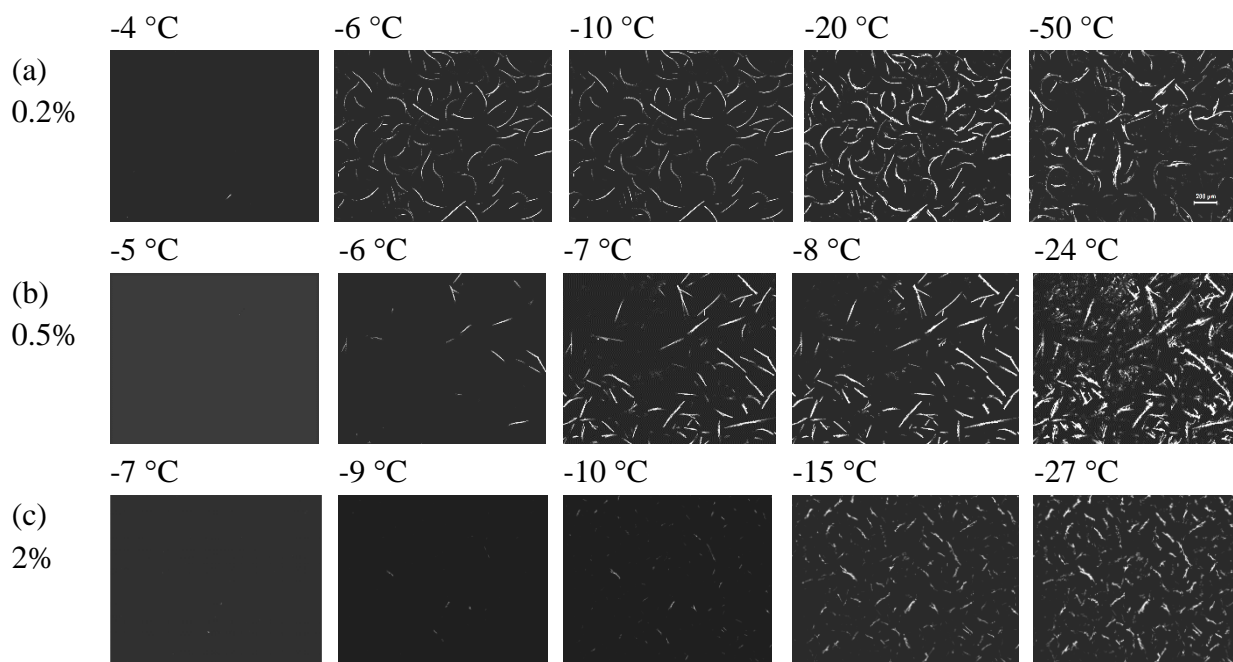
Figure A 9. Time-resolved PLM of Soy1500 with PLMA. (a) 0.2% PLMA, b) 0.5% PLMA and c) 2% PLMA. Images were taken at different temperatures while cooling from the melt at a rate of 3 °C/min. The temperatures were reported on the top of each image.

A6 References

[1] Hong JH, Oh CH, Cho JH. Stereocontrolled synthesis of novel 6 '(alpha)-hydroxy carbovir analogues. Tetrahedron. 2003;59(32):6103-8.

[2] Neises B, Steglich W. Simple Method for the Esterification of Carboxylic Acids. Angew Chem Int Ed. 1978;17.

[3] Hojabri L, Kong XH, Narine SS. Functional Thermoplastics from Linear Diols and Diisocyanates Produced Entirely from Renewable Lipid Sources. Biomacromolecules. 2010;11(4):911-8.

[4] Obika S, Yu W, Shimoyama A, Uneda T, Miyashita K, Doi T, et al. Symmetrical cationic triglycerides: An efficient synthesis and application to gene transfer. Bioorg Med Chem. 2001;9(2):245-54.

[5] Brown JH, Olenberg H. Isomorphous jojoba oil compositions containing trans-isomerized jojoba oil. In: patent Us, editor. United states patent. United states: Jojoba Growers & Processors Inc.; 1982. p. 6.

A7 Copy Right Release

RightsLink Printable License

Page 1 of 6

**ELSEVIER LICENSE
TERMS AND CONDITIONS**

Nov 25, 2015

This is a License Agreement between Athira Mohanan ("You") and Elsevier ("Elsevier") provided by Copyright Clearance Center ("CCC"). The license consists of your order details, the terms and conditions provided by Elsevier, and the payment terms and conditions.

All payments must be made in full to CCC. For payment instructions, please see information listed at the bottom of this form.

Supplier	Elsevier Limited The Boulevard,Langford Lane Kidlington,Oxford,OX5 1GB,UK
Registered Company Number	1982084
Customer name	Athira Mohanan
Customer address	Trent Centre for Biomaterials Research
	Peterborough, ON K9H7B8
License number	3663831265008
License date	Jul 07, 2015
Licensed Content Publisher	Elsevier
Licensed Content Publication	Energy
Licensed Content Title	Mitigating crystallization of saturated FAMES (fatty acid methyl esters) in biodiesel. 3. The binary phase behavior of 1,3-dioleoyl-2-palmitoyl glycerol – Methyl palmitate – A multi-length scale structural elucidation of mechanism responsible for inhibiting FAME crystallization
Licensed Content Author	Athira Mohanan,Bruce Darling,Laziz Bouzidi,Suresh S. Narine
Licensed Content Date	15 June 2015
Licensed Content Volume Number	86
Licensed Content Issue Number	n/a
Type of Use	reuse in a thesis/dissertation
Portion	full article
Format	both print and electronic
Are you the author of this Elsevier article?	Yes
Will you be translating?	No
Title of your thesis/dissertation	Mitigating Crystallization of Biodiesel: Strategies with Additives
Expected completion date	Sep 2015
	295

Estimated size (number of pages)	
Elsevier VAT number	GB 494 6272 12
Permissions price	0.00 CAD
VAT/Local Sales Tax	0.00 CAD / 0.00 GBP
Total	0.00 CAD

Terms and Conditions

INTRODUCTION

1. The publisher for this copyrighted material is Elsevier. By clicking "accept" in connection with completing this licensing transaction, you agree that the following terms and conditions apply to this transaction (along with the Billing and Payment terms and conditions established by Copyright Clearance Center, Inc. ("CCC"), at the time that you opened your Rightslink account and that are available at any time at http://myaccount.copyright.com).

GENERAL TERMS

2. Elsevier hereby grants you permission to reproduce the aforementioned material subject to the terms and conditions indicated.

3. Acknowledgement: If any part of the material to be used (for example, figures) has appeared in our publication with credit or acknowledgement to another source, permission must also be sought from that source. If such permission is not obtained then that material may not be included in your publication/copies. Suitable acknowledgement to the source must be made, either as a footnote or in a reference list at the end of your publication, as follows:

"Reprinted from Publication title, Vol /edition number, Author(s), Title of article / title of chapter, Pages No., Copyright (Year), with permission from Elsevier [OR APPLICABLE SOCIETY COPYRIGHT OWNER]." Also Lancet special credit - "Reprinted from The Lancet, Vol. number, Author(s), Title of article, Pages No., Copyright (Year), with permission from Elsevier."

4. Reproduction of this material is confined to the purpose and/or media for which permission is hereby given.

5. Altering/Modifying Material: Not Permitted. However figures and illustrations may be altered/adapted minimally to serve your work. Any other abbreviations, additions, deletions and/or any other alterations shall be made only with prior written authorization of Elsevier Ltd. (Please contact Elsevier at permissions@elsevier.com)

6. If the permission fee for the requested use of our material is waived in this instance, please be advised that your future requests for Elsevier materials may attract a fee.

7. Reservation of Rights: Publisher reserves all rights not specifically granted in the combination of (i) the license details provided by you and accepted in the course of this licensing transaction, (ii) these terms and conditions and (iii) CCC's Billing and Payment terms and conditions.

8. License Contingent Upon Payment: While you may exercise the rights licensed immediately upon issuance of the license at the end of the licensing process for the transaction, provided that you have disclosed complete and accurate details of your proposed use, no license is finally effective unless and until full payment is received from you (either by publisher or by CCC) as provided in CCC's Billing and Payment terms and conditions. If full payment is not received on a timely basis, then any license preliminarily granted shall be deemed automatically revoked and shall be void as if never granted. Further, in the event that you breach any of these terms and conditions or any of CCC's Billing and Payment

terms and conditions, the license is automatically revoked and shall be void as if never granted. Use of materials as described in a revoked license, as well as any use of the materials beyond the scope of an unrevoked license, may constitute copyright infringement and publisher reserves the right to take any and all action to protect its copyright in the materials.

9. Warranties: Publisher makes no representations or warranties with respect to the licensed material.

10. Indemnity: You hereby indemnify and agree to hold harmless publisher and CCC, and their respective officers, directors, employees and agents, from and against any and all claims arising out of your use of the licensed material other than as specifically authorized pursuant to this license.

11. No Transfer of License: This license is personal to you and may not be sublicensed, assigned, or transferred by you to any other person without publisher's written permission.

12. No Amendment Except in Writing: This license may not be amended except in a writing signed by both parties (or, in the case of publisher, by CCC on publisher's behalf).

13. Objection to Contrary Terms: Publisher hereby objects to any terms contained in any purchase order, acknowledgment, check endorsement or other writing prepared by you, which terms are inconsistent with these terms and conditions or CCC's Billing and Payment terms and conditions. These terms and conditions, together with CCC's Billing and Payment terms and conditions (which are incorporated herein), comprise the entire agreement between you and publisher (and CCC) concerning this licensing transaction. In the event of any conflict between your obligations established by these terms and conditions and those established by CCC's Billing and Payment terms and conditions, these terms and conditions shall control.

14. Revocation: Elsevier or Copyright Clearance Center may deny the permissions described in this License at their sole discretion, for any reason or no reason, with a full refund payable to you. Notice of such denial will be made using the contact information provided by you. Failure to receive such notice will not alter or invalidate the denial. In no event will Elsevier or Copyright Clearance Center be responsible or liable for any costs, expenses or damage incurred by you as a result of a denial of your permission request, other than a refund of the amount(s) paid by you to Elsevier and/or Copyright Clearance Center for denied permissions.

LIMITED LICENSE

The following terms and conditions apply only to specific license types:

15. **Translation**: This permission is granted for non-exclusive world **English** rights only unless your license was granted for translation rights. If you licensed translation rights you may only translate this content into the languages you requested. A professional translator must perform all translations and reproduce the content word for word preserving the integrity of the article. If this license is to re-use 1 or 2 figures then permission is granted for non-exclusive world rights in all languages.

16. **Posting licensed content on any Website**: The following terms and conditions apply as follows: Licensing material from an Elsevier journal: All content posted to the web site must maintain the copyright information line on the bottom of each image; A hyper-text must be included to the Homepage of the journal from which you are licensing at http://www.sciencedirect.com/science/journal/xxxxx or the Elsevier homepage for books at http://www.elsevier.com; Central Storage: This license does not include permission for a scanned version of the material to be stored in a central repository such as that provided by Heron/XanEdu.

Licensing material from an Elsevier book: A hyper-text link must be included to the Elsevier homepage at http://www.elsevier.com . All content posted to the web site must maintain the copyright information line on the bottom of each image.

Posting licensed content on Electronic reserve: In addition to the above the following clauses are applicable: The web site must be password-protected and made available only to bona fide students registered on a relevant course. This permission is granted for 1 year only. You may obtain a new license for future website posting.

17. **For journal authors**: the following clauses are applicable in addition to the above:
Preprints:

A preprint is an author's own write-up of research results and analysis, it has not been peer-reviewed, nor has it had any other value added to it by a publisher (such as formatting, copyright, technical enhancement etc.).

Authors can share their preprints anywhere at any time. Preprints should not be added to or enhanced in any way in order to appear more like, or to substitute for, the final versions of articles however authors can update their preprints on arXiv or RePEc with their Accepted Author Manuscript (see below).

If accepted for publication, we encourage authors to link from the preprint to their formal publication via its DOI. Millions of researchers have access to the formal publications on ScienceDirect, and so links will help users to find, access, cite and use the best available version. Please note that Cell Press, The Lancet and some society-owned have different preprint policies. Information on these policies is available on the journal homepage.

Accepted Author Manuscripts: An accepted author manuscript is the manuscript of an article that has been accepted for publication and which typically includes author-incorporated changes suggested during submission, peer review and editor-author communications.

Authors can share their accepted author manuscript:

- immediately
  - via their non-commercial person homepage or blog
  - by updating a preprint in arXiv or RePEc with the accepted manuscript
  - via their research institute or institutional repository for internal institutional uses or as part of an invitation-only research collaboration work-group
  - directly by providing copies to their students or to research collaborators for their personal use
  - for private scholarly sharing as part of an invitation-only work group on commercial sites with which Elsevier has an agreement
- after the embargo period
  - via non-commercial hosting platforms such as their institutional repository
  - via commercial sites with which Elsevier has an agreement

In all cases accepted manuscripts should:

- link to the formal publication via its DOI
- bear a CC-BY-NC-ND license - this is easy to do
- if aggregated with other manuscripts, for example in a repository or other site, be shared in alignment with our hosting policy not be added to or enhanced in any way to appear more like, or to substitute for, the published journal article.

Published journal article (JPA): A published journal article (PJA) is the definitive final record of published research that appears or will appear in the journal and embodies all value-adding publishing activities including peer review co-ordination, copy-editing, formatting, (if relevant) pagination and online enrichment.

Policies for sharing publishing journal articles differ for subscription and gold open access articles:

Subscription Articles: If you are an author, please share a link to your article rather than the full-text. Millions of researchers have access to the formal publications on ScienceDirect, and so links will help your users to find, access, cite, and use the best available version. Theses and dissertations which contain embedded PJAs as part of the formal submission can be posted publicly by the awarding institution with DOI links back to the formal publications on ScienceDirect.

If you are affiliated with a library that subscribes to ScienceDirect you have additional private sharing rights for others' research accessed under that agreement. This includes use for classroom teaching and internal training at the institution (including use in course packs and courseware programs), and inclusion of the article for grant funding purposes.

Gold Open Access Articles: May be shared according to the author-selected end-user license and should contain a CrossMark logo, the end user license, and a DOI link to the formal publication on ScienceDirect.

Please refer to Elsevier's posting policy for further information.

18. **For book authors** the following clauses are applicable in addition to the above: Authors are permitted to place a brief summary of their work online only. You are not allowed to download and post the published electronic version of your chapter, nor may you scan the printed edition to create an electronic version. **Posting to a repository:** Authors are permitted to post a summary of their chapter only in their institution's repository.

19. **Thesis/Dissertation**: If your license is for use in a thesis/dissertation your thesis may be submitted to your institution in either print or electronic form. Should your thesis be published commercially, please reapply for permission. These requirements include permission for the Library and Archives of Canada to supply single copies, on demand, of the complete thesis and include permission for Proquest/UMI to supply single copies, on demand, of the complete thesis. Should your thesis be published commercially, please reapply for permission. Theses and dissertations which contain embedded PJAs as part of the formal submission can be posted publicly by the awarding institution with DOI links back to the formal publications on ScienceDirect.

Elsevier Open Access Terms and Conditions

You can publish open access with Elsevier in hundreds of open access journals or in nearly 2000 established subscription journals that support open access publishing. Permitted third party re-use of these open access articles is defined by the author's choice of Creative Commons user license. See our open access license policy for more information.

Terms & Conditions applicable to all Open Access articles published with Elsevier: Any reuse of the article must not represent the author as endorsing the adaptation of the article nor should the article be modified in such a way as to damage the author's honour or reputation. If any changes have been made, such changes must be clearly indicated.

The author(s) must be appropriately credited and we ask that you include the end user license and a DOI link to the formal publication on ScienceDirect.

If any part of the material to be used (for example, figures) has appeared in our publication with credit or acknowledgement to another source it is the responsibility of the user to ensure their reuse complies with the terms and conditions determined by the rights holder.

Additional Terms & Conditions applicable to each Creative Commons user license:
CC BY: The CC-BY license allows users to copy, to create extracts, abstracts and new works from the Article, to alter and revise the Article and to make commercial use of the Article (including reuse and/or resale of the Article by commercial entities), provided the user gives appropriate credit (with a link to the formal publication through the relevant DOI), provides a link to the license, indicates if changes were made and the licensor is not represented as endorsing the use made of the work. The full details of the license are available at http://creativecommons.org/licenses/by/4.0.
CC BY NC SA: The CC BY-NC-SA license allows users to copy, to create extracts, abstracts and new works from the Article, to alter and revise the Article, provided this is not done for commercial purposes, and that the user gives appropriate credit (with a link to the formal publication through the relevant DOI), provides a link to the license, indicates if changes were made and the licensor is not represented as endorsing the use made of the work. Further, any new works must be made available on the same conditions. The full details of the license are available at http://creativecommons.org/licenses/by-nc-sa/4.0.
CC BY NC ND: The CC BY-NC-ND license allows users to copy and distribute the Article, provided this is not done for commercial purposes and further does not permit distribution of the Article if it is changed or edited in any way, and provided the user gives appropriate credit (with a link to the formal publication through the relevant DOI), provides a link to the license, and that the licensor is not represented as endorsing the use made of the work. The full details of the license are available at http://creativecommons.org/licenses/by-nc-nd/4.0.
Any commercial reuse of Open Access articles published with a CC BY NC SA or CC BY NC ND license requires permission from Elsevier and will be subject to a fee.
Commercial reuse includes:

- Associating advertising with the full text of the Article
- Charging fees for document delivery or access
- Article aggregation
- Systematic distribution via e-mail lists or share buttons

Posting or linking by commercial companies for use by customers of those companies.

20. Other Conditions:

v1.7

Questions? customercare@copyright.com **or +1-855-239-3415 (toll free in the US) or +1-978-646-2777.**

ELSEVIER LICENSE
TERMS AND CONDITIONS

Nov 25, 2015

This is a License Agreement between Athira Mohanan ("You") and Elsevier ("Elsevier") provided by Copyright Clearance Center ("CCC"). The license consists of your order details, the terms and conditions provided by Elsevier, and the payment terms and conditions.

All payments must be made in full to CCC. For payment instructions, please see information listed at the bottom of this form.

Supplier	Elsevier Limited The Boulevard,Langford Lane Kidlington,Oxford,OX5 1GB,UK
Registered Company Number	1982084
Customer name	Athira Mohanan
Customer address	Trent Centre for Biomaterials Research
	Peterborough, ON K9H7B8
License number	3755960014873
License date	Nov 25, 2015
Licensed Content Publisher	Elsevier
Licensed Content Publication	Energy
Licensed Content Title	Mitigating crystallization of saturated FAMES in biodiesel: 5. The unusual phase behavior of a structured triacylglycerol dimer and methyl palmitate binary system
Licensed Content Author	Athira Mohanan,Laziz Bouzidi,Shaojun Li,Suresh S. Narine
Licensed Content Date	15 December 2015
Licensed Content Volume Number	93
Licensed Content Issue Number	n/a
Type of Use	reuse in a thesis/dissertation
Intended publisher of new work	other
Portion	full article
Format	both print and electronic
Are you the author of this Elsevier article?	Yes
Will you be translating?	No
Title of your thesis/dissertation	Mitigating Crystallization of Biodiesel: Strategies with Additives
Expected completion date	Sep 2015
	295

Estimated size (number of pages)	
Elsevier VAT number	GB 494 6272 12
Permissions price	0.00 CAD
VAT/Local Sales Tax	0.00 CAD / 0.00 GBP
Total	0.00 CAD

Terms and Conditions

INTRODUCTION

1. The publisher for this copyrighted material is Elsevier. By clicking "accept" in connection with completing this licensing transaction, you agree that the following terms and conditions apply to this transaction (along with the Billing and Payment terms and conditions established by Copyright Clearance Center, Inc. ("CCC"), at the time that you opened your Rightslink account and that are available at any time at http://myaccount.copyright.com).

GENERAL TERMS

2. Elsevier hereby grants you permission to reproduce the aforementioned material subject to the terms and conditions indicated.

3. Acknowledgement: If any part of the material to be used (for example, figures) has appeared in our publication with credit or acknowledgement to another source, permission must also be sought from that source. If such permission is not obtained then that material may not be included in your publication/copies. Suitable acknowledgement to the source must be made, either as a footnote or in a reference list at the end of your publication, as follows:

"Reprinted from Publication title, Vol /edition number, Author(s), Title of article / title of chapter, Pages No., Copyright (Year), with permission from Elsevier [OR APPLICABLE SOCIETY COPYRIGHT OWNER]." Also Lancet special credit - "Reprinted from The Lancet, Vol. number, Author(s), Title of article, Pages No., Copyright (Year), with permission from Elsevier."

4. Reproduction of this material is confined to the purpose and/or media for which permission is hereby given.

5. Altering/Modifying Material: Not Permitted. However figures and illustrations may be altered/adapted minimally to serve your work. Any other abbreviations, additions, deletions and/or any other alterations shall be made only with prior written authorization of Elsevier Ltd. (Please contact Elsevier at permissions@elsevier.com)

6. If the permission fee for the requested use of our material is waived in this instance, please be advised that your future requests for Elsevier materials may attract a fee.

7. Reservation of Rights: Publisher reserves all rights not specifically granted in the combination of (i) the license details provided by you and accepted in the course of this licensing transaction, (ii) these terms and conditions and (iii) CCC's Billing and Payment terms and conditions.

8. License Contingent Upon Payment: While you may exercise the rights licensed immediately upon issuance of the license at the end of the licensing process for the transaction, provided that you have disclosed complete and accurate details of your proposed use, no license is finally effective unless and until full payment is received from you (either by publisher or by CCC) as provided in CCC's Billing and Payment terms and conditions. If full payment is not received on a timely basis, then any license preliminarily granted shall be deemed automatically revoked and shall be void as if never granted. Further, in the event that you breach any of these terms and conditions or any of CCC's Billing and Payment

terms and conditions, the license is automatically revoked and shall be void as if never granted. Use of materials as described in a revoked license, as well as any use of the materials beyond the scope of an unrevoked license, may constitute copyright infringement and publisher reserves the right to take any and all action to protect its copyright in the materials.

9. Warranties: Publisher makes no representations or warranties with respect to the licensed material.

10. Indemnity: You hereby indemnify and agree to hold harmless publisher and CCC, and their respective officers, directors, employees and agents, from and against any and all claims arising out of your use of the licensed material other than as specifically authorized pursuant to this license.

11. No Transfer of License: This license is personal to you and may not be sublicensed, assigned, or transferred by you to any other person without publisher's written permission.

12. No Amendment Except in Writing: This license may not be amended except in a writing signed by both parties (or, in the case of publisher, by CCC on publisher's behalf).

13. Objection to Contrary Terms: Publisher hereby objects to any terms contained in any purchase order, acknowledgment, check endorsement or other writing prepared by you, which terms are inconsistent with these terms and conditions or CCC's Billing and Payment terms and conditions. These terms and conditions, together with CCC's Billing and Payment terms and conditions (which are incorporated herein), comprise the entire agreement between you and publisher (and CCC) concerning this licensing transaction. In the event of any conflict between your obligations established by these terms and conditions and those established by CCC's Billing and Payment terms and conditions, these terms and conditions shall control.

14. Revocation: Elsevier or Copyright Clearance Center may deny the permissions described in this License at their sole discretion, for any reason or no reason, with a full refund payable to you. Notice of such denial will be made using the contact information provided by you. Failure to receive such notice will not alter or invalidate the denial. In no event will Elsevier or Copyright Clearance Center be responsible or liable for any costs, expenses or damage incurred by you as a result of a denial of your permission request, other than a refund of the amount(s) paid by you to Elsevier and/or Copyright Clearance Center for denied permissions.

LIMITED LICENSE

The following terms and conditions apply only to specific license types:

15. **Translation**: This permission is granted for non-exclusive world **English** rights only unless your license was granted for translation rights. If you licensed translation rights you may only translate this content into the languages you requested. A professional translator must perform all translations and reproduce the content word for word preserving the integrity of the article.

16. **Posting licensed content on any Website**: The following terms and conditions apply as follows: Licensing material from an Elsevier journal: All content posted to the web site must maintain the copyright information line on the bottom of each image; A hyper-text must be included to the Homepage of the journal from which you are licensing at http://www.sciencedirect.com/science/journal/xxxxx or the Elsevier homepage for books at http://www.elsevier.com; Central Storage: This license does not include permission for a scanned version of the material to be stored in a central repository such as that provided by Heron/XanEdu.

Licensing material from an Elsevier book: A hyper-text link must be included to the Elsevier homepage at http://www.elsevier.com . All content posted to the web site must maintain the copyright information line on the bottom of each image.

Posting licensed content on Electronic reserve: In addition to the above the following clauses are applicable: The web site must be password-protected and made available only to bona fide students registered on a relevant course. This permission is granted for 1 year only. You may obtain a new license for future website posting.

17. **For journal authors:** the following clauses are applicable in addition to the above:
Preprints:
A preprint is an author's own write-up of research results and analysis, it has not been peer-reviewed, nor has it had any other value added to it by a publisher (such as formatting, copyright, technical enhancement etc.).

Authors can share their preprints anywhere at any time. Preprints should not be added to or enhanced in any way in order to appear more like, or to substitute for, the final versions of articles however authors can update their preprints on arXiv or RePEc with their Accepted Author Manuscript (see below).

If accepted for publication, we encourage authors to link from the preprint to their formal publication via its DOI. Millions of researchers have access to the formal publications on ScienceDirect, and so links will help users to find, access, cite and use the best available version. Please note that Cell Press, The Lancet and some society-owned have different preprint policies. Information on these policies is available on the journal homepage.

Accepted Author Manuscripts: An accepted author manuscript is the manuscript of an article that has been accepted for publication and which typically includes author-incorporated changes suggested during submission, peer review and editor-author communications.

Authors can share their accepted author manuscript:

- immediately
  - via their non-commercial person homepage or blog
  - by updating a preprint in arXiv or RePEc with the accepted manuscript
  - via their research institute or institutional repository for internal institutional uses or as part of an invitation-only research collaboration work-group
  - directly by providing copies to their students or to research collaborators for their personal use
  - for private scholarly sharing as part of an invitation-only work group on commercial sites with which Elsevier has an agreement
- after the embargo period
  - via non-commercial hosting platforms such as their institutional repository
  - via commercial sites with which Elsevier has an agreement

In all cases accepted manuscripts should:

- link to the formal publication via its DOI
- bear a CC-BY-NC-ND license - this is easy to do
- if aggregated with other manuscripts, for example in a repository or other site, be shared in alignment with our hosting policy not be added to or enhanced in any way to appear more like, or to substitute for, the published journal article.

Published journal article (JPA): A published journal article (PJA) is the definitive final record of published research that appears or will appear in the journal and embodies all value-adding publishing activities including peer review co-ordination, copy-editing, formatting, (if relevant) pagination and online enrichment.

Policies for sharing publishing journal articles differ for subscription and gold open access articles:

Subscription Articles: If you are an author, please share a link to your article rather than the full-text. Millions of researchers have access to the formal publications on ScienceDirect, and so links will help your users to find, access, cite, and use the best available version. Theses and dissertations which contain embedded PJAs as part of the formal submission can be posted publicly by the awarding institution with DOI links back to the formal publications on ScienceDirect.

If you are affiliated with a library that subscribes to ScienceDirect you have additional private sharing rights for others' research accessed under that agreement. This includes use for classroom teaching and internal training at the institution (including use in course packs and courseware programs), and inclusion of the article for grant funding purposes.

Gold Open Access Articles: May be shared according to the author-selected end-user license and should contain a CrossMark logo, the end user license, and a DOI link to the formal publication on ScienceDirect.

Please refer to Elsevier's posting policy for further information.

18. **For book authors** the following clauses are applicable in addition to the above: Authors are permitted to place a brief summary of their work online only. You are not allowed to download and post the published electronic version of your chapter, nor may you scan the printed edition to create an electronic version. **Posting to a repository:** Authors are permitted to post a summary of their chapter only in their institution's repository.

19. **Thesis/Dissertation**: If your license is for use in a thesis/dissertation your thesis may be submitted to your institution in either print or electronic form. Should your thesis be published commercially, please reapply for permission. These requirements include permission for the Library and Archives of Canada to supply single copies, on demand, of the complete thesis and include permission for Proquest/UMI to supply single copies, on demand, of the complete thesis. Should your thesis be published commercially, please reapply for permission. Theses and dissertations which contain embedded PJAs as part of the formal submission can be posted publicly by the awarding institution with DOI links back to the formal publications on ScienceDirect.

Elsevier Open Access Terms and Conditions

You can publish open access with Elsevier in hundreds of open access journals or in nearly 2000 established subscription journals that support open access publishing. Permitted third party re-use of these open access articles is defined by the author's choice of Creative Commons user license. See our open access license policy for more information.

Terms & Conditions applicable to all Open Access articles published with Elsevier:
Any reuse of the article must not represent the author as endorsing the adaptation of the article nor should the article be modified in such a way as to damage the author's honour or reputation. If any changes have been made, such changes must be clearly indicated.

The author(s) must be appropriately credited and we ask that you include the end user license and a DOI link to the formal publication on ScienceDirect.

If any part of the material to be used (for example, figures) has appeared in our publication with credit or acknowledgement to another source it is the responsibility of the user to ensure their reuse complies with the terms and conditions determined by the rights holder.